THE ROLE OF ENVIRONMENTAL DYNAMICS AND BIOMOLECULAR STRUCTURE IN THE PROCESS OF MOLECULAR RECOGNITION

THESIS
SUBMITTED FOR THE DEGREE OF
DOCTOR OF PHILOSOPHY (SCIENCE)
OF
JADAVPUR UNIVERSITY
2007

BY

AJAY KUMAR SHAW

DEPARTMENT OF CHEMICAL, BIOLOGICAL AND
MACROMOLECULAR SCIENCES,
S. N. BOSE NATIONAL CENTRE FOR BASIC SCIENCES,
BLOCK JD, SECTOR III, SALT LAKE,
KOLKATA 700 098, INDIA

CERTIFICATE FROM THE SUPERVISOR

This is to certify that the thesis entitled "THE ROLE OF ENVIRONMENTAL DYNAMICS AND BIOMOLECULAR STRUCTURE IN THE PROCESS OF MOLECULAR RECOGNITION" submitted by Sri Ajay Kumar Shaw, who got his name registered on October 7, 2005 for the award of **Ph. D. (Science) degree** of **Jadavpur University**, is absolutely based upon his own work under the supervision of Dr. Samir Kumar Pal and that neither this thesis nor any part of it has been submitted for any degree/diploma or any other academic award anywhere before.

(Signature of Supervisor/date with official seal)

To My Mother

Acknowledgements

I would like to express my sincere gratitude to my supervisor Dr. Samir Kumar Pal for the excellent guidance and care that he has showered on me during my PhD tenure. His keen interest on minutest matter of the research work and his hard working qualities has proved to be a great boost for me while working. I am really thankful to him for his constant support and encouragement.

I would also like to thank Prof. Andy Monkman of Physics Department, University of Durham, UK and Dr. T. Pradeep of Department of Chemistry and Sophisticated Analytical Instrument Facility (SAIF), IIT Madras, for fruitful collaboration. My sincere thanks go to Dr. Kaustuv Das of CAT, Indore, Dr. Nilmoni Sarkar of IIT Kharagpur and Dr. Anindya Datta of IIT Bombay for facilitating the use of their time resolved fluorimeter during the initial stages of my research. I am really grateful to all my mentors of St. Thomas' Boys' School, Kolkata and University of Calcutta for their valuable teachings and blessings, which have allowed me to reach this stage. I am also obliged to the director of S. N. Bose National Centre for Basic Sciences, Prof. Arup Kumar Raychaudhari for his great effort in increasing the experimental facility at the centre, which has proved to be a boon for our research work. I am also thankful to all those faculty members of the centre whose activities at several instances have promoted our progress.

I gratefully acknowledge University Grant Commission, Government of India for providing scholarship.

I am also thankful to my labmates Shankara, Debapriya, Sudarson, Sachin, Protiti and Rajibda for providing me a homely and cheerful environment. I am, especially, thankful to Rupadi (my senior) who has helped me in learning the experimental techniques during my initial days of research and for the fruitful discussions that I had with her. I am also thankful to my friends, Anindita, Amritadi, Arnab, Mohitosh and Prasenjit of University of Calcutta and Debabratada of IIT Kharagpur who have very frequently helped me by providing study materials. I am also thankful to all my friends at this centre for providing company at several instances.

I am really grateful to my two elder brothers, Sanjay and Bijay, for their love and care. Finally I would like to express my gratitude towards my parents for their pains and the untiring efforts that they have put for my studies. Without their blessings this thesis would not have taken its shape.

Dated:
Department of Chemical, Biological
and Macromolecular Sciences,
S. N. Bose National Centre for Basic Sciences,
Salt Lake, Kolkata 700098,
India.

(Ajay Kumar Shaw)

Contents

Page

Chapter 1: Introduction

Chapter 2: Experimental Techniques and Systems

Page

Chapter 3: Instrumentation and Sample Preparation

Chapter 4: Exploration of Correlation between Environmental Dynamics and Biomolecular Structure: Enzyme Protein α-Chymotrypsin in Physiologically Relevant Environments

Chapter 5: Effect of Macromolecular Crowding on Structure and Function of Enzyme *Subtilisin Carlsberg*

Chapter 6: Exploration of the Role of Structure and Dynamics of Biomimetics, Genomic and Synthetic DNAs in Ligand Binding

Chapter 7: Encapsulation of a Genomic DNA in a Nanocage of AOT Reverse Micelle

Chapter 8: Molecular Recognition of Human Serum Albumin in various pH-induced Folded States: Use of a Molecular Ruler to Observe Protein-Folding Intermediates

Chapter 1

Introduction

1.1. Scope of the Role of Environmental Dynamics and Biomolecular Structure in the Process of Molecular Recognition:

"Molecular recognition" [1, 2] process refers to the weak non-covalent interaction [3] which takes place selectively and specifically between small ligand/drug molecules with biological macromolecules (proteins [4] and nucleic acids [5]) and also between biomolecules (protein-protein [6] and protein-DNA [7]). These weak non-covalent interactions, involving hydrophobic, electrostatic, van der Waal's and hydrogen bonding interactions, govern the ligand binding process during biomolecule-ligand interactions. One of the longstanding goals of enzymology has been to elucidate the physical origin of extraordinary specificity of an enzyme, i.e. molecular recognition. It has been proposed that the active site of an enzyme is pre-organized [8]. Hence, it is very interesting to know what happens to this assembly when a large dipole moment is created in the vicinity of this active site. The specific question that arises is: does the reorganization of the neighboring water molecules and protein side chains have any influence on the biological function of enzymes, i.e. enzymatic activity?

Again, a large number of clinically important drugs/ligands and antibiotics are believed to exert their primary biological action by means of non-covalent interactions with DNA and subsequent inhibition of template function. Ligands/drugs generally interact with DNA via two modes – (i) intercalation mode [9, 10], in which the ligand places itself between the adjacent base pairs of DNA and (ii) groove binding [11, 12], in which the ligand binds itself in the major or minor grooves of DNA. At this point, it is interesting to know how rigidly are the ligands bound to macromolecules and what are the consequences of binding on the macromolecular structure. Another major interest behind understanding of molecular recognition lies in the fact that the macromolecules inside the physiological system rarely exist and function alone. So, how are the molecular recognition properties affected *in vivo*? Molecular recognition events are the underlying processes leading to the phenomenon like “biological activity”, and understanding molecular recognition is central to drug design and discovery of new medicine [2] to benefit human health. Drugs/ligands interact with biomolecules at the latter’s active site and efficient biological activity demands good geometric fit as suggested by Emil Fischer in the “Lock and Key” principle along with a high degree of complementarities of polar and non-polar part of ligand and macromolecular binding sites. The other factors contributing to biological activity are ligand and binding site flexibility, distortion energies, desolvation effects, entropy and molecular electrostatic field complementarities [13].

The focus of this thesis is to explore (a) the role of immediate solvent environment around a proteolytic enzyme α-Chymotrypsin in solvent relaxation process that is important for optimal bioactivity, (b) the effect of macromolecular crowding on the enzymatic activity of *Subtilisin Carlsberg*, (c) photophysical studies of an antimalarial and antihelminthic drug, acridine orange used in recognition of biomimetics and nucleic acids, (d) molecular recognition as a tool to study DNA condensation inside reverse micelles and (e) structural intermediates of a transporter protein, Human Serum Albumin at different pH(s). Basically, the studies have been carried out employing organic ligands using their absorption and fluorescence properties. The experimental tools used for studying the dynamical processes involve picosecond time-resolved solvation dynamics, temporal fluorescence anisotropy, time-resolved area normalized emission spectra (TRANES), enzyme kinetics and Förster resonance energy transfer (FRET). The structural studies were done using steady-state absorption, fluorescence, circular dichroism (CD) and dynamic light scattering (DLS) techniques.

1.2. Objective:

Water plays an important role in biomolecular recognition at specific sites of proteins and nucleic acids [14]. Especially, the specific and nonspecific dynamical interactions of biological macromolecules with the water molecules (hydration water) in their close vicinity are essential for restoring biomolecular structure and functionality within a narrow range of temperature, pH and ionic strength [14, 15]. In the recent past significant efforts have been made in order to measure and understand the biomolecular surface hydration [16-20]. One of the early indications about the time scale of the dynamics of hydration came from dielectric measurements on protein solution [20]. The measurements show four distinct relaxation time constants (8.3 ps, 40 ps, 10 ns and 80 ns) of myoglobin solution in contrast to that of bulk water (8.2 ps) at 298 K. However, the lack of spatial resolution in the dielectric relaxation studies has brought complications in the interpretation of the results. The exploration of the hydration dynamics using nuclear magnetic resonance (NMR) technique belongs to two classes of experiments [16], those involving the nuclear overhauser effect (NOE) and the nuclear magnetic relaxation dispersion (NMRD). The ability to study the dynamics of hydration at a particular site of a biomolecule is a major strength of the NOE method. Nevertheless, the intrinsic limitation of time resolution of the NOE has made the dynamics accessible up to sub-nanosecond timescale, reporting 500–300 ps [18, 19].

On the other hand, from the frequency dependence of a typical NMRD experiment it has been possible to report the time scale in the range of 10-50 ps [16, 17]. In contrast to the NOE techniques, the lack of spatial resolution in the NMRD experiments has been considered as [17] one of the major limitations. Spatial and temporal limitations of the earlier experiments impose constraints on the exploration of complete picture of biomolecular hydration dynamics, and simultaneously stimulated molecular dynamics (MD) simulation [21] and femtosecond time-resolved fluorescence studies [15, 22, 23] to enter into the field. In an MD simulation study on the hydration dynamics of a protein plastocyanin, it was observed that the rotational relaxation of the water molecules on an average slows down significantly in the close proximity of the protein surface [21]. Femtosecond time-resolved fluorescence studies on an extrinsic dye probe in a protein pocket explored the solvation dynamics of polar amino acid residues and/or rigid water molecules on slower time scales [22, 23]. However, from these studies the time scales of surface waters of a biomolecule were not evident.

In a recent MD simulation study on the protein Monellin the role of water molecules in the slower (16 ps) hydration relaxation process has been argued. The MD simulation study [24] made a point that the 16 ps component recovered from the femtosecond time-resolved fluorescence stokes shift experiment [25] was too slow to be from water molecules alone as NMRD [26] and other MD simulation [27, 28] studies of aqueous proteins reveal up to 7 times slower water dynamics at the surfaces of the proteins. In another recent work [29] the observed 16 ps component is assigned to be due to *highly quenched conformer*, as the component shows positive (decay) amplitude even at longer wavelengths. The argument is further supported by an experimental observation of similar decay in the fluorescence of tryptophan in a small 22-mer peptide, where the origin of the decay is proposed to be due to a rotamer of the tryptophan [30].

In the context of the above discussion it is extremely important to observe the time scales of solvation of a probe by protein residues in contrast to those by water molecules alone. Here, we have explored the time scales of solvation of a probe by polar protein residues. The fluorescent probe dansyl was covalently attached to a polypeptide chain of a protein α-Chymotrypsin and other polar residues were allowed to come closer to the probe by complete structural denaturation of the protein. The solvation dynamics of the probe in denatured protein was compared with that of the probe at the surface of the protein in the native state, where the dynamics was assumed to be mainly due to water molecules. The temporal fluorescence anisotropy of the chromophore reflecting local microviscosity-controlled diffusion of the probe in the native and the denatured protein was also correlated with the solvation dynamics. The change in the solvation and reorientational dynamics of the probe in the protein upon encapsulation in a nanocage of reverse micelles (RMs) has also been reported.

Enzymatic activity of cytosolic enzymes *in vitro* condition where solution contains very low concentration of protein, substrate and salt, shows different behavior relative to that *in vivo* condition. In the living cell a significant fraction of the total volume is "crowded" by several other macromolecular solutes [31-33]. Crowding can also affect equilibrium of an enzymatic reaction by destabilizing either reactant or products, such that the most favored state excludes the least volume to the other macromolecular species present in the solution [32]. Therefore, considering the possible influence of crowding and/or confinement upon the reaction does an accurate evaluation of the physiological role of a particular reaction characterized *in vitro*. The catalytic properties of an enzyme in microheterogeneous micellar medium [34] and organic solvents [35-38] can be helpful in understanding the catalytic mechanism in the living cell. Sodium dodecyl sulfate (SDS), an anionic surfactant is known to bind strongly to most proteins and cause surfactant-induced unfolding [39-41]. Here we have reported the activity of an enzyme *Subtilisin Carlsberg* (SC) in an aqueous micellar solution. It is observed that the rate of enzymatic reaction of

SC on various substrates is retarded and depends heavily on the micellar concentration in the host solution. In order to understand the dependence of the enzymatic activity on micellar concentration, our experimental results were fitted to a theoretical "pseudophase" model [42] proposed recently for enzymatic activity in aqueous micellar solution. To follow the environmental change at a particular site of the enzyme SC upon interaction with the micelle, intrinsic single tryptophan residue (Trp113) was used as a fluorescent probe. The overall environmental change around SC in the micellar solution was followed from the steady-state and time-resolved fluorescence spectroscopy of a covalently attached dansyl chromophore (nonspecifically labeled) at the surface of the enzyme. Circular dichroism (CD) and dynamic light scattering (DLS) studies reveal the overall structural changes of the enzyme SC upon complexation with SDS micelle.

Dynamic supramolecular assemblies [43] like micelles and reverse micelles are excellent biomimetics for exploration of biological membranes and biologically confined water molecules. RMs resemble the water pockets present in bioaggregates such as proteins, membranes and mitochondria [44-47]. The Aerosol-OT (AOT) RM formed of sodium salt of bis(2-ethylhexyl)sulfosuccinate can compartmentalize a large amount of water in its central core, and the nanoscale aggregation process is fairly well-characterized with respect to size and shape at various water contents [48]. RMs are generally characterized by the degree of hydration, w_0 (ratio of molar concentration of water to that of surfactant) [49, 50], where the radius of the water pool (r in Å) is empirically defined as, $r= 2\times w_0$. In order to study various excited state processes of probe/ligand including proton transfer in different environments, RMs with varying degrees of hydration is a popular choice. Proton transfer playing a major role in many biological and chemical processes [51-53] has also been studied using fluorescence spectroscopy [44, 54-59]. These studies have shown that water inside the RM is generally of two types: (i) interfacial (bound) and (ii) core (free) water. One of the studies [60] has shown the existence of a third type of water (trapped) molecule present between the polar head groups of the individual surfactant molecules. Here, we have studied in detail the solvation and fluorescence depolarization dynamics of a fluorescent DNA interacalator, acridine orange (AO) in AOT RMs containing water (pH=6.9) and NaOH (pH=13.6), SDS, CTAB and TX100 normal micelles using picosecond time-resolved fluorescence spectroscopy. We have also applied wobbling-in-cone model [61] to analyze and interpret the time resolved fluorescence anisotropy decay data of AO in these restricted environments. We have further applied this model to AO intercalated inside genomic salmon sperm DNA and two synthetic oligonucleotides – (1) $(GCGCGCGCGCGC)_2$ [oligo1] and (2) $(CGCAAATTTGCG)_2$ [oligo2] to study the reorientational dynamics of the probe AO within the intercalation site and thus to predict the rigidity of genomic DNA and synthetic oligonucleotides.

The understanding of the mechanism of encapsulation of DNA in very small volumes is important as the media control structure, function, dynamics and thermodynamics of the DNA molecule in the confined region of space. These studies are also very relevant to understand important biological functions of DNA in nucleosome formation and chromatin condensation [62, 63]. In this work we have used homo-molecular (self-quenching) FRET technique to assess the distances between probe molecules (acridine orange; AO) attached with a genomic DNA (from salmon testes) before and after encapsulation of the DNA in anionic AOT RM. We have also carried out the circular dichroism study of the DNA in buffer solution and in the RM. Particular emphasis has been given to the DNA packaged in RMs as a model for condensed form of DNA. AO is known to interact with the DNA with two different mechanisms [5]; one is intercalation and other is electrostatic binding. The technique of FRET is frequently used for deducing intermolecular distances in the proteins and DNA [64] and well known as “molecular ruler”. By observing the picosecond to nanosecond dynamics of nonradiative energy transfer of the AO-DNA complex in buffer and in the RM, we have elucidated the change in distance between two AO molecules upon encapsulation of the DNA in the RM. These observations clearly indicate the signature of condensed form of the DNA in the nanospace. For comparison, we have also studied AO inside the RM without the DNA. In order to unravel the change in local geometrical restriction on the physical motions of the probe we have studied picosecond time-resolved polarization-analyzed anisotropy of AO in the RM without and with the DNA.

Studies on binding of various drugs/ligands to Human Serum Albumin (HSA) at its different folded states are important as the conformation of the carrier protein depends on its immediate physiological environment. It is known that HSA undergoes reversible conformational transformation with change in pH of the solution containing the protein

[65, 66]. At normal pH= 7, HSA assumes the normal form (N) which abruptly changes to fast migrating form at pH values less than 4.3. Upon further reduction in pH to less than 2.7 the F-form changes to the fully extended form (E). On the basic side of the normal pH above pH= 8, the N-form changes to basic form (B) and above pH= 10, the structure changes to another aged form (A) [67]. By using picosecond time-resolved polarization-gated spectroscopy we have explored the nature of binding of protoporphyrin IX (PPIX), which is demonstrated (x-ray crystallography) to reside in domain-IB of HSA [68] in various pH-induced conformers of the protein. The interactions of PPIX in domain-IB in the different conformers of the protein and significant spectral overlap of PPIX-absorption with that of the emission of Trp214 (domain-IIA) offer opportunity to measure inter-domain distances in various conformations of HSA by using picosecond time-resolved Förster resonance energy transfer (FRET) technique. We have also explored another inter-domain distance between PPIX (domain-IB) and an extrinsic fluorophore 2-p-toluidinylnaphthalene-6-sulfonate (TNS) (domain-IIIA). CD and DLS have been used to further characterize the pH-induced folded states.

As a continuation of the above work, in another report we have studied the conformational transformation of three pH-induced conformers of HSA at three different temperatures using CD and DLS techniques. We have also measured the inter-domain separation between domain-I and domain-II applying FRET between Trp214 (donor) in domain-IIA and PPIX (acceptor) in domain-IB using picosecond time-resolved fluorescence techniques.

1.3. Summary of the Work Done:

I. Exploration of Correlation between Environmental Dynamics and Biomolecular Structure: Enzyme α-Chymotryosin in Physiologically Relevant Environments [69]:

Protein dynamics is crucial for protein function, particularly the recognition by small molecules. Proteins in living systems are not isolated, but operate in networks and in a carefully regulated environment [70-72]. Understanding the external control of protein dynamics is consequently important. Hydration and solvent viscosity are among the two external agents [73, 74]. However, the dynamics of solvation of chromophores attached to a protein by amino acid residues in comparison to that by water molecules has remained a long-standing problem in the field of protein solvation dynamics. An attempt to unravel the existing controversy has been made by studying the solvation dynamics of dansyl labeled proteolytic enzyme α-Chymotrypsin in both native and denatured states. In the native state the probe at the surface of the protein reports a solvation time of 133 ps, where the dynamics is mainly due to the water molecules in the close vicinity of the protein (hydration water), whereas, in the denatured state the solvation relaxation of the probe in the randomly oriented polypeptide chain is mainly governed by the polar amino acid residues of the protein with two distinct time constants of ~131 ps and ~900 ps. Earlier it has been shown that the time scale of solvation by hydration water of various protein molecules is about 20 ps [15], which is beyond our instrumental resolution. Here, due to our limited instrumental resolution we miss a significant portion of solvation shift. The temporal fluorescence anisotropy of the probe that reflects typical dynamics of a side chain in the denatured protein is similar to dynamics of solvation of the probe in the microenvironment, reflecting significant interaction of the probe with neighboring polar residues of the protein. The rotational diffusion of the probe at the surface of the protein was found to be much retarded compared to that in the random conformation of the denatured protein. In order to show the effect of environmental restriction on the solvation dynamics, the protein in both native and denatured states have been encapsulated inside reverse micelles (RMs) of varying degree of hydration (w_0). The probe at the surface of the native protein in an aqueous nanospace of a RM (w_0=10) shows significantly slower solvation dynamics compared to that in the bulk buffer. However, upon increasing the size of the RM (w_0=20) the dynamics become faster. The faster solvation dynamics in the larger RM is consistent with the fact that the protein resides in the central water pool of the RM and in the larger sized RM the protein surface sees more core type free water. The solvation dynamics of the probe in the denatured protein in the w_0= 10 RM shows time constants those are different from that of native protein in w_0= 10 RM indicating a minor change of the denatured protein upon encapsulation in the nanospace. Simple theoretical models have been proposed in order to qualitatively understand the experimental findings. Thus, the method used in this work in order to explore key time scales of protein solvation can be effectively used in characterizing solvation patterns and dynamics of other proteins.

II. Effect of Macromolecular Crowding on Structure and Function of Enzyme *Subtilisin Carlsberg* [75]:

In physiological system proteins/enzymes are known to function in a crowded environment of several other cell organelles and thus their recognition properties are heavily influenced by this crowding effect [31-33]. In this study the enzymatic activity of a proteolytic enzyme *Subtilisin Carlsberg* (SC) in anionic sodium dodecyl sulfate (SDS) micellar medium has been explored and found to be retarded compared to that in bulk buffer. Circular Dichroism (CD) study reveals that SDS, which is a potential protein denaturant, has an insignificant denaturizing effect on SC. The structural integrity of the protein offers an opportunity to study the functionality of the enzyme SC in a macromolecular crowding of micelles. Dynamic light scattering data indicates no sandwich-like micelle-SC complex formation ruling out the possibility of interaction of the enzyme with the hydrophobic core of the micelle. The steady-state and time-resolved fluorescence anisotropy of a fluorescent tag dansyl at the nonspecific sites of the enzyme, which essentially probes polarity and geometrical restriction on the surface of the enzyme SC show evidence of micellar crowding in the vicinity of the enzyme. However, the moderate change in the emission properties and temporal anisotropy dynamics of the intrinsic fluorophore Trp113 at a specific site of the enzyme reflects participation of specific site/sites (excluding Trp113) of the enzyme for the interaction with SDS micelle. Our studies on the enzyme kinetics of native-like SC in the micellar solution support a theoretical “pseudophase” model [42] where the interaction of SC with the micelle through its stern layer is assumed. The model also assumes that the surfactant core of the micelle segregates the substrates in the micellar solution. Our anisotropy studies on AAF-AMC substrate in the micellar solution are consistent with the segregation picture. The reported experimental observation on the enzymatic activity of SC, with structural integrity retained (from CD studies) in a macromolecular crowding, would be useful in the understanding of the functionality of enzymes under physiological condition.

III. Exploration of the Role of Structure and Dynamics of Biomimetics, Genomic and Synthetic DNAs in Ligand Binding [76]:

This study provides a detailed picture of dynamics and location of a fluorescent DNA intercalator, acridine orange (AO) in biomimetics (micelles and reverse micelles

(RMs)) and in DNA. The equivalent nature of solvation correlation curve of AO in w_0=2.5 and 10 RMs containing water indicates almost similar environment (i.e., interface) around AO in RMs. In the RM containing NaOH, presence of an isoemissive point indicates the existence of two types of AO – basic AO in the isooctane phase and protonated AO at the interface. Despite the pH of NaOH being higher than the excited state pKa (13.3) of AO, protonated AO is observed at the interface, which indicates that interfacial pH is lower than the pH at the core. The lower value of longer solvation correlation time constant for AO in SDS micelle compared to that in RM indicates that the bound water in RM is much more rigid than that in normal SDS micelle. Wobbling-in-cone [61] data analysis of temporal fluorescence anisotropy decay indicates that AO wobbles much more freely in larger RM inscribing larger semicone angles. Among the micelles, largest semicone angle is exhibited in CTAB micelle, which is due to repulsion between cationic AO and positively charged head groups of CTAB micelle that pushes AO away from the micellar surface. The generalized order parameter (S^2) for AO in genomic salmon sperm DNA is lower than that in synthetic DNA which indicates that AO intercalated to synthetic DNA experiences much more restriction. Again, comparison of two synthetic DNAs – $(GCGCGCGCGCGC)_2$ [oligo1] and $(CGCAAATTTGCG)_2$ [oligo2], indicates that AT containing oligo2 is much more rigid than GC-rich oligo1 as indicated by the S^2 and semicone angle values. Also comparison with previous study [77] on DNA shows that AO is much freer to wobble in their intercalation site than EB. Finally this study would prove to be very useful for predicting mechanisms of reactions involving acridine orange in biomimetics and DNA.

IV. Encapsulation of a Genomic DNA in a Nanocage of AOT Reverse Micelle [78]:

In this report structural compaction of a genomic DNA, an important mechanism for the chromatin condensation [62, 63], in a nanospace of an anionic AOT (bis(2-ethylhexyl)sulfosuccinate) reverse micelles (RMs) has been studied. The homo-molecular picosecond time-resolved Förster resonance energy transfer studies on the DNA-bound acridine orange encapsulated in the RM indicate that the DNA in the nanospace is condensed and shows an insignificant dependency of the structural compaction of the DNA on the degree of hydration (w_0) of the microenvironment. Circular dichroism spectrum shows that condensed DNA assumes the psi-form [79, 80]. Temporal fluorescence anisotropy decay of AO and AO-DNA in RM has been found to coincide, indicative of compartmentalization of DNA inside RM. It may also signify slight perturbation of intercalation upon condensation of DNA, as has been observed in another subsequent study from our group on the interaction of ethidium bromide with DNA (genomic and synthetic) inside RM [81].

V. Molecular Recognition of Human Serum Albumin in various pH-induced Folded States: Use of a Molecular Ruler to Observe Protein-Folding Intermediates:

A. Resonance Energy Transfer and Ligand Binding Studies on pH-induced Folded States of Human Serum Albumin:

Human Serum Albumin (HSA) is a very important transporter protein in the circulatory system. It is a multi-domain binding protein, which binds a wide variety of ligands in its multiple binding sites and aids in transport, distribution and metabolism of many endogenous and exogenous ligands. With change in pH, HSA is known to undergo conformational transformation, which is very essential for picking up and releasing them at sites of differing pH inside physiological system. Hence, the characterization of ligand binding to these pH-induced conformers is extremely important. The binding interaction of a ligand protoporphyrin IX (PPIX), which is demonstrated (x-ray crystallography) to reside in domain-IB [68] at the various pH-induced folded states of HSA has been explored. The ligand PPIX is found to remain attached to all the HSA conformers which offers an opportunity to use Förster resonance energy transfer (FRET) between an intrinsic donor fluorophore (Trp214) located in domain-IIA and the acceptor ligand PPIX to characterize the inter-domain separation between IB and IIA. Additionally, FRET between an extrinsic fluorophore 2-p-toluidinylnaphthalene-6-sulfonate (TNS) possibly located in domain-IIIA and PPIX is also undertaken to quantify the inter-domain separation between IB and IIIA. Circular dichroism and dynamic light scattering studies have been done in conjunction with picosecond time-resolved fluorescence and polarization-gated spectroscopy to determine respectively the secondary and tertiary structures of various pH-induced folded states of the protein. Severe structural perturbation including swelling of the protein is observed in the low pH-induced conformer of HSA as evidenced from all the techniques used. Thus, PPIX a non-covalent binder is proven to be a very efficient acceptor in reporting the inter-domain distances of different pH-induced conformers of HSA.

B. Spectroscopic Studies on the Effect of Temperature on pH-induced Folded States of Human Serum Albumin [82]:

As a continuation of the above study, in this work we have characterized the temperature-induced unfolded states of an important multi-domain transporter protein, Human serum albumin (HSA). Using steady state and time resolved fluorescence spectroscopy we have characterized three different pH-induced conformers of HSA at three different temperatures. Applying Förster resonance energy transfer between the intrinsic donor fluorophore (Trp214) present in domain-IIA and a photosensitizer protoporphyrin IX (PPIX) (acceptor) bound to domain-IB of HSA, we have found out the distance between the donor and acceptor in the different temperature-induced folded conformers of HSA. Circular dichroism studies carried out for different conformers at various pHs indicate significant loss of secondary structures in comparison to the native HSA at neutral pH. Dynamic light scattering studies show that, although there occurs a significant temperature-induced unfolding for N-form HSA, no such unfolding is observed for the other acid and alkali-induced conformers. From the FRET study, it is observed that with increase in temperature the distance between donor and acceptor decreases for E and N conformers of HSA while that for A conformer the distance remains unchanged which is consistent with the salt stabilized HSA at higher ionic strength in alkaline solution. Through this study the non-covalently bound PPIX is shown to be an efficient FRET probe in reporting the different temperature-induced folded states of HSA in buffer solutions of widely differing pH values.

1.4. Plan of Thesis:

The plan of the thesis is as follows:

Chapter 1: This chapter gives a brief introduction to the scope and motivation behind the thesis work. A brief summary of the work done is also included in this chapter.

Chapter 2: This chapter provides a brief overview of the dynamical and steady-state tools, the structural aspects of biologically important systems (proteins, DNAs and biomimetics) and probes to study the molecular recognition processes.

Chapter 3: Details of instrumentation, data analysis and experimental procedure (preparation and purification of materials) has been discussed in this chapter.

Chapter 4: In this chapter molecular recognition of an enzyme α-Chymotrypsin (CHT) in physiologically relevant environments has been discussed.

Chapter 5: Effect of macromolecular crowding on structure and function of enzyme *Subtilisin Carlsberg* (SC) has been discussed in this chapter.

Chapter 6: Exploration of structure and dynamics of biomimetics, genomic and synthetic DNAs has been discussed.

Chapter 7: DNA condensation in a nanocage by using a molecular ruler (FRET) has been discussed in this chapter.

Chapter 8: Molecular recognition of a transporter protein, Human Serum Albumin (HSA) in various pH-induced Folded States using FRET techniques has been discussed in this chapter.

References

[1] P.B. Dervan, Molecular recognition of DNA by small molecules, Bioorg. Med. Chem. 9 (2001) 2215-2235.

[2] H.-J. Böhm and G. Schneider, Protein-Ligand Interactions: From Molecular Recognition to Drug Design in: R. Mannhold, H. Kubinyi and G. Folkers (Eds.), Methods and Principles in Medicinal Chemistry. WILEY-VCH Verlag GmbH & Co., Weinheim, (2002), p. 243.

[3] A. Karshikoff: Non-covalent interactions in proteins, Imperial College Press, London, (2006).

[4] J.K.A. Kamal, T. Xia, S.K. Pal, L. Zhao and A.H. Zewail, Enzyme functionality and solvation of Subtilisin *Carlsberg*: From hours to femtoseconds, Chem. Phys. Lett. 387 (2004) 209-215.

[5] M.B. Lyles, and Cameron, I. L., Interactions of the DNA intercalator acridine orange, with itself, with caffeine, and with double stranded DNA, Biophys. Chem. 96 (2002) 53-76.

[6] C. Capasso, M. Rizzi, E. Menegatti, P. Ascenzi and M. Bolognesi, Crystal structure of the bovine α-Chymotrypsin:kunitz inhibitor complex. An example of multiple protein:protein recognition sites, J. Mol. Recognit. 10 (1997) 26-35.

[7] T.-K. Kim, R.H. Ebright and D. Reinberg, Mechanism of ATP-Dependent Promoter Melting by Transcription Factor IIH, Science 288 (2000) 1418-1421.

[8] S. Guha, K. Sahu, D. Roy, S.K. Mondal, S. Roy and K. Bhattacharyya, Slow Solvation Dynamics at the Active Site of an Enzyme: Implications for Catalysis, Biochemistry 44 (2005) 8940-8947.

[9] L.S. Lerman, Structural considerations in the interaction of DNA and acridines., J. Mol. Biol. 3 (1961) 18-30.

[10] L.S. Lerman, The Structure of the DNA-Acridine Complex, Proc. Natl. Acad. Sci. USA 49 (1963) 94-102.

[11] B.H. Geierstanger and D.E. Wemmer, Complexes of the Minor Groove of DNA, Annu. Rev. Biophys. Biomol. Struct. 24 (1995) 463-493.

[12] P.B. Dervan, Design of sequence-specific DNA-binding molecules, Science 232 (1986) 464-471.

[13] D.L. Nelson and M.M. Cox: Lehninger Principles of Biochemistry, W. H. Freeman & Co., New York, (2000).

[14] J.A. Rupley and G. Careri, Protein hydration and function, Adv. Prot. Chem. 41 (1991) 37-172.

[15] S.K. Pal and A.H. Zewail, Dynamics of Water in Biological Recognition, Chem. Rev. 104 (2004) 2099-2123.

[16] B. Halle and V.P. Denisov, Water and monovalent ions in the minor groove of B-DNA oligonucleotides as seen by NMR, Biopolymers 48 (1998) 210-233.

[17] V.P. Denisov and B. Halle, Protein hydration dynamics in aqueous solution, Faraday Discuss. 103 (1996) 227-244.

[18] K. Wüthrich, M. Billeter, P. Güntert, P. Luginbühl, R. Riek and G. Wider, NMR studies of the hydration of biological macromolecules, Faraday Discuss. 103 (1996) 245-253.

[19] G. Otting, E. Liepinsh and K. Wuthrich, Protein hydration in aqueous solution, Science 254 (1991) 974-980.

[20] R.B. Gregory: Protein-Solvent Interactions, Marcel Dekker, New York, (1995).

[21] C. Rocchi, A.R. Bizzarri and S. Cannistraro, Water dynamical anomalies evidenced by molecular-dynamics simulations at the solvent-protein interface, Phys. Rev. E 57 (1998) 3315-3325.

[22] X.J. Jordanides, M.J. Lang, X. Song and G.R. Fleming, Solvation Dynamics in Protein Environments Studied by Photon Echo Spectroscopy, J. Phys. Chem. B 103 (1999) 7995-8005.

[23] P. Changenet-Barret, C.T. Choma, E.F. Gooding, W.F. DeGrado and R.M. Hochstrasser, Ultrafast Dielectric Response of Proteins from Dynamics Stokes Shifting of Coumarin in Calmodulin, J. Phys. Chem. B 104 (2000) 9322-9329.

[24] L. Nilsson and B. Halle, Molecular Origin of Time-Dependent Fluorescence Shifts in Proteins, Proc. Natl. Acad. Sci. USA 102 (2005) 13867-13872.

[25] J. Peon, Pal, S. K., Zewail, A. H., Hydration at the surface of the protein Monellin: Dynamics with femtosecond resolution, Proc. Natl. Acad. Sci. USA 99 (2002) 10964-10969.

[26] B. Halle, Protein hydration dynamics in solution: a critical survey, Philos. Trans. R. Soc. London B 359 (2004) 1207-1224.

[27] A.R. Bizzarri and S. Cannistraro, Molecular dynamics of water at the protein-solvent interface, J. Phys. Chem. B 106 (2002) 6617-6633.

[28] M. Marchi, F. Sterpone and M. Ceccarelli, Water Rotational Relaxation and Diffusion in Hydrated Lysozyme, J. Am. Chem. Soc. 124 (2002) 6787-6791.

[29] J. Xu, D. Toptygin, K.J. Graver, R.A. Albertini, R.S. Savtchenko, N.D. Meadow, S. Roseman, P.R. Callis, L. Brand and J.R. Knutson, Ultrafast Fluorescence Dynamics of Tryptophan in the Proteins Monellin and IIA, J. Am. Chem. Soc. 128 (2006) 1214-1221.

[30] O.F.A. Larsen, I.H.M. van Stokkum, A. Pandit, R. van Grondelle and H. van Amerongen, Ultrafast Polarized Fluorescence Measurements on Tryptophan and a Tryptophan-Containing Peptide, J. Phys. Chem. B 107 (2003) 3080-3085.

[31] S.B. Zimmerman and A.P. Minton, Macromolecular Crowding: biochemical, biophysical and physiological consequences, Annu. Rev. Biophys. Biomol. Struct. 22 (1993) 27-75.

[32] B.V.D. Berg, R. Wain, C.M. Dobson and R.J. Ellis, Macromolecular crowding perturbs protein refolding kinetics: implications for folding inside the cell, EMBO J. 19 (2000) 3870-3875.

[33] A.P. Minton, The influence of macromolecular crowding and macromolecular confinement on biological reactions in physiological media, J. Biol. Chem. 276 (2001) 10577-10580.

[34] M.S. Celej, M.G. D'Adrea, P.T. Campana, G.D. Fidelio and M.L. Bianconi, Superactivity and conformational changes on α-Chymotrypsin upon interfacial binding to cationic micelles, Biochem. J. 378 (2004) 1059-1066.

[35] K. Griebenow and A.M. Klibanov, On protein denaturation in aqueous-organic mixtures but not in pure organic solvents, J. Am. Chem. Soc. 118 (1996) 11695-11700.

[36] R. Affleck, C.A. Haynes and D.S. Clark, Solvent Dielectric Effects on Protein Dynamics, Proc. Natl. Acad. Sci. USA 89 (1992) 5167-5170.

[37] K. Griebenow, M. Vidal, C. Baez, A.M. Santos and G. Barletta, Nativelike Enzyme Properties Are Important for Optimum Activity in Neat Organic Solvents, J. Am. Chem. Soc. 123 (2001) 5380-5381.

[38] S.G. Martinez, E. Alvira, L.V. Cordero, A. Ferrer, I. Montanes-Clemente and G. Barletta, High Initial Activity but Low Storage Stability Observed for Several Preparations of Subtilisin Carslberg Suspended in Organic Solvents, Biotechnol. Prog. 18 (2002) 1462-1466.

[39] M.N. Jones, Surfactant interactions with biomembranes and proteins, Chem. Soc. Rev. 21 (1992) 127-136.

[40] C. Tanford: The Hydrophobic effect: formation of micellar and biological membranes, Wiley Interscience, New York, (1980).

[41] N.J. Turro, X.-G. Lei, K.P. Anantapadmanabhan and M. Aronson, Spectroscopic probe analysis of Protein-Surfacatant Interactions: The BSA/SDS System, Langmuir 11 (1995) 2525-2533.

[42] P. Viparelli, F. Alfani and M. Cantarella, Models for enzyme superactivity in aqueous solutions of surfactants, Biochem. J. 344 (1999) 765-773.

[43] K. Ariga and T. Kunitake: Supramolecular Chemistry – Fundamentals and Applications, Springer-Verlag, Heidelberg, (2006).

[44] B.E. Cohen, D. Huppert, K.M. Solntsev, Y. Tsfadia, E. Nachiel and M. Gutman, Excited State Proton Transfer in Reverse Micelles, J. Am. Chem. Soc. 124 (2002) 7539-7547.

[45] K. Bhattacharyya, Solvation Dynamics and Proton Transfer in Supramolecular Assemblies, Acc. Chem. Res. 36 (2003) 95-101.

[46] K. Bhattacharyya and B. Bagchi, Slow Dynamics of Constrained Water in Complex Geometries, J. Phys. Chem. A 104 (2000) 10603-10613.

[47] N. Nandi, K. Bhattacharyya and B. Bagchi, Dielectric relaxation and solvation dynamics of water in complex chemical and biological systems, Chem. Rev. 100 (2000) 2013-2046.

[48] K. Kalyanasundaram: Photochemistry in microheterogeneous systems, Academic Press, New York, (1987).

[49] P.L. Luisi, M. Giomini, M.P. Pileni and B.H. Robinson, Reverse micelles as hosts for proteins and small molecules, Biochim. Biophys. Acta 947 (1988) 209-246.

[50] M.P. Pileni, Water in oil collidal droplets used as microreactors., Adv. Colloid Interface Sci. 46 (1993) 139-163.

[51] L.S. Brown and K. Jung, Bacteriorhodopsin-like proteins of eubacteria and fungi: the extent of conservation of the haloarchaeal proton-pumping mechanism, Photochem. Photobiol. Sci. 5 (2006) 538-546.

[52] A.-N. Bondar, J.C. Smith and S. Fischer, Structural and energetic determinants of primary proton transfer in bacteriorhodopsin, Photochem. Photobiol. Sci. 5 (2006) 547-552.

[53] B. Borucki, Proton transfer in the photoreceptors phytochrome and photoactive yellow protein, Photochem. Photobiol. Sci. 5 (2006) 553-566.

[54] E. Bardez, B.T. Goguillon, E. Keh and B. Valeur, J. Phys. Chem. 88 (1984) 1909-1913.

[55] E. Bardez, E. Monnier and B. Valeur, Dynamics of excited-state reactions in reversed micelles. 2. Proton transfer involving various fluorescent probes according to their sites of solubilization, J. Phys. Chem. 89 (1985) 5031-5036.

[56] D. Mandal, S.K. Pal, D. Sukul and K. Bhattacharyya, Photophysical Processes of Merocyanine 540 in Solutions and in Organized Media, J. Phys. Chem. A 103 (1999) 8156-8159.

[57] J.R. Escabi-Perez and J.H. Fendler, Ultrafast excited-state proton transfer in reversed micelles, J. Am. Chem. Soc. 100 (1978) 2234-2236.

[58] O.-H. Kwon and D.-J. Jang, Excited-State Double Proton Transfer of 7-Azaindole in Water Nanopools, J. Phys. Chem. B 109 (2005) 20479-20484.

[59] L. Giestas, C. Yihwa, J.C. Lima, C. Vautier-Giongo, A. Lopes, A.L. Macanita and F.H. Quina, The Dynamics of Ultrafast Excited State Proton Transfer in Anionic Micelles, J. Phys. Chem. A 107 (2003) 3263-3269.

[60] T.K. Jain, M. Varshney and A. Maitra, Structural studies of Aerosol OT reverse micellar aggregates by FT-IR spectroscopy, J. Phys. Chem. 93 (1989) 7409-7416.

[61] G. Lipari and A. Szabo, Effect of librational motion on fluorescence depolarization and nuclear magnetic resonance relaxation in macromolecules and membranes, Biophys. J. 30 (1980) 489-506.

[62] D. Zhong, S.K. Pal and A.H. Zewail, Femtosecond studies of protein-DNA binding and dynamics: Histone I, Chem. Phys. Chem. 2 (2001) 219-227.

[63] J. Bednar, R.A. Horowitz, J. Dubochet and C.L. Woodcock, Chromatin Conformation and Salt-induced Compaction: Three-dimensional Structural Information from Cryoelectron Microscopy, J. Cell. Biol. 131 (1995) 1365-1376.

[64] J.R. Lakowicz: Principles of Fluorescence Spectroscopy, Kluwer Academic/Plenum, New York, (1999).

[65] J.A. Luetscher, Serum Albumin. II. Identification of More than One Albumin in Horse and Human Serum by electrophoretic Mobility in Acid Solution, J. Am. Chem. Soc. 61 (1939) 2888-2890.

[66] J.F. Foster: The Plasma Proteins, Academic Press, New York, (1960).

[67] W. Qiu, L. Zhang, O. Okobiah, Y. Yang, L. Wang, D. Zhong and A.H. Zewail, Ultrafast Solvation Dynamics of Human Serum Albumin: Correlations with Conformational Transitions and Site-Selected Recognition, J. Phys. Chem. B 110 (2006) 10540-10549.

[68] M. Wardell, Z. Wang, J.X. Ho, J. Robert, F. Ruker, J. Ruble and D.C. Carter, The Atomic Structure of Human Methemalbumin at 1.9 Å, Biochem. Biophys. Res. Comm. 291 (2002) 813-819.

[69] A.K. Shaw, R. Sarkar, D. Banerjee, S. Hintschich, A. Monkman and S.K. Pal, Direct observation of protein residue solvation dynamics, J. Photochem. Photobiol. A: Chem. 185 (2006) 76-85.

[70] L.H. Hartwell, J.J. Hopfield, S. Leibler and A.W. Murray, From molecular to modular cell biology, Nature 402 (1999) 47–52.

[71] S. Fields, Proteomics in genomeland, Science 291 (2000) 1221-1224.

[72] T. Misteli, Nuclear structure: protein dynamics: implications for nuclear architecture and gene expression, Science 291 (2001) 843-847.

[73] H. Frauenfelder, P.W. Fenimore and B.H. McMahon, Hydration, slaving and protein function, Biophys. Chem. 98 (2002) 35-48.

[74] P.W. Fenimore, H. Frauenfelder, B.H. McMahon and F.G. Parak, Slaving: Solvent fluctuations dominate protein dynamics and functions, Proc. Natl. Acad. Sci. USA 99 (2002) 16047-16051.

[75] A.K. Shaw and S.K. Pal, Activity of Subtilisin Carlsberg in macromolecular crowding, J. Photochem. Photobiol. B: Biol. 86 (2007) 199-206.

[76] A.K. Shaw and S.K. Pal, Fluorescence Relaxation Dynamics of Acridine Orange in Nanosized Micellar Systems and DNA, J. Phys. Chem. B 111 (2007) 4189-4199.

[77] D.P. Millar, R.J. Robbins and A.H. Zewail, Direct Observation of the Torsional Dynamics of DNA and RNA by Picosecond Spectroscopy, Proc. Natl. Acad. Sci. USA 77 (1980) 5593-5597.

[78] A.K. Shaw, R. Sarkar and S.K. Pal, Direct Observation of DNA condenasation in a nanocage using a molecular ruler, Chem. Phys. Lett. 408 (2005) 366-370.

[79] T. Maniatis, J.J.H. Venable and L.S. Lerman, The Structure of Psi DNA, J. Mol. Biol. 88 (1974) 37-56.

[80] A.V. Pietrini and P.L. Luisi, Circular dichroism properties and average dimensions of DNA containing reverse micellar aggregates, Biochim. Biophys. Acta 1562 (2002) 57-62.

[81] R. Sarkar and S.K. Pal, Ligand-DNA Interaction in a Nanocage of Reverse Micelle, Biopolymers 83 (2006) 675–686.

[82] A.K. Shaw and S.K. Pal, Spectroscopic studies on the effect of temperature on pH-induced folded states of Human Serum Albumin, J. Photochem. Photobiol. B: Biol. (2007) (in Press).

Chapter 2

Experimental Techniques and Systems

In order to investigate the various processes involved in course of molecular recognition study the different dynamical and steady-state tools that have been used are solvation dynamics, fluorescence anisotropy, wobbling-in-cone model, Rouse chain dynamics, Förster resonance energy transfer theory, enzyme kinetics, excited state proton transfer, dynamic light scattering and circular dichroism. In this chapter a brief discussion about these tools has been provided. Also in this chapter, a brief overview of the various systems used has been provided.

2.1. Dynamical and Steady-State Tools:

2.1.1. Solvation Dynamics:

Almost all biological macromolecules, proteins (enzymes) and DNAs, are inactive in the absence of water. Solvation of a protein/enzyme by water molecules (hydration) is particularly important for the stability of the structure and function, especially the recognition at a specific site. This role of hydration in enzyme catalysis is well known and has recently been reviewed in a number of publications [1-3].

(i) Theory: Solvation dynamics refer to the process of reorganization of solvent dipoles around a dipole created instantaneously or an electron/proton injected suddenly in a polar liquid. In order to understand the meaning and scope of solvation dynamics, let us first visualize the physical essence of the dynamical process involved for a solute molecule in a polar solvent [4-6]. A change in the solute is made at time t= 0, by an excitation pulse, which leads to the creation of a dipole. This dipole gives rise to an instantaneous electric field on the solvent molecules. Because of the interaction of permanent dipoles of the solvent with the electric field, the free energy minimum of the solvent shifts to a non-zero value of the polarization. The solvent motion is critical (figure 2-1). Since the solute is excited instantaneously (a Franck-Condon transition as far as the nuclear degrees of freedom are concerned), the solvent molecules at t= 0 find themselves in a relatively high-energy configuration. Subsequently, the solvent molecules begin to move and rearrange themselves to reach their new equilibrium positions (figure 2-2). The nuclear motion involved can be broadly classified into rotational and translational motions.

When the solvent is bulk water, rotational motion would also include hindered rotation, libration, while translation would include the intermolecular vibration due to the extensive hydrogen bonding. The two specific motions, libration and intermolecular vibration, are relatively high in frequency and are expected to play a dominant role in the initial part of solvation [7]. The molecular motions involved are shown schematically in figure 2-1, and in figure 2-3 we show a typical solvation time correlation function. For clarity, we approximate the motions responsible for decay in different regions.

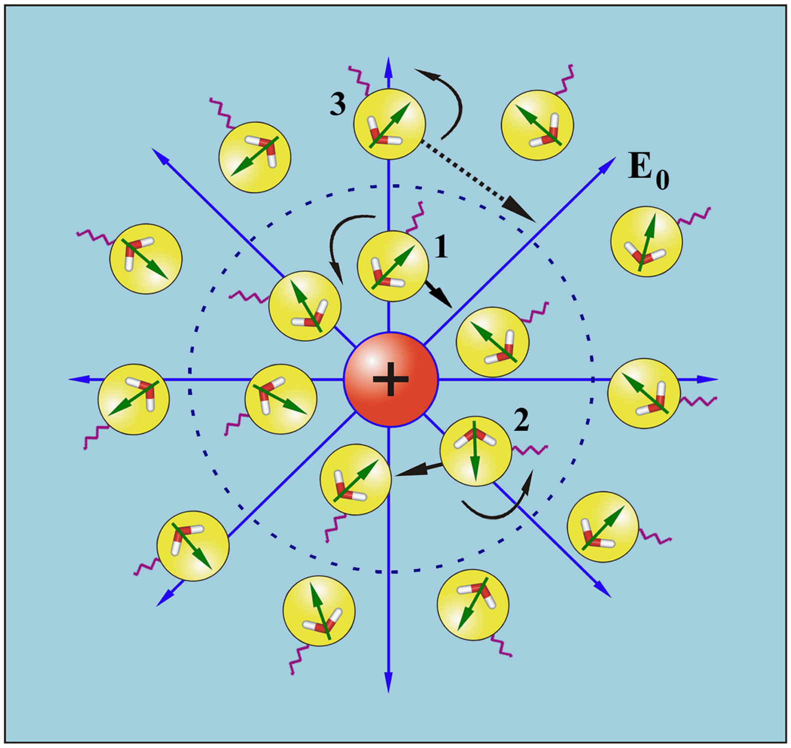

Fig. 2-1. Schematic illustration of solvation of an ion (or dipole) by water. The neighboring molecules (numbered 1 and 2) can either rotate or translate to attain the minimum energy configuration. On the other hand distant water molecule 3 can only rotate to attain minimum energy configuration. The field is shown as E_0. The springs connected to the molecules are meant to denote hydrogen bonding.

A simple way to address the dynamics of polar solvation is to start with the following expression for the solvation energy, $E_{solv}(t)$ [4, 8],

$$E_{solv}(t) = -\frac{1}{2}\int d\mathbf{r}\ \ \mathbf{E_0}(\mathbf{r})\cdot\mathbf{P}(\mathbf{r},t) \qquad (2\text{-}1)$$

where $\mathbf{E_0(r)}$ is the instantaneously created, position dependent electric field from the ion or the dipole of the solute and $\mathbf{P}(\mathbf{r},t)$ is the position and time dependent polarization. The latter is defined by the following expression,

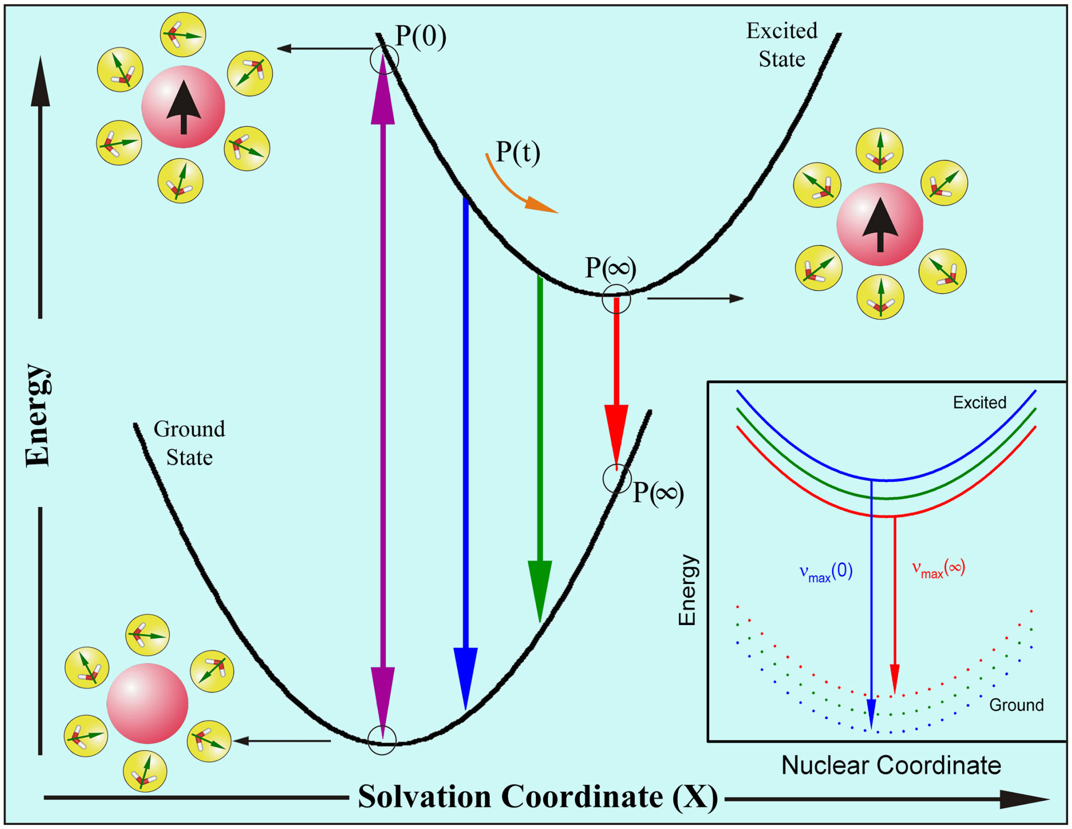

Fig. 2-2. Schematic representation of the potential energy surfaces involved in solvation dynamics showing the water orientational motions along the solvation coordinate together with instantaneous polarization P. In the inset we show the change in the potential energy along the intramolecular nuclear coordinate. As solvation proceeds the energy of the solute comes down giving rise to a red shift in the fluorescence spectrum. Note the instantaneous P, e.g., P(∞), on the two connected potentials.

$$\mathbf{P}(\mathbf{r},t) = \int d\mathbf{\Omega}\ \boldsymbol{\mu}(\mathbf{\Omega})\ \rho\ (\mathbf{r},\mathbf{\Omega},t) \qquad (2\text{-}2)$$

where $\boldsymbol{\mu}(\mathbf{\Omega})$ is the dipole moment vector of a molecule at position $\mathbf{r}$, and $\rho\ (\mathbf{r},\mathbf{\Omega},t)$ is the position, orientation and time dependent density. Therefore, the time dependence of the solvation energy is determined by the time dependence of polarization that is in turn determined by the time dependence of the density. If the perturbation due to the probe on dynamics of bulk water is negligible, then the time dependence of polarization is dictated by the natural dynamics of the liquid.

The theoretical analysis of the time-dependent density is usually carried out using a molecular hydrodynamic approach that is based on the basic conservation (density, momentum and energy) laws and includes the effects of intermolecular (both spatial and

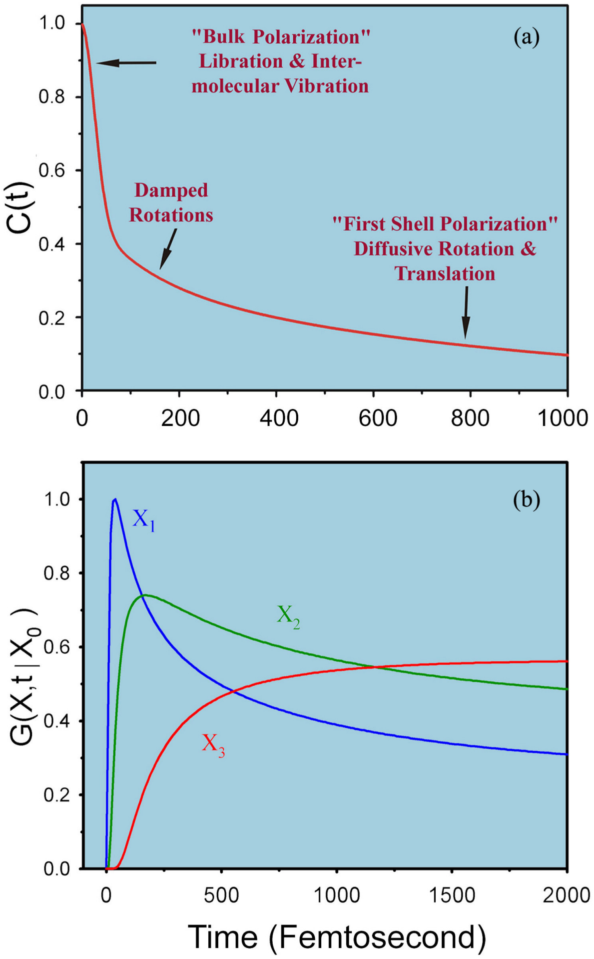

Fig. 2-3. (a) A typical solvation time correlation function for water is shown here. The time correlation function exhibits three distinct regions: The initial ultrafast decay, an intermediate decay of about 200 fs and the last slow decay with time constant of 1 ps. The physical origin of each region is indicated on the plot itself; see text. (b) Green's function $G(X,t \mid X_0)$ for population relaxation along the solvation coordinate (X) is plotted against time in femtosecond. In G, X_0 is the initial position at t= 0. This figure shows the position and time dependence of the population, fluorescence intensity. At early times (when the population is at X_1) there is ultrafast rise followed by an ultrafast decay. At intermediate times (when the population is at X_2) there is a rise followed by a slow decay as shown by the green line. At long times when the population is nearly relaxed (position X_3, red line) we see only a rise.

orientational) correlations. The latter provides the free energy surface on which solvation proceeds. The equation of motion of the density involves both orientational and translational motions of the solvent molecules. The details of the theoretical development are reported in literature [6]; here we shall present a simple physical picture of the observed biphasic solvation dynamics.

Within linear response theory, the solvation correlation function is directly related to the solvation energy as,

$$C(t) = \frac{\langle \delta E(0) \cdot \delta E(t) \rangle}{\langle \delta E^2 \rangle} = \frac{\langle E(t) \rangle - \langle E(\infty) \rangle}{\langle E(0) \rangle - \langle E(\infty) \rangle} \qquad (2\text{-}3)$$

where δE is the fluctuation of solvation energy from the average, equilibrium value. Note that the equality in equation (2-3) indicates the direct relation for the average of the fluctuations over the equilibrium distribution (left) and the non-equilibrium function (right) which relates to observables; without $\langle E(\infty) \rangle$ the correspondence is clear, and $\langle E(\infty) \rangle$ is rigorously the result of the equilibrium term in the numerator and for normalization in the denominator.

The ultrafast component in the solvation time correlation function (see figure 2-3(a)), originates from the initial relaxation in the steep collective solvation potential. The collective potential is steep because it involves the total polarization of the system [4, 6]. This initial relaxation couples mainly to the hindered rotation (that is, libration) and the hindered translation (that is, the intermolecular vibration), which are the available high frequency modes of the solvent; neither long amplitude rotation nor molecular translation are relevant here. The last part in the decay of the solvation correlation function involves larger amplitude rotational and translational motions of the nearest neighbor molecules in the first solvation shell. In the intermediate time, one gets contributions from the moderately damped rotational motions of water molecules. In a sense, with the above description one recovers the famous Onsager's "inverse snow-ball" picture of solvation [9]. The slowest time constant is ~1 ps, which is determined by the individual rotational and translational motions of the molecules in the "first solvation shell" nearly close to the probe. The femtosecond component is dominated by the high frequency hindered rotational and translational (vibration) [7, 10, 11] polarization.

Figure 2-2 shows a schematic of the solvation potential and the orientational motions for the water molecules involved. From the shape of the potential, it can be seen that the transient behavior for the population during solvation should be a decay function on the blue edge of the spectrum and a rise function on the red edge. These wavelength-dependent features can be explained nicely within a generalized model of relaxation in which a Gaussian wave packet relaxes on a harmonic surface. The relaxation is non-exponential and a Green's function can describe the approach of the wave packet along the solvation coordinate, X, to its equilibrium value. For the general non-Markovian case it is given by [12],

$$G(X,t|X_0) = \frac{1}{\sqrt{2\pi\langle X^2\rangle[1-C^2(t)]}} \exp\left[-\frac{[X-X_0C(t)]^2}{2\langle X^2\rangle[1-C^2(t)]}\right] \quad (2\text{-}4)$$

where $\langle X^2\rangle$ is the equilibrium mean square fluctuation of the polarization coordinate in the excited state surface, C(t) is the solvation correlation function described in equation (2-3) and X_0 is the initial value of the packet on the solvation coordinate. Equation (2-4) describes the motion of the wave packet (polarization density) beginning at t= 0 (X_0) as a delta function and according to the solvation time correlation function. As $t\rightarrow \infty$, $C(t)\rightarrow 0$ and we recover the standard Gaussian distribution. At early times ($t\rightarrow 0$), the exponential is large, so the decay is ultrafast, but at long times, the relaxation slows down, ultimately to appear as a rise. In figure 2-3 (bottom), we present calculations of $G(X,t|X_0)$ at different positions along the solvation coordinate: A decay at X_1 and X_2, but with different time constants, and a rise at X_3, as demonstrated experimentally.

The structure and dynamics of solvents at the interface of self organized assemblies (micelles and RMs) and proteins are widely different from their bulk properties [13-18]. As evidenced from literature, solvation dynamics of the interfacial water molecules are about two to three orders of magnitude slower than that of bulk water [19, 20] and this slow solvation dynamics play an important role in many natural biological processes e.g. electron transfer, ion transport, molecular recognition in hydrophobic cavities of proteins and membrane lipid bilayers [21, 22]. The origin of the slow component is attributed to a dynamical equilibrium between bound and free type water [23]; the former one is assumed to form hydrogen bond with polar groups on macromolecules while the later one retains bulk type behavior. This dynamic equilibrium is extremely sensitive to the external environments such as temperature, pressure and according to the activation energy barrier crossing model for the transition of bound water to free water at the macromolecular interface (considering the transition to be of Arrhenius type), the slow component (τ_{slow}) of solvation dynamics at the interface can be expressed as a function of temperature as, [15, 17, 23]

$$\frac{1}{\tau_{s\,low}} = k_{bf} = \frac{k_B T}{h} \exp\left(-\Delta G^0_{bf}/RT\right) \qquad (2\text{-}5)$$

where h, T, k_B, k_{bf} and ΔG_{bf}° are the Planck's constant, temperature in Kelvin, Boltzmann constant, rate constant and binding energy for bound water to free water interconversion, respectively.

(ii) Experimental methods: In order to study solvation dynamics of a probe in an environment, a number of fluorescence transients (about twenty) are taken at different wavelengths across the emission spectrum of the probe. As described earlier, blue and red ends of the emission spectrum are expected to show decay and rise respectively in the transients. The observed fluorescence transients are fitted by using a nonlinear least square fitting procedure to a function $\left(X(t) = \int_0^t E(t')R(t-t')dt'\right)$ comprising of convolution of the IRF (E(t)) with a sum of exponentials $\left(R(t) = A + \sum_{i=1}^{N} B_i \exp(-t/\tau_i)\right)$ with pre-exponential factors (B_i), characteristic lifetimes (τ_i) and a background (A). Relative concentration in a multi-exponential decay is finally expressed as; $\alpha_n = \frac{B_n}{\sum_{i=1}^{N} B_i}$. The relative contribution of a particular decay component (f_n) in the total fluorescence is defined as, $f_n = \frac{\tau_n B_n}{\sum_{i=1}^{N} B_i \tau_i} \times 100$.

The quality of the curve fitting was evaluated by reduced chi-square (0.9-1.1) and residual data. The purpose of the fitting is to obtain the decays in an analytic form suitable for further data analysis.

To construct time-resolved emission spectra (TRES) we follow the technique described in references [24, 25]. As described above the emission intensity decays are analyzed in terms of the multi-exponential model,

$$I(\lambda, t) = \sum_{i=1}^{N} \alpha_i(\lambda) \exp(-t/\tau_i(\lambda)) \qquad (2\text{-}6)$$

where $\alpha_i(\lambda)$ are the pre-exponential factors, with $\Sigma\alpha_i(\lambda) = 1.0$. In this analysis we compute a new set of intensity decays, which are normalized so that the time-integrated intensity at each wavelength is equal to the steady-state intensity at that wavelength. Considering $F(\lambda)$ to be the steady-state emission spectrum, we calculate a set of $H(\lambda)$ values using,

$$H(\lambda) = \frac{F(\lambda)}{\int_0^\infty I(\lambda, t)dt} \qquad (2\text{-}7)$$

which for multiexponential analysis becomes,

$$H(\lambda) = \frac{F(\lambda)}{\sum_i \alpha_i(\lambda)\tau_i(\lambda)} \qquad (2\text{-}8)$$

Then, the appropriately normalized intensity decay functions are given by,

$$I'(\lambda, t) = H(\lambda)I(\lambda, t) = \sum_{i=1}^{N} \alpha'_i(\lambda) \exp\left(-t/\tau_i(\lambda)\right) \qquad (2\text{-}9)$$

where $\alpha'_i(\lambda) = H(\lambda)\alpha_i(\lambda)$. The values of $I'(\lambda,t)$ are used to calculate the intensity at any wavelength and time, and thus the TRES. The values of the emission maxima and spectral width are determined by nonlinear least-square fitting of the spectral shape of the TRES. The spectral shape is assumed to follow a lognormal line shape [24],

$$I(\bar{\nu}) = I_0 \exp\left\{-\left[\ln 2\left(\frac{\ln(\alpha+1)}{b}\right)^2\right]\right\} \qquad (2\text{-}10)$$

with $\alpha = \frac{2b(\bar{\nu} - \overline{\nu_{max}})}{b} - 1$ where I_0 is amplitude, $\bar{\nu}_{max}$ is the wavenumber of the emission maximum and spectral width is given by, $\Gamma = \Delta\left[\frac{\sinh(b)}{b}\right]$. The terms b and Δ are asymmetry and width parameters, respectively and equation (2-9) reduces to a Gaussian function for b= 0.

The time dependent fluorescence Stoke's shifts, as estimated from TRES are used to construct the normalized spectral shift correlation function or the solvent correlation function C(t) and is defined as,

$$C(t) = \frac{\bar{\nu}(t) - \bar{\nu}(\infty)}{\bar{\nu}(0) - \bar{\nu}(\infty)} \qquad (2\text{-}11)$$

where, $\bar{\nu}(0)$, $\bar{\nu}(t)$ and $\bar{\nu}(\infty)$ are the emission maxima (in cm^{-1}) of the TRES at time zero, t and infinity, respectively. The $\bar{\nu}(\infty)$ value is considered to be the emission frequency beyond which insignificant or no spectral shift is observed. The C(t) function represents the temporal response of the solvent relaxation process, as occurs around the probe following its photoexcitation and the associated change in the dipole moment.

Time resolved area normalized emission spectroscopy (TRANES), an extension to TRES, is a novel, model-free method for the analysis of intrinsic or extrinsic fluorescent probes in complex chemical and biological systems [26-28]. TRANES gives the fluorescence spectra that are analogous to the absorption spectra of transient species [28]. In particular, an isoemissive wavelength in TRANES has the same significance as an isosbestic wavelength in absorption spectra. An isoemissive point must be observed in TRANES if there are two emissive species, irrespective of the origin of the species or their kinetics [26]. An isoemissive point in TRANES occurs at the frequency $\bar{\nu}$, where the ratio of the frequency-dependent radiative rates is equal to the ratio of the total radiative rates of the two emitting species [26]. TRANES can be constructed by normalizing the area of each spectrum in TRES such that the area of the spectrum at time t is equal to the area of the spectrum at t= 0 [26].

2.1.2. Rouse Chain Model:

The random coil structures adopted by denatured protein has its surface residues sampling through various conformations, including those that are exposed to bulk water, hydrophobic cores and charged sites. In the denatured state, the dynamics of the protein can be described using models developed for polymeric chains [29]. For this case, we consider the time correlation function for the chain's solvation energy fluctuations as a multiexponential function: $\langle \delta E(0) \delta E(t) \rangle = \sum \alpha_i \exp(-t/\tau_i)$, where δE is the fluctuation of solvation energy from the average equilibrium value and τ_i represents different solvation correlation time. An approximate estimate of τ_i can be obtained by assuming a Rouse chain dynamics for a homopolymer [30]. From this model the eigen values of the normal modes are given by,

$$\lambda_l = \frac{3D_0 l^2 \pi^2}{N^2 b^2}, \; l = 1,3,5,\ldots,(N-1) \qquad (2\text{-}12)$$

where N is the number of monomers in the chain, b^2 is the mean square bond length and D_0 is the translational diffusion coefficient of a monomer. An estimate of D_0 can be obtained from the Stokes-Einstein relation with a stick boundary condition. The characteristic time constant (τ_l) corresponding to a given eigen value of a normal mode (λ_l) is given by, $\tau_l = 1/\lambda_l$.

2.1.3. Fluorescence Anisotropy:

Anisotropy is defined as the extent of polarization of the emission from a fluorophore. Anisotropy measurements are commonly used in biochemical applications of fluorescence. It provides information about the size and shape of proteins or the rigidity of various molecular environments. Anisotropy measurements have also been used to measure protein-protein associations, fluidity of membranes and for immunoassays of numerous substances. These measurements are based on the principle of photoselective excitation of those fluorophore molecules whose absorption transition dipoles are parallel to the electric vector of polarized excitation light. In an isotropic solution, fluorophores are oriented randomly. However, upon selective excitation, partially oriented population of fluorophores with polarized fluorescence emission results. The relative angle between the absorption and emission transition dipole moments determines the maximum measured anisotropy (r_0). The fluorescence anisotropy (r) and polarization (P) are defined by,

$$r = \frac{I_{II} - I_{\perp}}{I_{II} + 2I_{\perp}} \qquad (2\text{-}13)$$

$$P = \frac{I_{II} - I_{\perp}}{I_{II} + I_{\perp}}, \qquad (2\text{-}14)$$

where I_{II} and $I_{\perp}$ are the fluorescence intensities of vertically and horizontally polarized emission when the fluorophore is excited with vertically polarized light. Polarization and anisotropy are interrelated as,

$$r = \frac{2P}{3-P} \qquad (2\text{-}15)$$

and $$P = \frac{3r}{2+r}. \qquad (2\text{-}16)$$

Although polarization and anisotropy provides the same information, anisotropy is preferred since the latter is normalized by total fluorescence intensity ($I_T = I_{II} + 2I_{\perp}$) and in case of multiple emissive species anisotropy is additive while polarization is not. Several phenomena, including rotational diffusion and energy transfer, can decrease the measured anisotropy to values lower than maximum theoretical values. Following a pulsed excitation the fluorescence anisotropy, r(t) of a sphere is given by,

$$r(t) = r_0 \exp(-t/\phi) \qquad (2\text{-}17)$$

where r_0 is the anisotropy at time t= 0 and ϕ is the rotational correlation time of the sphere.

(i) Theory: For a radiating dipole the intensity of light emitted is proportional to the square of the projection of the electric field of the radiating dipole onto the transmission axis of the polarizer. The intensity of parallel and perpendicular projections are given by,

$$I_{II}(\theta,\psi) = \cos^2\theta \qquad (2\text{-}18)$$

$$I_{\perp}(\theta,\psi) = \sin^2\theta \sin^2\psi \qquad (2\text{-}19)$$

where θ and ψ are the orientational angles of a single fluorophore relative to the z and y-axes, respectively (figure 2-4a). In solution, fluorophores remain in random distribution and the anisotropy is calculated by excitation photoselection. Upon photoexcitation by polarized light, the molecules having absorption transition moments aligned parallel to the electric vector of the polarized light have the highest probability of absorption. For the excitation polarization along z-axis, all molecules having an angle ψ with respect to the y-axis will be excited. The population will be symmetrically distributed about the z-axis. For experimentally accessible molecules, the value of ψ will be in the range from 0 to 2π with equal probability. Thus, the ψ dependency can be eliminated.

$$\langle \sin^2\psi \rangle = \frac{\int_0^{2\pi} \sin^2\psi \, d\psi}{\int_0^{2\pi} d\psi} = \frac{1}{2} \qquad (2\text{-}20)$$

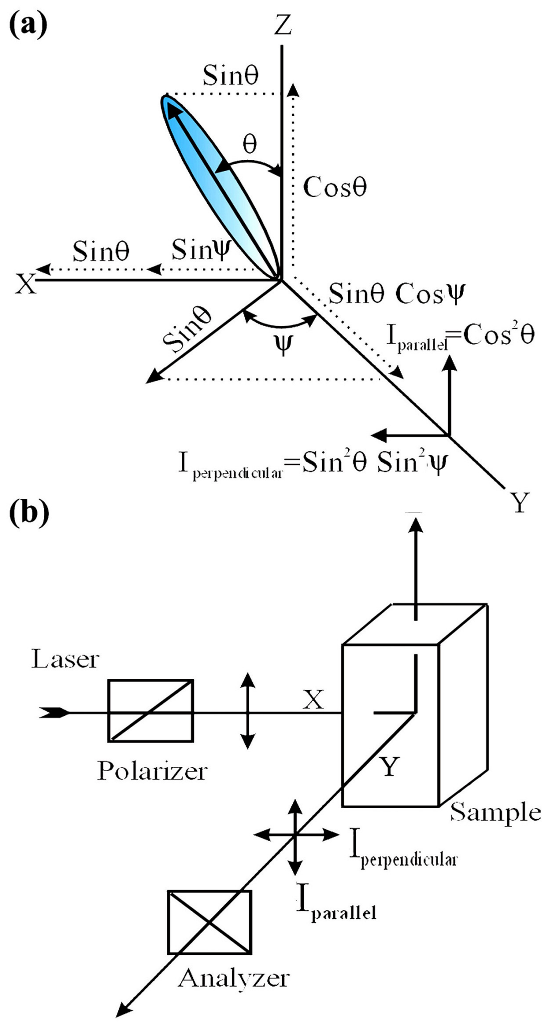

Fig. 2-4. (a) Emission intensity of a single fluorophore (blue ellipsoid) in a coordinate system. (b) Schematic representation of the measurement of fluorescence anisotropy.

and $$I_{II}(\theta) = \cos^2\theta \qquad (2\text{-}21)$$

$$I_{\perp}(\theta) = \frac{1}{2}\sin^2\theta \qquad (2\text{-}22)$$

Consider a collection of molecules oriented relative to the z-axis with probability f(θ). Then, measured fluorescence intensities for this collection after photoexcitation are,

$$I_{II} = \int_0^{\pi/2} f(\theta)\cos^2\theta \, d\theta = k\langle\cos^2\theta\rangle \qquad (2\text{-}23)$$

$$I_{II} = \int_0^{\pi/2} f(\theta)\sin^2\theta d\theta = \frac{k}{2}\left\langle \sin^2\theta \right\rangle \quad (2\text{-}24)$$

where f(θ) dθ is the probability that a fluorophore is oriented between θ and θ +dθ and is given by,

$$f(\theta)d\theta = \cos^2\theta \sin\theta d\theta \quad (2\text{-}25)$$

k is the instrumental constant. Thus, the anisotropy (r) is defined as,

$$r = \frac{3\left\langle \cos^2\theta \right\rangle - 1}{2} \quad (2\text{-}26)$$

when θ= 54.7° i.e. when $\cos^2\theta$= 1/3, the complete loss of anisotropy occurs. Thus, the fluorescence taken at θ= 54.7° with respect to the excitation polarization is expected to be free from the effect of anisotropy and is known as magic angle emission. For collinear absorption and emission dipoles, the value of $\langle\cos^2\theta\rangle$ is given by the following equation,

$$\left\langle \cos^2\theta \right\rangle = \frac{\int_0^{\pi/2} \cos^2\theta f(\theta) d\theta}{\int_0^{\pi/2} f(\theta) d\theta}. \quad (2\text{-}27)$$

Substituting equation (2-25) in equation (2-27) one can get the value of $\langle\cos^2\theta\rangle$= 3/5 and anisotropy value to be 0.4 (from equation (2-26)). This is the maximum value of anisotropy obtained when the absorption and emission dipoles are collinear and when no other depolarization process takes place. However, for most fluorophore, the value of anisotropy is less than 0.4 and it is dependent on the excitation wavelength. It is demonstrated that as the displacement of the absorption and emission dipole occurs by an angle γ relative to each other, it causes further loss of anisotropy (reduction by a factor 2/5) [25] from the value obtained from equation (2-26). Thus, the value of fundamental anisotropy, r_0 is given by,

$$r_0 = \frac{2}{5}\left(\frac{3\cos^2\gamma - 1}{2} \right) \quad (2\text{-}28)$$

For any fluorophore randomly distributed in solution, with one-photon excitation, the value of r_0 varies from -0.2 to 0.4 for γ values varying from 90° to 0°.

(ii) Experimental Methods: For time resolved anisotropy (r(t)) measurements (figure 2-4b), emission polarization is adjusted to be parallel and perpendicular to that of the excitation polarization. Spencer and Weber [31] have derived the relevant equations for the time dependence of $I_{II}(t)$ (equation (2-29)) and $I_{\perp}(t)$ (equation (2-30)) for single rotational and fluorescence relaxation times, ϕ and τ_f, respectively,

$$I_{II}(t) = \exp(-t/\tau_f)(1 + 2r_0 \exp(-t/\phi)) \qquad (2\text{-}29)$$

$$I_{\perp}(t) = \exp(-t/\tau_f)(1 - r_0 \exp(-t/\phi)) \qquad (2\text{-}30)$$

The total fluorescence is given by,

$$F(t) = I_{II}(t) + 2I_{\perp}(t) = 3\exp(-t/\tau_f) = F_0 \exp(-t/\tau_f) \qquad (2\text{-}31)$$

The time dependent anisotropy, r(t) is given by,

$$r(t) = \frac{I_{II}(t) - I_{\perp}(t)}{I_{II}(t) + 2I_{\perp}(t)} = r_0 \exp(-t/\phi) \qquad (2\text{-}32)$$

F(t) depends upon τ_f and r(t) only upon ϕ so that these two lifetimes can be separated. This separation is not possible in steady state measurements. It should be noted that the degree of polarization (P) is not independent of τ_f and is therefore not as useful a quantity as r. For reliable measurement of r(t), three limiting cases can be considered.

(a) If $\tau_f < \phi$, the fluorescence decays before the anisotropy decays, and hence only r_0 can be measured.

(b) If $\phi < \tau_f$, in contrast to steady state measurements, ϕ can be measured in principle. The equations (2-29) and (2-30) show that the decay of the parallel and perpendicular components depends only upon ϕ. The only experimental disadvantage of this case is that those photons emitted after the period of a few times ϕ can not contribute to the determination of ϕ, but provided the signal-to-noise ratio is favorable, this need not be of great concern.

(c) If $\phi \approx \tau_f$, then it becomes the ideal situation since almost all photons are counted within the time (equal to several rotational relaxation times) in which r(t) shows measurable changes.

For systems with multiple rotational correlation times, r(t) is given by,

$$r(t) = r_0 \sum_i \beta_i e^{-t/\phi_i} \qquad (2\text{-}33)$$

where $\sum_i \beta_i = 1$. It should be noted that the instrument monitoring the fluorescence, particularly the spectral dispersion element, responds differently to different polarizations of light, thus emerging the need for a correction factor. For example, the use of diffraction gratings can yield intensities of emission, which depend strongly upon orientation with respect to the plane of the grating. It is inevitably necessary when using such instruments to correct for the anisotropy in response. This instrumental anisotropy is usually termed as G-factor (grating factor) and is defined as the ratio of the transmission efficiency for vertically polarized light to that for horizontally polarized light ($G = I_{II}/I_{\perp}$). Hence, values of fluorescence anisotropy, r(t) corrected for instrumental response, would be given by [32],

$$r(t) = \frac{I_{II}(t) - GI_{\perp}(t)}{I_{II}(t) + 2GI_{\perp}(t)}. \qquad (2\text{-}34)$$

The G-factor at a given wavelength can be determined by exciting the sample with horizontally polarized excitation beam and collecting the two polarized fluorescence decays, one parallel and other perpendicular to the horizontally polarized excitation beam. G-factor can also be determined following longtime tail matching technique [32]. If $\phi < \tau_f$, it can be seen that the curves for $I_{II}(t)$ and $I_{\perp}(t)$ should become identical. If in any experiment they are not, it can usually be assumed that this is due to a non-unitary G-factor. Hence normalizing the two decay curves on the tail of the decay eliminates the G-factor in the anisotropy measurement.

2.1.4. Wobbling-in-Cone Model

Biexponential anisotropy decay can be analyzed using two step and wobbling-in-cone model [33, 34]. According to this model (figure 2-5) the observed slow rotational relaxation with larger rotational time constant (τ_s) is described as a convolution of lateral diffusional relaxation with time constant (τ_L) of the probe along the macromolecular interface and the overall tumbling motion of the macromolecule with time constant (τ_M) [35]. The faster rotational relaxation with shorter rotational time constant (τ_f) is described as the motion of a restricted rotor (probe) having its transition dipole moment undergoing orientation diffusion within a semicone of angle θ_w about an imaginary axis with wobbling time constant (τ_w). Thus, the faster and slower rotational time constants can be written as,

$$\frac{1}{\tau_s} = \frac{1}{\tau_L} + \frac{1}{\tau_M} \qquad (2\text{-}35)$$

$$\frac{1}{\tau_f} = \frac{1}{\tau_w} + \frac{1}{\tau_s} \qquad (2\text{-}36)$$

τ_M i.e., the rotational time constant for overall micellar tumbling can be obtained using Stokes-Einstein-Debye relation [36],

$$\tau_M = \frac{4\pi\eta r_H^3}{3k_B T} \qquad (2\text{-}37)$$

where η is the viscosity of the dispersant (solvent), r_H is the hydrodynamic radius of the micelle, k_B is the Boltzmann constant, T is the absolute temperature. The lateral diffusion coefficient [37] is defined as,

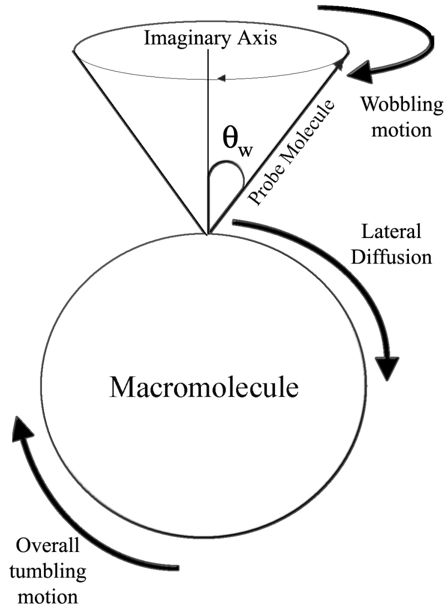

Fig. 2-5. Schematic diagram of Wobbling-in-Cone Model

$$D_L = \frac{r_M^2}{6\tau_L}, \qquad (2\text{-}38)$$

where r_M is the radius of spherical surface of micelle along which the probe translates.

According to this model, the rotational anisotropy decay function is denoted as,

$$r(t) = r_0[\beta + (1-\beta)\exp(-t/\tau_f)]\exp(-t/\tau_s) \qquad (2\text{-}39)$$

Again, $\beta = S^2$ where S^2 is the generalized order parameter that describes the degree of restriction on the wobbling-in-cone orientational motion. S^2 satisfies the inequality $0 \le S^2 \le 1$, where $S^2 = 0$ describes unrestricted reorientation while $S^2 = 1$ means no wobbling-in-cone orientational motion. The semicone angle θ_w is obtained from the ordered parameter as follows:

$$S^2 = \beta = \left[\frac{1}{2}(\mathrm{Cos}\,\theta_w)(1 + \mathrm{Cos}\,\theta_w)\right]^2 \qquad (2\text{-}40)$$

For $\theta_w \le 30^\circ$, the wobbling-in-cone diffusion constant D_W is given by,

$$D_w \cong 7\theta^2 / 24\tau_w \qquad (2\text{-}41a)$$

with θ in radians. However, for $\theta_W \ge 30^\circ$ and all θ_w the D_w is given by,

$$D_w = \frac{1}{[(1-S^2)\tau_w]}\left[\frac{x^2(1+x)^2}{2(x-1)}\left\{\ln\left(\frac{1+x}{2}\right) + \frac{(1-x)}{2}\right\} + \frac{(1-x)}{24}\left(6 + 8x - x^2 - 12x^3 - 7x^4\right)\right]$$

$$(2\text{-}41b)$$

where $x = \mathrm{Cos}\theta_w$, when $\theta_w = 180^\circ$, i.e., there is no restriction to orientation, $S^2 = 0$ and $D_W = 1/6\tau_W$. In case of dansyl labeled α-Chymotrypsin, D_w designated as D_{perp} was defined as,

$$D_{perp} = \frac{1-S^2}{6\phi_{int}}, \qquad (2\text{-}41c)$$

where ϕ_{int} is analogous to τ_w [38]. Cases where the r(t) of fluorescent probes attached to macromolecules does not decay to zero but to a finite value (r_∞) at longer times indicates that the macromolecular reorientation time is much longer than the fluorescence lifetime of the attached fluorophore and the fluorophore is not able to sample through all possible orientations [39]. In these cases the difference (r_0-r_∞) has been used to extract the dynamical parameters.

2.1.5. Förster Resonance Energy Transfer (FRET):

Förster resonance energy transfer [40] is an electrodynamic phenomenon involving the non-radiative transfer of the excited state energy from the donor dipole (D) to an acceptor dipole (A) in the ground state (figure 2-6a). FRET has got wide applications in all fluorescence applications including medical diagnostics, DNA analysis and optical imaging. Since FRET can measure the size of a protein molecule or the thickness of membrane, it is also known as "spectroscopic ruler" [41]. FRET is very often used to measure the distance between two sites on a macromolecule. Basically, FRET is of two types- (a) Homo-molecular FRET and (b) Hetero-molecular FRET. In the former case the same fluorophore acts both as energy donor and acceptor, while in the latter case two different molecules act as donor and acceptor.

Each donor-acceptor (D-A) pair participating in FRET is characterized by a distance known as Förster distance (R_0) that is the D-A separation at which energy transfer is 50% efficient. The R_0 value ranges from 20 to 60 Å. The rate of resonance energy transfer (k_T) from donor to an acceptor is given by [25],

$$k_T = \frac{1}{\tau_D}\left(\frac{R_0}{r}\right)^6 \qquad (2\text{-}42)$$

where τ_D is the lifetime of the donor in the absence of acceptor, R_0 is the Förster distance and r is the donor to acceptor (D-A) distance. The rate of transfer of donor energy depends upon the extent of overlap of the emission spectrum of the donor with the absorption spectrum of the acceptor ($J(\lambda)$), the quantum yield of the donor (Q_D), the relative orientation of the donor and acceptor transition dipoles (κ^2) and the distance between the donor and acceptor molecules (r). In order to estimate FRET efficiency of the donor and hence to determine distances of donor-acceptor pairs, the methodology described below is followed [25]. The Förster distance (R_0) is given by,

$$R_0 = 0.211\left[\kappa^2 n^{-4} Q_D J(\lambda)\right]^{1/6} \text{ (in Å)} \qquad (2\text{-}43)$$

where κ^2 is a factor that describes the relative orientation in space (figure 2-6b) of the transition dipoles of the donor and acceptor, n is the refractive index of the medium, Q_D is the quantum yield of the donor and $J(\lambda)$ is the overlap integral. κ^2 is defined as,

$$\kappa^2 = \left(\cos\theta_T - 3\cos\theta_D\cos\theta_A\right)^2 = \left(\sin\theta_D\sin\theta_A\cos\varphi - 2\cos\theta_D\cos\theta_A\right)^2 \qquad (2\text{-}44)$$

where θ_T is the angle between the emission transition dipole of the donor and the absorption transition dipole of the acceptor, θ_D and θ_A are the angles between these dipoles and the vector joining the donor and acceptor and φ is angle between the planes of the

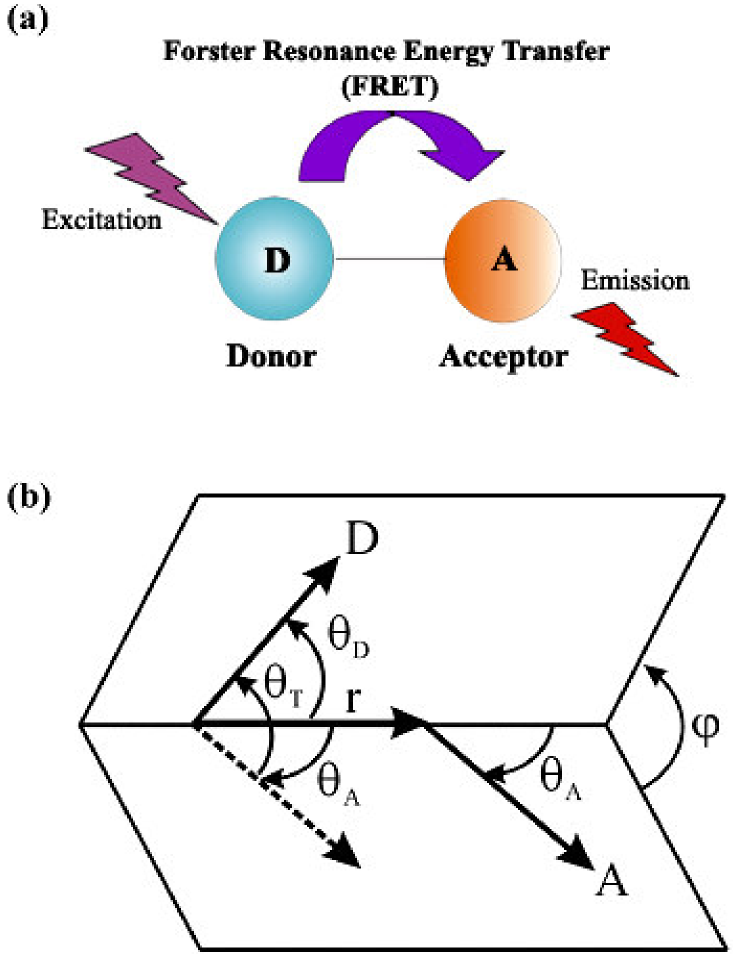

Fig. 2-6. (a) Schematic illustration of the Förster resonance energy transfer (FRET) process. (b) Dependence of the orientation factor κ^2 on the directions of the emission and absorption dipoles of the donor and acceptor respectively.

donor and acceptor (figure 2-6 b). κ^2 value can vary from 0 to 4. For collinear and parallel transition dipole, $\kappa^2 = 4$; for parallel dipole, $\kappa^2 = 1$; and for perpendicularly oriented dipoles, $\kappa^2 = 0$. For donor and acceptors that randomize by rotational diffusion prior to energy transfer, the magnitude of κ^2 is assumed to be 2/3. J(λ), the overlap integral, which expresses the degree of spectral overlap between the donor emission and the acceptor absorption, is given by,

$$J(\lambda) = \frac{\int_0^\infty F_D(\lambda)\varepsilon_A(\lambda)\lambda^4 d\lambda}{\int_0^\infty F_D(\lambda) d\lambda} \qquad (2\text{-}45)$$

where $F_D(\lambda)$ is the fluorescence intensity of the donor in the wavelength range of λ to $\lambda+d\lambda$ and is dimensionless. $\varepsilon_A(\lambda)$ is the extinction coefficient (in $M^{-1}cm^{-1}$) of the acceptor at λ. If λ is in nm, then $J(\lambda)$ is in units of $M^{-1}cm^{-1}nm^4$.

Once the value of R_0 is known, the efficiency of energy transfer can be calculated. The efficiency of energy transfer (E) is the fraction of photons absorbed by the donor which are transferred to the acceptor and is defined as,

$$E = \frac{k_T(r)}{\tau_D^{-1} + k_T(r)} \qquad (2\text{-}46)$$

or

$$E = \frac{R_0^6}{r^6 + R_0^6} \qquad (2\text{-}47)$$

The transfer efficiency is measured using the relative fluorescence intensity of the donor, in absence (F_D) and presence (F_{DA}) of the acceptor as,

$$E = 1 - \frac{F_{DA}}{F_D} \qquad (2\text{-}48a)$$

For D-A systems decaying with multiexponential lifetimes, E is calculated from the amplitude weighted lifetimes $\langle\tau\rangle = \sum_i \alpha_i \tau_i$ [25] of the donor in absence (τ_D) and presence (τ_{DA}) of the acceptor as,

$$E = 1 - \frac{\tau_{DA}}{\tau_D} \qquad (2\text{-}48b)$$

The D-A distances can be measured using equations (2-47), (2-48a) and (2-48b). The distances measured using equations (2-48a) and (2-48b) are revealed as R^S (steady state measurement) and R^{TR} (time resolved measurement), respectively. In one of our recent studies [42], we have reported the potential danger of using equation (2-48a) to conclude the nature of energy transfer as Förster type. The study shows that the energy transfer efficiency E, calculated from steady state experiment (equation (2-48a)) might be due to re-absorption of donor emission, but *not* due to dipole-dipole interaction (FRET).

2.1.6. Enzyme Kinetics:

In order to measure enzymatic activity of CHT in various environments, we follow a mechanism originally proposed by Michaelis and Menten. According to this mechanism [43] a simple enzymatic reaction might be written as,

$$E+S \underset{k_{-1}}{\overset{k_1}{\rightleftharpoons}} ES \xrightarrow{k_2} E+P$$

where E, S and P represent the enzyme, substrate and product. ES is the transient complex of the enzyme with the substrate. The scheme assumes the following facts:

i) Enzyme first combines with substrate to form enzyme-substrate complex in a relatively fast reversible step.

ii) The ES complex then breaks down in a slower second step to yield free enzyme and reaction product P.

As the breakdown of ES to product is the slowest step, rate of reaction,

$$v_0 = k_2[ES] \qquad (2\text{-}50)$$

Total enzyme concentration at any instant $[E_t]$= sum of free and substrate bound enzyme.

Free enzyme at any instant $= [E_t] - [ES]$ (2-51)

Rate of formation of $ES = k_1[E][S] = k_1\{[E_t] - [ES]\}[S]$ (2-52)

Rate of breakdown of $ES = (k_{-1} + k_2)[ES]$ (2-53)

Applying Steady State concept,

$$k_1\{[E_t] - [ES]\}[S] = (k_{-1} + k_2)[ES] \qquad (2\text{-}54)$$

or $$k_1[E_t][S] - k_1[ES][S] = k_{-1}[ES] + k_2[ES]$$

or $$k_1[E_t][S] = \{k_1[S] + (k_{-1} + k_2)\}[ES]$$

or $$[ES] = k_1[E_t][S]/\{k_{-1} + k_2 + k_1[S]\}$$

or $$[ES] = [E_t][S]/\{((k_{-1} + k_2)/k_1) + [S]\}$$

or $$[ES] = [E_t][S]/(K_M + [S]) \qquad (2\text{-}55)$$

K_M is called Michaelis constant, $K_M = (k_{-1} + k_2)/k_1$ (2-56)

Now, $$v_0 = k_2[ES] = k_2([E_t][S])/(K_M + [S]).$$

At high [S], $[S] >> K_M$, $v_0 = v_{max}$.

$$\therefore v_0 = v_{max} = k_2[E_t][S]/[S] = k_2[E_t]$$

$$\therefore v_0 = \frac{v_{max}[S]}{K_M + [S]} \qquad (2\text{-}57)$$

This equation is known as *Michaelis-Menten* equation. It is the rate equation for one-substrate catalyzed reaction. At $v_0 = 0.5\ v_{max}$, it is found that $K_M = [S]$. Hence, K_M is the substrate concentration at which $v_0 = 0.5\ v_{max}$. If we take the reciprocal of both sides of Michaelis-Menten equation, we get,

$$\frac{1}{v_0} = \frac{K_M + [S]}{v_{max}[S]}$$

or

$$\frac{1}{v_0} = \frac{K_M}{v_{max}[S]} + \frac{1}{v_{max}} \qquad (2\text{-}58)$$

This form of Michaelis-Menten Equation is known as Lineweaver-Burk equation**.** For enzymes obeying Michaelis-Menten Equation, a plot of $1/v_0$ vs $1/[S]$ would be a straight line.

The quantity v_{max} varies greatly from enzyme to enzyme. For two steps enzyme reaction, $v_{max} = k_2\ [E_t]$ where k_2 is the rate limiting. If for three steps mechanism k_3 is rate limiting, then $v_{max} = k_3\ [E_t]$. Therefore it is more general to designate rate constant of rate limiting step as k_{cat}. For two steps, $k_2 = k_{cat}$; for three steps, $k_3 = k_{cat}$. Therefore, Michaelis-Menten equation becomes,

$$v_0 = v_{max}[S]/(K_M + [S]) = k_{cat}[E_t][S]/(K_M + [S]) \qquad (2\text{-}59)$$

k_{cat} is a first order rate constant and has units of reciprocal time. To compare catalytic efficiencies of enzymes the ratios of k_{cat}/K_M of different enzymes are to be compared. It is called specificity constant, which is the rate constant for the conversion of (E+S) to (E+P). When $[S] \ll K_M$,

$$v_0 = \frac{k_{cat}}{K_M}[E_t][S] \qquad (2\text{-}60)$$

v_0 depends on $[E_t]$ and [S]. k_{cat}= second order rate constant. Therefore, the unit of k_{cat}/K_M is $M^{-1}s^{-1}$.

2.1.7. Pseudophase Model:

In order to understand the retardation of enzymatic activity in the micellar medium, the theoretical “pseudophase” model, initially introduced for enzymes encapsulated in reverse micelles [44] and recently advanced for enzymes in aqueous micellar environments [45] has been used. According to the model [45] the substrate can partition between three pseudophases of the micelle, namely, free water, bound water and surfactant aggregate.

Here we consider the interaction of the enzyme with the micelle through bound water (stern layer) and *not* directly with the hydrophobic part of the surfactant molecule. The overall rate of substrate consumption, r, is given by [45],

$$r = \frac{k_{cat}^{ff}[E_f][S_f]}{K_M^{ff} + [S_f]} + \frac{k_{cat}^{fb}[E_f][S_b]}{K_M^{fb} + [S_b]} + \frac{k_{cat}^{bf}[E_b][S_f]}{K_M^{bf} + [S_f]} + \frac{k_{cat}^{bb}[E_b][S_b]}{K_M^{bb} + [S_b]} \qquad (2\text{-}57)$$

where [E] and [S] indicate enzyme and substrate concentrations respectively. The subscripts, f and b refer to the free water and bound water phase, respectively. The double superscripts refer to the pseudophases in which the enzyme (first superscript) and substrate (second superscript) are confined. K_M and k_{cat} indicate Michaelis constant and catalytic rate constant of the enzymatic reaction, respectively. A thermodynamic equilibrium of substrate between the free water and the whole micellar aggregate is assumed as follows,

$$[S_f]+[D_N] \xrightleftharpoons{K_s} [S_m] \qquad (2\text{-}58)$$

where K_s is the association constant, $[S_m]$ is the substrate concentration associated with micelle and $[D_N]$ is the concentration of surfactant micellar aggregates, which can be determined from the difference between the CMC and the total concentration of surfactant in the system. Partition equilibrium between the substrate in the bound water, $[S_b]$, and that associated with the micellized surfactant, $[S_s]$, subscript ‘s’ stands for surfactant, is introduced as follows,

$$[S_b] \xrightleftharpoons{P_{bs}} [S_s] \qquad (2\text{-}59)$$

where P_{bs} is the partition coefficient. The above conditions lead to the following relationships for the concentrations of substrate able to react in the presence of micelles,

$$[S_f] = \frac{[S_t]}{1 + K_s[D_N]} \qquad (2\text{-}60)$$

$$[S_b] = \frac{K_s[D_N]}{(1 + K_S[D_N])(1 + P_{bs})}[S_t] \qquad (2\text{-}61)$$

where $[S_t]$ is the total concentration of the substrate in the solution. To describe the enzyme partition in the pseudophases, the following equilibrium is assumed:

$$[E_f]+[D_N] \underset{}{\overset{K_E}{\rightleftharpoons}} [E_b] \tag{2-62}$$

where K_E is the constant of association between the enzyme and micelle. We also have,

$$[E_f]=\frac{[E_t]}{1+K_E[D_N]} \tag{2-63}$$

$$[E_b]=\frac{K_E[D_N][E_t]}{1+K_E[D_N]} \tag{2-64}$$

In principle, substituting equations (2-60), (2-61), (2-63) and (2-64) in equation (2-57) one can obtain the overall enzymatic reaction rate (r). In order to disregard the change in the rate due to interaction of surfactant monomer with the enzyme, a relative rate (r/r_0) with various micellar concentrations can be considered, where r_0 is the reaction rate at the critical micellar concentration (CMC). According to the model, where the concentration of the substrate in the bound phase is negligible in comparison to that of the substrate associated with the surfactant, $[S_b]<<[S_s]$, the substrate aggregated in the micelles is all segregated by the surfactant. The condition is attained at $P_{bs}>>1$ and implies that $[S_m]\approx[S_s]$. This assumption determines that $[S_b]\approx 0$, independently of the equilibrium constant of the substrate-micelle association, K_s. As a consequence, the second and fourth reactions in equation (2-57) can be neglected. Thus, the final form of rate of catalysis is as follows:

$$r=\frac{[E_t][S_t]}{1+K_E[D_N]}\left\{\frac{\eta_{ff}}{(1+K_S[D_N])+\left([S_t]\big/K_m^{ff}\right)}+\frac{[D_N]K_E\eta_{bf}}{(1+K_S[D_N])+\left([S_t]\big/K_m^{bf}\right)}\right\} \tag{2-65}$$

2.1.8. Dynamic Light Scattering:

According to semiclassical theory of light scattering, when light impinges on matter, the electric field of the light induces an oscillating polarization of electrons in the molecules. Hence, the molecules provide a secondary source of light and subsequently scatter light. The frequency shift, the angular distribution, the polarization, and the intensity of scattered light are determined by size, shape and molecular interactions in the scattering material. Dynamic light scattering (DLS) also known as photon correlation spectroscopy (PCS) or Quasi-Elastic Light Scattering (QELS) is one of the most popular technique used to determine the size of the particle.

(i) Theory: DLS experiments are based on two assumptions:

i) Particles exhibit Brownian motion (also called ‘random walk’). The probability density function is given by the formula,

$$P(r,t|0,0) = (4\pi Dt)^{3/2} \exp(-r^2/4Dt) \qquad (2\text{-}66)$$

where D is the translational diffusion coefficient.

ii) The particles are spherical in shape with particles of molecular dimensions. If it is so, then it is possible to apply the Stoke-Einstein relation and hence have a formula that easily gives the diffusion constant,

$$D = \frac{k_B T}{3\pi\eta d_H} \qquad (2\text{-}67)$$

where d_H is the hydrodynamic diameter of the particles, k_B is the Boltzmann constant, T is the temperature in Kelvin degrees and η is the viscosity of the solvent.

(ii) Experimental Methods: It has been seen that particles in dispersion are in a constant, random Brownian motion and that this causes the intensity of scattered light to fluctuate as a function of time. The correlator used in a PCS instrument constructs the intensity autocorrelation function $G(\tau)$ of the scattered intensity:

$$G(\tau) = \langle I(t)I(t+\tau)\rangle \qquad (2\text{-}68)$$

where τ is the time difference (the sample time) of the correlator. For a large number of monodisperse particles in Brownian motion, the correlation function (given the symbol [G]) is an exponential decaying function of the correlator time delay τ:

$$G(\tau) = A[1 + B.\exp(-2\Gamma\tau)] \qquad (2\text{-}69)$$

where A is the baseline of the correlation function, B is the intercept of the correlation function. Γ is the first cumulant and is related to the translational diffusion coefficient as, $\Gamma = Dq^2$, where q is the scattering vector and its magnitude is defined as,

$$q = \left(\frac{4\pi n}{\lambda_0}\right)\sin\left(\frac{\theta}{2}\right) \qquad (2\text{-}70)$$

where n is the refractive index of dispersant, λ_0 is the wavelength of the laser, θ, the scattering angle. For polydisperse samples, the equation can be written as,

$$G(\tau) = A\left[1 + B\left|g^{(1)}(\tau)\right|^2\right] \qquad (2\text{-}71)$$

where the correlation function $g^{(1)}(\tau)$ has no longer a single exponential decay and can be written as the Laplace transform of a continuous distribution $G(\Gamma)$ of decay times:

$$g^{(1)}(\tau) = \int_0^\infty G(\Gamma)\exp(-\Gamma\tau)d\Gamma\,. \qquad (2\text{-}72)$$

The size distribution of the particles are obtained by fitting, using non-linear least square fitting or CONTIN program, the autocorrelation function to multiexponential function. The size distribution obtained is a plot of the relative intensity of light scattered by particles in various size classes and is therefore known as an intensity size distribution. Note that in the intensity distribution graph, the area of the peak for the larger particles will appear at least 10^6 times larger than the peak for the smaller particles. This is because large particles scatter much more light than small particles, as the intensity of scattering of a particle is proportional to the sixth power of its diameter (Rayleigh's approximation). As a result large particles would always be seen even when present in negligible amount.

2.1.9. Circular Dichroism:

Circular dichroism (CD) is now a routine tool in many laboratories with applications to determine whether a chiral molecule has been synthesized or resolved into pure enantiomers and probing the structures of biomoleccules, in particular determining the α-helical content of proteins [46, 47].

(i) Theory: When a plane polarized light passes through an optically active substance, not only do the left (L) and right (R) circularly polarized light rays travel at different speeds, $c_L \neq c_R$, but these two rays are absorbed to a different extent, i.e. $A_L \neq A_R$. The difference in the absorbance of the left and right circularly polarized light, i.e., $\Delta A = A_L - A_R$, is defined as circular dichroism (CD). Circular dichroism spectroscopy follows Beer-Lambert law. If I_0 is the intensity of light incident on the cell, and I, that of emergent light, then absorbance is given by,

$$A = \log_{10}\left(\frac{I_0}{I}\right) = \varepsilon cl \qquad (2\text{-}73)$$

i.e., A is proportional to concentration (c) of optically active substance and optical pathlength (l). If 'c' is in moles/litre and 'l' is in cm, then ε is called the molar absorptivity or molar extinction coefficient. In an optically active medium, two absorbances, A_L and A_R

are considered, where $A_L = \log_{10}(I_0/I_L)$ and $A_R = \log_{10}(I_0/I_R)$. At the time of incidence on the sample, intensity of left and right circularly polarized light are same, i.e. $I_0=I_L=I_R$. Any dicrograph passes periodically changing light through the medium, oscillating between left and right circular polarization, and the difference in absorbances are recorded directly.

$$\Delta A = A_L - A_R = \log_{10}\left(\frac{I_0}{I_L}\right) - \log_{10}\left(\frac{I_0}{I_R}\right) = \log_{10}\left(\frac{I_R}{I_L}\right) \qquad (2\text{-}74)$$

or $$\Delta A = (\Delta\varepsilon)cl. \qquad (2\text{-}75)$$

As seen from equation (2-74), I_0 does not appear in this final equation, so there is no need for a reference beam. The instruments are, therefore, of single beam type.

After passing through an optically active substance, light is changed in two aspects. The maximal amplitude of intensity is no longer confined to a plane; instead it traces out an ellipse. Ellipticity is defined as the arctangent of the ratio of minor axis to the major axis of the ellipse (figure 2-7). The orientation of ellipse is another aspect. The major axis of the ellipse no longer remains parallel to the polarization of the incident light. Thus, after passing through an optically active substance, neither do the absorbance nor do the radii of the emergent left and right circularly polarized light remains same. Hence, CD is equivalent to ellipticity.

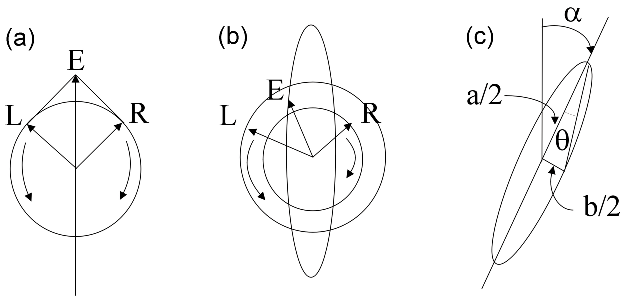

Fig 2-7. (a) Left (L) and right (R) circularly polarized light component having same intensities and phases lying in one plane and oscillating with same magnitude, (b) R component being less intense (more absorbed) than L component leading to elliptically polarized light and (c) θ, ellipticity is the angle made by semimajor and semiminor axes of ellipse. The major axis has rotated through angle a corresponding to optical rotation.

Most of the CD spectropolarimeters, although they measure differential absorption, produce a CD spectrum in units of ellipticity (θ) expressed in millidegrees versus λ, rather than ΔA versus λ. The relation between ellipticity and CD is given by,

$$\theta = \frac{2.303 \times 180 \times (A_L - A_R)}{4\pi} \text{ degrees.} \qquad (2\text{-}76)$$

To compare the results from different samples, optical activity is computed on a molar or residue basis. Molar ellipticity, [θ] is defined as,

$$[\theta] = \frac{\theta}{cl}, \qquad (2\text{-}77)$$

where 'θ' is in degrees, 'c' is in moles per litre and 'l' is in cm. The unit of molar ellipticity is deg.M^{-1}.cm^{-1}. Sometimes, CD is reported as $\Delta\varepsilon = \Delta\varepsilon_L - \Delta\varepsilon_R$. From Beer-Lambert law and molar ellipticity relation it can be shown that,

$$[\theta] = 3300.\Delta\varepsilon . \qquad (2\text{-}78)$$

(ii) Experimental Methods: In biophysical studies, CD is mostly used to determine the secondary structures of proteins and nucleic acids and the changes in secondary structures upon recognition by small molecules and other biomolecules. Through CD spectropolarimeter, we obtain CD spectrograph having a plot of optical rotation in millidegrees versus wavelength in nm. In order to obtain information about the secondary structures of proteins, the graph is fitted with non-linear least square fitting method using freely available software. The percentages of different secondary structures are calculated by matching the experimental data with that of reference standard. In proteins, the secondary structural content includes α-helix, β-sheet, β-turn and random coil while for DNA, CD is used to determine the structures of different A, B, Z and condensed forms of DNA. The CD spectrum of α–helix contains two negative peaks, one at 208 nm (π–π* transition) and 222 nm (n–π* transition). β-sheet has a negative band at 216 nm and a positive band of similar magnitude at 195 nm. β-turn has weak negative peak at 225 nm (n–π* transition), a strong positive peak between 200 nm and 205 nm due to π–π* transition and a strong negative band between 180 nm and 190 nm. Random coil or unordered conformation has a strong negative band below 200 nm; a positive band at 218 nm and in some cases has a very weak negative band at 235 nm. A positive band centered at 275 nm and a negative band at 240 nm with crossover at 258 nm characterizes B-DNA. Under high salt condition, the band at 275 nm collapse due to reduction in number of base pairs per turn. A-DNA has a positive band at 260 nm, a very weak band at 190 nm and fairly intense negative band at 210 nm. Z-form DNA has a negative and a positive band at 290 nm and 260 nm, which are mirror images of B-DNA spectrum. Condensed DNA has a negative peak between 250 nm and 260 nm and long stretching positive molar ellipticity above 300 nm, not observed for normal B-form DNA.

2.1.10. Excited State Proton Transfer

Excited state proton transfer is a subject of intense research [48-53] due to its great importance in chemistry and biology. It is observed that the acid-base properties of many organic acids and bases differ significantly in the excited state in comparison to ground state due to redistribution of electron densities in the excited state [54, 55]. The effect has been first investigated by Förster and Weller [56, 57]. Those organic acids (such as hydroxyaryls and aromatic amines) for which the excited state possess less pK_a than its ground state becomes more acidic in the excited state and are known as *photoacids* while molecules (such as nitrogen heteroaromatics) with enhanced basic properties in the excited state are known as *photobases*. Excited state proton transfer generally results in dual emission bands, one being due to neutral form and other due to the deprotonated (anion) or protonated species and exhibits large stokes shift. Basically, excited state proton transfers are of three types: (a) excited state intermolecular proton transfer (ESPT), (b) excited state intramolecular proton transfer (ESIPT), and (c) excited state double proton transfer (ESDPT).

In case of ESPT, the proton transfer takes place between two different molecules and the analysis of temporal decay of the neutral and anion emission reveals the rate of deprotonation/protonation. The rate of deprotonation/protonation depends on the medium and its pH. In ESPT solvent molecules play a very important role in solvating and stabilizing the released proton. It was suggested by Robinson et al. [58] that in aqueous solutions (4±1) water molecules are needed to solvate a proton in order to form $H^+(H_2O)_{4\pm1}$. In an organized assemblies like micelles and reverse micelles the local pH is different from that of the bulk pH due to the surface charge of these macromolecules [59, 60]. As a result ESPT is affected at surface of these macromolecules. Example of ESPT includes deprotonation of 2-naphthol [61].

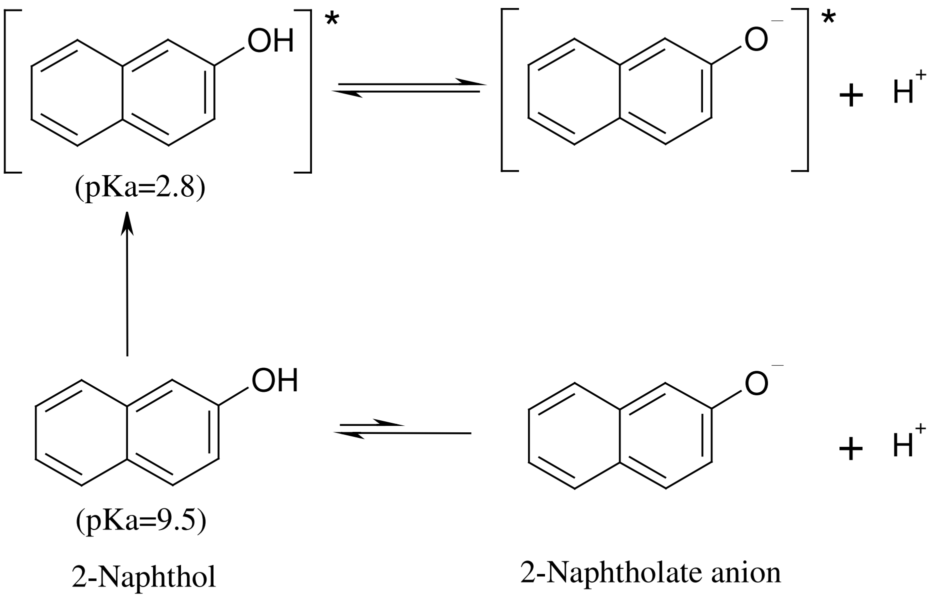

ESIPT process involves the transfer of proton from one group to another within the same molecule. The product of ESIPT is a phototautomer (excited state tautomer). This phenomenon is observed for molecules, in which the proton-donor and acceptor group are in close proximity and are intramolecularly hydrogen bonded. The ESIPT was first proposed by Weller [57] to explain the dual emission of methyl salicylate with emission maxima at 340 nm (for normal or open form (I)) and 450 nm (phototautomer (II)).

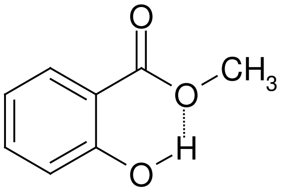

(I)

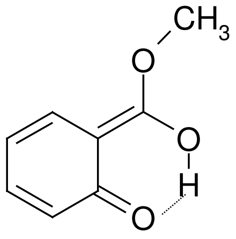

(II)

Any process leading to the disruption of intramolecular H-bonding between the migrating proton and the acceptor atom leads to inhibition of ESIPT as in case of one of the tautomers of 2,2’-hydroxyphenyl-benzimidazole (HBI) [62].

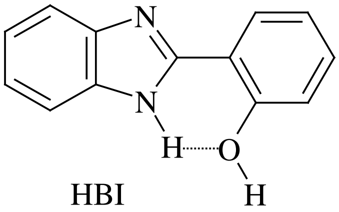

HBI

The 7-azaindole (7AI) hydrogen-bonded complex has been recognized as a simplified model for the hydrogen-bonded base pair of DNA and might provide

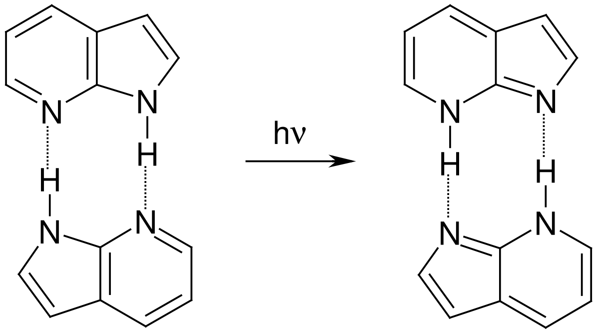

7-AI dimer Tautomer

information on the possible role of tautomerization in mutation [63-65]. Kasha et al. first proposed that the hydrogen-bonded dimer of 7AI undergoes ESDPT process. Dimer fluorescence of 7AI is known to decay biexponentially with time constants 0.2 ps and 1.1 ps [66]. Sekiuchi and Tahara [66] concluded that there are two excited states for 7AI and the ultrafast component is due to transition from upper state to the lower state and the fast component is due to ESDPT, which occurs in the lowest state.

2.2. Systems

2.2.1. Organized Assemblies (Biomimetics):

Amphiphilic molecules like surfactant, aggregates to form macromolecular assemblies like micelles and reverse micelles, which very often resemble the structural properties of biomolecules. In the following section we will discuss about these entities.

A. Micelles:

Micelles are spherical or nearly spherical aggregates of amphiphilic surfactant molecules formed in aqueous solution above a concentration known as critical micellar concentration

(CMC). Micelles are formed above a critical temperature called "Kraft point" which is different for different surfactants. Micellar aggregates have diameter varying within 10 nm and the aggregation number, i.e., the number of surfactant molecules per micelle, ranges from 20 to 200. Israelachvili et al. [67] have proposed that surfactant molecular packing considerations are determinant in the formation of large surfactant aggregates. In particular, it is considered that the surfactant packing parameter θ, defined by, $\theta = \nu/\sigma l$, where ν is the surfactant molecular volume; σ, the area per polar head; and l, the length of hydrophobic part; gives a good idea of the shape of aggregates which will form spontaneously [67]. It is considered that normal or direct rod-like micelles are formed when $2<\theta<3$ [68]. Micelles can be both neutral (Triton X-100) and ionic (Sodium dodecyl sulfate, SDS (anionic) and cetyl trimethyl ammonium bromide, CTAB (cationic)). The structure of a typical micelle is schematically shown in figure 2-8(a). The core of a micelle is essentially "dry" and consists of the hydrocarbon chains with the polar and charged head groups projecting outward toward the bulk water. The Stern layer, surrounding the core, comprises of the ionic or polar head groups, bound counter ions and water molecules. Between the Stern layer and the bulk water there is a diffused Guoy-Chapman (GC) layer, which contains the free counter ions and water molecules. In non-ionic polyoxyethylated surfactants e.g. Triton X-100 (TX-100), the hydrocarbon core is surrounded by a palisade layer, which consists of the polyoxyethylene groups hydrogen-bonded to water molecules [69]. Small angle X-ray and neutron scattering have provided detailed information on the structure of the CTAB micelles [70, 71]. According to these studies, CMC and aggregation number of CTAB micelle are 0.8 mM and 52 respectively and the thickness of the Stern layer is 6-9 Å [70-73]. The overall radius of CTAB micelle is about 50 Å. For TX-100 micelle, the CMC, thickness of the palisade layer and overall radius of the hydrophobic core are reported to be 0.1 mM, 51 Å and 25-27 Å, respectively and that of SDS micelles are 8.6 mM [74], 33 Å [75] and 5 Å, respectively [76].

B. Reverse micelles:

Reverse micelles (RMs) or water-in-oil microemulsion (figure 2-8b) are nanopools of polar solvent protected by a monolayer of surfactant molecules at the periphery with polar head groups pointing inward into the polar solvent, and the hydrocarbon tails are directed toward the non-polar organic solvents [77, 78]. RMs with water nanopools resemble the water pockets found in various bioaggregates such as proteins, membranes and

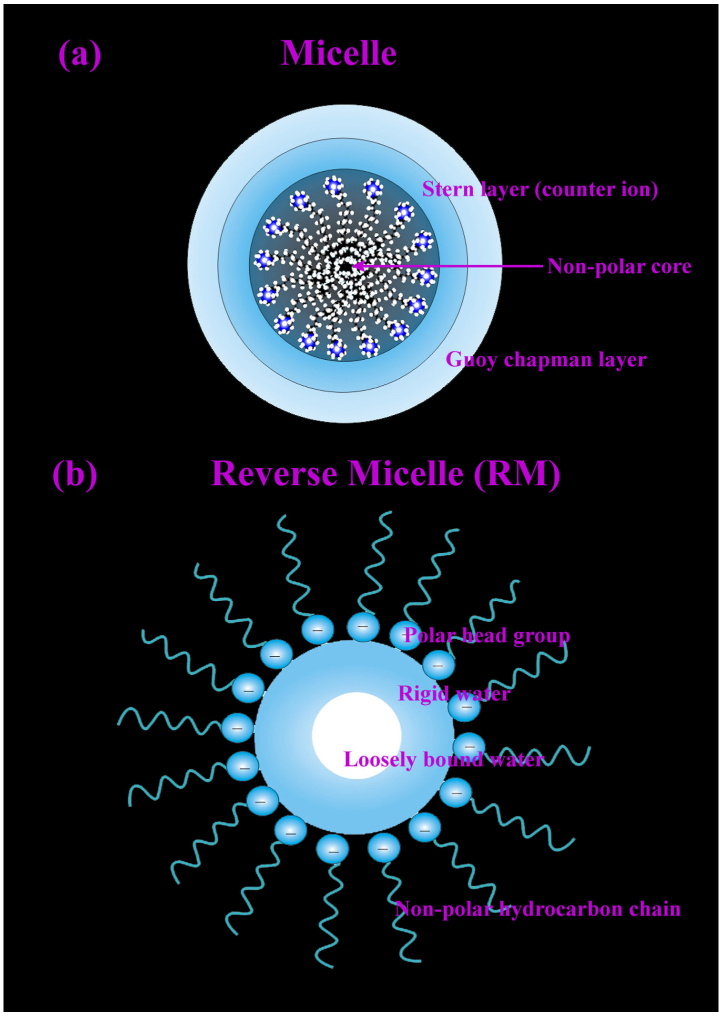

Fig. 2-8. Schematic representation of the structure of (a) micelle (b) reverse micelle.

mitochondria. Thus, these systems are very often considered as excellent biomimetics for exploration of biological membranes and biologically confined water molecules [18, 79-81]. Aqueous RMs are generally characterized by the degree of hydration (w_0), which is the ratio of molar concentration of water to that of surfactant, where the radius of the water pool (r in Å) is empirically defined as, $r = 2 \times w_0$ [82]. Shapes and sizes of the surfactant aggregates depend strongly on the type and concentration of the surfactant, and on the nature of counterion [83-86] and external solvent [87]. Reverse micelles can be formed in principle in the presence and in the absence of solubilized water [88]. However, it has generally been proposed that if the medium is completely water-free, there is not a well defined CMC and the aggregates formed are very small and polydisperse, indicating a minimum of cooperativity in the surfactant association. This has been particularly established for AOT in several organic solvents [88-90]. Zulauf and Eicke [90] suggested that water serves as ‘gluing’ agent and is a prerequisite for micellization in a polar media. RMs with w_0 values less than 20 are stable and monodisperse over a wide range of temperatures [77]. The aerosol-OT (AOT)-alkane-water system is interesting as the solution is homogeneous and optically transparent over a wide range of temperature, pressure, and pH. The AOT RM can compartmentalize a large amount of water in its central core, and the nanoscale aggregation process is fairly well-characterized with respect to size and shape at various water contents [91]. The CMC of AOT in hydrocarbon solvent is about 0.1 mM [92]. In liquid alkanes, AOT RMs (w_0= 0) are completely associated and each micelle contains 23 monomers. The structures of these RMs are slightly asymmetric and are of round cylindrical nature [91]. Spherical RMs are generally formed by surfactants with high values of the packing parameter, $\theta>3$ [68]. AOT reverse micelles can dissolve large amounts of water, being able to reach w_0 values as large as 40-60, depending on the surrounding non-polar organic medium and temperature [93]. At low w_0 values, the systems are usually referred to as reverse micelle, whereas the term water-in-oil microemulsions is frequently used for higher w_0 values. The structures of AOT RMs have been extensively studied using several methods such as ^{1}H NMR [94-96], IR [97-100], ESR [101], photon correlation spectroscopy [90, 102], SANS [103, 104], dielectric study [105, 106] and molecular dynamics simulation [107]. Fluorescence spectroscopy has also been extensively used to study the AOT RM system. Fluorescent probes have been used to determine the viscosity, binding site, rigidity and proximity within the water pool. These studies have shown that water inside the RM is generally of two types – i) interfacial (bound) and ii) core (free) water. One of the studies [97] has shown the existence of third type of water (trapped) molecules present between the polar head groups of the individual surfactant molecules. Thus, the interior of RMs is extremely heterogeneous. Dielectric relaxation studies indicate the presence of 7 ns component for bound water in RM, very similar to those of water molecules in the close vicinity of biological macromolecule (biological water). In contrast to AOT which does not require any cosurfactant to form reverse micelles, cationic surfactant do not form RMs in the absence of cosurfactants [108]. Several non-ionic or neutral surfactant (triton X-100) have been reported to form RMs in pure and mixed hydrocarbon solvents [109-112]. Finally apart from water, confinement of other polar solvents such as acetonitrile, alcohol and formamide have been reported in such microemulsions [113, 114].

2.2.2. Molecular probes:

In this section we will discuss about the different probe molecules that have been used in the course of study.

A. Acridine Orange (AO):

Acridine orange (AO) is a planar heterocyclic aromatic compound. In aqueous solution, it exists as a cation (see figure 2-9) having absorption and emission maxima at ~492 nm (α-band) (molar extinction coefficient, ε= 63,800 $M^{-1}cm^{-1}$) [115] and ~535 nm. AO is known to form aggregates at concentration above ~2 μM. It exhibits absorption peak due to dimer at ~465 nm (β-band) and that of higher aggregates at 450 nm (γ-band). AO having ground state pKa= 10.2, exhibit proton transfer equilibrium between its neutral (absorption peak ~435 nm, and emission peak ~550 nm) and protonated form [116, 117]. AO interacts with DNA and RNA by intercalation or electrostatic attraction, respectively. AO is a nucleic acid selective metachromatic stain useful for cell cycle determination [118] and finds wide usage in photodynamic therapy [119, 120]. DNA intercalated AO fluoresces green (525 nm); RNA electrostatically bound AO fluoresces red (>630nm) [121-123]. The excited state lifetimes of AO in water and upon intercalation inside DNA are 1.8 ns and 6 ns, respectively. The intercalation property of AO has made it useful for studying the molecular dynamics of DNA [124, 125]. Acridine dyes have also been used as antibacterial and antimalarial drugs during World War II.

B. Dansyl Chloride (DC):

Dansyl chloride (DC, 5-dimethylaminonaphthalene-1-sulfonyl chloride) having molecular weight 270 Da (ε= 4,300 $M^{-1}cm^{-1}$ at 327 nm) [126] is one of the widely used extrinsic probes in biological labeling [127, 128]. The chemical structure is shown in figure 2-9. DC reacts with free amino groups of a protein that fluoresce at blue region of the visible spectrum. DC is non-fluorescent until it reacts with amines. The resulting dansyl amides have environmentally sensitive fluorescence quantum yields and emission maxima along with large Stokes shifts. Its fluorescence spectrum is greatly perturbed by the local environment. Upon UV excitation, in polar media dansyl chromophore undergoes a twisted intramolecular charge transfer (CT) reaction [128, 129]. In non-polar solvents, the emission is mainly from locally excited (LE) state (i.e. before charge separation). Its locally excited state lifetime is ~12 ns [130]. In polar solvents, the fluorescence decreases and is dominated by emission from the CT state. The solvent polarity and rigidity of the environment around the probe determine the wavelength and yield of emission. A molecular picture of solvation for the probe has been detailed in reference [128].

C. 2-p-Toluidinylnaphthalene-6-sulfonate (TNS):

TNS or 2,6-TNS (2-p-Toluidinylnaphthalene-6-sulfonate) is a well-known probe for many biological systems [131, 132] (see figure 2-9). In aqueous solution, the emission quantum yield of TNS is very small (0.001) with emission peak at ~490 nm and the lifetime is also very short (60 ps) [133]. TNS has multiple absorption peaks at 270, 320 and 360 nm. Its molar extinction coefficient at 350 nm is 6640 $M^{-1}cm^{-1}$ [134, 135]. On binding to various organized media, as the probe TNS is transferred from bulk water to the less polar interior of the organized media, the emission intensity increases markedly by about 200 fold [131, 132] with huge blue shift. The fluorescence enhancement of TNS in organized media is attributed to suppression of the main nonradiative pathway, namely, intramolecular charge transfer (ICT) in the relatively nonpolar interior of the organized assemblies [136-140]. In 1,4-dioxane (dielectric constant ~2.2), TNS shows emission peak at 412 nm [141]. This concomitant blue shift and fluorescence enhancement has made TNS an efficient probe for reporting the polarity of its immediate environment and folded states of protein as different folded states creates different polarity around the probe. TNS has been used to study solvation dynamics in many biological systems [128, 142, 143]. Zhong et al. detected subpicosecond components in the solvation dynamics of TNS in Histone [128]. Pierce and Boxer [143] and Bashkin et al. [142] on the other hand, reported solvation dynamics of TNS on a 10 ns timescale in other proteins.

D. Protoporphyrin IX (PPIX):

Porphyrins are a class of tetrapyrrole rings having fully conjugated 26 π-electron systems. Protoporphyrin IX (PPIX) is the iron-free hemin, one of the most common natural porphyrins. Its IUPAC name is 7,12-Diethenyl-3,8,13,17-tetramethylporphyrin-2,18-

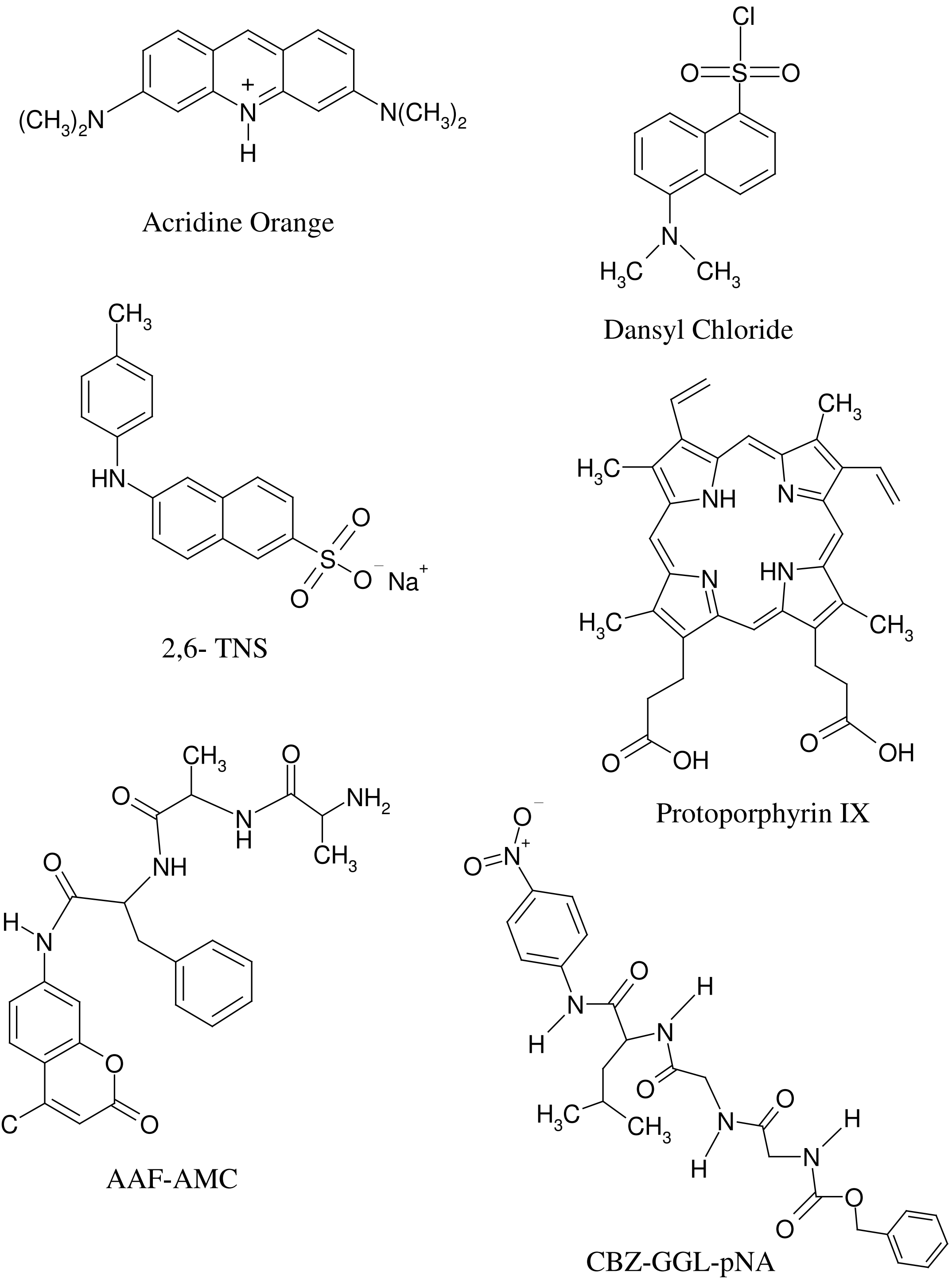

Acridine Orange

Dansyl Chloride

2,6- TNS

Protoporphyrin IX

AAF-AMC

CBZ-GGL-pNA

Fig. 2-9. Molecular structures of the probes Acridine Orange, Dansyl Chloride, 2,6-TNS, Protoporphyrin IX, AAF-AMC and CBZ-GGL-PNA.

dipropanoic acid. The structure of the molecule is shown in figure 2-9. Its formula forming dimers and micelle like polymers, within the nanomolar to micromolar weight of 563 Da. Porphyrin compounds tend to aggregate in aqueous solutions. PPIX is a monomer in the pH range 0-3, dimer in pH range greater than 8 and higher aggregates are present in the pH range 3-7. PPIX exhibits amphiphilic behavior, forming vesicles and molecular bilayers, due to the presence of two peripheral ionizable propionate groups and a large hydrophobic surface. The aggregation process occurs through π-π interaction. Porphyrin aggregates are generally of two types: (i) J-aggregates, where molecular rearrangement is end-to-end with red shift of absorption and (ii) H-aggregates, where the rearrangement is face-to-face with blue shift of absorption band as predicted by Exciton theory [144]. PPIX monomer shows the well-known visible spectrum consisting of an intense Soret band peaking around 390-415 nm (molar extinction coefficient at 405 nm $\sim 1.24 \times 10^5$ $M^{-1}cm^{-1}$) and four weaker bands (Q bands) in the 450-700 nm interval. The fluorescence emission spectrum (in the 550-750 nm region) contains two characteristics bands, whose maxima depend on the chemical structure of the porphyrin and the solvent (around 620-640 and 660-690 nm). Fluorescence Lifetime of PPIX has a characteristics fluorescence lifetime of ~14 ns. Serum albumins and low and high density lipoproteins acts as the endogenous carriers of porphyrins in circulation [145, 146]. PPIX has been shown to bind to domain-IB of HSA, as evident from the x-ray crystallographic study [147]. PPIX has been extensively studied and is responsible for the photosensitizing phenomena shown by porphyric patients. Stimulation of endogenous PPIX by topical applications of 5-aminolevulinic acid, a precursor of PPIX in the biosynthetic pathway of haem, has appeared promising for the photodynamic treatment of superficial basal cell and squamous cell carcinoma [148]. Photosensitization is based on the generation of very toxic short-lived species upon absorption of light by porphyrins. Thus the photosensitizing properties of these compounds are strictly correlated with the properties of their excited states. Evidence suggests that porphyrin-mediated cell killing is mainly the result of photodamage induced by O_2 ($^1\Delta_g$) formed via energy transfer from the lowest excited triplet state of the porphyrin to molecular oxygen in its triplet ground state (type II mechanism) [149-152]. PPIX also plays important roles in biological events, such as photosynthetic light energy conversion, oxygen transport, and biological catalysis.

E. Ala-Ala-Phe-7-amido-4-methylcoumarin (AAF-AMC):

Ala-Ala-Phe-7-amido-4-methylcoumarin (AAF-AMC) is a fluorescent aromatic tripeptide substrate (figure 2-9) suitable for cleavage by serine protease. Its concentration is determined using extinction coefficient, $\varepsilon= 16\ mM^{-1}cm^{-1}$ at 325 nm. The rate of catalytic activity is determined by monitoring absorbance of cleaved product (7-amido-4-methylcoumarin) having $\varepsilon= 7.6\ mM^{-1}cm^{-1}$ at 370 nm in aqueous buffer solution [153].

F. N-CBZ-Gly-Gly-Leu-p-Nitroanilide (CBZ-GGL-pNA):

N-CBZ-Gly-Gly-Leu-p-Nitroanilide (CBZ-GGL-pNA) is another aromatic tripeptide (figure 2-9) substrate. Its concentration is determined using $\varepsilon= 14\ mM^{-1}cm^{-1}$ at 315 nm. The rate of catalytic activity is determined by monitoring absorbance of cleaved product (p-Nitroanilide) having $\varepsilon= 8.8\ mM^{-1}cm^{-1}$ at 410 nm [153].

2.2.3. Proteins:

Three types of model proteins; α–Chymotrypsin (CHT), Subtilisin Carlsberg (SC) and Human Serum Albumin (HSA) have been used.

A. Human Serum Albumin (HSA):

Serum albumins are multi-domain proteins forming the major soluble protein constituent (60% of the blood serum) of the circulatory system [154]. Human Serum Albumin (HSA) (molecular weight 66,479 Da) is a heart-shaped tridomain protein with each domain comprising of two identical subdomains – A and B with each domain depicting specific structural and functional characteristics [155]. HSA having 585 amino acid residues assumes solid equilateral triangular shape with sides ~80 Å and depth ~30 Å [156]. Its amino acid sequence comprises of 17 disulfide bridges distributed over all domains, one free thiol (Cys34) in domain-I and a tryptophan residue (Trp214) in domain-IIA. About 67 % of HSA is α-helical while the rest of the structure being turns and extended polypeptides [156]. Each domain contains 10 principle helices (h1-h10). Subdomains – A and B share a common motif that includes h1, h2, h3 and h4 for subdomain-A, and h7, h8, h9, h10 for subdomain-B. The non-existence of disulfide linkage connecting h1 and h3 in subdomain-IA is an exception. HSA is engaged with various

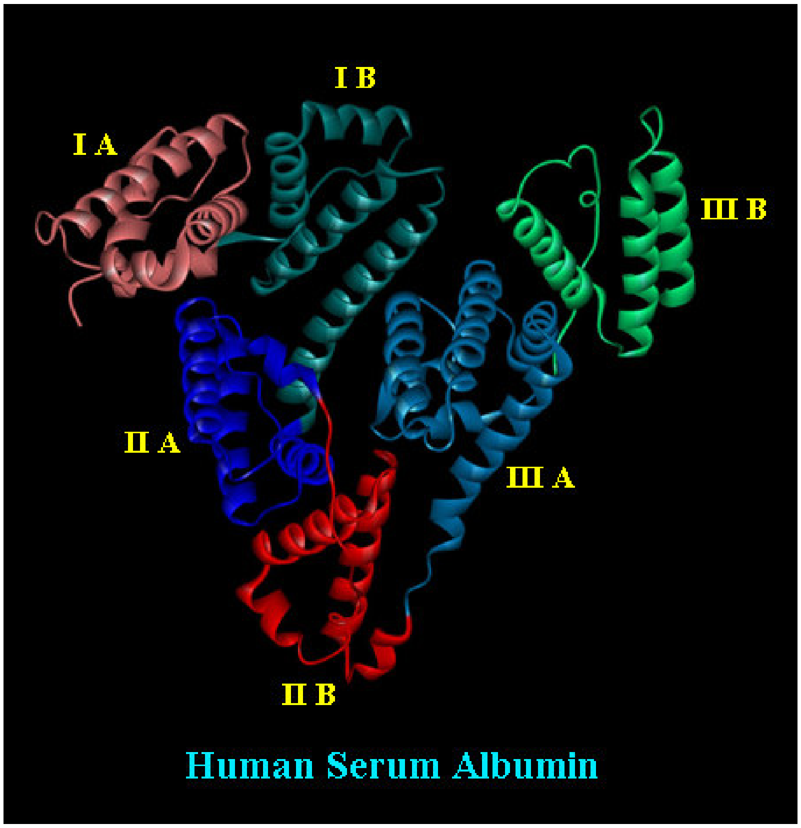

Fig. 2-8. X-Ray Crytallographic structure (PDB code: 1N5U) of Human Serum Albumin depicting the different domains.

physiological functions involving maintenance of osmotic blood pressure, transportation of a wide variety of ligands in and out of the physiological system. The protein binds various kinds of ligands [157] including photosensitizing drugs [147] and the principal binding regions are located in subdomains – IIA and IIIA of which IIIA binding cavity is the most active one [156] and binds digitoxin, ibuprofen and tryptophan. Warfarin, however, occupies a single site in domain-IIA. It is known that HSA undergoes reversible conformational transformation with change in pH of the protein solution [158, 159], which is very essential for picking up and releasing them at sites of differing pH inside physiological system. At normal pH= 7, HSA assumes the normal form (N) which abruptly changes to fast migrating form (F) at pH values less than 4.3 at pH values less than 4.3, as this form moves “fast” upon gel electrophoresis [154]. Upon further reduction in pH to less than 2.7 the F-form changes to the fully extended form (E). On the basic side of the normal pH above pH= 8, the N-form changes to basic form (B) and above pH= 10, the structure changes to another aged form (A). Serum albumin undergoes an ageing process when stored at low ionic strength at alkaline pH. The aging process is catalyzed by the free sulfhydryl group and involves sulfhydryl-disulfide interchange that results in the conservation of the sulfhydryl at its origin position. This A-form is stable and does not undergo N-F transition [160, 161].

B. α-Chymotrypsin (CHT):

α-Chymotrypsin (CHT) [enzyme commission number, EC: 3.4.21.1] isolated from bovine pancreas is a member of the family serine endopeptidase having molecular weight of 25,191 Da [43] catalyzing the hydrolysis of proteins in the small intestine. The three

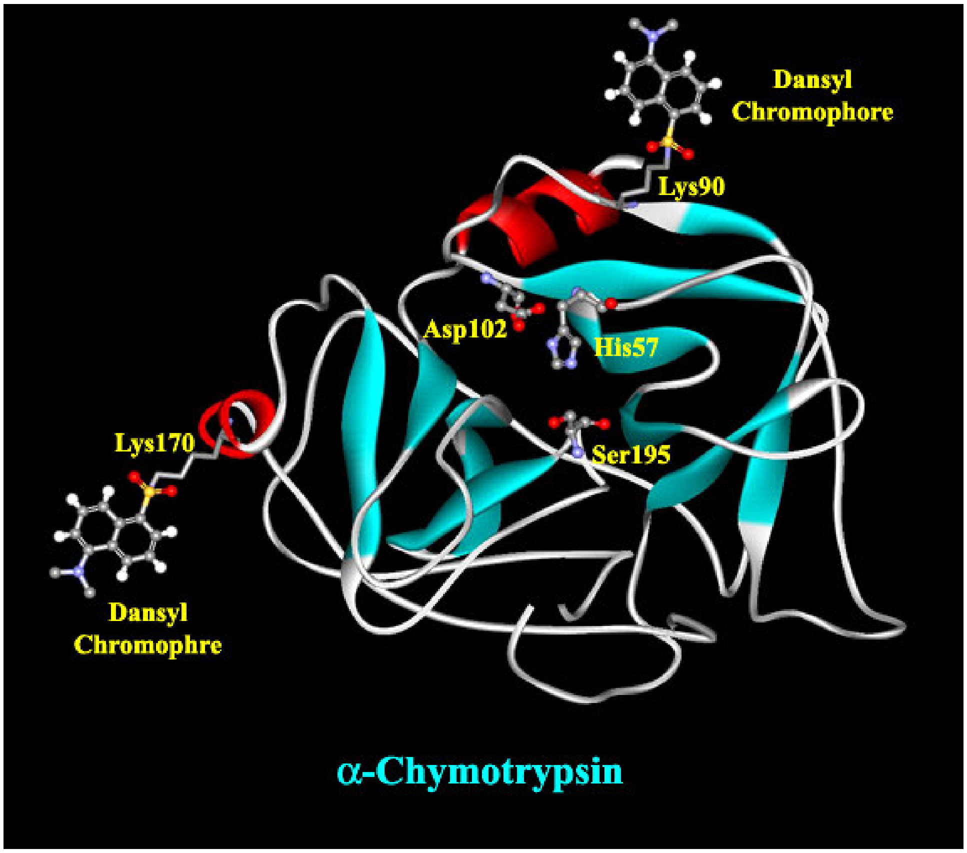

Fig. 2-9. X-Ray Crytallographic structure (PDB code: 2CHA) of α-Chymotrypsin depicting the catalytic triad (His57, Asp102 and Ser195) and two dansyl chromophore binding sites (Lys170 and lys90).

dimensional structure of CHT was solved by David Blow [162]. The molecule is a three dimensional ellipsoid of dimensions 51×40×40 Å and comprises of 245 amino acid residues. CHT contains several antiparallel β-pleated sheet regions and little α-helix. All charged groups are on the surface of the molecule except the *catalytic triad* of His57, Asp102 and Ser195 which are essential for catalysis. The Ser195 residue is H-bonded to His57 residue, which in turn is H-bonded to β-carboxyl group of Asp102. An oxyanion hole is formed by amide nitrogens of Gly193 and Ser195. It is selective for hydrolyzing peptide bonds on the carboxyl side of the aromatic side chains of tyrosine, tryptophan, and phenylalanine and of large hydrophobic residues such as methionine. It also catalyzes the hydrolysis of ester bonds [163]. CHT enhances the rate of peptide hydrolysis by a factor of 10^9. The reaction has two distinct phases– acylation and deacylation of the enzyme. Upon binding of the substrate, the hydroxyl group of the Ser195 attacks the carbonyl group of peptide bond to generate a tetrahedral intermediate. In this transient structure, the oxygen atom of the substrate now occupies the oxyanion hole. The acyl-enzyme intermediate now forms, assisted by proton donation of His57. The N-terminal portion is now released and replaced by water. The acyl-enzyme intermediate subsequently undergoes hydrolysis and the enzyme is regenerated. Proflavin is known to bind to active site of CHT and inhibits its activity [164].

C. *Subtilisin Carlsberg* (SC):

Subtilisin Carlsberg (SC) [EC: 3.4.21.62] extracted from *Bacillus licheniformis* having molecular weight of 27,600 Da [165] is another member of serine protease. It is also known as *Subtilisin A*, *Subtilopeptidase A* and *Alcalase Novo* and was discovered by Linderstrom-Lang and Ottensen [166] while they were studying the conversion of ovalbumin to plakalbumin. It contains a single polypeptide chain of 274 amino acid residues with two Ca^{2+} ion binding sites [167-169]. SC has 34 % α-helix content [170]. It was observed that 119 water molecules are bound to SC in aqueous solution [171]. The amino acid sequence contains a single tryptophan (Trp113) and thirteen tyrosine (Tyr) [165] with no cysteine residues. In this enzyme, Tyr fluorescence overwhelms the fluorescence of Trp which is not the case in other proteins due to energy transfer from Tyr to Trp residue. The *catalytic triad* of SC comprises of Asp32, His64 and Ser221 residues

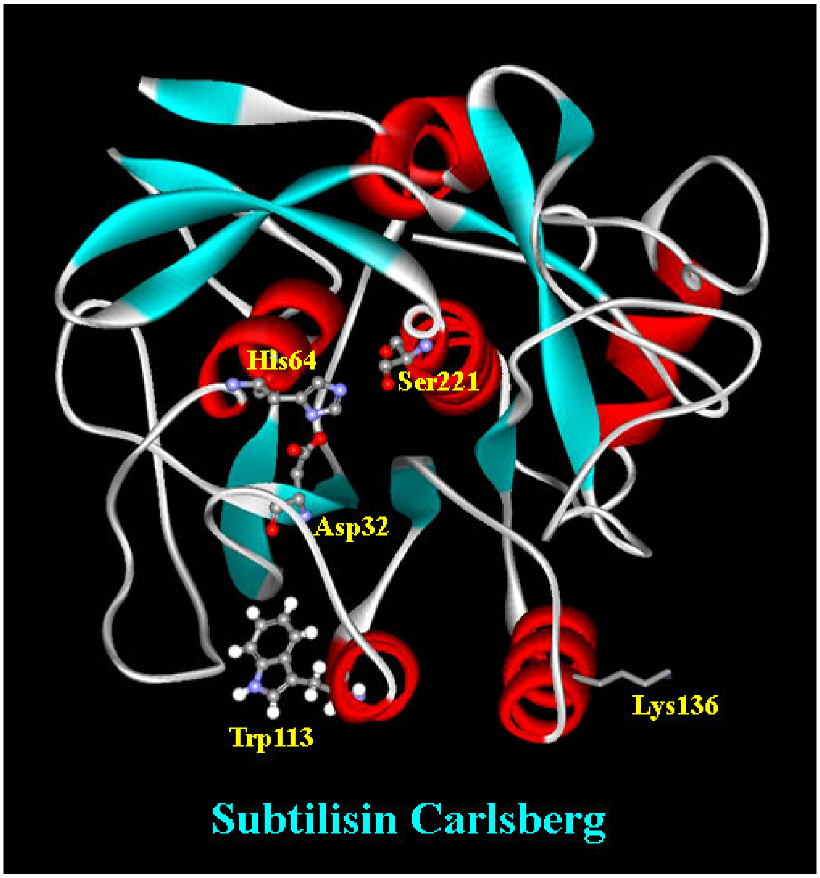

Fig. 2-10. X-Ray Crytallographic structure (PDB code: 1SCD) of Subtilisin Carlsberg depicting the catalytic triads and dansyl binding residue lysine (Lys136).

[172] and it catalyzes the hydrolysis of peptides and esters by the same acyl-enzyme mechanism as for CHT. It is important to note that *subtilisin* differs from the pancreatic enzymes by having a shallow binding groove on the surface, rather than the deep binding pocket of the pancreatic enzymes, to which it is related by convergent evolution [173]. Subtilisins are of considerable interest not only scientifically but also industrially, for they are used in such diverse applications as meat tenderizers, laundry detergents, and proteolytic medicines [174, 175]. Furthermore, their catalytic efficiency and specificity in organic media would enhance practical uses related to synthetic applications [176-179]. Subtilisins are covalently inactivated by standard serine protease inhibitors such as PMSF and DFP, and also by peptidyl-halomethanes [180, 181] and peptidyl-boronic acids [182].

2.2.4. Deoxyribonucleic Acids (DNAs):

Nucleic acids form the central molecules in transmission, expression and conservation of genetic information. DNA serves as carrier of genetic information [183, 184]. The classic example of how biological function follows from biomolecular structure comes from the elucidation of double helical structure of DNA by Watson and Crick [185]. DNAs are polynucleotide with each nucleotide comprising of deoxyribose sugar, purine and pyrimidine bases and phosphate groups. The main bases whose intermolecular hydrogen bonding holds the DNA strands together are adenine, guanine, thymine and cytosine. There are generally three forms of DNA- A, B and Z-form. Natural DNA, however, exists in B-form. Natural DNA is about metre long and comprises of hundreds of base pairs. The distance between two base pairs in B-DNA is 3.4 Å [43]. In about 4 M NaCl, B-form

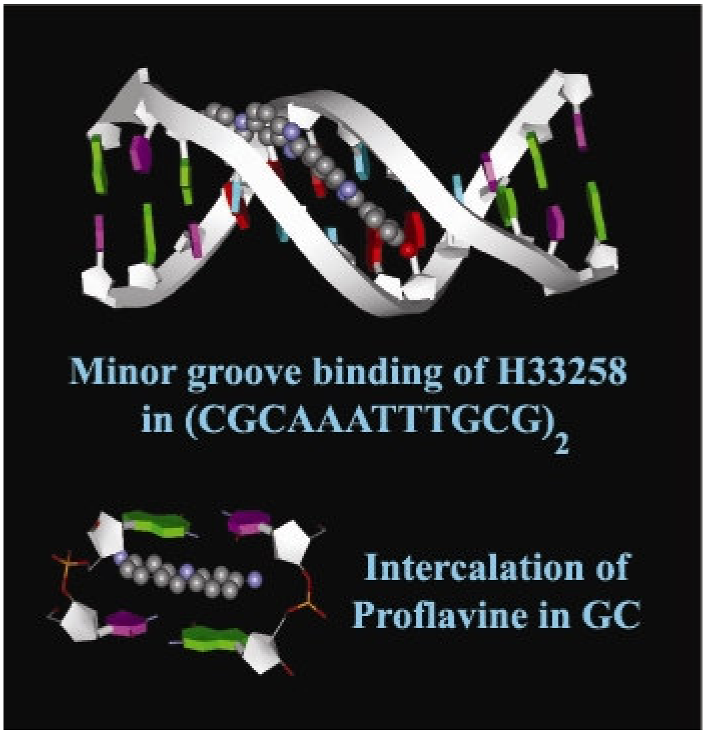

Fig. 2-11. Schematic representation of minor groove binding and intercalation of H33258 and proflavine, respectively. The DNA structures are downloaded from the nucleic acid data bank and handled with the WEBLAB VIEWERLITE program.

assumes Z-form. DNA structures consist of major and minor grooves and intercalation spaces through which DNA interacts with ligands. There are two modes of interaction of DNA with ligands- (i) intercalation, where the planar polycyclic heteroaromatic ligands sit in between the base pairs of DNA and interact through π–π interaction [122, 123], and (ii) groove binding where the ligands bind in the major and minor grooves of DNA [186]. The water molecules at the surface of DNA are critical to the structure and to the recognition of other molecules, proteins and drugs.

In our studies two genomic DNAs from Salmon Sperm and Calf Thymus and two synthetic DNAs- $(GCGCGCGCGCGC)_2$ [oligo1] and $(CGCAAATTTGCG)_2$ [oligo2] have been used. X-ray crystallographic study shows that A-T containing oligonucleotide sequence $(CGCAAATTTGCG)_2$ (figure 2-11) including central five base pairs are responsible for DNA minor groove binding [187]. On the other hand poly GC sequence of $(CGCGCGCGCGCG)_2$ is ideal for the intercalation interaction (figure 2-11) [188]. As reported in the literature the molecular weight of the calf thymus DNA (containing less than 3% protein) is $(6.6\text{-}8.6)\times10^6$ Da [189]. The molecular weight of the salmon sperm DNA is reported to be 9.2×10^4 Da [190].

References

[1] J.A. Rupley and G. Careri, Protein hydration and function, Adv. Prot. Chem. 41 (1991) 37-172.

[2] J.A. Kornblatt and M.J. Kornblatt, Water as it applies to the function of enzymes, Int. Rev. Cytology 215 (2002) 49-73.

[3] Y. Pocker, Water in enzyme reaction: biophysical aspects of hydration-dehydration processes, Cell. Mol. Life Sci. 57 (2000) 1008-1017.

[4] B. Bagchi, Dynamics of Solvation and Charge Transfer Reactions in Dipolar Liquids, Annu. Rev. Phys. Chem. 40 (1989) 115-141.

[5] G.R. Fleming and M. Cho, Chromophore-Solvent Dynamics, Ann. Rev. Phys. Chem. 47 (1996) 109-134.

[6] B. Bagchi and R. Biswas, Polar and nonpolar solvation dynamics, ion diffusion, and vibrational relaxation: Role of biphasic solvent response in chemical dynamics, Adv. Chem. Phys. 109 (1999) 207-432.

[7] R. Jimenez, G.R. Fleming, P.V. Kumar and M. Maroncelli, Femtosecond Solvation Dynamics of Water, Nature 369 (1994) 471-473.

[8] S.K. Pal, J. Peon, B. Bagchi and A.H. Zewail, Biological water: Femtosecond dynamics of macromolecular hydration, J. Phys. Chem. B 106 (2002) 12376-12395.

[9] L. Onsager, Comments on: "Effects of phase density on ionization processes and electron localization in fluids" by J. Jortner and A. Gaathon, Can. J. Chem. 55 (1977) 1801-1819.

[10] R.M. Stratt and M. Maroncelli, Nonreactive Dynamics in Solution: The Emerging Molecular View of Solvation Dynamics and Vibrational Relaxation, J. Phys. Chem. 100 (1996) 12981-12996.

[11] C.-P. Hsu, X. Song and R.A. Marcus, Time-Dependent Stokes Shift and Its Calculation from Solvent Dielectric Dispersion Data, J. Phys. Chem. B 101 (1997) 2546-2551.

[12] J.T. Hynes, Outer-sphere electron-transfer reactions and frequency-dependent friction, J. Phys. Chem. 90 (1986) 3701-3706.

[13] S.H. Lee and P.J. Rossky, A comparison of the structure and dynamics of liquid water at hydrophobic and hydrophilic surfaces—a molecular dynamics simulation study, J. Chem. Phys. 100 (1994) 3334-3345.

[14] S. Vajda, R. Jimenez, S.J. Rosenthal, V. Filder, G.R. Fleming and E.W. Castner, Jr., Femtosecond to nanosecond solvation dynamics in pure water and inside the γ-cyclodextrin cavity, J. Chem. Soc., Faraday Trans. 91 (1995) 867-873.

[15] S. Pal, S. Balasubramanian and B. Bagchi, Identity, Energy, and Environment of Interfacial Water Molecules in a Micellar Solution, J. Phys Chem. B 107 (2003) 5194-5202.

[16] S. Pal, S. Balasubramaian and B. Bagchi, Temperature dependence of water dynamics at an aqueous micellar surface: Atomistic molecular dynamics simulation studies of a complex system, J. Chem. Phys. 117 (2002) 2852-2859.

[17] S. Balasubramaian, S. Pal and B. Bagchi, Hydrogen-Bond Dynamics near a Micellar Surface: Origin of the Universal Slow Relaxation at Complex Aqueous Interfaces, Phys. Rev. Lett. 89 (2002) 115505.

[18] N. Nandi, K. Bhattacharyya and B. Bagchi, Dielectric relaxation and solvation dynamics of water in complex chemical and biological systems, Chem. Rev. 100 (2000) 2013-2046.

[19] M. Fukuzaki, N. Miura, N. Shinyashiki, D. Kurita, S. Shioya, M. Haida and S. Mashimo, Comparison of Water Relaxation Time in Serum Albumin Solution Using Nuclear Magnetic Resonance and Time Domain Reflectometry, J. Phys. Chem. 99 (1995) 431-435.

[20] X.J. Jordanides, M.J. Lang, X. Song and G.R. Fleming, Solvation Dynamics in Protein Environments Studied by Photon Echo Spectroscopy, J. Phys. Chem. B 103 (1999) 7995-8005.

[21] M. Marchi, F. Sterpone and M. Ceccarelli, Water Rotational Relaxation and Diffusion in Hydrated Lysozyme, J. Am. Chem. Soc. 124 (2002) 6787-6791.

[22] M.M. Teeter, A. Yamano, B. Stec and U. Mohanty, On the nature of a glassy state of matter in a hydrated protein: Relation to protein function, Proc. Natl. Acad. Sci. USA 98 (2001) 11242-11247.

[23] N. Nandi and B. Bagchi, Dielectric Relaxation of Biological Water, J. Phys. Chem. B 101 (1997) 10954-10961.

[24] M.L. Horng, J.A. Gardecki, A. Papazyan and M. Maroncelli, Subpicosecond measurements of polar solvation dynamics: coumarin 153 revisited, J. Phys. Chem. 99 (1995) 17311-17337.

[25] J.R. Lakowicz: Principles of Fluorescence Spectroscopy, Springer, New York, (2006).

[26] A.S.R. Koti, M.M.G. Krishna and N. Periasamy, Time-resolved area-normalized emission spectroscopy (TRANES): A novel method for confirming emission from two excited states, J. Phys. Chem. A 105 (2001) 1767-1771.

[27] A.S.R. Koti and N. Periasamy, Application of time resolved area normalized emission spectroscopy to multicomponent systems, J. Chem. Phys. 115 (2001) 7094-7099.

[28] N. Periasamy and A.S.R. Koti, Time resolved fluorescence spectroscopy: TRES and TRANES, Proc. Indian Natl. Sci. Acad. 69A (2003) 41-48.

[29] M. Doi and S.F. Edwards: Theory of polymer dynamics, Clarendon Press, Oxford, (1986).

[30] G. Srinivas, K.L. Sebastian and B. Bagchi, Time-dependent survival probability in diffusion-controlled reactions in a polymer chain: Beyond the Wilemski–Fixman theory, J. Chem. Phys. 116 (2002) 7276-7282.

[31] R.D. Spencer and G. Weber, Measurement of subnanosecond fluorescence lifetimes with a cross-correlation phase fluorometer, Ann. N. Y. Acad. Sci. 158 (1969) 361-384.

[32] D.V. O'Conner and D. Philips, Time Correlated Single Photon Counting, Academic Press, London (1984).

[33] G. Lipari and A. Szabo, Effect of librational motion on fluorescence depolarization and nuclear magnetic resonance relaxation in macromolecules and membranes, Biophys. J. 30 (1980) 489-506.

[34] C.C. Wang and R. Pecora, Time-correlation functions for restricted rotational diffusion, J. Chem. Phys. 72 (1980) 5333-5340.

[35] E.L. Quitevis, A.H. Marcus and M.D. Fayer, Dynamics of ionic lipophilic probes in micelles: picosecond fluorescence depolarization measurements, J. Phys. Chem. 97 (1993) 5762-5769.

[36] P. Debye: Polar Molecules, Dover, New York, (1929).

[37] N.C. Maiti, Krishna, M.M.G., Britto, P.J. and Periasamy N., Fluorescence Dynamics of Dye Probes in Micelles, J. Phys. Chem. B 101 (1997) 11051-11060.

[38] V.N.D. Taran, C. Veeger and A.J. Visser, Comparison of the dynamic structure of α-chymotrypsin in aqueous solution and in reversed micelles by fluorescent active-site probing, Eur. J. Biochem. 211 (1993) 47-55.

[39] A. Szabo, Theory of fluorescence depolarization in macromolecules and membranes, J. Chem. Phys. 81 (1984) 150-167.

[40] T. Forster, Intermolecular energy migration and fluorescence, Ann. Phys. 2 (1948) 55-75.Translated by R. S. Knox, Department of Physics and Astronomy, University of Rochester, Rochester, NY 14627.

[41] L. Stryer, Fluorescence energy transfer as a spectroscopic ruler, Annu. Rev. Biochem. 47 (1978) 819-846.

[42] P. Majumder, R. Sarkar, A.K. Shaw, A. Chakraborty and S.K. Pal, Ultrafast dynamics in a nanocage of enzymes: Solvation and fluorescence resonance energy transfer in reverse micelles, J. Colloid Int. Sci. 290 (2005) 462–474.

[43] D.L. Nelson and M.M. Cox: Lehninger Principles of Biochemistry, W. H. Freeman & Co., New York, (2000).

[44] R. Bru, A. Sanchez-Ferrer and F. Garcia-Garmona, A theoretical study on the expression of enzymic activity in reverse micelles., Biochem. J. 259 (1989) 355-361.

[45] P. Viparelli, F. Alfani and M. Cantarella, Models for enzyme superactivity in aqueous solutions of surfactants, Biochem. J. 344 (1999) 765-773.

[46] A. Rodger and B. Norden: Circular Dichroism and Linear Dichroism, Oxford University Press, Oxford, (1997).

[47] N. Berova, K. Nakanishi and R.W. Woody: Circular Dichroism, Wiley-VCH, New York, (2000).

[48] J. Waluk, A. Grabowsha, B. Pakula and J. Sepiol, Viscosity vs. temperature effects in excited-state double proton transfer. Comparison of 1-azacarbazole with 7-azaindole, J. Phys. Chem. 88 (1984) 1160-1162.

[49] Y. Chen, R.L. Rich, F. Gai and J.W. Petrich, Fluorescent species of 7-azaindole and 7-azatryptophan in water, J. Phys. Chem. 97 (1993) 1770-1780.

[50] P.-T. Chou, C.-Y. Wei, C.-P. Chang and M.-S. Kou, Structure and Thermodynamics of 7-Azaindole Hydrogen-Bonded Complexes, J. Phys. Chem. 99 (1995) 11994-12000.

[51] P.T. Chou, M.L. Martinez, W.C. Copper, S.T. Collins, D.P. McMorrow and M. Kasha, Monohydrate catalysis of excited-state double-proton transfer in 7-azaindole, J. Phys. Chem. 96 (1992) 5203-5205.

[52] C.-P. Chang, W.-C. Huang, M.-S. Kou, P.-T. Chou and J.H. Clements, Acid Catalysis of Excited-State Double-Proton Transfer in 7-Azaindole, J. Phys. Chem. 98 (1994) 8801-8805.

[53] T.C. Swinney and D.F. Kelley, Proton transfer dynamics in substituted 3-hydroxyflavones: Solvent polarization effects, J. Chem. Phys. 99 (1993) 211-221.

[54] M.R. Loken, J.W. Hayes, J.R. Gohlke and L. Brand, Excited-state proton transfer as a biological probe. Determination of rate constants by means of nanosecond fluorometry, Biochemistry 11 (1972) 4779-4786.

[55] A. Gafni and L. Brand, Excited state proton transfer reactions of acridine studied by nanosecond fluorometry, Chem. Phys. Lett. 58 (1978) 346-350.

[56] T. Forster, Influence of pH on the fluorescence of naphthalene derivatives, Z. Elektrochem. 54 (1950) 531-535.

[57] A. Weller, Fast Reactions of Excited Molecules in: G. Porter (Ed.) Prog. React. Kinet. Pergamon Press, Oxford, (1961), p. 187-214.

[58] G.W. Robinson, P.J. Thistlethwaite and J. Lee, Molecular aspects of ionic hydration reactions, J. Phys. Chem. 90 (1986) 4224-4233.

[59] P. Mukerjee and K. Banerjee, A study of Surface pH using solubilized indicator dyes, J. Phys. Chem. 68 (1964) 3567-3574.

[60] H. Fujii, T. Kawai, H. Nishikawa and G. Ebert, Determination of pH in reverse micelles, Colloid Polym. Sci. 260 (1982) 697-701.

[61] N. Agmon, Elementary Steps in Excited-State Proton Transfer, J. Phys. Chem. A 109 (2005) 13-35.

[62] K. Das, N. Sarkar, D. Majumdar and K. Bhattacharyya, Excited-state intramolecular proton transfer and rotamerism of 2-(2'-hydroxyphenyl) benzimidazole, Chem. Phys. Lett. 198 (1992) 443-448.

[63] K.C. Ingham, M. Abu-Elgheit and M.A. El-Bayoumi, Confirmation of biprotonic phototautomerism in 7-azaindole hydrogen-bonded dimers, J. Am. Chem. Soc. 93 (1971) 5023 - 5025.

[64] K.C. Ingham and M.A. El-Bayoumi, Photoinduced double proton transfer in a model hydrogen bonded base pair. Effects of temperature and deuterium substitution, J. Am. Chem. Soc. 96 (1974) 1674 - 1682.

[65] C.A. Taylor, M.A. El-Bayoumi and M. Kasha, Excited-State Two-Proton Tautomerism in Hydrogen-Bonded N-Heterocyclic Base Pairs, Proc. Natl. Acad. Sci. USA 63 (1969) 253-260.

[66] S. Takeuchi and T. Tahara, Femtosecond Ultraviolet-Visible Fluorescence Study of the Excited-State Proton-Transfer Reaction of 7-Azaindole Dimer, J. Phys. Chem. A 102 (1998) 7740 - 7753.

[67] J.N. Israelachvili, D.J. Mitchell and B.W. Ninham, Theory of self-assembly of hydrocarbon amphiphiles into micelles and bilayers, J. Chem. Soc. Faraday Trans. 2 72 (1976) 1525-1568.

[68] D.J. Mitchell and B.W. Ninham, Micelles, vesicles and microemulsions, J. Chem. Soc. Faraday Trans. 2 (1981) 601-629.

[69] H.H. Paradies, Shape and size of a nonionic surfactant micelle. Triton X-100 in aqueous solution, J. Phys. Chem. 84 (1980) 599-607.

[70] S.S. Berr, Solvent isotope effects on alkytrimethylammonium bromide micelles as a function of alkyl chain length, J. Phys. Chem. 91 (1987) 4760-4765.

[71] S.S. Berr, E. Caponetti, J.S. Johnson, J.R.R.M. Jones and L.J. Magid, Small-angle neutron scattering from hexadecyltrimethylammonium bromide micelles in aqueous solutions, J. Phys. Chem. 90 (1986) 5766-5770.

[72] H.L. Tavernier, F. Laine and M.D. Fayer, Photoinduced Intermolecular Electron Transfer in Micelles: Dielectric and Structural Properties of Micelle Headgroup Regions, J. Phys. Chem. A 105 (2001) 8944-8957.

[73] X.-G. Lei, G.-H. Zhao, Y.-C. Liu and N.J. Turro, Influence of binding strength of added electrolytes on the properties of micelles and of micellized radical pairs, Langmuir 8 (1992) 475-480.

[74] N.J. Turro, X.-G. Lei, K.P. Anantapadmanabhan and M. Aronson, Spectroscopic probe analysis of Protein-Surfacatant Interactions: The BSA/SDS System, Langmuir 11 (1995) 2525-2533.

[75] P.A. Hassan, S.R. Raghavan and E.W. Kaler, Microstructural changes in SDS micelles induced by hydrotropic salt, Langmuir 18 (2002) 2543-2548.

[76] A.K. Shaw and S.K. Pal, Activity of Subtilisin Carlsberg in macromolecular crowding, J. Photochem. Photobiol. B: Biol. 86 (2007) 199-206.

[77] P.L. Luisi, M. Giomini, M.P. Pileni and B.H. Robinson, Reverse micelles as hosts for proteins and small molecules, Biochim. Biophys. Acta 947 (1988) 209-246.

[78] T.K. De and A. Maitra, Solution behavior of aerosol OT in non-polar solvents, Adv. Colloid Interface Sci. 59 (1995) 95-193.

[79] K. Bhattacharyya, Solvation Dynamics and Proton Transfer in Supramolecular Assemblies, Acc. Chem. Res. 36 (2003) 95-101.

[80] K. Bhattacharyya and B. Bagchi, Slow Dynamics of Constrained Water in Complex Geometries, J. Phys. Chem. A 104 (2000) 10603-10613.

[81] B.E. Cohen, D. Huppert, K.M. Solntsev, Y. Tsfadia, E. Nachiel and M. Gutman, Excited State Proton Transfer in Reverse Micelles, J. Am. Chem. Soc. 124 (2002) 7539-7547.

[82] M.P. Pileni, Water in oil collidal droplets used as microreactors., Adv. Colloid Interface Sci. 46 (1993) 139-163.

[83] M. Camardo, M. D'Angelo, S. Mannaioli, G. Onori and A. Santucci, Effect of surfactant counterion on spectroscopic properties of water in oil microemulsions, Coll. Surf. A: Physicochem. Eng. Aspects 119 (1996) 183-187.

[84] E. Bardez, N. Cao Vy and T. Zemb, Counterion-driven sphere to cylinder transition in reverse micelles: a small angle x-ray scattering and conductometric study, Langmuir 11 (1995) 3374-3381.

[85] F. Caboi, P. Capuzzi, P. Baglioni and M. Monduzzi, Microstructure of Ca-AOT/Water/Decane w/o Microemulsions, J. Phys. Chem. B 101 (1997) 10205-10212.

[86] F. Mantegazza, V. Degiorgio, M.E. Giardini, A.L. Price, D.C. Steytler and B.H. Robinson, Transient Electric Birefringence Study of Rod-Shaped Water-in-Oil Microemulsions, Langmuir 14 (1998) 1-7.

[87] J.H. Fendler: Membrane Mimetic Chemistry, Chapter 3, John Wiley, New York, (1982).

[88] D. Langevin, Structure and Reactivity in Reversed Micelles in: M.P. Pileni (Ed.). Elsevier, Amsterdam, (1989).

[89] M. Ueda and Z.A. Schelly, Mean aggregation number and water vapor pressure of AOT reverse micellar systems determined by controlled partial pressure-vapor pressure osmometry (CPP-VPO), Langmuir 4 (1988) 653-655.

[90] M. Zulauf and H.-F. Eicke, Inverted Micelles and Microemulsions in the Ternary System H_2O/Aerosol-OT/Isooctane as studied by Photon Correlation Spectroscopy, J. Phys. Chem. 83 (1979) 480-486.

[91] K. Kalyanasundaram: Photochemistry in microheterogeneous systems, Academic Press, New York, (1987).

[92] Y.-C. Jean and H.J. Ache, Determination of critical micelle concentrations in micellar and reversed micellar systems by positron annihilation techniques, J. Am. Chem.. Soc. 100 (1978) 984-985.

[93] C. Petit, P. Lixon and M.P. Pileni, Structural study of divalent metal bis(2-ethylhexyl) sulfosuccinate aggregates, Langmuir 7 (1991) 2620-2625.

[94] J.H. Fendler, E.J. Fendler, R.T. Medary and V.A. Woods, Catalysis by reversed micelles in nonpolar solvents. Mutarotation of 2,3,4,6-tetramethyl-α-D-glucose in benzene and in cyclohexane, J. Am. Chem. Soc. 94 (1972) 7288-7295.

[95] O.A. El Seoud, E.J. Fendler and J.H. Fendler, Proton magnetic resonance investigations of alkylammonium carboxylate micelles in non-aqueous solvents.

Part 5.-Effects of dodecylammonium propionate on solubilizates in benzene and in deuterochloroform, J. Chem. Soc. Faraday Trans.1 70 (1974) 459-470.

[96] A. Maitra, Determination of size parameters of water-Aerosol OT-oil reverse micelles from their nuclear magnetic resonance data, J. Phys. Chem. 88 (1984) 5122-5125.

[97] T.K. Jain, M. Varshney and A. Maitra, Structural studies of Aerosol OT reverse micellar aggregates by FT-IR spectroscopy, J. Phys. Chem. 93 (1989) 7409-7416.

[98] H.S. Tan, I.R. Piletic and M.D. Fayer, Orientational dynamics of water confined on a nanometer length scale in reverse micelles, J. Chem. Phys. 122 (2005) 1745011-1745019.

[99] I.R. Piletic, D. Moilanen, D.B. Spry, N.E. Levinger and M.D. Fayer, Testing the Core/Shell Model of Nanoconfined Water in Reverse Micelles Using Linear and Nonlinear IR Spectroscopy, J. Phys. Chem. A 110 (2006) 4985-4999.

[100] I.R. Piletic, D. Moilanen, N.E. Levinger and M.D. Fayer, What Nonlinear-IR Experiments Can Tell You about Water that the IR Spectrum Cannot, J. Am. Chem. Soc. 128 (2006) 10366-10367.

[101] M. Hu and L. Kevan, Photoionization of alkylphenothiazine sulfonates in reversed micelles: effects of cosurfactants and location of chromophore, J. Phys. Chem. 94 (1990) 5348-5351.

[102] R.A. Day, B.H. Robinson, J.H. Clarke and J.V. Doherty, Characterisation of water-containing reversed micelles by viscosity and dynamic light scattering methods, J. Chem. Soc. Faraday Trans.1 75 (1979) 132-139.

[103] C. Cabos and P. Delord, Study by neutron small angle scattering, of addition of an electrolyte to reversed micellar solution, J. Phys. Lett. 41 (1980) 455-458.

[104] P.D.I. Fletcher, B.H. Robinson and J. Tabony, A quasi-elastic neutron scattering study of water-in-oil microemulsions stabilised by aerosol-OT. Effect of additives including solubilised protein on molecular motions, J. Chem. Soc. Faraday Trans.1 82 (1986) 2311-2321.

[105] M.D. Angelo, D. Floretto, G. Onori, L. Palmitori and A. Santucci, Dynamics of water-containing sodium bis(2-ethylhexyl)sulfosuccinate (AOT) reverse micelles: A high-frequency dielectric study, Phys. Rev. E 54 (1996) 993-996.

[106] M.A. Middleton, R.S. Schetchter and K.P. Johnston, Dielectric properties of anionic and nonionic surfactant microemulsions, Langmuir 6 (1990) 920-928.

[107] J. Faeder and B.M. Ladanyi, Solvation Dynamics in Reverse Micelles: The Role of Headgroup-Solute Interactions, J. Phys. Chem. B 109 (2005) 6732-6740.

[108] J. Lang, N. Lalem and R. Zana, Quaternary water in oil microemulsions. 1. Effect of alcohol chain length and concentration on droplet size and exchange of material between droplets, J. Phys. Chem. 95 (1991) 9533-9541.

[109] D.-M. Zhu, X. Wu and Z.A. Schelly, Reverse micelles and water in oil microemulsions of Triton X 100 in mixed solvents of benzene and n-hexane. Dynamic light scattering and turbidity studies, Langmuir 8 (1992) 1538-1540.

[110] D.-M. Zhu, X. Wu and Z.A. Schelly, Reverse micelles of Triton X-100 in cyclohexane: effects of temperature, water content, and salinity on the aggregation behavior, J. Phys. Chem. 96 (1992) 2382-2385.

[111] H. Caldararu, A. Caragheorgheopol, M. Dimonie, D. Donescu, I. Dragutan and N. Marinescu, Structure of reversed micelles in the cyclohexane/polyoxyethylene(4)nonylphenol/water system, as studied by the spin probe technique, J. Phys. Chem. 96 (1992) 7109-7115.

[112] A. Amararene, M. Gindre, J.-Y. Le Huerou, C. Nicot, W. Urbach and M. Waks, Water Confined in Reverse Micelles: Acoustic and Densimetric Studies, J. Phys. Chem. B 101 (1997) 10751-10756.

[113] R.E. Riter, J.R. Kimmel, E.P. Undiks and N.E. Levinger, Novel Reverse Micelles Partitioning Nonaqueous Polar Solvents in a Hydrocarbon Continuous Phase, J. Phys. Chem. B 101 (1997) 8292-8297.

[114] A. Ahamd-Zadeh Samii, A. de Savignac, I. Rico and A. Lattes, Waterless microemulsions - IV : Diels-Alder reaction of cyclopentadiene and methylacrylate as a probe of formamide microemulsions, Tetrahedron 41 (1985) 3683-3688.

[115] L. Costantino, G. Guarino, O. Ortona and V. Vitagliano, Acridine orange association equilibrium in aqueous solution, J. Chem. Eng. Data 29 (1984) 62-66.

[116] S.M. Andrade and S.M.B. Costa, The aqueous environment in AOT and Triton X-100 (w/o) microemulsions probed by fluorescence, Photochem. Photobiol. Sci. 1 (2002) 500-506.

[117] R.D. Falcone, N.M. Correa, M.A. Biasutti and J.J. Silber, Acid-Base and Aggregation Processes of Acridine Orange Base in n-heptane/AOT/Water Reverse Micelles, Langmuir 18 (2002) 2039-2047.

[118] J.-M. Petit, M.D. Gray and M.-H. Ratinaud, Assessment of fluorochromes for cellular structure and function studies by flow cytometry, Biol. Cell. 78 (1993) 1-13.

[119] M.S. Chan and J.R. Bolton, Mechanism of the photosensitized redox reactions of acridine orange in aqueous solutions-a system of interest in the photochemical storage of solar energy, Photochem. Photobiol. 34 (1981) 537-547.

[120] H. Schmidt, A. Al-Ibrahim, U. Dietzel and B. L., Photochem. Photobiol. 33 (1981) 127-130.

[121] A.I. Kononov, Photophysical Processes in the Complexes of DNA with Ethidium Bromide and Acridine Orange: A Femtosecond Study, J. Phys. Chem. B 105 (2001) 535-541.

[122] L.S. Lerman, The Structure of the DNA-Acridine Complex, Proc. Natl. Acad. Sci. USA 49 (1963) 94-102.

[123] M.B. Lyles, and Cameron, I. L., Interactions of the DNA intercalator acridine orange, with itself, with caffeine, and with double stranded DNA, Biophys. Chem. 96 (2002) 53-76.

[124] E.B. Brauns, C.J. Murphy and M.A. Berg, Local Dynamics in DNA by Temperature-Dependent Stokes Shifts of an Intercalated Dye, J. Am. Chem. Soc. 120 (1998) 2449-2456.

[125] S.A. Mosalenko, V.A. Sinyak and Y.-G. Shekun, Laser radiation influence on DNA and acridine orange complexes, Phys. Lett. A 110A (1982) 432-434.

[126] R.F. Chen, Dansyl labeled proteins: Determination of extinction coefficient and number of bound residues with radioactive dansyl chloride, Analytical Biochemistry 25 (1968) 412-416.

[127] S.K. Pal, J. Peon and A.H. Zewail, Biological water at the protein surface: Dynamical solvation probed directly with femtosecond resolution, Proc. Natl. Acad. Sci. USA 99 (2002) 1763-1768.

[128] D. Zhong, S.K. Pal and A.H. Zewail, Femtosecond studies of protein-DNA binding and dynamics: Histone I, Chem. Phys. Chem. 2 (2001) 219-227.

[129] B. Ren, F. Gao, Z. Tong and Y. Yan, Solvent polarity scale on the fluorescence spectra of a dansyl monomer copolymerizable in aqueous media, Chem. Phys. Lett. 307 (1999) 55-61.

[130] A.K. Shaw, R. Sarkar, D. Banerjee, S. Hintschich, A. Monkman and S.K. Pal, Direct observation of protein residue solvation dynamics, J. Photochem. Photobiol. A: Chem. 185 (2006) 76-85.

[131] W.O. McClure and G.M. Edelman, Fluorescent Probes for Conformational States of Proteins. I. Mechanism of Fluorescence of 2-p-Toluidinylnaphthalene-6-sulfonate, a Hydrophobic Probe, Biochemistry 5 (1966) 1908-1919.

[132] R.B. Macgregor and G. Weber, Estimation of the polarity of the protein interior by optical spectroscopy, Nature 319 (1986) 70-72.

[133] S. Mukherjee, P. Sen, A. Halder, S. Sen, P. Dutta and K. Bhattacharyya, Solvation dynamics in a protein-surfactant aggregate. TNS in HSA-SDS, Chem. Phys. Lett. 379 (2003) 471-478.

[134] A. Gafni, R.P. DeToma, R.E. Manrow and L. Brand, Nanosecond Decay Studies of a Fluorescence Probe bound to Apomyoglobin, Biophys. J. 17 (1977) 155-168.

[135] E. Bismuto, I. Sirangelo and G. Irace, Conformational substates of myoglobin detected by extrinsic dynamic fluorescence studies, Biochemistry 28 (1989) 7542-745.

[136] K. Rothkiewicz, K.H. Grellman and Z.R. Grabowski, Reinterpretation of the anomalous fluorescense of p-n,n-dimethylamino-benzonitrile, Chem. Phys. Lett. 19 (1973) 315-318.

[137] N. Sarkar and K. Bhattacharyya, Effect of urea on micelles: fluorescence of p-toluidinonaphthalenesulphonate, Chem. Phys. Lett. 180 (1991) 283-286.

[138] K. Bhattacharyya and M. Chowdhury, Environmental and magnetic field effects on exciplex and twisted charge transfer emission, Chem. Rev. 93 (1993) 507-535.

[139] K. Das, N. Sarkar, D. Nath and K. Bhattacharyya, Non-radiative pathways of anilino-naphthalene sulphonates: twisted intramolecular charge transfer versus intersystem crossing, Spectrochim. Act A 48A (1992) 1701-1705.

[140] N. Sarkar, K. Das, D. Nath and K. Bhattacharyya, Twisted charge transfer processes of nile red in homogeneous solutions and in faujasite zeolite, Langmuir 10 (1994) 326-329.

[141] G.M. Edelman and W.O. McClure, Fluorescent Probes and the Conformation of Proteins, Acc. Chem. Res. 1 (1968) 65-70.

[142] J.S. Bashkin, G. Mcledon, S. Mukamel and J. Marohn, Influence of medium dynamics on solvation and charge separation reactions: comparison of a simple alcohol and a protein "solvent", J. Phys. Chem. 94 (1990) 4757-4761.

[143] D.W. Pierce and S.G. Boxer, Dielectric relaxation in a protein matrix, J. Phys. Chem. 96 (1992) 5560-5566.

[144] A.S. Davydov: Theory of Molecular Excitons, Plenum Press, New York, (1971).

[145] D. Kessel, Porphyrin-lipoprotein association as a factor in porphyrin localization, Cancer Lett. 33 (1986) 183-188.

[146] V. Jain and H. Goel, in V. Jain (Ed.), Selected topics in photobiology. Indian Photobiological Society, New Delhi, (1992), p. 130-147.

[147] M. Wardell, Z. Wang, J.X. Ho, J. Robert, F. Ruker, J. Ruble and D.C. Carter, The Atomic Structure of Human Methemalbumin at 1.9 Å, Biochem. Biophys. Res. Comm. 291 (2002) 813-819.

[148] J.C. Kennedy and R.H. Pottier, Endogenous protoporphyrin IX, a clinically useful photosensitizer for photodynamic therapy, J. Photochem. Photobiol. B: Biol. 14 (1992) 275-292.

[149] D. Dolphin, Photomedicine and photodynamic therapy, Can. J. Chem. 72 (1994) 1005-1013.

[150] D. Valenzeno, Photomodification of biological membranes with emphasis on singlet oxygen mechanisms, Photochem. Photobiol. 46 (1987) 146-160.

[151] J.P. Keene, D. Kessel, E.J. Land, R.W. Redmond and T.G. Truscott, Direct detection of singiet oxygen sensitized by haematoporphyrin and related compounds, Photochem. Photobiol. 43 (1986) 117-120.

[152] S. Sandberg and I. Romslo, Porphyrin-induced photodarnage at the cellular and the subcellular level as related to the solubility of the porphyrin, Clin. Chim. Acta 109 (1981) 193-201.

[153] J.K.A. Kamal, T. Xia, S.K. Pal, L. Zhao and A.H. Zewail, Enzyme functionality and solvation of Subtilisin *Carlsberg*: From hours to femtoseconds, Chem. Phys. Lett. 387 (2004) 209-215.

[154] J.F. Foster, Some aspects of the structure and conformational properties of serum albumin in: V.M. Rosenoer, M. Oratz and M.A. Rothschild (Eds.), Albumin, Structure, Function and Uses. Pergamon, Oxford, (1977).

[155] M. Dockal, D.C. Carter and F. Ruker, The Three Recombinant Domains of Human Serum Albumin, J. Biol. Chem. 274 (1999) 29303-29310.

[156] X.M. He and D.C. Carter, Atomic structure and chemistry of human serum albumin, Nature 358 (1992) 209-215.

[157] J. Ghuman, P.A. Zunszain, I. Petitpas, A.A. Bhattacharya, M. Otagiri and S. Curry, Structural Basis of the Drug-binding Specificity of Human Serum Albumin, J. Mol. Biol. 353 (2005) 38-52.

[158] J.A. Luetscher, Serum Albumin. II. Identification of More than One Albumin in Horse and Human Serum by electrophoretic Mobility in Acid Solution, J. Am. Chem. Soc. 61 (1939) 2888-2890.

[159] J.F. Foster: The Plasma Proteins, Academic Press, New York, (1960).

[160] H.J. Nikkel and J.F. Foster, A Reversible Sulfhydryl-Catalyzed Structural Alteration of Bovine Mercaptalbumin, Biochemistry 10 (1971) 4479-4486.

[161] C.N. Cornell and L.J. Kaplan, Spin-Label Studies of the Sulfhydryl Environment in Bovine Plasma Albumin. 2. The Neutral Transition and the A Isomer, Biochemistry 17 (1978) 1755-1758.

[162] J.J. Birktoft and D.M. Blow, The Structure of Crystalline α-Chymotrypsin, V. The Atomic Structure of Tosyl-α-Chymotrypsin at 2 Angstroms Resolution, J. Mol. Biol. 68 (1972) 187-240.

[163] L. Stryer: Biochemistry, W. H. Freeman & Co., New York, (1995).

[164] S.A. Bernhard, B.A. Lee and Z.H. Tashjian, On the interaction of alpha Chymotrypsin with Chromophores: Proflavin binding and Enzyme conformation During Catalysis., J. Mol. Biol. 18 (1966) 405-420.

[165] R.J. DeLange and E.L. Smith, Subtilisin Carlsberg I. Amino Acid Composition; Isolation and Composition of Peptides from the Tryptic Hydrolysate, J. Biol. Chem. 243 (1968) 2134-2142.

[166] K. Linderstrom-Lang and M. Ottensen, A new protein from ovalbumin, Nature 159 (1947) 807.

[167] W. Bode, E. Papamokos and D. Musil, The high-resolution X-ray crystal structure of the complex formed between subtilisin Carlsberg and eglin c, an elastase inhibitor from the leech Hirudo medicinalis, Eur. J. Biochem. 166 (1987) 673–692.

[168] C.A. McPhalen and M.N.G. James, Structural comparison of two serine proteinase-protein inhibitor complexes: eglin-c-subtilisin Carlsberg and CI-2-subtilisin Novo, Biochemistry 27 (1988) 6582–6598.

[169] D.J. Neidhart and G.A. Petsko, The refined crystal structure of subtilisin Carlsberg at 2.5 Å resolution, Protein Eng. 2 (1988) 271–276.

[170] J.L. Schmitke, L.J. Stern and A.M. Klibanov, The crystal structure of subtilisin Carlsberg in anhydrous dioxane and its comparison with those in water and acetonitrile, Proc. Natl. Acad. Sci. USA 94 (1997) 4250-4255.

[171] P.A. Fitzpatrick, A.C.U. Steinmetz, D. Ringe and A.M. Klibanov, Enzyme crystal structure in a neat solvent, Proc. Natl. Acad. Sci. USA 90 (1993) 8653-8657.

[172] P. Castner and J.A. Wells, Dissecting the catalytic triad of serine protease, Nature 332 (1988) 564-568.

[173] A. Fersht: Enzyme Structure and Mechanism in Protein Science: A Guide to Enzyme Catalysis and Protein Folding, W. H. Freeman and company, New York, (1985).

[174] N. Genov, B. Filippi, D. Dolashka, K.S. Wilson and C. Betzel, Stability of subtilisins and related proteinases (subtilases), Int. J. Peptide Protein Res. 45 (1995) 391-400.

[175] P.A. Fitzpatrick, D. Ringe and A.M. Klibanov, X-Ray Crystal Structure of Cross-Linked Subtilisin Carlsberg in Water vs Acetonitrile, Biochem. Biophys. Res. Commun. 198 (1994) 675-681.

[176] J. Broos, A.J.W.G. Visser, J.F.J. Engbersen, W. Verboom, A. van Hoek and D.N. Reinhoudt, Flexibility of enzymes suspended in organic solvents probed by time-

resolved fluorescence anisotropy: evidence that enzyme activity and enantioselectivity are directly related to enzyme flexibility., J. Am. Chem. Soc. 117 (1995) 12657–12663.

[177] S. Chatterjee and A.J. Russell, Kinetic analysis of the mechanism for subtilisin in essentially anhydrous organic solvents, Enzyme Micro. Technol. 15 (1993) 1022–1029.

[178] A.K. Chaudhary, S.V. Kamat, E.J. Beckman, D. Nurok, R.M. Kleyle, P. Hajdu and A.J. Russell, Control of subtilisin substrate specificity by solvent engineering in organic solvents and supercritical fluoroform, J. Am. Chem. Soc. 118 (1996) 12891–12901.

[179] T. Kijima, S. Yamamoto and H. Kise, Fluorescence spectroscopic study of subtilisins as relevant to their catalytic activity in aqueous-organic media, Bull. Chem. Soc. Jpn. 67 (1994) 2819-2824.

[180] K. Morihara and T. Oka, Subtilisin BPN': inactivation by chloromethyl ketone derivatives of peptide substrates, Arch. Biochem. Biophys. 138 (1970) 526-531.

[181] T.L. Poulos, R.A. Alden, S.T. Freer, J.J. Birktoft and J. Kraut, Polypeptide halomethyl ketones bind to serine proteases as analogs of tetrahedral intermediate, J. Biol. Chem. 251 (1976) 1097-1103.

[182] D.A. Matthews, R.A. Alden, J.J. Birktoft, S.T. Freer and J. Kraut, X-ray crystallographic study of boronic acid adducts with subtilisin BPN' (Novo), J. Biol. Chem. 250 (1975) 7120-7126.

[183] O. Avery, C. Macleod and M. MacCarty, Studies on the chemical nature of the substances inducing transformation of the substances inducing transformation of pneumococcal types, J. Expt. Med. 7 (1944) 137-157.

[184] A.D. Harshey and M. Chase, Independent Functions of Viral Protein and Nucleic Acid in Growth of Bacteria, J. Gen. Physiol 36 (1952) 39-56.

[185] J.D. Watson and F.H.C. Crick, Molecular Structure of Nucleic Acids. A Structure for Deoxyribose Nucleic Acid, Nature 171 (1953) 737-738.

[186] P.B. Dervan, Molecular recognition of DNA by small molecules, Bioorg. Med. Chem. 9 (2001) 2215-2235.

[187] M.C. Vega, I.G. Saez, J. Aymami, R. Eritja, G.A.V.D. Marel, J.H.V. Boom, A. Rich and M. Coll, Three-dimensional crystal structure of the A-tract DNA dodecamer d(CGCAAATTTGCG) complexed with the minor-groove-binding drug Hoechst 33258, Eur. J. Biochem. 222 (1994) 721-726.

[188] V.C. Sheffield, D.R. Cox, L.S. Lerman and R.M. Myers, Attachment of a 40-Base-Pair G+C-Rich Sequence (GC-Clamp) to Genomic DNA Fragments by the Polymerase Chain Reaction Results in Improved Detection of Single-Base Changes, Proc. Natl. Acad. Sci. USA 86 (1989) 232-236.

[189] D. Roy, K. Karmakar, S.K. Mondal, K. Sahu and K. Bhattacharya, Excited state proton transfer from pyranine to acetate in a CTAB micelle, Chem. Phys. Lett. 339 (2004) 147-151.

[190] C.-J. Chang, J.D. Gomes and S.R. Byrn, Chemical modification of deoxyribonucleic acids: a direct study by NMR spectroscopy, J. Am. Chem. Soc. 103 (1981) 2892-2894.

Chapter 3

Instrumentation and Sample Preparation

In this Chapter we will describe the details of instrumental setup and sample preparation techniques used in our studies.

3.1. Instrumental Setup: Steady-state absorption and emission spectra of the probe molecules were measured with Shimadzu UV-2450 spectrophotometer and Jobin Yvon

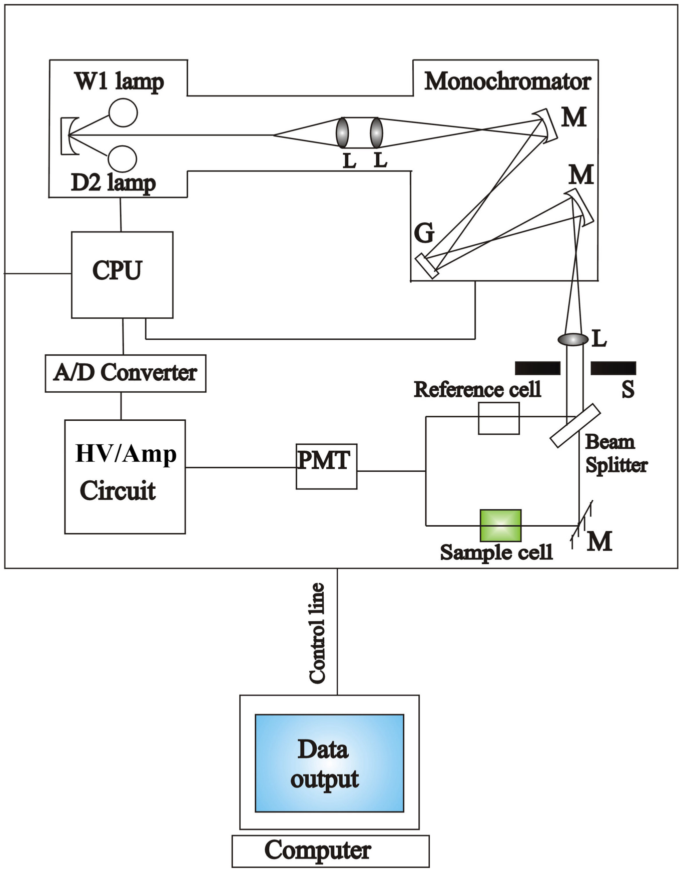

Fig. 3-1. Schematic ray diagram of an absorption spectrophotometer. Tungsten halogen (W1) and Deuterium lamps (D2) are used as light sources in the visible and UV regions respectively. M, G, L, S, PMT designate mirror, grating, lens, shutter and photomultiplier tube respectively. CPU, A/D converter and HV/Amp indicate central processing unit, analog to digital converter and High-voltage/Amplifier circuit respectively.

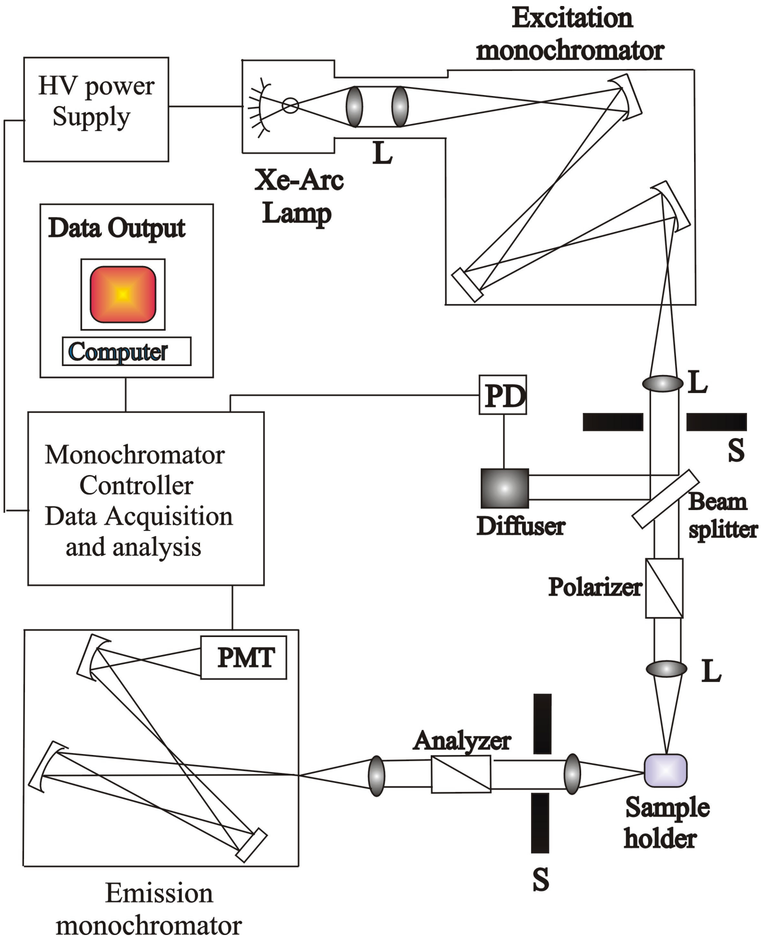

Fig. 3-2. Schematic ray diagram of an emission spectrofluorimeter. M, G, L, S, PMT and PD represent mirror, grating, lens, shutter, photomultiplier tube and reference photodiode respectively.

Fluoromax-3 fluorimeter, respectively. Schematic ray diagrams of these two instruments are shown in figures 3-1 and 3-2. The circular dichroism (CD) measurements were done in JASCO spectropolarimeters with a temperature controller attachment (Peltier) (figure 3-3). The CD spectra were acquired using quartz cell of pathlength 1 cm. For proteins, the typical concentration used for CD measurements were within 10 μM while that for DNA were about 20 μM. The secondary structural data of the CD spectra were analyzed using CDSSTR program of CDPro software [1, 2] and CDNN deconvolution program. All the fluorescence transients were recorded using picosecond-resolved time correlated single photon counting (TCSPC) technique. The schematic block diagram of a TCSPC system is shown in figure 3-4. TCSPC setup from IBH and Edinburgh instruments, UK were used during fluorescence decay acquisitions. The instrument response functions (IRFs) of the laser sources at different excitation wavelengths are mentioned in our published articles.

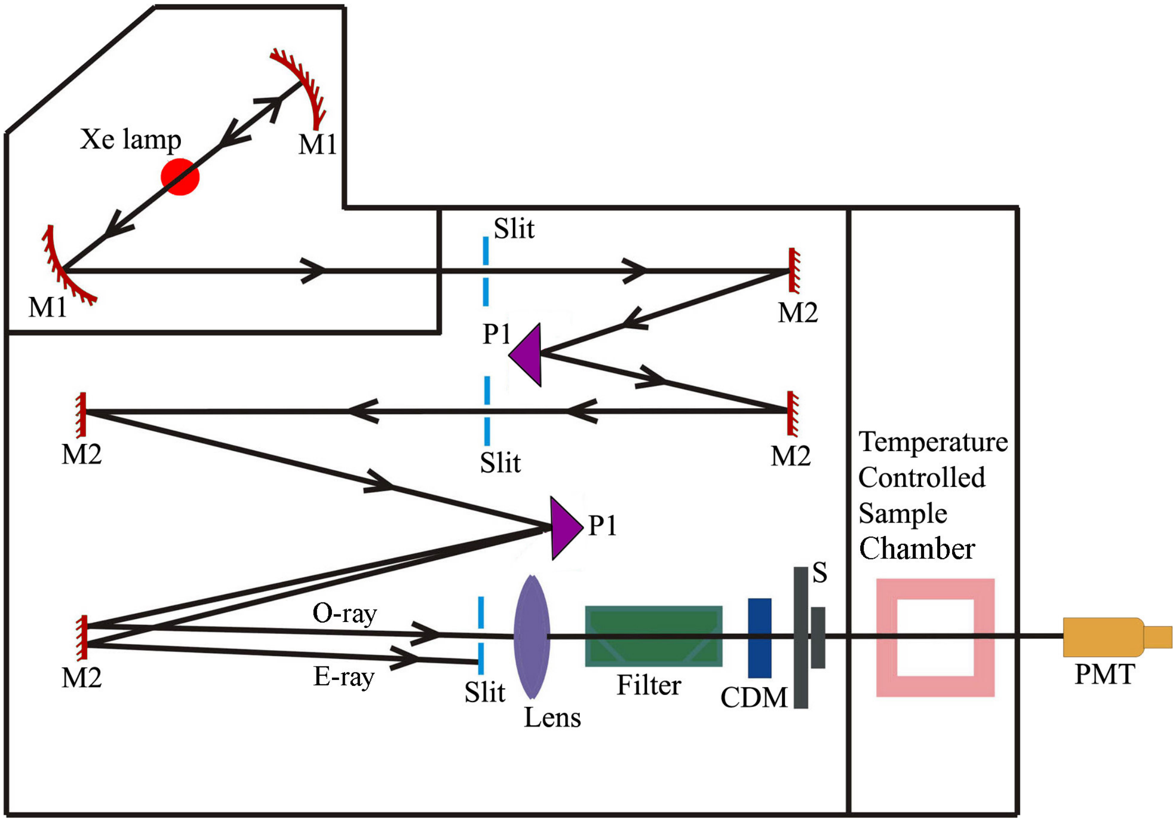

Fig. 3-3. Schematic ray diagram of a circular dichroism (CD) spectropolarimeter. M1, M2, P1, S, PMT, CDM, O-ray and E-ray represent concave mirror, plain mirror, , reflecting prism, shutter, photomultiplier tube, CD-modulator, Ordinary ray and extraordinary ray, respectively.

The fluorescence from the sample was detected by a photomultiplier after dispersion through a grating monochromator. For all transients the polarizer in the emission side was adjusted to be at 54.7° (magic angle) with respect to the polarization axis of excitation beam. In order to measure fluorescence anisotropy decay, the fluorescence decays were taken with emission polarizer aligned in parallel and perpendicular directions with respect to vertical polarization of excitation light.

Streak camera setup at Durham University, UK was used for acquisition of picosecond time-resolved emission spectra. Samples were excited at 365 nm (3.4 eV) by a frequency doubled Ti:Sapphire laser (Mira 900, Coherent) with an output pulse width of less than 2 ps and a repetition rate of 76.3 MHz. Perpendicular to the excitation path, the sample emission was passed through a monochromator (Acton Spectra Pro 2300i), and finally the emission spectrum is detected by the photocathode of a Hamamatsu streak camera (C5680) (figure 3-5). In these settings, the scattered excitation beam was observed with a half pulse width of 20 ps, which corresponds to the overall time resolution of the

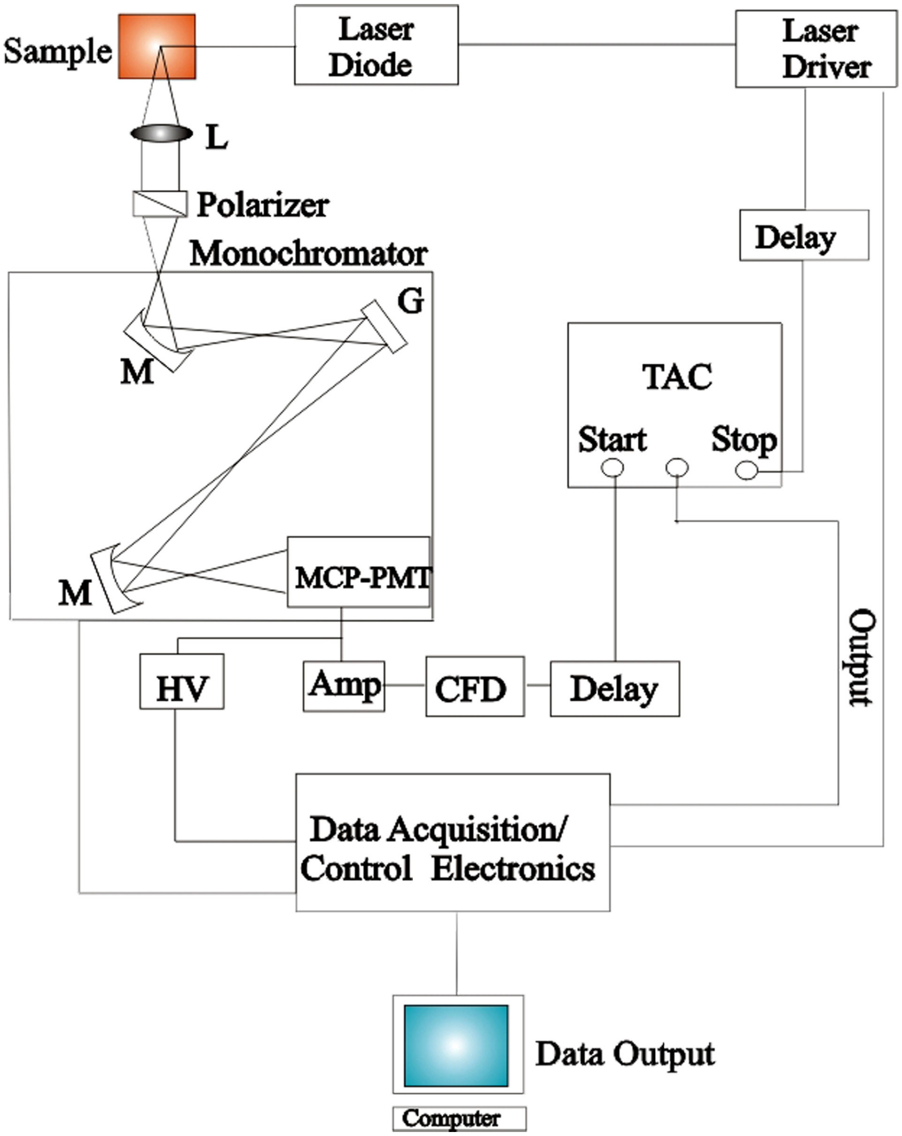

Fig. 3-4. Schematic ray diagram of a time correlated single photon counting (TCSPC) spectrophotometer. A signal from microchannel plate photomultiplier tube (MCP-PMT) is amplified (Amp) and connected to start channel of time to amplitude converter (TAC) via constant fraction discriminator (CFD) and delay. The stop channel of the TAC is connected to the laser driver via a delay line. L, M, G and HV represent lens, mirror, grating and high voltage source respectively.

setup. This exceeds the laser pulse width because, for the presented experiments, the sweep speed of the streak apparatus was set as slow as possible in order to monitor sample emission as far as 2 ns. A spectral resolution of 4 nm has been determined using an argon calibration lamp. Finally, all images were corrected for curvature, shading and spectral response via computer. Spectra at fixed points in time were then read out as profiles of a specified image section.

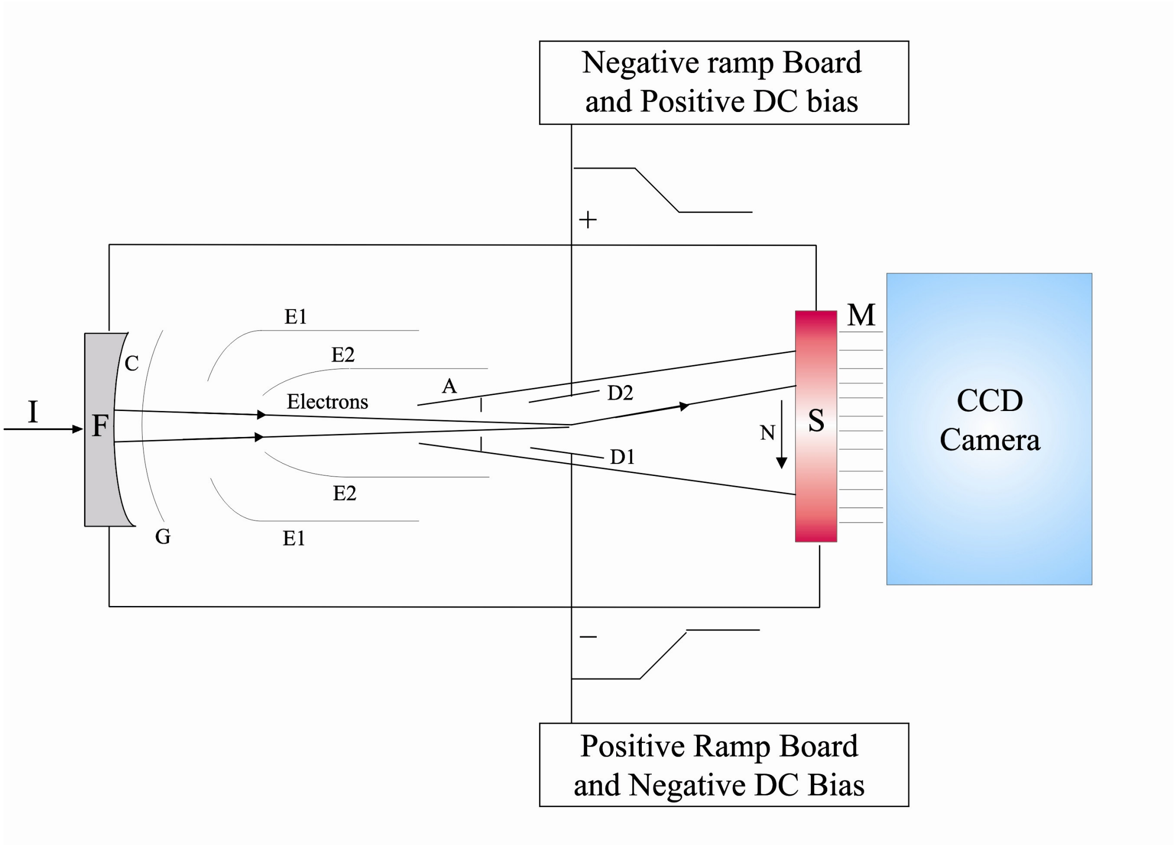

Fig. 3-5. Schematic ray diagram of a streak camera set up. A, C, F, G, I, M and S represent anode, photocathode, input face plate, grating grid, input fluorescence light, microchannel plate image intensifier and phosphor screen, respectively. E1, E2 and D1, D2 represent focusing electrodes and deflecting plates, respectively. Arrow N indicates movement of electron beam (streak) from top to bottom.

Dynamic light scattering (DLS) measurements were done with Nano S Malvern instruments, UK employing a 4 mW He-Ne laser (λ= 632.8 nm) and equipped with a thermostatted sample chamber. All the scattered photons were collected at 173° scattering angle at 298K. The scattering intensity data were processed using the instrumental software to obtain the hydrodynamic diameter (d_H) and the size distribution of the scatterer in each sample. The instrument measures the time dependent fluctuation in intensity of light scattered from the particles in solution at a fixed scattering angle. In a typical size distribution graph from the DLS measurement, X-axis shows a distribution of size classes in nm, while the Y-axis shows the relative intensity of the scattered light. The ray diagram of the DLS setup is shown in figure 3-6.

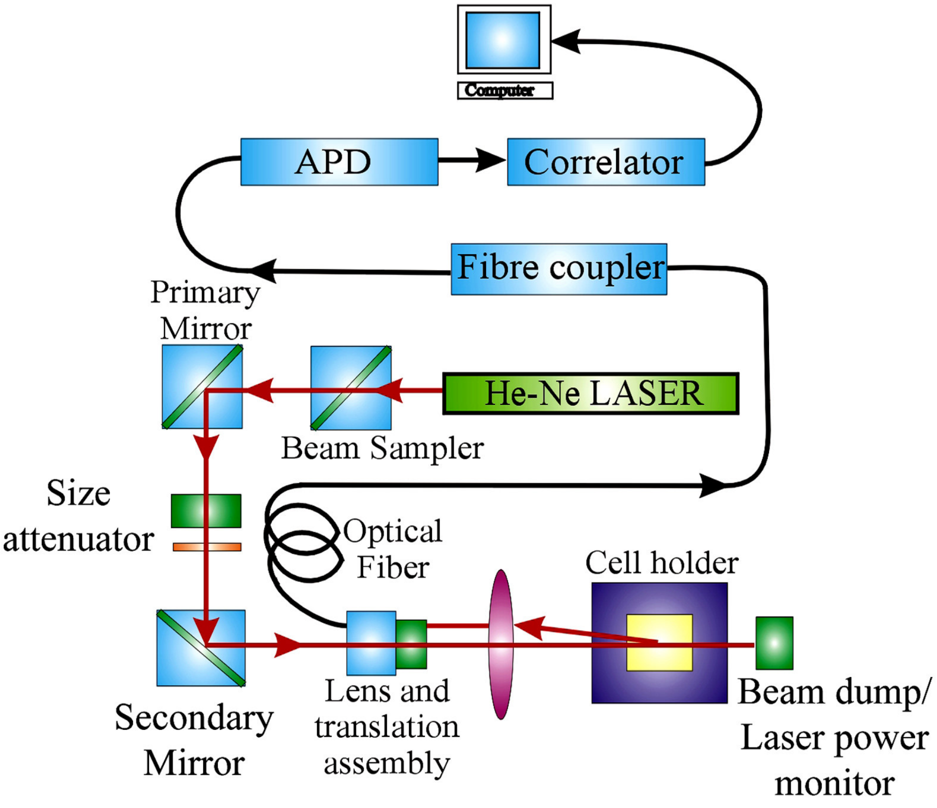

Fig. 3-6. Schematic ray diagram of Dynamic Light Scattering (DLS) instrument. The avalanche photo diode (APD) is connected to preamplifier/amplifier assembly and finally to correlator. It has to be noted that lens and translational assembly, laser power monitor, size attenuator, laser are controlled by the computer.

3.2. Sample Preparation:

In this section the different sample preparation methods have been discussed. All the aqueous solutions were prepared using deionized water from Millipore system. Acridine Orange (molecular biology grade), Protoporphyrin IX (≥ 95% pure), sodium salt of 2-p-toluidinonaphthalene-6-sulfonic acid (99% pure), AAF-AMC and GGL-pNA of highest commercially available grade were purchased from Sigma Chemicals. Dansyl Chloride (99.9% pure) was procured from Molecular Probes. The proteins, α-Chymotrypsin, *Subtilisin Carlsberg* and Human Serum Albumin were purchased from Sigma Chemicals. Genomic DNA from Salmon testes was procured from Sigma chemicals. The proteins and DNA were of highest purity grade. The purified (reverse phase cartridge) synthetic DNA oligonucleotides of 12 bases (dodecamer) with sequences GCGCGCGCGCGC and CGCAAATTTGCG were obtained from Gene Link. The surfactant salts, SDS (99% pure), TritonX 100 (99% pure) and AOT (99% pure) were purchased from Sigma Chemicals while CTAB (> 99% pure) from Fluka. Isooctane and dimethyl formaamide were purchased from Spectrochem. All the phosphate buffer salts (99% pure) used were from Sigma Chemicals.

3.2.1. Preparation of Micellar solution:

The micellar solutions were prepared by dissolving surfactant salts in 0.1 M NaCl solutions. Micellar solutions of the probe were prepared by addition of known concentrated aqueous probe solution to micellar solution of desired concentration with simultaneous stirring of the mixture for an hour. Reverse micellar solutions of specific degree of hydration (w_0) were prepared by addition of calculated volume of aqueous solution of the probe/protein/DNA in known volume of 100 mM AOT solution in isooctane. In order to ensure that each micelle/reverse micelle contains not more than one probe molecule, the overall probe concentration was kept less than that of micellar concentration ([Micelle]= ([Surfactant]-CMC)/N_{agg}) where terms in third bracket indicate the concentration and N_{agg} is the aggregation number of a particular surfactant in a micelle.

3.2.2. Preparation of Synthetic and Genomic DNA solution:

In order to reassociate the single strand DNA into self-complimentary double stranded DNA (oligo1 and oligo2), thermal annealing was performed as per the methodology prescribed by the vendor. The aqueous solutions of oligo1 and oligo2 were then dialyzed exhaustively against Millipore water prior to further use. Aqueous sample solutions of genomic DNA were prepared in phosphate buffer (pH ~7). The procedure for making genomic DNA aqueous solution was similar to that of the references [3] and [4]. In our studies the concentration of base pair of a DNA was considered as overall concentration of the DNA. The nucleotide concentrations were determined by absorption spectroscopy using the average extinction coefficient per nucleotide of the DNA (6,600 $M^{-1}cm^{-1}$ at 260 nm) [3].

3.2.3. Preparation of Acridine Orange-DNA complex:

In order to prepare solution of AO-DNA complex of definite AO:DNA ratio, calculated volume of known concentrated AO solution was added dropwise under vigorous stirring to a given volume of DNA solution of known concentration. The solution was then allowed to stir for two hours for better complex formation.

3.2.4. Labeling of Proteins with Dansyl Chloride:

Protein solutions are prepared by solubilizing lyophilized powder in buffer solutions of required pH. In order to study the dynamical properties at the surface of proteolytic enzymes, α-Chymotrypsin (CHT) and *Subtilsin Carlsberg* (SC), the proteins were non-specifically labeled with dansyl chloride (DC) as follows. The covalent attachment of dansyl chloride (DC) to the enzymes was achieved following the procedure from Molecular Probes [5]. Briefly, DC was first dissolved in a small amount of dimethyl formamide and then injected into the sodium bicarbonate solution (0.1 M) of the proteins (pH 8.3). The reaction was terminated by adding a small amount of freshly prepared hydroxylamine (1.5 M, pH 8.5) after incubating it for 1 hour at 4–8 ^{o}C with continuous stirring. The solution was then dialyzed exhaustively against 0.1 M phosphate buffer to separate adducts (DC–protein) from any unreacted DC and its hydrolysis product. It should be noted that DC-CHT and DC-SC complexes were quantitatively formed in the ratio 2:1 (DC:protein) because of covalent synthesis. In order to obtain completely denatured DC-CHT, the complex was kept for 24 hour in 9M urea solution.

3.2.5. Labelling of Human Serum Albumin with Protoporphyrin IX:

A Stock solution of Human Serum Albumin (HSA) was prepared in 10 mM phosphate buffer solution. HSA was labeled with protoporphyrin IX (PPIX) as follows. About 3.5 mg of PPIX was dissolved in 100 μl DMF and injected in 5 aliquots of 20 μl each, to 2 ml of phosphate buffer containing 200 μM HSA at an interval of 15 minutes under vigorous stirring condition. The mixture was allowed to vigorously stir for 1 hour and then a mild dialysis was carried out against phosphate buffer for 4.5 hours to remove the unreacted PPIX. The HSA-PPIX complex is formed in the ratio 1:1, which ensures better energy transfer. The HSA-PPIX solution was added in equal amounts to measured volumes of acidic/alkaline pH solutions and allowed to stir vigorously for two hours in order to achieve various pH-induced conformers of HSA-PPIX complexes. In order to label HSA and HSA-PPIX complex with TNS, calculated volume of concentrated TNS solution was added to a definite volume of HSA solution, so that the concentration ratio of TNS:HSA remains 1:1 and the mixture was then stirred vigorously for an hour. Complexes of TNS with HSA and HSA-PPIX were then used for various steady state and time-resolved experiments. The acidic and alkaline pH solutions were prepared by addition of 0.1 M HCl and 0.1 M NaOH to 0.1 M acetate and phophate buffers, respectively.

3.2.6. Measurement of Enzymatic Activity of *Subtilisin Carlsberg*:

For enzymatic activity measurement of SC, the substrates used were AAF-AMC and GGL-pNA. The concentration of the enzyme and substrates were maintained at 15 μM and 150 μM, respectively. The rate of formation of product was followed by measuring the absorbance of product at a wavelength where the substrate's absorption was nil. For the products, AMC and pNA, the monitored wavelengths were 370 nm and 410 nm, respectively. The absorbance of the product was converted to molar concentration term by using the extinction coefficients of the product at the respective wavelength. In order to measure the enzymatic activity in micellar solution of different concentration, the protein was initially mixed with the micellar solution and then the substrates were added.

References

[1] N. Sreerama and R.W. Woody, A Self-Consistent Method for the analysis of Protein Secondary Structure from Circular Dichroism, Anal. Biochem. 209 (1993) 32-44.

[2] N. Sreerama and R.W. Woody, Estimation of protein secondary structure from CD spectra: Comparison of CONTIN, SELCON and CDSSTR methods with an expanded reference set, Anal. Biochem. 282 (2000) 252-260.

[3] G. Cosa, K.-S. Focsaneanu, R.N. McLean, J.P. McNamee and J.C. Scaiano, Photophysical properties of fluorescent DNA-dyes bound to single and double-stranded DNA in aqueous buffered solution, Photochem. Photobiol. 73 (2001) 585-599.

[4] S.R. Gallagher, In Current Protocols in Molecular Biology in: F.M. Ausubel, R. Brent, K.E. Kingston, D.D. Moore, J.G. Seidman, J.A. Smith and K. Struhl (Eds.). Greene and Wiley-Interscience, New York, (1994).

[5] R.P. Haugland: Handbook of Fluorescent Probes and Research Chemicals, Molecular Probes, Eugene, OR, (1996).

Chapter 4

Exploration of Correlation between Environmental Dynamics and Biomolecular Structure: Enzyme α-Chymotrypsin in Physiologically Relevant Environments

4.1. Introduction:

In this study we have explored the time scales of solvation of a probe by polar protein residues and biological water. Also, we have tried to throw some light on the controversy existing over the contribution of polar protein residues and biological water to the solvation dynamics in the biological water layer at the protein surface. A fluorescent probe dansyl (DC) has been covalently attached to a polypeptide chain of a protein α-chymotrypsin (CHT) to form DC-CHT complex and other polar residues are allowed to come closer to the probe by complete structural denaturation of the protein. The solvation dynamics has been compared with that of the probe at the surface of the protein in the native state, where the dynamics is assumed to be mainly due to water molecules. The temporal fluorescence anisotropy of the chromophore reflecting local microviscosity controlled diffusion of the probe in the native and the denatured protein has also been correlated with the solvation dynamics. The change in the solvation and reorientational dynamics of the probe in the protein upon encapsulation in a nanocage of reverse micelle has also been reported.

4.2. Direct Observation of Protein Residue Solvation Dynamics [1]:

4.2.1. Native and denatured DC-CHT in buffer:

A. Steady-state studies:

Figure 4-1(a) shows the emission spectra of the native DC-CHT (maximum at 2.39 eV, λ_{max}= 529 nm) in the buffer (pH= 7) and denatured DC-CHT (maximum at 2.35 eV, λ_{max}= 519 nm) in 9M urea solution. Thus, we find a blue shift of about 10 nm upon denaturation of native DC-CHT. This is a clear indication of the fact that dansyl molecules, which were covalently bound to the positively charged amino acid residues, lysines and arginines at the surface of CHT, were initially in a more polar hydration layer of the protein. Upon denaturation, the native protein unfolds and assumes a random coil conformation. This in turn brings the dansyl molecules at the surface of CHT to a slightly non-polar environment of randomly oriented peptide residues causing a blue shift to occur. The blue shift may also be due to unfavorable interaction of excited state dipole

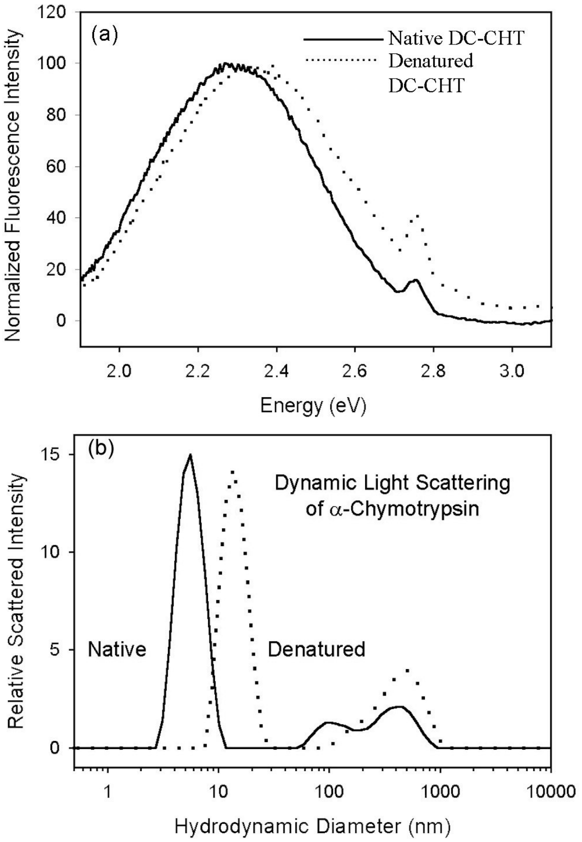

Fig. 4-1. (a) Steady-state emission spectra of dansyl labeled α-chymotrypsin (DC-CHT) (native and denatured). (b) Size distribution graph from dynamic light scattering for α-Chymotrypsin (native and denatured).

with the opposing water dipoles in the protein electric field [2]. The sharp peak at 2.76 eV in figure 4-1(a) is due to Raman scattering. A significant structural (secondary) perturbation of CHT in 9M urea solution is also evident from circular dichroism study. Dynamic light scattering (DLS) studies on CHT in buffer solution shows a major scattering peak at 5.85 nm (figure 4-1(b)). The estimated diameter from the X-ray crystallographic

(PDB code: 2CHA) structure of the protein is 4.4 nm [3]. The difference in the diameters from DLS and X-ray experiments clearly reveals the thickness of the hydration layer of CHT to be ~0.7 nm. The structural perturbation of CHT in the urea solution is distinctly evidenced in figure 4-1(b) (dotted line). In the denaturant solution the main peak shows hydrodynamic diameter to be 12 nm indicating swelling of the protein structure upon denaturation. The peaks due to particles with higher hydrodynamic diameter (200 nm and larger) could be due to the presence of aggregates of the solutes in the solutions. Note that in the intensity distribution graph the intensity of the peak for the larger particles will appear at least 10^6 times larger than the peak for the smaller particles. This is because larger particles scatter much more light than smaller particles, as the intensity of scattering of a particle is proportional to the sixth power of its diameter (Rayleigh's approximation). Thus the number densities of larger particles in our solutions are negligibly small.

B. Time-resolved studies:

Figure 4-2(a) shows time resolved emission spectra (TRES) of native DC-CHT in the buffer. The center of gravity (cg) of the emission spectra just after the excitation (at time, t= 0) was at 2.41 eV (515 nm) and it rapidly shifts to 2.35 eV (528 nm) in 2 ns time window, which corresponds to a solvation shift of 478 cm^{-1}, the final wavelength being very close to the emission maxima of DC-CHT in the buffer (529 nm). Total estimated solvation shift of the cg as evidenced from emission spectra of DC in nonpolar and polar solvents is 3268 cm^{-1} [4], on taking the time zero emission spectrum of the probe to be similar to that in nonpolar solvent [5]. The cg of the emission spectrum of DC in a nonpolar solvent (n-heptane) is 21786 cm^{-1}. Thus the observed solvation shift in our time window is only 14.6% of the estimated total shift and the missing component of the dynamics in the early time due to our limited time resolution (20 ps) is 72.5%, giving an insignificant pending shift after 2 ns. Note that using femtosecond time-resolved fluorescence spectroscopy the longer surface hydration time constants of CHT were found to be 28 and 43 ps in the active and inactive states of the protein, respectively [6]. The observation indicates that the non-specifically labeled dansyl chromophore is solvated very fast by the polar hydration layer of the protein in the native state. The dynamics may include relaxation by the collective water motion caused by protein conformational

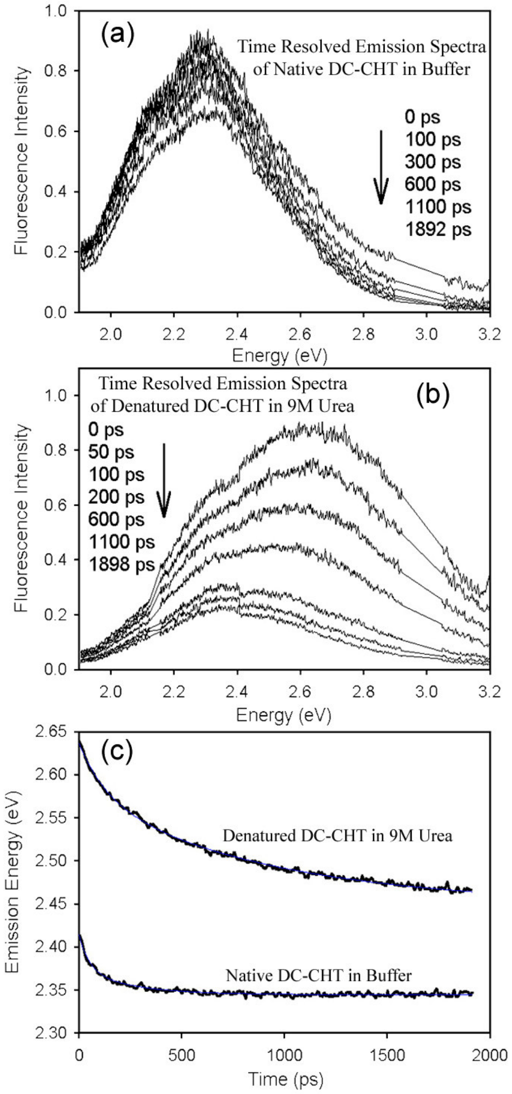

Fig. 4-2. (a) Time-resolved emission spectra of native DC-CHT in buffer. (b) Time-resolved emission spectra of denatured DC-CHT in buffer. (c) Temporal emission decay curve for native and denatured DC-CHT in the buffer.

fluctuation [7]. The temporal change of the cg of the emission spectrum of native DC–CHT in the buffer shows single exponential decay of time constant 133 ps (figure 4-2(c)). The time constant is analogous to the solvation relaxation, which is found to be 150 ps in our previous study on CHT [4].

However, the TRES of denatured DC-CHT (figure 4-2(b)) having cg of emission spectrum at 2.64 eV (470 nm at t= 0) shows a red shift of cg by 1356 cm^{-1} in 2 ns time window. The observed temporal shift (figure 4-2(c)), which is analogous to the solvation

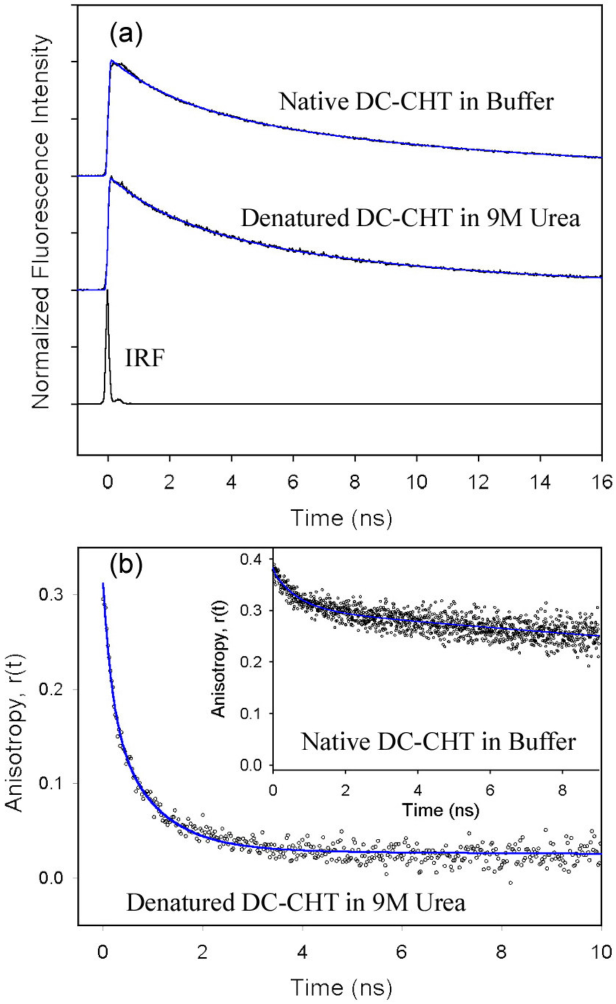

Fig. 4-3. (a) Fluorescence decays of DC-CHT (native and denatured) in buffer at 520 nm along with instrument response function (IRF). (b) Temporal fluorescence anisotropy decay of native (inset) and denatured DC-CHT at 520 nm.

correlation function [4] shows a double exponential decay with a fast component 131 ps (12.9%) and a slow component of 900 ps (28.6%). The observed shift is much larger (41.5%) compared to that of the probe at the surface of the native protein (14.6%). The faster solvation time constant (~130 ps) of the native and denatured states of DC-CHT is almost same which indicates that the faster mode of solvation is same for both the states of DC-CHT. The slower component (900 ps) in the denatured state of the protein clearly indicates a significant contribution from the amino acid side-chain in addition to the contribution from the water of hydration. Here the missing components in the early time due to the limited time resolution and after 2 ns time window are 15.6% and 42.9% of the total solvation shift, respectively.

Figure 4-3(a) shows the fluorescence decays of native DC-CHT and urea denatured DC-CHT measured at 520 nm. Both show biexponential decays with faster components of 2.2 ns (38.6%) for native DC-CHT and 2.1 ns (36.7%) for denatured DC-CHT while the slower component of 11.5 ns (61.4%) for native and 8.8 ns (63.3%) for denatured DC-CHT. The faster component is due to intramolecular charge transfer while the slower component is the locally excited state lifetime of the dansyl chromophore [4]. Figure 4-3(b) shows the temporal fluorescence anisotropy decays of the dansyl in the denatured and native DC-CHT complexes. From the figure it is clear that the dansyl in the native DC-CHT is in a more restricted environment with rotational correlation time constants (ϕ): 0.61 ns (21.1%) and 47.3 ns (78.9%); the initial anisotropy (r_0) at time t= 0 is 0.3 (table 4-1). The observation is in agreement with other studies involving specifically-labeled CHT by a different probe [8]. The faster time constant corresponds to the local reorientational motion of the dansyl probe while slower one corresponds to the global motion of CHT molecule. The temporal fluorescence anisotropy of the denatured DC-CHT shows triple exponential decay with time constants of 0.18 ns (41.9%), 0.90 ns (48.4%) and 88 ns (9.7%). The faster components are considered to be due to the reorientational motion of the probe or segmental motion of the protein while the slower component is due to the global motion of the denatured CHT. The closeness of the solvation times of the

Table 4-1. Time-resolved fluorescence anisotropy data for DC in DC-CHT under various conditions (numbers within parentheses denote the percentage of the component)

Sample	ϕ_1 ns	ϕ_2 ns	ϕ_3 ns
Native DC-CHT in Buffer	0.61 (21.1)	47.3 (78.9)	-
Denatured DC-CHT in Buffer	0.18 (41.9)	0.90 (48.4)	88.0 (9.7)
Native DC-CHT in w_0= 10 RM	0.09 (30.8)	2.03 (30.8)	50.0 (39.4)
Native DC-CHT in w_0= 20 RM	0.09 (42.2)	2.10 (22.5)	50.0 (42.3)
Denatured DC-CHT in w_0= 10 RM	0.10 (40.0)	3.13 (31.4)	45.5 (28.6)

denatured DC–CHT with that of its two faster rotational time constants also supports the fact that upon denaturation initially buffer exposed dansyl probes find themselves in a randomly fluctuating protein environment, where they are being largely relaxed by protein side-chains. Diffusion coefficients of the probe calculated using equations (2-40) and (2-41c) are given in table 4-2. It is evident from table 4-2 that diffusion coefficient of the dansyl at the surface of the native CHT (0.05765 ns^{-1}) is smaller than that in the denatured protein (0.83611 and 0.16722 ns^{-1}). The observation indicates that dansyl chromophores bound to the more compact native CHT are more constrained compared to those in the denatured CHT due to random fluctuation of the protein conformation upon denaturation. Two distinct diffusion coefficients of the chromophores in the denatured state of the protein could be due to the conformational heterogeneity of the denatured protein.

Table 4-2. Calculated value of diffusion coefficient of covalently bound dansyl chromophore under various conditions.

Sample	**$(\phi_{int})^1$ ns**	**$(\phi_{int})^2$ ns**	**(ϕ_{prot}) ns**	**S^2**	**$(D_{perp})^1$ ns^{-1}**	**$(D_{perp})^2$ ns^{-1}**
Native DC-CHT in Buffer	-	0.61	47.3	0.789	-	0.05765
Denatured DC-CHT in Buffer	0.18	0.90	88	0.097	0.83611	0.16722
Native DC-CHT in w_0= 10	0.09	2.03	50.0	0.500	0.92593	0.04105
Native DC-CHT in w_0= 20	0.09	2.10	50.0	0.500	0.92593	0.03968
Denatured DC-CHT in w_0= 10	0.10	3.13	45.5	0.286	1.19000	0.03802

4.2.2. Native and denatured DC-CHT inside reverse micelles:

A. Steady-state studies:

In order to explore the nature of change in solvation of the probe bound to the protein in a more restricted environment, both the native and the denatured DC-CHT have been encapsulated in nanometer-sized aqueous pools of AOT RMs of varying degree of hydration (w_0). Recent studies using circular dichroism (CD), electron paramagnetic resonance (EPR) and Fourier transformed infrared (FTIR) spectroscopy [9, 10] have shown that there is an insignificant change in the structure of CHT inside RM of w_0= 10 and onwards. Figure 4-4(a) shows the emission spectra of the native DC-CHT in w_0= 10 RM (maximum at 2.40 eV, λ_{max}= 518 nm) and w_0= 20 RM (maximum at 2.35 eV, λ_{max}=

528 nm) and that of the denatured DC-CHT in w_0= 10 RM (λ_{max}= 515 nm). The 10 nm blue shift of emission maximum of native DC-CHT in w_0= 10 RM compared to that in w_0= 20 RM indicates that in w_0= 10 dansyl chromophores at the surface of CHT experience a low polarity environment due to lesser availability of more polar core type water molecules. However, in w_0= 20 RM, the CHT staying at the center of RM finds a more polar environment due to greater availability of core type free water causing complete hydration [11, 12]. Hence, the emission maxima of the DC-CHT in w_0= 20 RM matches with that of the native DC-CHT in the buffer. Upon encapsulation of the denatured DC-CHT in w_0= 10 RM, not only does the emission maximum shows a greater blue shift compared to that of native DC-CHT in w_0= 10 RM but there also appears an increase in emission intensities at blue wavelengths causing the overall emission spectrum to be broad. The observation indicates that dansyl molecules in the denatured CHT in the RM find themselves in a mixed polar and non-polar environment [13, 14].

B. Time-resolved studies:

Figure 4-4(b-c) shows the TRES of native DC-CHT in w_0= 10 and 20 RM. The temporal behavior of the cg of the emission spectra of native DC–CHT in the RMs of w_0= 10, 20 are shown in figure 4-4(d). Note the spectral overlap in the (2.0–2.3 eV) red side of the TRES. In a typical solvation relaxation the rate of decay in the red side is expected to be slower than that in the blue end. The absence of faster solvation decay component and presence of rise component are major reasons for the slower decay in the red end. The observed shifts are found to be 17.7% and 22.4% for w_0= 10 and 20 RM, respectively of total estimated solvation shift of 3268 cm^{-1}. The missing solvation shift in the early time (57.1% for w_0= 10, and 54.7% for w_0= 20) and after 2 ns time window (27.2% for w_0= 10, and 22.9% for w_0= 20) are comparable for both the RMs. The temporal behavior of the emission cg of the native DC–CHT in w_0= 10 shows a single exponential decay with time constant of 808 ps while that in w_0= 20 shows a double exponential decay with time constants of 61 ps (2.5%) and 636 ps (19.9%). From the observation it is evident that for w_0= 10 RM the solvation relaxation is mainly due to bound type water molecules in the AOT/water interface. However, the DC at the surface of the protein in the RM of w_0= 20 gets both the core associated and bound interfacial type water molecules for the solvation

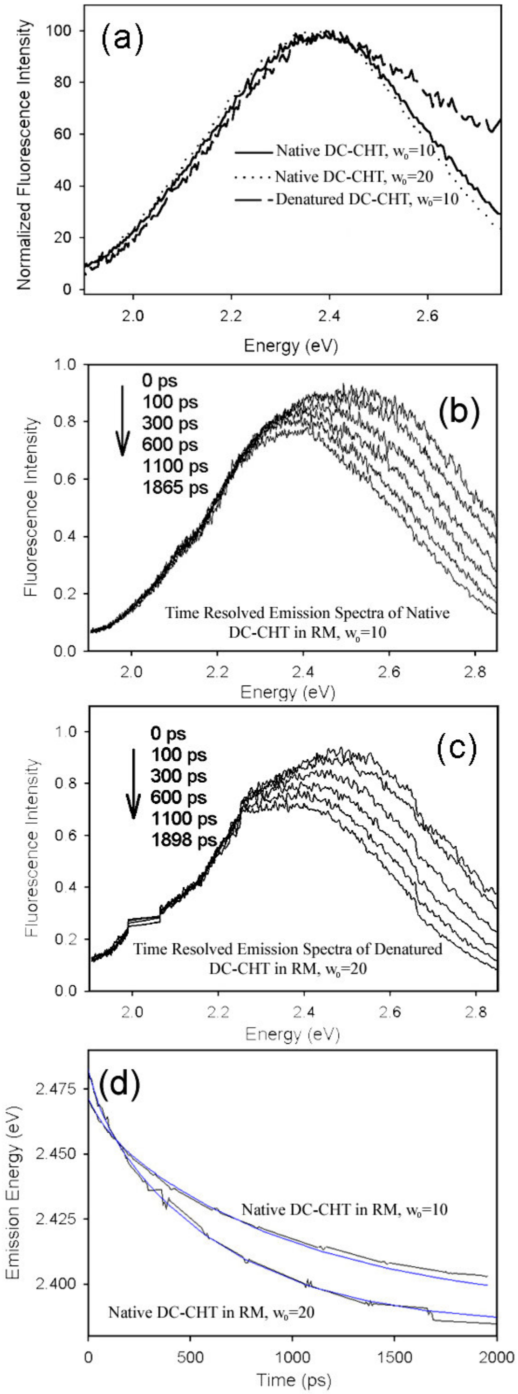

Fig. 4-4. (a) Steady-state emission spectra of DC-CHT in w_0= 10 and w_0= 20 RM (native and denatured). (b) Time-resolved emission spectra of native DC-CHT in w_0= 10 RM. (c) Time-resolved emission spectra of native DC-CHT in w_0= 20 RM. (d) Temporal emission decay curve for native DC-CHT in w_0= 10 and w_0= 20 RM.

relaxation. Figure 4-5(a-b) shows respectively the TRES and the temporal behavior of the emission cg of the denatured DC-CHT in w_0= 10 RM. From the temporal behavior of the emission cg the observed shift is 15.7% of total estimated solvation shift of 3268 cm^{-1}. Significant components in the early time (49.7%) and after the 2 ns time window (34.6%) are missing. The time constants of 89 ps (2.0%) and 777 ps (13.7%) of the temporal decay of the emission cg of denatured DC-CHT in the RM (w_0= 10) differ from that of the native DC-CHT in w_0= 10 RM, which somewhat ensures that denatured CHT does not get renatured upon encapsulation in the RM. The time scales of temporal anisotropy and diffusion constants of the probe dansyl in the protein upon encapsulation in the reverse micelles are tabulated in tables 4-1 and 4-2, respectively.

In order to understand the dynamics of denatured protein and to extract the theoretical time constants due to the solvation by amino acid side-chain residues, Rouse chain model was adopted for the denatured DC–CHT in buffer and in the RM (w_0= 10). The eigen values of the normal modes of the Rouse chain dynamics of the denatured protein in the buffer are estimated as follows. Here we consider N= 245, b= 5Å and D_0= 8.3×10^{-6} cm^2s^{-1} [15]**.** The slowest and fastest time constants obtained by setting *l*= 1 and 244 in equation (2-12) are 608 ns and 10 ps, respectively. These time scales show that the dynamical process of the denatured CHT occurs within this time span. It is found from our calculation that the normal mode corresponding to *l*= 70 (τ= 124 ps) and *l*= 26 (τ= 900 ps) match very well with the faster (131 ps) and slower solvation time constant (900 ps) of the denatured CHT. Substituting the value of D_0 to be 2.3×10^{-6} cm^2s^{-1} [11] inside the RM (w_0= 10) in equation (2-12) one can obtain for *l*= 1 and 244 the dynamical time constants of protein fluctuation to be 2203 ns and 37 ps, respectively. Inside the RM where the viscosity is high (η= 6cP [11]) the motion of the polar side-chains of CHT is slowed down as reflected from the larger values of faster and slower time scales in comparison to that in the aqueous urea solution. The observed solvation time constants of the denatured CHT in the RM closely correspond to *l*= 157 (89 ps) and *l*= 53 (785 ps). Thus applying Rouse chain model to denatured CHT in free-state and when confined in RM, we can actually point out the modes of protein motion participating in solvation.

Figure 4-6(a) shows the fluorescence decays of the native DC-CHT in w_0= 10 and 20 RMs and that of denatured DC-CHT in w_0= 10 RM. All the decays measured at 500 nm are biexponential in nature. The faster time constants of the native DC–CHT are

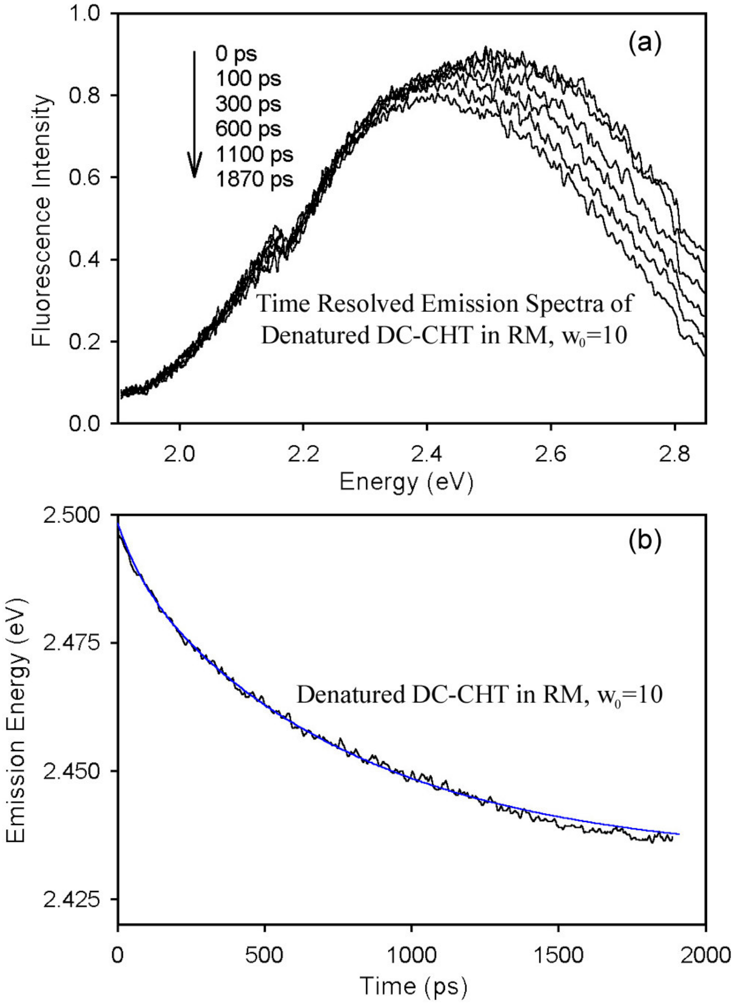

Fig. 4-5. (a) Time-resolved emission spectra of denatured DC-CHT in w_0= 10 RM. (b) Temporal emission decay curve for denatured DC-CHT in w_0= 10 RM.

1.8 ns (27.4%) in w_0= 10 RM and 1.57 ns (33.7%) in w_0= 20 RM, correspond to charge transfer dynamics of dansyl chromophore while the longer time constants of 11.4 ns (72.6%) in w_0= 10 RM and 10.6 ns (66.3%) in w_0= 20 RM correspond to locally excited state lifetime of the chromophore. For the denatured DC-CHT in w_0= 10 RM the time constants are 2.7 ns (20.9%) and 11.9 ns (79.1%). Figure 4-6(b–d) shows the temporal fluorescence anisotropy of native DC–CHT in w_0= 10, 20 RMs and that of denatured DC–CHT in w_0= 10 RM, respectively. From table 4-1, it is found that upon incorporation of the protein in the RM the temporal anisotropy data show three rotational correlation time constants: ~0.09, ~2 and ~50 ns. For native DC-CHT in w_0= 10 the 2 ns component corresponds to the local reorientational motion of the dansyl chromophore and the 50 ns component corresponds to the global motion of the protein filled RM. We find that upon incorporation of DC–CHT in the RM due to increase in local viscosity of the water pool

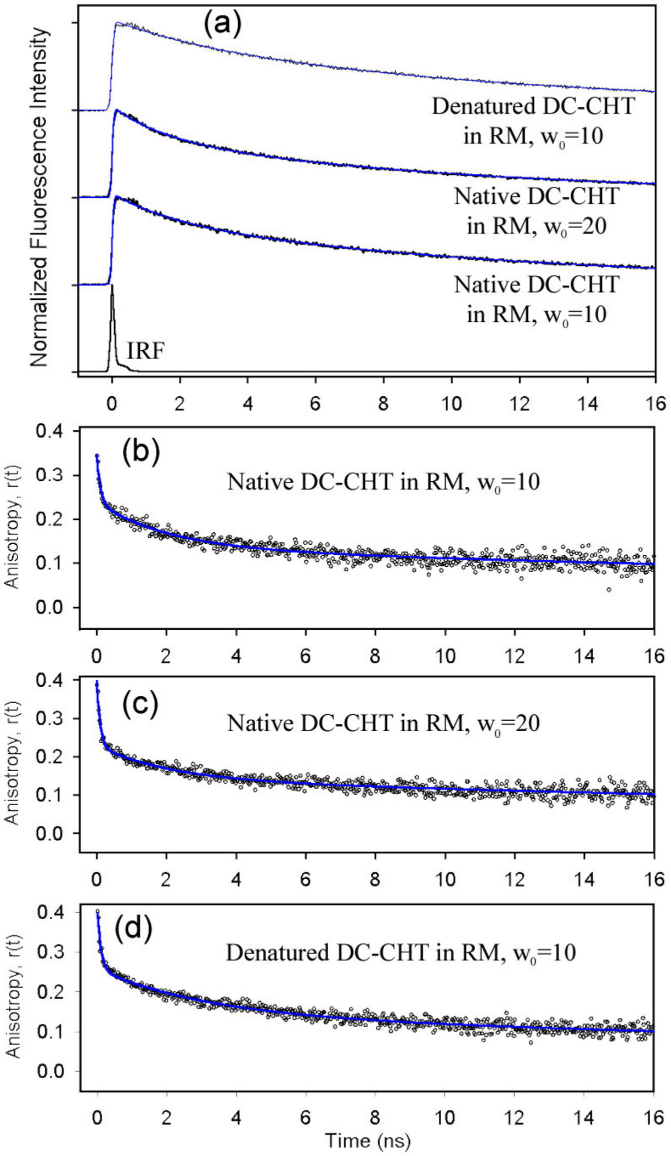

Fig. 4-6. (a) Fluorescent decays of dansyl native DC-CHT in w_0= 10 and 20 RM and that of denatured DC-CHT in w_0= 10 RM at 500 nm along with instrument response function IRF. (b), (c) and (d) show the temporal fluorescence anisotropy.

within RM, the local orientational motion of the chromophore gets slowed down with increase in magnitude of time constant from 0.6 ns (in the buffer) to ~2 ns (in RM). The fastest time constant of 0.09 ns may be due to the local motion of the chromophore in some perturbed site of CHT created upon incorporation in RM [9, 10]. For denatured DC–CHT in w_0= 10 RM, the rotational correlation time constants obtained are 0.18 ns (41.9%), 0.9 ns (48.4%) and 88 ns (9.7%). Since the compact structure of CHT is transformed into random coil in denatured CHT, the dansyl chromophore finds itself at sites that differ widely in their local viscosities thus, giving rise to two distinct local reorientational time constants. This fact is evident from the calculated values of diffusion coefficient of the local motion of the dansyl chromophore (see table 4-2).

4.3. Conclusion:

Studies of picosecond resolved dynamics of a covalently attached fluorescence probe at the surface of a digestive protein α-chymotrypsin and in the matrix of a randomly oriented polypeptide chain of the denatured protein elucidate the key time scales involved in the solvation of the probe by hydration water and polar residues of the protein. In the native state the probe at the surface of the protein reports a solvation time of 133 ps, where the dynamics is mainly due to collective water motion caused by protein conformation fluctuation. This result is further supported by a femtosecond study on protein surface hydration done by site-specific mutation of enzyme *Staphylococcal* nuclease [16]. Note that the solvation shift recovered in our experiment is only 14.6% with a huge missing shift of 72.5% of the total estimated dynamical fluorescence stokes shift of the probe. Earlier it has been shown that the time scale of solvation by hydration water of various protein molecules is about 20 ps [17], which is beyond our instrumental resolution. On the other hand the solvation of the probe by polar protein residues shows two distinct time constants of 131 and 900 ps, giving much slower dynamics compared to that of hydration water, where the longer solvation time is due to solvation by polar protein side-chain. Here the missing dynamics in the early time due to our limited instrumental time resolution is only 15.6%. The temporal fluorescence anisotropy of the probe, which reflects a typical dynamics of a side-chain in the denatured protein, is similar to dynamics of solvation of the probe in the microenvironment, reflecting significant interaction of the probe with neighboring polar residues of the protein. The rotational diffusion of the probe at the surface of the protein is found to be much retarded compared to that in the random conformation of the denatured protein.

The probe at the surface of the native protein in an aqueous nanospace of a reverse micelle (w_0= 10) shows significantly slower solvation dynamics compared to that in the bulk buffer. However, upon increasing the size of the reverse micelle (w_0= 20) the dynamics become faster. The faster solvation dynamics in the larger reverse micelle is consistent with the fact that the protein resides in the central water pool of the reverse micelle and in the larger sized reverse micelle the protein surface sees more core associated water. The solvation dynamics of the probe in the denatured protein in the reverse micelle shows similar time constants to that in the bulk denaturant solution indicating a minor change of the denatured protein upon encapsulation in the nanospace. Thus, the method used in this work in order to explore key time scales of protein solvation can be effectively used in characterizing solvation patterns and dynamics of other proteins.

References

[1] A.K. Shaw, R. Sarkar, D. Banerjee, S. Hintschich, A. Monkman and S.K. Pal, Direct observation of protein residue solvation dynamics, J. Photochem. Photobiol. A: Chem. 185 (2006) 76-85.

[2] J.T. Vivian and P.R. Callis, Mechanisms of Tryptophan Fluorescence Shifts in Proteins, Biophys. J. 80 (2001) 2093-2109.

[3] J.J. Birktoft and D.M. Blow, The Structure of Crystalline α-Chymotrypsin, V. The Atomic Structure of Tosyl-α-Chymotrypsin at 2 Angstroms Resolution, J. Mol. Biol. 68 (1972) 187-240.

[4] R. Sarkar, M. Ghosh, A.K. Shaw and S.K. Pal, Ultrafast surface solvation dynamics and functionality of an enzyme Chymotrypsin upon interfacial binding to a cationic micelle, J. Photochem. Photobiol. B: Biology 79 (2005) 67-78.

[5] R.S. Fee and M. Maroncelli, Estimating the time-zero spectrum in time-resolved emmsion measurements of solvation dynamics, Chem. Phys. 183 (1994) 235-247.

[6] S.K. Pal, J. Peon and A.H. Zewail, Ultrafast surface hydration dynamics and expression of protein functionality: α-chymotrypsin, Proc. Natl. Acad. Sci. USA 99 (2002) 15297-15302.

[7] L. Nilsson and B. Halle, Molecular Origin of Time-Dependent Fluorescence Shifts in Proteins, Proc. Natl. Acad. Sci. USA 102 (2005) 13867-13872.

[8] V.N.D. Taran, C. Veeger and A.J. Visser, Comparison of the dynamic structure of α-chymotrypsin in aqueous solution and in reversed micelles by fluorescent active-site probing, Eur. J. Biochem. 211 (1993) 47-55.

[9] A.L. Creagh, J.M. Prausnitz and H.W. Blanch, Structural and catalytic properties of enzymes in reverse micelles, Enzyme Microb. Tech. 15 (1993) 383-392.

[10] J. Liu, J. Xing, R. Shen, C. Yang and H. Liu, Effects of reverse micelles on the secondary structure of α-Chymotrypsin and Subtilisin Carlsberg by FTIR Spectroscopy, AIChE Annual meeting, conference proceeding, Austin, Texas (2004).

[11] S.M. Andrade and S.M.B. Costa, The location of Tryptophan, N-Acetyl Tryptophan and α-Chymotrypsin in Reverse Micelles of AOT: A Fluorescence Study, Photochem. Photobiol. 72 (2000) 444-450.

[12] S.M. Andrade and S.M.B. Costa, Structural changes of α-chymotrypsin in reverse micelles of AOT studied by steady state and transient state fluorescence spectroscopy, J. Mol. Struct. 565-566 (2001) 219-223.

[13] D.B. Watlaufer, S.K. Malik, L. Stoller and R.L. Coffin, Nonpolar Group Participation in the Denaturation of Proteins by Urea and Guanidinium Salts. Model Compound Studies, J. Am. Chem. Soc. 86 (1964) 508-514.

[14] F. Vanzi, B. Madan and K. Sharp, Effect of the Protein Denaturants Urea and Guanidinium on Water Structure: A Structural and Thermodynamic Study, J. Am. Chem. Soc. 120 (1998) 10748-10753.

[15] S.K. Pal, J. Peon, B. Bagchi and A.H. Zewail, Biological water: Femtosecond dynamics of macromolecular hydration, J. Phys. Chem. B 106 (2002) 12376-12395.

[16] W. Qiu, Y.-T. Kao, L. Zhang, Y. Yang, L. Wang, W.E. Stites, D. Zhong and A.H. Zewail, Protein surface hydration mapped by site-specific mutations, Proc. Natl. Acad. Sci. USA 103 (2006) 13979-13984.

[17] S.K. Pal and A.H. Zewail, Dynamics of Water in Biological Recognition, Chem. Rev. 104 (2004) 2099-2123.

Chapter 5

Effect of Macromolecular Crowding on Structure and Function of Enzyme *Subtilisin Carlsberg*

5.1. Introduction:

Here we report activity of an enzyme *Subtilisin Carlsberg* (SC) in aqueous anionic micellar solution of sodium dodecyl sulfate (SDS). We have observed that the rate of enzymatic reaction of SC on substrates (Ala-Ala-Phe 7-amido-4-methyl coumarin (AAF-AMC) and N–CBZ-Gly-Gly-Leu p-nitroanilide (CBZ–GGL–pNA)) is retarded and depends heavily on the micellar concentration in the host solution. In order to understand the dependence of the enzymatic activity on micellar concentration, we fit our experimental results to a theoretical "pseudophase" model [1] proposed recently for enzymatic activity in aqueous micellar solution. To follow the environmental change at a particular site of the enzyme SC upon interaction with the micelle, intrinsic single tryptophan residue (Trp113) has been used as a fluorescent probe. The overall change of SC in the micellar solution is followed from the steady state and time resolved fluorescence spectroscopy of a covalently attached dansyl-probe (nonspecifically labeled) at the surface of the enzyme. Circular dichroism (CD) and dynamic light scattering (DLS) studies have been employed to follow the secondary structural change and overall size of the protein upon complexation with SDS micelles.

5.2. Activity of *Subtilisin Carlsberg* in macromolecular crowding [2]:

Subtilisin Carlsberg (SC) is a serine protease with a tryptophan residue (Trp113) at the surface and a catalytic triad (Asp32, His64 and Ser221) at the active site (see figure 2-10). Figure 5-1 shows the CD spectra of SC in 100 mM phosphate buffer, 1, 40 and 100 mM SDS solutions. The fitted data reveals helicity of 34.8% (buffer), 32.2% (1 mM SDS), 34.6% (40 mM SDS) and 31.3% (100 mM SDS). The α-helical content is consistent with that of the native SC (34%) in the crystalline state [34], indicating insignificant structural perturbation of the enzyme upon interaction with SDS micelle. It has been shown earlier that SDS monomers below their critical micellar concentration (CMC; 3.3 mM in buffer) are associated with other transport protein, Bovine Serum Albumin (BSA) through hydrophobic interaction and denature the protein at higher SDS concentration (much above CMC) to form necklace-bead type structure in the solution [3]. Similar interaction of the SDS molecules with the enzyme SC is expected to lead to a different secondary structure of SC at higher SDS concentration than that at a lower concentration of SDS. Our observation of the persistency of structural integrity of SC below and much above the CMC of SDS rules out the possibility of any specific interaction of monomeric SDS molecules with the enzyme.

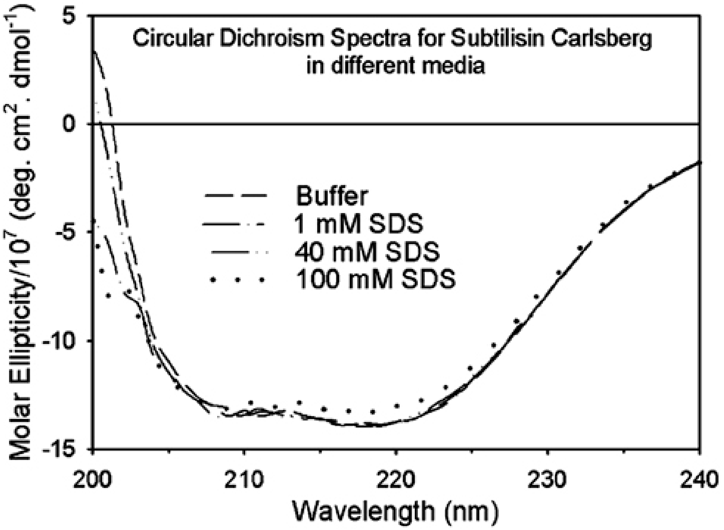

Fig. 5-1. CD spectra of SC in buffer and SDS solutions of various concentrations.

Figure 5-2(a) shows the rate of formation of AMC-product (7-amido-4-methylcoumarin) upon enzymatic activity of SC on AAF-AMC in buffer and in SDS solutions of different concentrations. The velocities of AMC-product formation in buffer, 1mM SDS and 40mM SDS are 41.5x10^{-3}, 18.1x10^{-3} and 0.2x10^{-3} μM.s^{-1}, respectively. It is clear that the activity of the enzyme is retarded by 2.3 and 244 times in 1 mM and 40 mM SDS, respectively, compared to that in buffer solution. We have also checked the activity of the enzyme on a different hydrophobic substrate CBZ-GGL-pNA (figure 5-2(b)) and the activity is found to be much higher compared to the case of AAF-AMC (344.9x10^{-3} and 30.2x10^{-3} μM.s^{-1} in 1mM and 40mM SDS solutions, respectively). The higher enzymatic activity on CBZ-GGL-pNA could be due to much higher affinity of the substrate towards the enzyme [4]. In order to check the enzymatic activity of SC on this substrate in bulk buffer, we have measured the enzymatic reaction rate in acetonitrile- buffer (8% v/v) solution. The rate is much faster (1.551 μM.s^{-1}) than that in surfactant solutions.

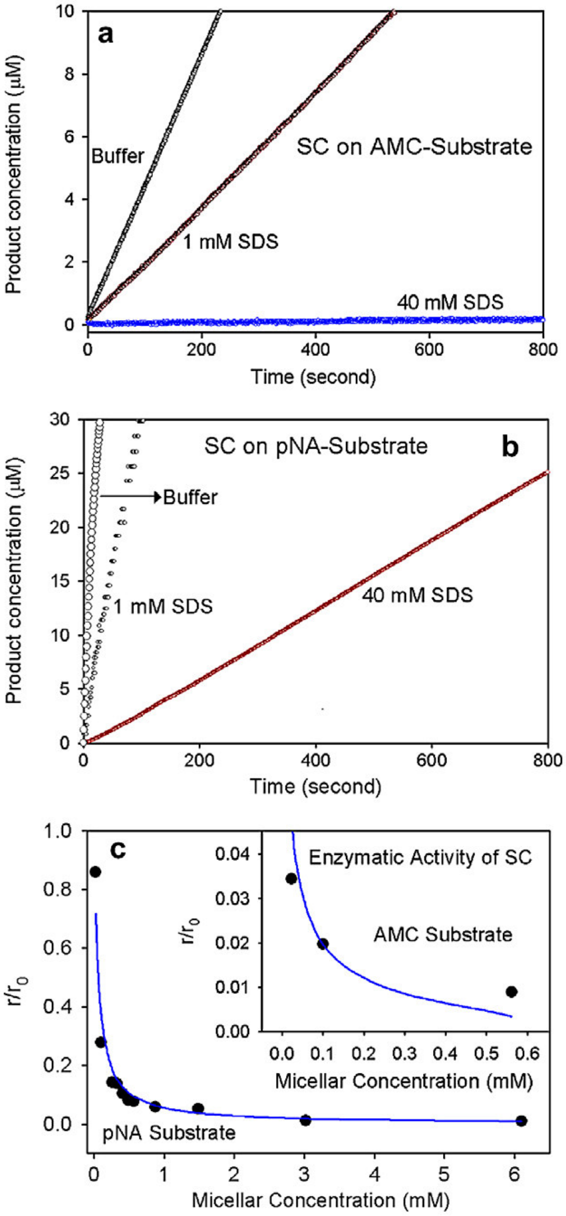

Fig. 5-2. Enzymatic activities of SC on various substrates: (a) AAF-AMC, (b) CBZ-GGL-pNA and (c) the relative rate of enzymatic activities of the enzyme SC on CBZ-GGL-pNA substrate. The solid line corresponds to the fitting data according to the pseudophase model (see text).

In order to understand the retardation of enzymatic activity in the micellar solution we measured the rates of enzymatic catalysis by SC in the surfactant solutions with various micellar concentrations and fitted the data points by simplex method using the theoretical "pseudophase" model (see section 2.1.7 for detail), initially introduced for enzymes encapsulated in reverse micelles [5] and recently advanced for enzymes in aqueous micellar environments [1]. In figure 5-2(c) the plot of (r/r_0) refers to the relative rates of substrate consumption at different concentration of SDS micelles. In this study we considered r_0 at 1 mM SDS concentration instead of that at CMC. This is because SC interacts neither with SDS monomers nor with SDS micelles as seen from CD (figure 5-1) and DLS data (figure 5-3(a)). It is found that the enzymatic activity monotonically decreases with increasing concentration of micelle. The solid line (figure 5-2(c)) fitted following equation (2-65) indicates that decreasing enzymatic activity corresponds to a model where the concentration of the substrate in the bound water phase is negligible in comparison to that of the substrate associated with the surfactant, i.e. the substrates aggregated in the bound water phase of the micelles are all segregated by the surfactant. Here we have maintained the enzyme and substrate concentrations to be 15 and 150 μM, respectively. The initial velocity (rate) of substrate consumption was measured upto a surfactant concentration of 400 mM for CBZ–GGL–pNA. From the simulation (figure 5-2(c), solid line) the parameter η_{ff} is found to be five orders of magnitude higher for CBZ–GGL–pNA substrate compared to that for the AAF-AMC, which is consistent with a previous report [4]. Since the enzymatic activity of SC with the substrate AAF-AMC falls much more steeply with the surfactant concentration (inset of figure 5-2(c)) compared to that with CBZ–GGL–pNA, only few data points were obtained. Evaluation of six parameters from the numerical fitting of only modest number of experimental points is not reliable. However, the agreement of the trend of the experimental data points with that of the model fitting is clear from the inset of figure 5-2(c).

DLS experiments (figure 5-3(a)) reveal hydrodynamic diameter of the micelle (40 mM SDS) and SC (native) to be 4.35 nm and 5.10 nm, respectively. Considering typical thickness of the hydration layer to be ~0.5 nm, our experimental observations are in good agreement with actual diameters of the micelle and the native protein, which are reported

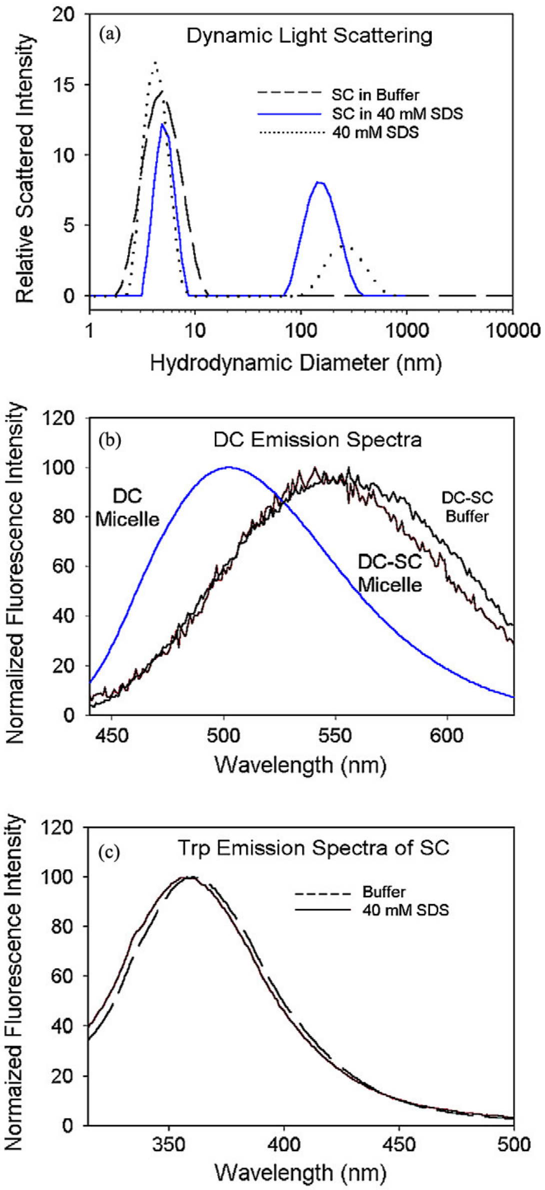

Fig. 5-3. (a) The dynamic light scattering spectra of SC in buffer (dash), SC in 40 mM SDS (solid) and 40 mM SDS micelle (dot). (b) The emission spectra of dansyl probe in DC–micelle complex, DC–SC–micelle complex and DC–SC complex in buffer. (c) The emission spectra of Trp113 residue of SC in buffer and 40 mM SDS solutions.

to be 3.3 and 4.2 nm, respectively [6, 7]. The peaks due to particles with higher hydrodynamic diameter (100 nm and larger) in surfactant solutions could be due to the presence of higher micellar aggregates in the solutions. The hydrodynamic diameter of SC in presence of the micelle is found to be 5.20 nm revealing the intactness of the globular structure of the enzyme in the surfactant solution. The intactness of the secondary structure as evident from CD studies along with the preservation of globular structure indicates the retention of tertiary structure of the enzyme in the surfactant solution. The observation also rules out the possibility of formation of sandwich-like complex where the resulting diameter is expected to be ~10 nm. However, the interaction of the enzyme with the micelle is clearly evident from steady-state fluorescence spectrum of the DC-SC complex (figure 5-3(b)). The emission maximum of DC-SC in buffer at 555 nm shifts to 541 nm in 40 mM SDS indicating that DC bound to SC finds itself close to the surface of SDS micelle, namely, stern layer. The inclusion of the enzyme into the micelle can also be ruled out from the steady-state emission studies as the emission maximum of DC-SC-micelle complex (541 nm) is considerably red shifted compared to that of DC embedded in SDS micelle (502 nm).

Figure 5-4(a-b) shows the temporal fluorescence anisotropy (r(t)) decays of AAF-AMC in buffer and 40 mM SDS, respectively. Figure 5-4(c) shows temporal evolution of r(t) of the AMC chromophore (product) in 40 mM SDS. The rotational correlation time (ϕ) of AAF-AMC in 40 mM SDS (202 ps (15%), 1334 ps (56%) with a much longer time constant which does not decay in our experimental time window) is much slower than that in bulk buffer solution (222 ps). This considerable slowing down of rotational time constant of AAF-AMC in 40 mM SDS medium indicates strong affinity of the substrate to the micelle. However, AMC-product in 40 mM SDS micelle reveals two ϕ values; 184 ps (64%) and 1800 ps (15%) with a much longer time constant, which does not decay in our experimental time window. The existence of faster time constant (64%) in the fluorescence anisotropy of the AMC-product reflects lesser micellar affinity compared to that of the substrate. The higher affinity of the substrate for the micelle indicates the segregation possibility of the substrate into the hydrophobic core of the micelle. The fluorescence anisotropy data of pNA-substrate and product are quite complicated due to its intricate internal dynamics.

In order to investigate the nature of complexation of SC with the micelle, we have also studied the emission properties of single tryptophan (Trp113) residue of the enzyme (figure 5-3(c)). The emission maximum of Trp113 in buffer (λ_{max}= 360 nm) shifts to 358 and 356 nm in 40 and 100 mM SDS micellar solutions, respectively. The minute change in the emission maximum of Trp113 compared to that of the enzyme-bound DC might

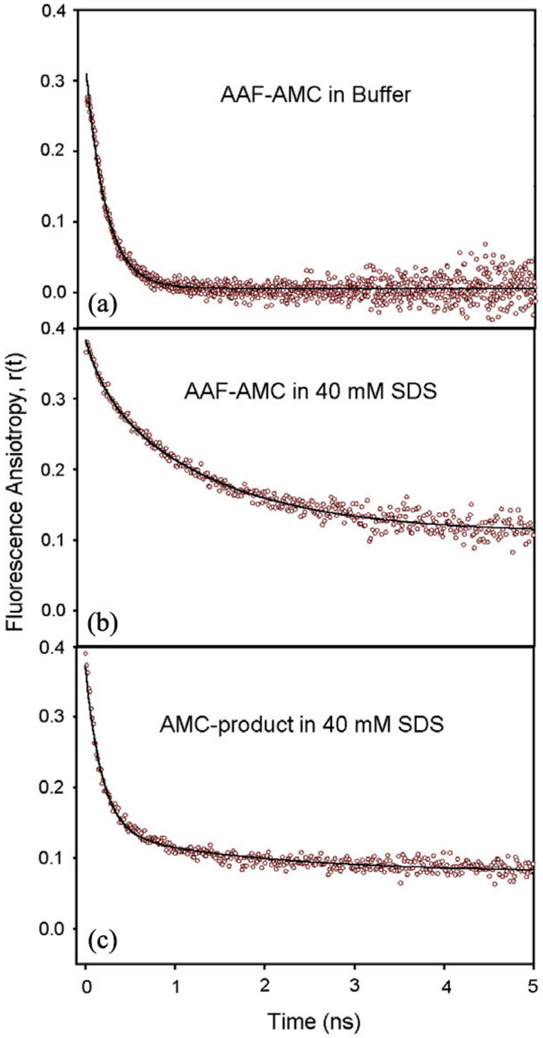

Fig. 5-4. The temporal fluorescence anisotropy decay curve of: (a) AAF-AMC substrate in buffer, (b) AAF-AMC substrate in 40 mM SDS and (c) AMC-product in 40 mM SDS.

indicate involvement of specific site/sites (excluding Trp113) of SC for the interaction with SDS micelle. The temporal fluorescence anisotropy decay of Trp113 in buffer (ϕ= 496 ps (70%) with a much longer time component which does not decay in our experimental time window) is comparable to that of SC–SDS complex (451 ps (68%) with a much longer time component which does not decay in our experimental time window) as shown in figure 5-5(a-b). The observation excludes any significant interaction of SC with

SDS micelle through the Trp113 site. Another possibility of the negligible change in the

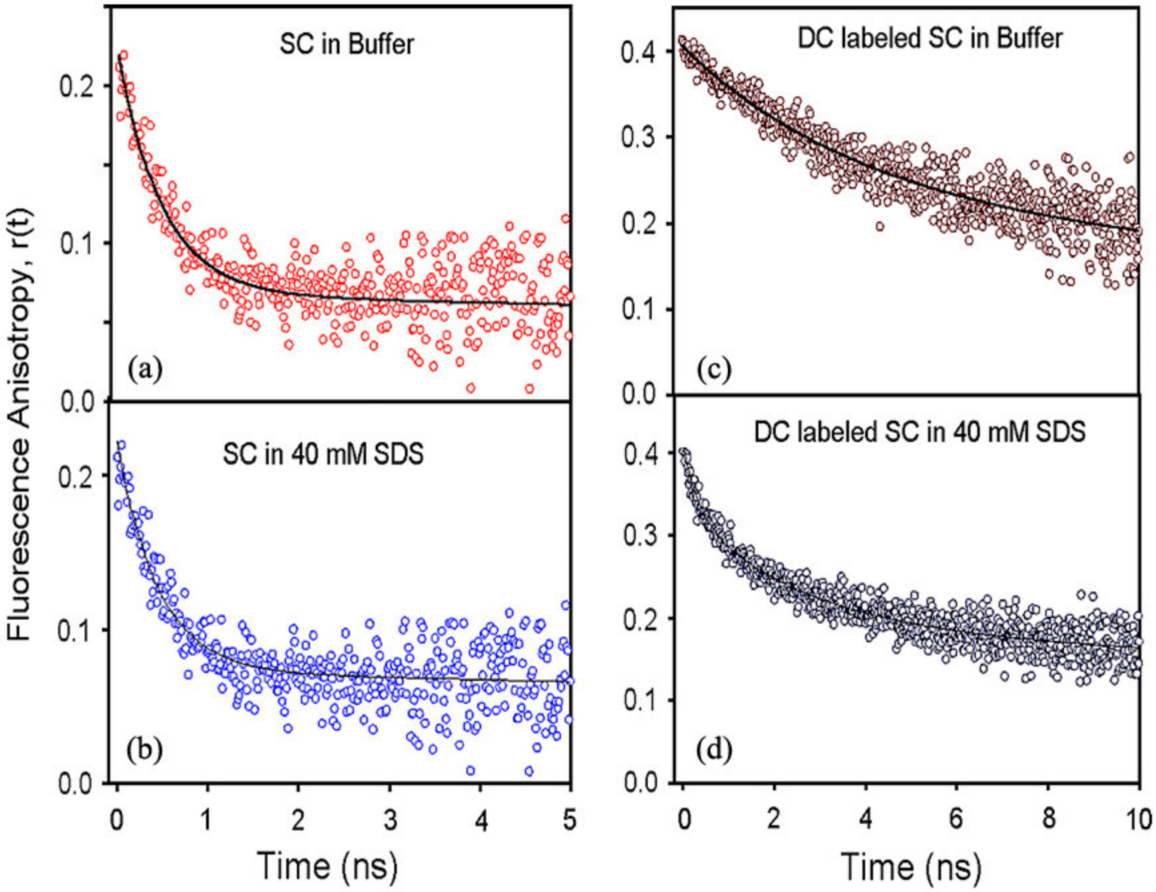

Fig. 5-5. The temporal fluorescence anisotropy decay curve of Trp113 of SC in (a) buffer and (b) 40 mM SDS while that of DC–SC complex in (c) buffer and (d) 40 mM SDS.

fluorescence anisotropy decay of Trp113 could be due to the buried nature of Trp113 in SC. However, our steady-state fluorescence studies indicate that the emission maximum of Trp113 has no shift compared to that of the free tryptophan in bulk buffer reflecting significant exposure of the Trp113 residue of the SC towards bulk buffer. The conclusion is further supported by a recent MD simulation study [8], which confirmed that Trp113 residue of SC is edge exposed and the contribution to the Stokes shift from the bulk water is much larger (70%) than that from the protein environment (polar/charged residues). Thus, the less change in the fluorescence anisotropy of the probe Trp113 upon interaction with SDS micelle cannot be due to the buried nature of the probe in the enzyme SC. The fluorescence anisotropy decay of the nonspecific label DC, which essentially probes all the surface sites of the enzyme in buffer (figure 5-5(c)), shows time constants of 3970 ps

(47%) and 50 000 ps (53%). The faster and slower time constants can be attributed to the local tumbling motion of the probe and global rotational motion of the labeled protein respectively. In 40 mM SDS (figure 5-5(d)) solution the DC-labeled enzyme shows three distinct time constants in the fluorescence anisotropy decay; 334 ps (19%), 2555 ps (36%) and 71156 ps (45%). The presence of the faster time constant (334 ps, 19%) in the DC–SC–micelle complex in contrast to the native DC–SC may indicate a minute local structural perturbation reflecting reorientation of a particular dansyl chromophore in the perturbed site of the enzyme. However, the global rotational motion of the enzyme in the micellar crowding is indeed slowed down considerably.

5.3. Conclusion:

From the present study it is found that SC retains its structural integrity in SDS solution, which is a potential protein denaturant. From DLS experiments no evidence of sandwich-like SC–SDS complex formation is found indicating that SC does not encroach into the hydrophobic surfactant core of SDS micelle to form an elongated structure. Nonspecifically and specifically labeled fluorescence probes have been employed in order to investigate the nature of the complexation. The steady-state and time-resolved fluorescence anisotropy of a fluorescent tag DC at the nonspecific sites of the enzyme, which essentially probes polarity and geometrical restriction on the surface of the enzyme SC, show evidence of micellar crowding in the vicinity of the enzyme. However, the moderate change in the emission properties and temporal fluorescence anisotropy dynamics of the intrinsic fluorophore Trp113 at a specific site of the enzyme reflects participation of specific site/sites (excluding Trp113) of the enzyme for the interaction with SDS micelle. Our studies on the enzyme kinetics of native-like SC in the micellar solution support a model where the interaction of SC with the micelle through its stern layer is assumed. The model also assumes that the surfactant core of the micelle segregates the substrates in the micellar solution. Our fluorescence anisotropy studies on AAF-AMC substrate in the micellar solution are consistent with the segregation picture. Thus, this study reveals that the retardation of enzymatic activity of SC in the micellar crowd is *not* solely due to structural perturbation of the protein; rather the affinity of the substrate and enzyme towards the micelle is the determining factor for the retardation. The reported experimental observation on the enzymatic activity of SC, with structural integrity retained (from CD studies) in a macromolecular crowding, would be useful in the understanding of the functionality of enzymes under physiological condition.

References

[1] P. Viparelli, F. Alfani and M. Cantarella, Models for enzyme superactivity in aqueous solutions of surfactants, Biochem. J. 344 (1999) 765-773.

[2] A.K. Shaw and S.K. Pal, Activity of Subtilisin Carlsberg in macromolecular crowding, J. Photochem. Photobiol. B: Biol. 86 (2007) 199-206.

[3] N.J. Turro, X.-G. Lei, K.P. Anantapadmanabhan and M. Aronson, Spectroscopic probe analysis of Protein-Surfacatant Interactions: The BSA/SDS System, Langmuir 11 (1995) 2525-2533.

[4] J.K.A. Kamal, T. Xia, S.K. Pal, L. Zhao and A.H. Zewail, Enzyme functionality and solvation of Subtilisin *Carlsberg*: From hours to femtoseconds, Chem. Phys. Lett. 387 (2004) 209-215.

[5] R. Bru, A. Sanchez-Ferrer and F. Garcia-Garmona, A theoretical study on the expression of enzymic activity in reverse micelles., Biochem. J. 259 (1989) 355-361.

[6] P.A. Fitzpatrick, D. Ringe and A.M. Klibanov, X-Ray Crystal Structure of Cross-Linked Subtilisin Carlsberg in Water vs Acetonitrile, Biochem. Biophys. Res. Commun. 198 (1994) 675-681.

[7] P.A. Hassan, S.R. Raghavan and E.W. Kaler, Microstructural changes in SDS micelles induced by hydrotropic salt, Langmuir 18 (2002) 2543-2548.

[8] J.T. Vivian and P.R. Callis, Mechanisms of Tryptophan Fluorescence Shifts in Proteins, Biophys. J. 80 (2001) 2093-2109.

Chapter 6

Exploration of the Role of Structure and Dynamics of Biomimetics, Genomic and Synthetic DNAs in Ligand Binding

6.1. Introduction:

In this chapter we will discuss in detail the solvation and fluorescence depolarization dynamics of a DNA intercalator, acridine orange (AO) in AOT reverse micelles (RMs) containing water (pH= 6.9) and NaOH (pH= 13.6), SDS, CTAB and TX100 normal micelles using picosecond time-resolved fluorescence spectroscopy. Time resolved area normalized emission spectra (TRANES) has been constructed to determine the various acridine species present in the system and/or the various environments experienced by the AO molecules in their excited states. We have applied the wobbling-in-cone model to analyze and interpret the time-resolved fluorescence anisotropy decay data of AO in these restricted environments. We have further applied this model to AO intercalated inside genomic salmon sperm DNA (SS-DNA) and two synthetic oligonucleotides: (1) $(GCGCGCGCGCGC)_2$ (oligo1) and (2) $(CGCAAATTTGCG)_2$ (oligo2) to study the reorientational dynamics of the probe AO within the intercalation site and thus to predict the rigidity of genomic DNA and synthetic oligonucleotides.

6.2. Fluorescence Relaxation Dynamics of Acridine Orange in Nano-sized Micellar Systems and DNA [1]:

Figure 6-1(a) shows the absorption spectra of AO in water (pH= 6.9) and RM containing water. The absorption spectra show a slight red shift from 492 nm in water to 495 nm in AOT RM, which indicates a finite interaction between AO and RM. The shoulder at 467 nm in the absorption spectrum of AO in water is due to the formation of dimeric AO in water [2]. It is known that AO is more sensitive to polarizability of environment than the polarity [3]. The red shift may indicate the location of AO closer to the reverse micellar interface with higher polarizability than the central water core of the

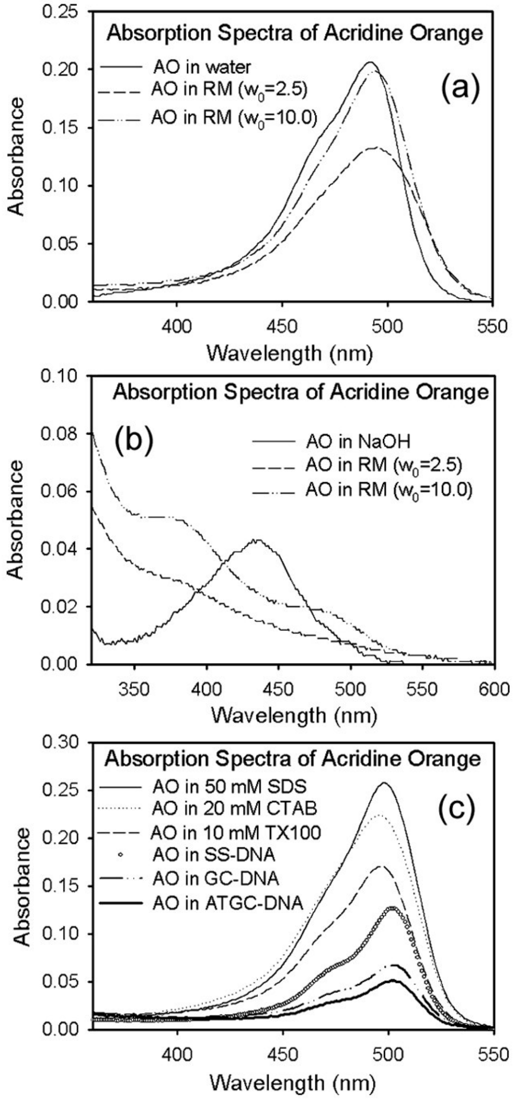

Fig. 6-1. Abosrption spectra of acridine orange (AO) in (a) RM containing water, (b) RM containing NaOH and (c) Micelles (SDS, CTAB and TX100) and DNA (Salmon sperm, oligo1 and oligo2).

RM. Also, in w_0= 2.5 RM the full width at half maximum (FWHM) of absorption spectrum is higher than that in water indicative of AO being present in a heterogeneous environment. However, in w_0= 10 RM the FWHM is close to that of water which may indicate that AO molecules are little away from the interface towards core water than in w_0= 2.5 RM. This may seem obvious because the diameter of w_0= 2.5 RM water pool is

~10 Å while the diameter of AO is 6.9 Å [4]. Thus AO is much closer to the interface in w_0= 2.5 RM.

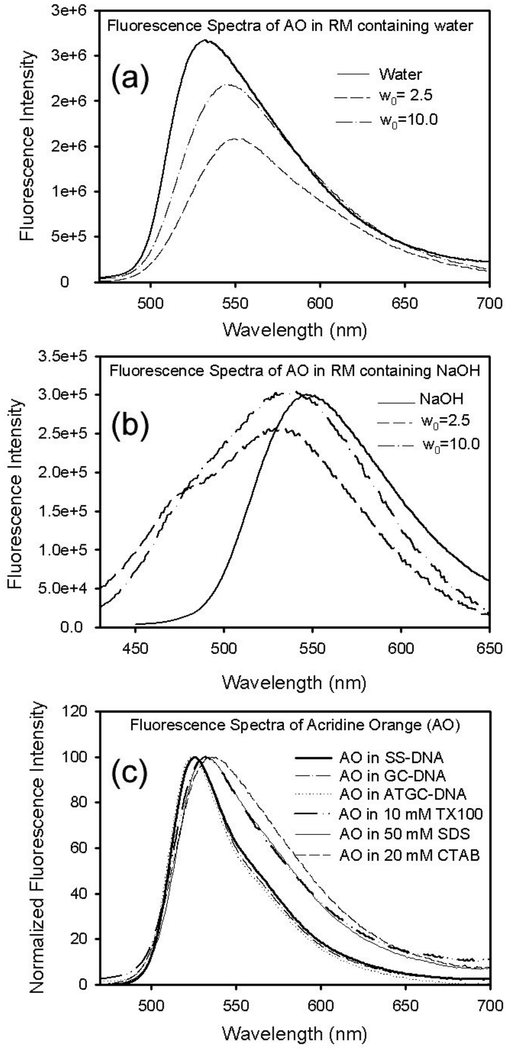

Fig. 6-2. Fluorescence spectra of acridine orange (AO) in (a) RM containing water, (b) RM containing NaOH and (c) Micelles (SDS, CTAB and TX100) and DNA (Salmon sperm, oligo1 and oligo2).

Figure 6-2(a) shows the fluorescence spectra of AO in water and RM containing water. The fluorescence maximum of AO in water is at 532 nm while that in w_0= 2.5 and 10 RMs are at 549 and 545 nm, respectively. The slight blue shift of fluorescence maximum of AO in w_0= 10 RM than that in w_0= 2.5 RM once again proves the location of AO slightly away from the reverse micellar interface towards core water in w_0= 10 RM than in w_0= 2.5 RM. Figures 6-1(b) and 6-2(b) show the absorption and emission spectra of AO in NaOH (pH= 13.6) and that in RM containing NaOH. AO in NaOH solution has an absorption peak at 435 nm while the emission maximum is at 546 nm. These peaks correspond to that of deprotonated basic acridine orange (Scheme 6-1) [2]. However, in RM (w_0= 2.5 and 10) containing NaOH, a peak at 375 nm with a shoulder at 460 nm in the absorption spectra and a peak at ~535 nm with a shoulder at ~470 nm in the emission spectra are observed. These two peaks in the absorption and emission spectra indicate the existence of two types of AO — i) basic AO in the non-polar isooctane phase (absorption peak= 375 nm and emission peak= 470 nm) and ii) protonated AO lying at the RM interface (absorption peak= 460 nm). The peaks at 533 nm (w_0= 2.5 RM) and 538 nm (w_0= 10 RM) could be due to formation of AO protonated at terminal amino groups [2] and/or intracyclic imino group.

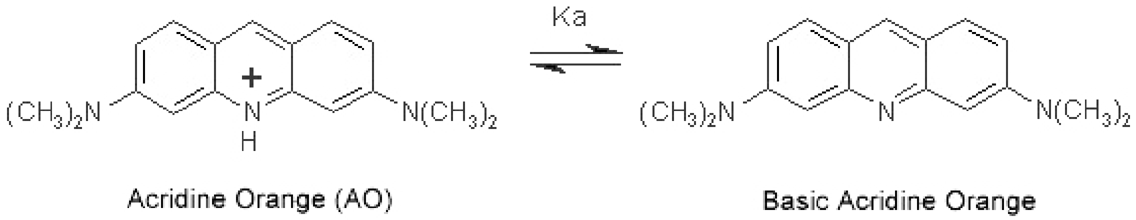

Scheme 6-1: Acid-Base Equilibrium of Acridine Orange

Figures 6-1(c) and 6-2(c) show the absorption and emission spectra of AO in 50 mM SDS (anionic), 20 mM CTAB (cationic) and 10 mM TX100 (neutral) surfactant solutions and that in genomic salmon sperm DNA and two synthetic DNA oligomers – oligo1 and oligo2. In all the micelles the absorption and emission spectra indicate AO to be present in the stern layer of the micelles (table 6-1). However, in both genomic and synthetic DNAs the absorption and emission spectra are 10 nm red shifted and 6 nm blue shifted, respectively compared to that of AO in water, indicating AO to be intercalated inside the DNA [3, 5] . The absorption and fluorescence peaks of AO in various environments are given in table 6-1.

Figure 6-3(a-b) shows the fluorescence decay transients of AO in RM (w_0= 2.5) containing water and that containing NaOH at various wavelengths. In case of RM

Table 6-1. Steady state absorption and fluorescence data of acridine orange in various environments.

Systems	Absorption Peak (nm)	Fluorescence Peak (nm)
Water (pH= 6.9)	492	532
NaOH (pH= 13.6)	435	546
RM with water (w_0= 2.5)	495	549
RM with water (w_0= 10.0)	494	545
RM with NaOH (w_0= 2.5)	375, 460	470, 533
RM with NaOH (w_0= 10.0)	375, 460	477, 538
20 mM CTAB	496	536
50 mM SDS	498	531
10 mM TX100	496	532
SS-DNA	502	526
$(GCGCGCGCGCGC)_2$ (oligo1)	502	526
$(CGCAAATTTGCG)_2$ (oligo2)	502	523

containing water the fluorescence transients are found to decay at blue wavelengths and a corresponding rise is seen at red wavelengths. This observation is consistent with the clear case of solvation of AO within the RM [6] (see below). However, in case of RM containing NaOH only decay components are observed at all wavelengths with comparatively longer components at higher wavelengths. This observation may indicate the presence of more than one species, which may or may not be kinetically coupled in the excited or ground state or a single species having more than one type of environment. The fitted fluorescence decay data of AO under various conditions are given in table 6-2. Figures 6-4(a) and 6-5(a) shows the time resolved emission spectra (TRES) of AO in RM containing water of w_0= 2.5 and 10, respectively. The constructed solvation correlation functions (figures 6-4(b) and 6-5(b)) with solvation shifts 671 cm^{-1} (w_0= 2.5) and 711 cm^{-1} (w_0= 10) show a biexponential decay. The solvation time constants are given in table 6-3. The similarity of both the faster and slower time constants indicates the presence of AO in similar environment near the interface in both the RMs. The faster and slower time constants correspond to solvation by free water (core type) and bound water (interfacial type) molecules, respectively. It has to be noted that the TRANES of AO in the RMs of w_0= 2.5 and 10 containing water do not exhibit any isoemissive point indicating that the dynamics of solvation of the probe in the RMs are essentially due to a single species.

Table 6-2. Fitted fluorescence transients of acridine orange in various environments.

Systems	**Wavelength (nm)**	**τ_1 (ns)**	**τ_2 (ns)**	**τ_3 (ns)**
Water (pH= 6.9)	532	0.46 (10.5%)	1.85 (89.5%)	-
NaOH (pH= 13.6)	550	0.28 (26.4%)	1.46 (31.1%)	6.20 (42.5%)
RM with water (w_0= 2.5)	550	0.38 (11.4%)	2.78 (72.9%)	5.12 (15.7%)
RM with water (w_0= 10.0)	550	0.29 (8.9%)	2.19 (77.4%)	3.97 (13.7%)
RM with NaOH (w_0= 2.5)	470	0.12 (44.4%)	0.77 (21.7%)	2.77 (23.8%)
	530	0.28 (36.5%)	2.39 (41.7%)	9.21 (21.8%)
RM with NaOH (w_0= 10.0)	480	0.19 (46.6%)	2.06 (31.3%)	6.44 (22.1%)
	540	0.31 (26.2%)	2.79 (51.0%)	8.00 (22.8%)
20 mM CTAB	536	0.77 (23.6%)	1.65 (74.3%)	9.53 (2.1%)
50 mM SDS	530	0.23 (5%)	3.08 (90%)	5.51 (5%)
10 mM TX100	532	0.35 (7.8%)	2.20 (88.5%)	5.66 (3.7%)
SS-DNA	530	-	3.09 (23.3%)	5.38 (76.7%)
$(GCGCGCGCGCGC)_2$ (oligo1)	530	-	1.62 (19.6%)	4.76 (80.4%)
$(CGCAAATTTGCG)_2$ (oligo2)	530	-	2.33 (32.1%)	5.15 (67.9%)

Table 6-3. Solvation correlation data for AO in various environments.

Systems	**Blue/Red End**	**τ_1 (ns)**	**τ_2 (ns)**
RM with Water (w_0= 2.5)	-	0.40 (48.5%)	3.65 (51.5%)
RM with Water (w_0= 10.0)	-	0.55 (43.0%)	3.30 (57.0%)
RM with NaOH (w_0= 2.5)	**NP1**	0.30 (70.3%)	8.00 (29.7%)
	NP2	0.40 (49.7%)	2.55 (50.3%)
RM with NaOH (w_0= 10.0)	**NP1**	0.25 (63.4%)	1.70 (36.6%)
	NP2	0.10 (60.8%)	1.10 (39.2%)
50 mM SDS	**-**	0.55 (32.8%)	1.65 (67.2%)

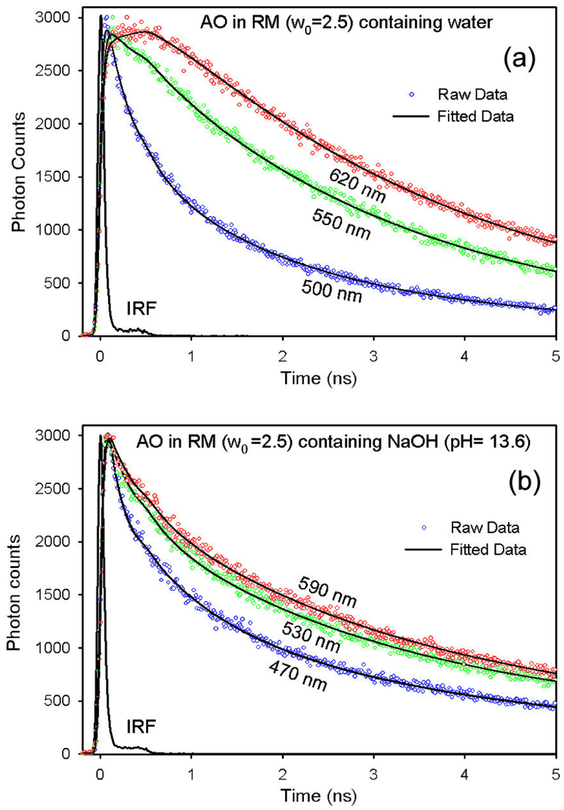

Fig. 6-3. Fluorescence decay transients at various wavelengths of AO in RM (w_0= 2.5) containing (a) water and (b) NaOH.

Inserts of figures 6-4(b) and 6-5(b) show the temporal fluorescence anisotropy decay, r(t) of AO in w_0= 2.5 and 10 RMs containing water. The rotational correlation time constants are given in table 6-4. It is found that both the slower and faster anisotropy time constants have decreased for AO in RM (w_0= 10) compared to that in w_0= 2.5 RM. This is an indication of the fact that in larger RM, AO is much freer to move. The wobbling-in-cone model analysis of the r(t) data shows that the semicone angle inscribed by AO in smaller RM is 22.21° while that in larger one is 25.26° (equation 2-40). Also the diffusion constant of lateral diffusion of AO in smaller RM (w_0= 2.5) is two orders of magnitude lower than that in larger one (w_0= 10). The rotational time constants and diffusion coefficients for overall micellar motion, lateral diffusion of AO along the interface and wobbling-in-cone motion of AO, calculated using equations (2-37) to (2-41) are given in table 6-5. The lateral diffusion time constant of 16.8 ns in w_0= 2.5 RM shows that there is no appreciable translation of AO within its lifetime in this small RM.

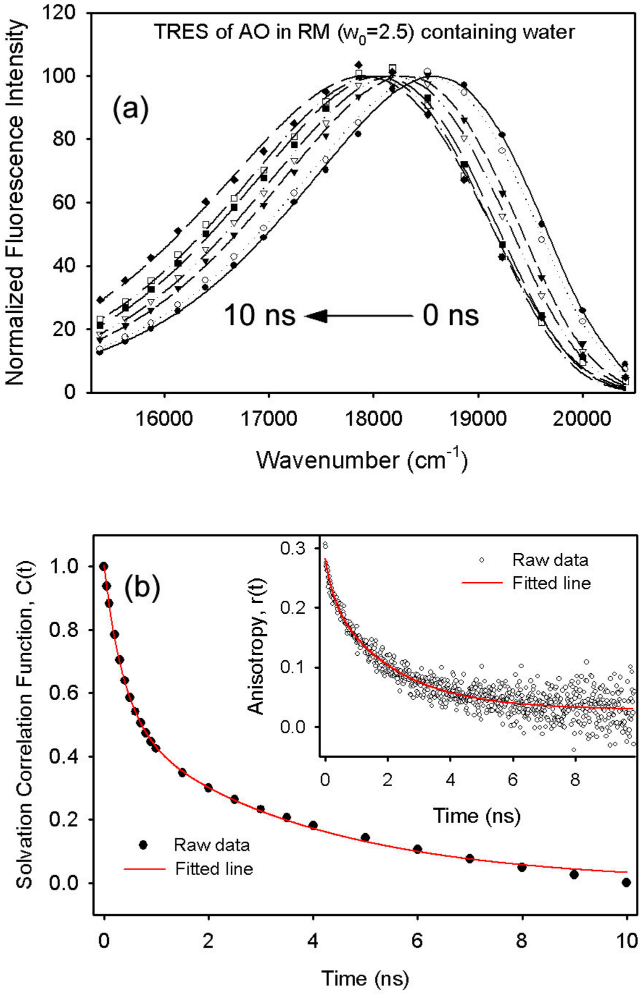

Fig. 6-4. (a) Time resolved emission spectra (TRES) of AO in RM (w_0= 2.5) containing water, (b) Solvation correlation curve and temporal anisotropy decay curve (insert) of AO in RM (w_0= 2.5) containing water.

Figures 6-6(a) and 6-7(a) show the TRANES of AO in RM of w_0= 2.5 and 10 containing NaOH, respectively. In both the spectra an isoemissive point is observed (503 nm for w_0= 2.5 and 514 nm for w_0= 10 RMs. In both the cases the intersection points lie in between the emission maxima of basic AO in isooctane phase and that of protonated AO at the reverse micellar interface. Thus, RM containing NaOH has two types of AO, basic AO and protonated AO. Although RMs containing NaOH has pH= 13.6 which is higher than the excited pK_a (13.3) of basic AO [2], signature of protonated AO is found because

Table 6-4. Temporal fluorescence anisotropy decay data for acridine orange in various environments.

Systems	Wavelength (nm)	ϕ_1 (ns)	ϕ_2 (ns)	r_0	r_∞
Water (pH= 6.9)	532	0.11 (100.0%)	-	0.359	0.000
NaOH (pH= 13.6)	550	0.14 (100.0%)	-	0.336	0.000
RM with water (w_0= 2.5)	550	0.27 (20.5%)	2.10 (79.5%)	0.254	0.014
RM with water (w_0= 10.0)	550	0.16 (25.8%)	1.31 (74.2%)	0.266	0.010
RM with NaOH (w_0= 2.5)	470	0.20 (33.4%)	3.20 (66.7%)	0.249	0.003
	530	0.22 (18.7%)	2.74 (81.4%)	0.209	0.006
RM with NaOH (w_0= 10.0)	480	0.19 (46.8%)	1.20 (53.2%)	0.241	0.012
	540	0.28 (34.8%)	2.23 (65.2%)	0.226	0.013
20 mM CTAB	536	0.09 (68.3%)	0.90 (31.7%)	0.243	0.002
50 mM SDS	530	0.12 (60.0%)	1.12 (40.0%)	0.364	0.001
10 mM TX100	532	0.30 (44.2%)	2.49 (55.8%)	0.194	0.000
SS-DNA	530	0.13 (53.4%)	5.52 (46.6%)	0.212	0.095
$(GCGCGCGCGCGC)_2$ (oligo1)	530	0.08 (33.5%)	2.08 (66.5%)	0.182	0.000
$(CGCAAATTTGCG)_2$ (oligo2)	530	0.36 (16.8%)	2.18 (83.2%)	0.173	0.000

it is known that pH at the interface of anionic micelles or reverse micelles is less than that of the bulk water or free water at the center of the RM [7, 8]. Since RMs containing NaOH have two types of AO in two different environments, the TRES of AO in these RMs (w_0= 2.5 and 10) showed two peaks corresponding to two different types of AO molecules from the time zero itself. As a result the TRES of AO in these RMs could not be fitted with a single lognormal function, but with a double lognormal one. We have followed the peak

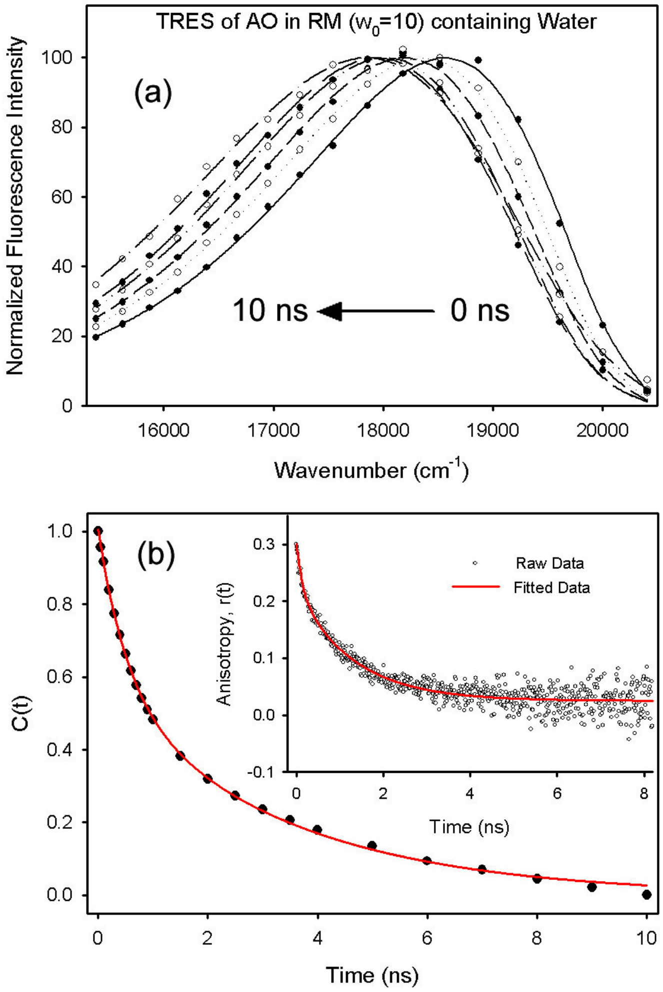

Fig. 6-5. (a) Time resolved emission spectra (TRES) of AO in RM (w_0= 10) containing water, (b) Solvation correlation curve and temporal anisotropy decay curve (insert) of AO in RM (w_0= 10) containing water.

shift of these two peaks one at red end (NP1) and the other at blue end (NP2) with time to determine the solvation relaxation time scales of these two different AO molecules. Similar spectral deconvolution is reported in the recent literature [9].

Figure 6-6(b) shows the temporal fluorescence peak shift at red wavelength NP1 (for protonated AO at the interface) and blue wavelength NP2 (for basic AO in isooctane phase) [insert of figure 6-6(b)] derived from the TRES of AO in RM (w_0= 2.5) containing NaOH. The shorter time constants are same at both wavelengths indicating long range dipolar relaxation due to reorganization of core type water molecules, while longer time constants correspond to relaxation by interfacial water (2.55 ns) of protonated AO and

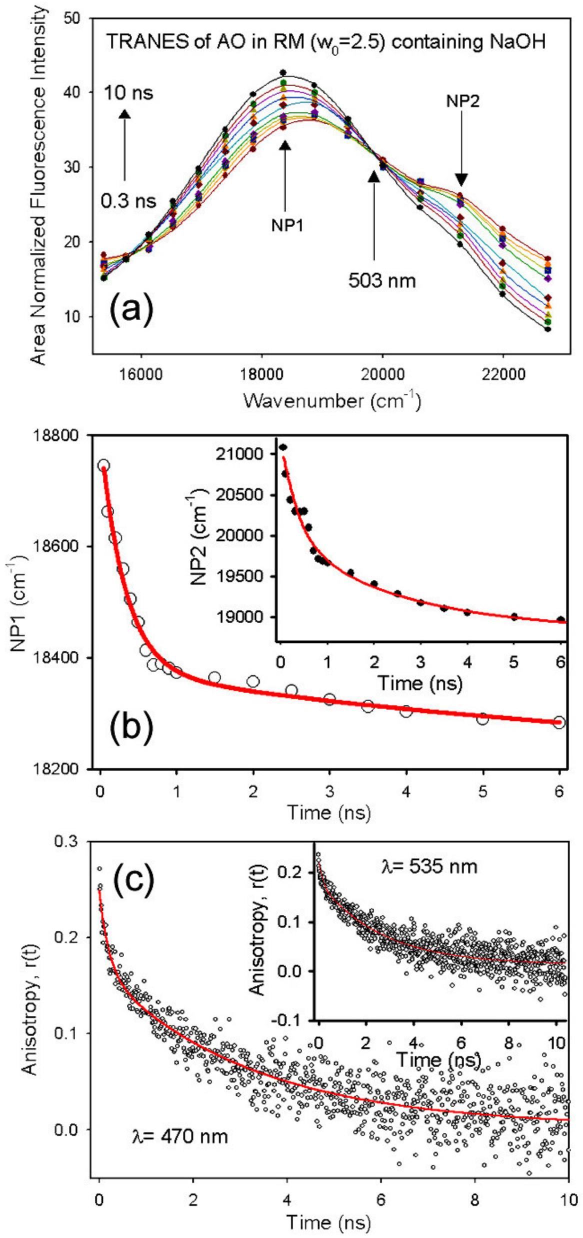

Fig. 6-6. (a) Time resolved area normalized emission spectra (TRES) of AO in RM (w_0= 2.5) containing NaOH, (b) Temporal peak shift at red wavelength (NP1) and blue wavelength (NP2) (insert) and (c) Temporal anisotropy decay curve at 470 nm and 535 nm (insert) of AO in RM (w_0= 2.5) containing water.

Table 6-5. Wobbling-in-cone data of acridine orange in various environments (emission wavelength in nm are indicated in the first column).

Systems	τ_f (ns)	τ_s (ns)	S^2	θ (degree)	τ_M (ns)	τ_L (ns)	τ_W (ns)	D_Mx10^{-6} (s^{-1})	D_wx10^{-8} (s^{-1})	D_Lx10^{6} (cm^2s^{-1})
RM with water (w_0=2.5) 550 nm	0.27	2.10	0.795	22.21	2.40	16.80	0.309	69.44	1.42	0.05
RM with water (w_0=10) 550 nm	0.16	1.31	0.742	25.26	22.39	1.39	0.181	7.44	3.13	4.36
RM with NaOH (w_0=2.5) 470 nm	0.20	3.20	0.667	29.29	2.09	-	0.216	79.74	3.54	-
RM with NaOH (w_0=2.5) 530 nm	0.22	2.74	0.814	21.07	2.09	-	0.234	79.74	1.68	-
RM with NaOH(w_0=10) 480 nm	0.19	1.99	0.532	36.16	13.64	2.32	0.208	12.22	5.59	5.56
RM with NaOH(w_0=10) 540 nm	0.28	2.23	0.652	30.06	13.64	2.67	0.318	12.22	2.52	4.17
20 mM CTAB 536 nm	0.09	0.90	0.317	47.70	27.37	0.93	0.104	6.09	19.50	8.43
50 mM SDS 530 nm	0.12	1.12	0.400	43.06	8.64	1.29	0.133	19.29	12.38	3.60
10 mM TX100 532 nm	0.30	2.49	0.558	34.87	96.86	2.56	0.338	1.72	3.19	12.05
SS-DNA 530 nm	0.13	5.52	0.466	39.56	-	-	0.135	-	10.28	-
oligo1 530 nm	0.08	2.08	0.665	29.38	-	-	0.084	-	9.10	-
oligo2 530 nm	0.36	2.18	0.832	19.88	-	-	0.427	-	0.82	-

deep trap water (8 ns) of basic AO in the nonpolar phase (table 6-3). Similarly figure 6-7(b) shows the temporal fluorescence peak shift of AO in the non-polar isooctane phase and interface in w_0= 10 RM containing NaOH. The longer time constant of 8 ns is not observed here since in larger RM, AOT monomers are properly arranged in a monolayer about the aqueous pool [10] and the number of deep trap water, may be too sparse to contribute to the relaxation. In this case also a biexponential decay is observed indicating solvation by free water and bound interfacial water. Figures 6-6(c) and 6-7(c) show the fluorescence anisotropy decay of AO in RM (w_0= 2.5 and 10) containing NaOH. In both the cases the decay are found to be biexponential (table 6-4). From wobbling-in-cone model analysis (table 6-5) the semicone angle for AO in isooctane phase is found to be larger than that at the interface indicating greater restriction at the interface. The time constants and diffusion coefficients for wobbling, lateral motion of AO and overall macromolecular motion in various environments, calculated using equations (2-37) to

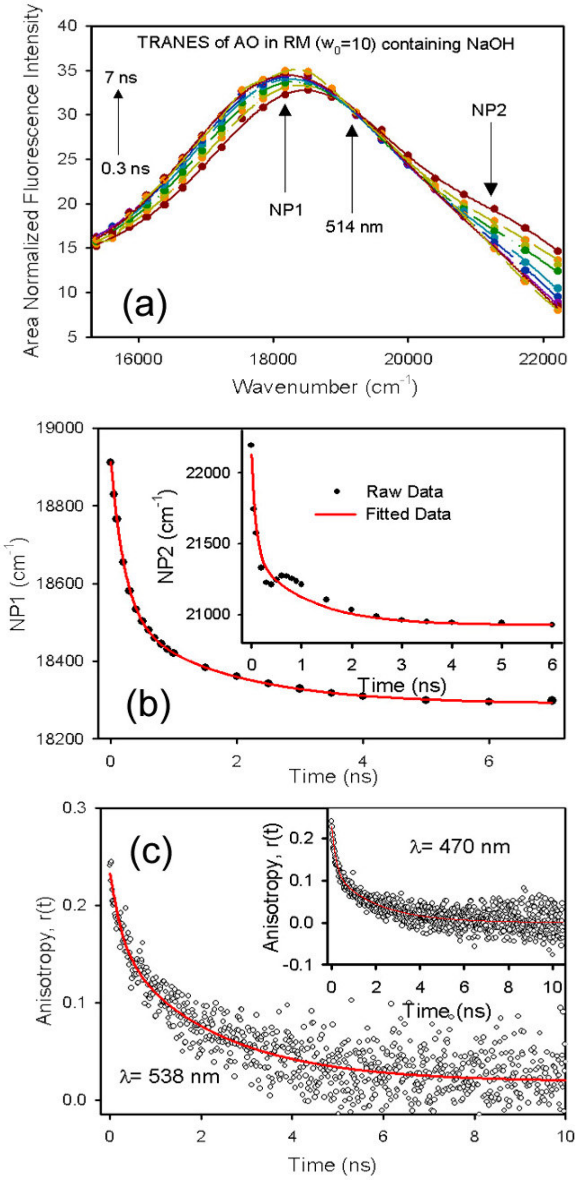

Fig. 6-7. (a) Time resolved area normalized emission spectra (TRES) of AO in RM (w_0= 10) containing NaOH, (b) Temporal peak shift at red wavelength (NP1) and blue wavelength (NP2) (insert) and (c) Temporal anisotropy decay curve at 538 nm and 470 nm (insert) of AO in RM (w_0= 2.5) containing water.

(2-41) are tabulated in table 6-5**.** However, in w_0= 2.5 RM containing NaOH, translational diffusion time constant is found to be negative for both types of AO, which indicates that the lateral diffusion time constant for this particular case cannot be extracted from equations (2-35) and (2-38) and appeals further investigation.

In order to compare the solvation and rotational dynamics of AO in RM with that in normal micelles we have studied the AO in 50 mM SDS (anionic), 20 mM CTAB (cationic) and 10 mM TX100 (neutral) micelles. Figure 6-8(a) shows the TRANES of AO in 50 mM SDS, an isoemissive point is observed at 530 nm. It is known that AO interacts with SDS micelle both through hydrophobic and electrostatic interactions. Thus the hydrophobic aromatic rings of the AO molecule remain within the hydrophobic core of SDS micelle while the charged intracyclic imino group and the two terminal polar amino groups remain directed towards the stern layer [11-13]. This in turn results in an isoemissive point at 530 nm. The solvation correlation curve of AO in SDS (figure 6-8(b), insert) is biexponential in nature with a faster time constant (550 ps) due to reorganization of bulk type water molecules and slower time constant (1.65 ns) due to reorganization of bound water in the stern layer. It is observed that slower time constant in SDS micelle is smaller than that in RM which may indicate that bound water is much more rigid in RM than in normal micelle. Figure 6-8(b) shows the temporal fluorescence anisotropy decay of AO in 50 mM SDS, 20 mM CTAB and 10 mM TX100 micelles. In all these micelles biexponential decay of temporal fluorescence anisotropy decays are observed (table 6-4). Both the faster and slower rotational time constants of AO in CTAB micelles are much faster than those in other micelles. This is due to the fact that AO being cationic in nature is away from the positively charged micellar surface. However, possibility of hydrophobic interaction of AO with this micelle may not be completely ruled out [13]. Hence, due to hydrophobic interaction AO remains partly in stern layer of CTAB micelle with major portion of AO in bulk water. Since in this case AO is more in bulk type water, solvation is much faster. The time scale of this solvation is faster than our instrumental time resolution and could not be detected. This is supported by the similarity of fluorescence decay at all wavelengths. In case of AO in CTAB since AO is least restricted, largest semicone angle (47.7°) and lateral diffusion coefficient (8.43×10^{-6} cm^2s^{-1}) are exhibited indicating faster lateral diffusion. The interaction of AO with neutral TX100 micelles is mainly hydrophilic in nature [14]. AO and water molecules compete for hydrating the polyoxyethylenic head

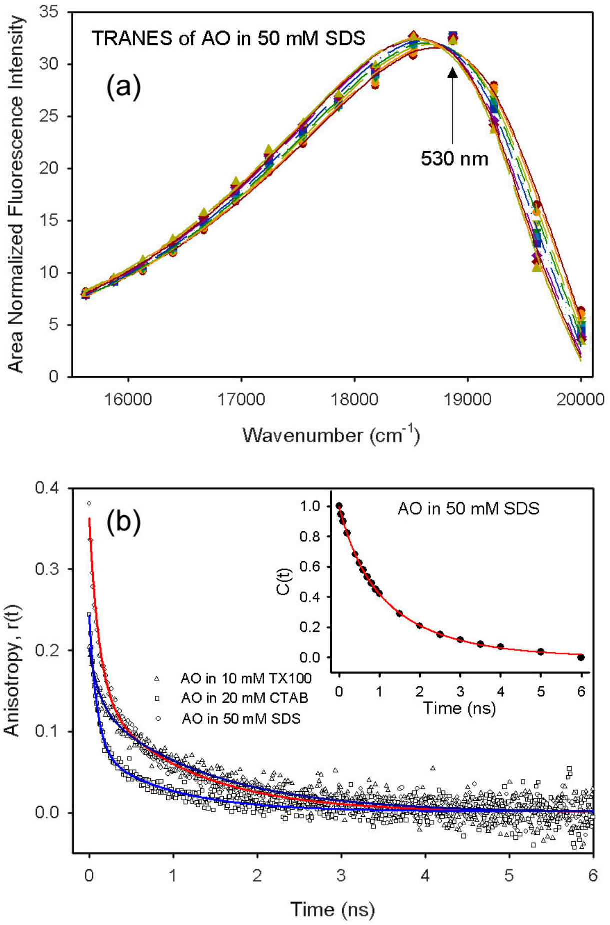

Fig. 6-8. (a) Time resolved area normalized emission spectra (TRES) of AO in 50 mM SDS solution and (b) Temporal anisotropy decay curve of AO in 10 mM TX100, 20 mM CTAB and 50 mM SDS solutions and solvation correlation curve of AO in 50 mM SDS solution (insert).

group of TX100 micelles. So, AO is located preferentially in the hydration zone of the oxyethylenic chains. The two rotational correlation time constants of 300 ps and 2.49 ns for AO in TX100 micelles (table 6-4) are slower than that in other micelles indicating greater restriction on the wobbling motion (τ_w= 338 ps) and lateral diffusion (τ_L= 2.56 ns) of AO in TX100 micelles. However, lateral diffusion coefficient appears to be larger in TX100 than that in other micelles despite the higher τ_L. This is due to the large size of the TX100 micelle revealing larger D_L values from equation (2-38). In all the cases of micelles, the r_0 values and wobbling-in-cone data are tabulated in tables 6-4 and 6-5. In case of TX100 micelles also there is no appreciable difference in temporal decay transients at blue and red wavelengths depicting faster solvation shift with time scales faster than our instrumental time resolution.

The bending and flexing motions of DNA along with the internal motions are very important for chemical reactions taking place at a given site of DNA and for the process of DNA condensation [15-18]. Hence, knowing the time scales of internal motions in DNA gives a complete physical picture of DNA. The relaxation dynamics of DNA environments [3, 19-21] and water molecules in the close vicinity of minor groove of genomic and synthesized DNAs [22, 23] have been explored by using time-dependent stokes shift methods. Fluorescence polarization techniques, utilizing ethidium bromide (EB) as an intercalator, have been extensively used to study the internal and overall motions in DNA [24-27]. Both steady state [28] and time-resolved [24-27, 29] measurements of temporal fluorescence anisotropy have been used to examine motions with correlation times ranging from 0.1 to more than 100 ns. Barkley and Zimm [18] in their elastic continuum model of DNA predicted that fluorescence polarization anisotropy of an intercalated dye is complex containing exponentials in $t^{1/2}$ due to torsion (twisting) and in $t^{1/4}$ due to bending motions, which is equivalent to the bead spring model developed by Allison and Schurr [30] and LeBret [16]. In the bead-spring model, in addition to twisting motion at intermediate times, initial exponential decay characteristics of uncoupled motions of individual beads at short times were observed. It has been found by Millar et al. that torsional rigidity of different varieties of DNA are different and initial loss in anisotropy is either due to rapid internal motion of the double helix or independent motion of the dye [25]. For an intercalating dye within DNA, there is no water and the entire dynamics is essentially controlled by the electric field of DNA. To study the wobbling motion of the polynuclear heteroaromatic dye AO in the DNAs we have applied the wobbling-in-cone model to the temporal anisotropy of the intercalated dye [31-33]. We have prepared complexes of AO with genomic salmon sperm DNA (40% GC content [34]) and two synthetic DNA dodecamers – oligo1 and oligo2. Although binding of AO to DNA is sequence-independent, slight preferential binding of AO to GC base pairs have been noted [35]. In all the three AO-DNA complexes, the structural integrity of the DNAs was restored as confirmed through CD study. Figure 6-9(a) shows the temporal fluorescence anisotropy decay of AO intercalated to oligo1 and oligo2. The fluorescence anisotropy data are tabulated in table 6-4.

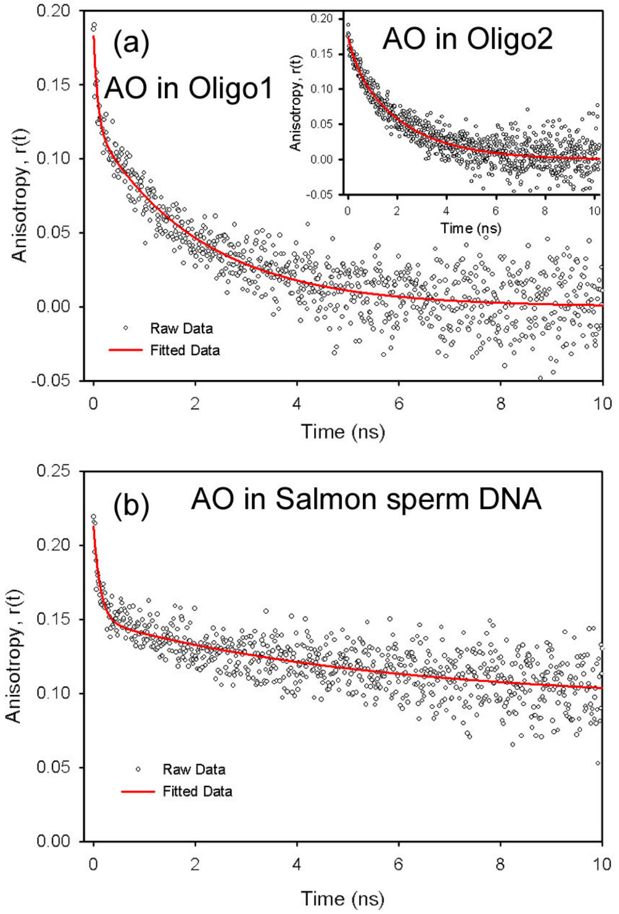

Fig.6-9. Temporal fluorescence anisotropy decay curves of AO in (a) oligo1 and oligo2 (insert) and (b) Salmon sperm DNA.

Figure 6-9(b) shows the temporal anisotropy decay of AO complexed with SS-DNA. It is found that the r(t) decays to zero within 10 ns for the dodecamers and there remains an offset (r_∞) of 0.095 for SS-DNA. This fact indicates that the large genomic DNA executing end-over-end rotations does not rotate appreciably within the fluorescence lifetime of the intercalator AO. From figure 6-9, it is also observed that the temporal fluorescence anisotropy decay is readily fit into biexponential decay for all the DNAs. From table 6-4 the faster rotational time constant for AO in oligo1 is about four times lesser than that in oligo2. This could be due to charge transfer between AO and GC base pairs flanking the intercalated AO in oligo1 [29, 31, 36] which is hindered in oligo2 and SS-DNA (mixed polymers of AT and GC base pairs). This is also reflected in the faster fluorescence decay of AO in oligo1 compared to oligo2 (see table 6-2). The slower rotational time constants are, however, same for both the DNA oligomers, which may be due to similarity of length and volumes of the two oligomers. The slower anisotropy time constant of 5.52 ns in SS-DNA may be due to the local tumbling motion of DNA segments. In this case we cannot expect lateral diffusion of AO along DNA-water interface as at [AO]:[DNA]= 1:100 all the AO molecules are intercalated to DNA [33]. From table 6-5, it is observed that the semicone angle inscribed by the wobbling AO is in the order: SS-DNA> oligo1> oligo2. Comparison of the two synthetic DNA indicates that AO is much free to wobble in GC site than AT binding site and/or the GC-rich DNA (oligo1) is less rigid than dodecamer containing both AT and GC base pairs. However, in SS-DNA it is still larger, may be the twisting motion of the DNA chain combines with the internal wobbling of the dye to produce a larger semicone angle. Here we find that the semicone angle inscribed by the restricted motion of AO in the intercalation site is larger than that inscribed by ethidium bromide (EB) (15°) [24]. This may be due to the fact that AO suffers less hindrance compared to EB because of the absence of phenyl group and possible hydrogen bonding between amino protons of EB and the DNA phosphate backbone [27]. Another interesting factor to note is that the generalized order parameters for synthetic oligonucleotides are larger than that for the genomic DNA, which indicate that the smaller DNAs are much more rigid than larger genomic DNA providing greater restriction to the internal wobbling motion of the dye.

6.3. Conclusions:

This study provides a detailed picture of dynamics and location of acridine orange in biomimetics (micelles and reverse micelles) and in DNA. The equivalent nature of solvation correlation curve of AO in w_0= 2.5 and 10 RMs containing water indicates almost similar environment (i.e., interface) around AO in RMs. In RM containing NaOH presence of an isoemissive point in the TRANES indicates the existence of two types of AO – basic AO in the isooctane phase and protonated AO at the interface. Despite the pH of NaOH being higher than the excited state pKa (13.3) of AO, protonated AO is observed at the interface, which indicates that interfacial pH is lower than the pH at the core. The lower value of longer solvation correlation time constant for AO in SDS compared to that in RM indicates that the bound water in RM is much more rigid than that in normal SDS micelle. Wobbling-in-cone data analysis indicates that AO wobbles much more freely in larger RM inscribing larger semicone angles. Among the micelles, largest semicone angle is exhibited in CTAB micelle, which is due to repulsion between cationic AO and positively charged head groups of CTAB micelle that pushes AO away from the micellar surface. The generalized order parameter for AO in genomic salmon sperm DNA is lower than that in synthetic DNA which indicates that AO intercalated to synthetic DNA experiences much more restriction. Again comparison of two synthetic DNAs – oligo1 and oligo2, indicates that AT containing synthetic DNA (oligo2) is much more rigid than GC-rich DNA (oligo1) as indicated by the S^2 and semicone angle values. Also comparison with previous studies on DNA shows that AO is much freer to wobble in their intercalation site than EB. This work on the DNA intercalator, acridine orange with various micelles, reverse micelles and DNA would be very useful for understanding the dynamical interactions of AO with different biomolecules such as proteins, nucleic acids and membranes under varied conditions.

References

[1] A.K. Shaw and S.K. Pal, Fluorescence Relaxation Dynamics of Acridine Orange in Nanosized Micellar Systems and DNA, J. Phys. Chem. B 111 (2007) 4189-4199.

[2] R.D. Falcone, N.M. Correa, M.A. Biasutti and J.J. Silber, Acid-Base and Aggregation Processes of Acridine Orange Base in n-heptane/AOT/Water Reverse Micelles, Langmuir 18 (2002) 2039-2047.

[3] E.B. Brauns, C.J. Murphy and M.A. Berg, Local Dynamics in DNA by Temperature-Dependent Stokes Shifts of an Intercalated Dye, J. Am. Chem. Soc. 120 (1998) 2449-2456.

[4] V.K. Sharma , P.D. Sahare, R.C. Rastogi, S.K. Ghoshal and D. Mohan, Excited state characteristics of acridine dyes: acriflavine and acridine orange, Spectrochimica Acta Part A: Molecular and Biomolecular Spectroscopy 59 (2003) 1799-1804.

[5] A.K. Shaw, R. Sarkar and S.K. Pal, Direct Observation of DNA condenasation in a nanocage using a molecular ruler, Chem. Phys. Lett. 408 (2005) 366-370.

[6] N. Periasamy and A.S.R. Koti, Time resolved fluorescence spectroscopy: TRES and TRANES, Proc. Indian Natl. Sci. Acad. 69A (2003) 41-48.

[7] P. Mukerjee and K. Banerjee, A study of Surface pH using solubilized indicator dyes, J. Phys. Chem. 68 (1964) 3567-3574.

[8] H. Fujii, T. Kawai, H. Nishikawa and G. Ebert, Determination of pH in reverse micelles, Colloid Polym. Sci. 260 (1982) 697-701.

[9] M. Vincent, B. de Foresta and J. Gallay, Nanosecond Dynamics of a Mimicked Membrane-Water Interface Observed by Time-Resolved Stokes Shift of Laurdan, Biophys. J. 88 (2005) 4337-4350.

[10] A. Maitra, Determination of size parameters of water-Aerosol OT-oil reverse micelles from their nuclear magnetic resonance data, J. Phys. Chem. 88 (1984) 5122-5125.

[11] J.W. Park and H. Chung, Aggregation and Dissolution of Dicationic Dyes with an Anionic Surfactant, Bull. Korean. Chem. Soc. 7 (1986) 113-116.

[12] A.M. Wiosetek-Reske and S. Wysocki, Spectral studies of N-nonyl acridine orange in anionic, cationic and neutral surfactants, Spectrochim. Act A 64 (2006) 1118-1124.

[13] S.P. Moulik, S. Ghosh and A.R. Das, Interaction of acridine orange monochloride dye with sodium dodecyl sulfate (SDS), cetyl trimethyl ammonium bromide (CTAB) and p-tert-octylphenoxypoloxy ethanol (TritonX) surfactant, Colloid Polym. Sci. 257 (1979) 645-655.

[14] S.M. Andrade and S.M.B. Costa, The aqueous environment in AOT and Triton X-100 (w/o) microemulsions probed by fluorescence, Photochem. Photobiol. Sci. 1 (2002) 500-506.

[15] T. Maniatis, J.J.H. Venable and L.S. Lerman, The Structure of Psi DNA, J. Mol. Biol. 88 (1974) 37-56.

[16] M. Le Bret, Relationship between the energy of superhelix formation, the shear modulus, and the torsional brownian motion of DNA, Biopolymers 17 (1978) 1939-1955.

[17] C.J. Benham, An elastic model of the large-scale structure of duplex DNA, Biopolymers 18 (1979) 609-623.

[18] M.D. Barkley and B.H. Zimm, Theory of twisting and bending of chain macromolecules; analysis of the fluorescence depolarization of DNA, J. Chem. Phys. 70 (1979) 2991-3007.

[19] E.B. Brauns, M.L. Madaras, R.S. Coleman, C.J. Murphy and M.A. Berg, Measurement of Local DNA Reorganization on the Picosecond and Nanosecond Time Scales, J. Am. Chem. Soc. 121 (1999) 11644-11649.

[20] E.B. Brauns, M.L. Madaras, R.S. Coleman, C.J. Murphy and M.A. Berg, Complex local dynamics in DNA on the picosecond and nanosecond time scales, Phys. Rev. Lett. 88 (2002) 158101-158104.

[21] D. Banerjee and S.K. Pal, Ultrafast charge transfer and solvation of DNA minor groove binder: Hoechst 33258 in restricted environments, Chem. Phys. Lett. 432 (2006) 257-262.

[22] S.K. Pal, L. Zhao and A.H. Zewail, Water at DNA surfaces: ultrafast dynamics in minor groove recognition, Proc. Natl. Acad. Sci. USA 100 (2003) 8113-8118.

[23] S.K. Pal, L. Zhao, T. Xia and A.H. Zewail, Site and sequence selective ultrafast hydration of DNA, Proc. Natl. Acad. Sci. USA 100 (2003) 13746 -13751.

[24] D.P. Millar, R.J. Robbins and A.H. Zewail, Direct Observation of the Torsional Dynamics of DNA and RNA by Picosecond Spectroscopy, Proc. Natl. Acad. Sci. USA 77 (1980) 5593-5597.

[25] D.P. Millar, R.J. Robbins and A.H. Zewail, Torsion and bending of nucleic acids studied by subnanosecond time resolved fluorescence depolarization of intercalated dyes, J. Chem. Phys. 76 (1982) 2080-2094.

[26] D. Magde, M. Zappala, W.H. Knox and T.M. Nordlund, Picosecond fluorescence anisotropy decay in the ethidium/DNA complex, J. Phys. Chem. 87 (1983) 3286-3288.

[27] T. Haerd and D.R. Kearns, Anisotropic motions in intercalative DNA-dye complexes, J. Phys. Chem. 90 (1986) 3437-3444.

[28] D. Genest, P.A. Mirau and D.R. Kearns, Investigation of DNA dynamics and drug-DNA interaction by steady state fluorescence anisotropy, Nucl. Acids. Res. 13 (1985) 2603-2615.

[29] T. Haerd, P. Fan, D. Magde and D.R. Kearns, On the flexibility of DNA: time-resolved fluorescence polarization of intercalated quinacrine and 9-amino-6-chloro-2-methoxyacridine, J. Phys. Chem. 93 (1989) 4338-4345.

[30] S.A. Allison and J.M. Schurr, Torsion dynamics and depolarization of fluorescence of linear macromolecules.1. Theory and Application to DNA, Chem. Phys. 41 (1979) 35-59.

[31] A.I. Kononov, Photophysical Processes in the Complexes of DNA with Ethidium Bromide and Acridine Orange: A Femtosecond Study, J. Phys. Chem. B 105 (2001) 535-541.

[32] L.S. Lerman, The Structure of the DNA-Acridine Complex, Proc. Natl. Acad. Sci. USA 49 (1963) 94-102.

[33] M.B. Lyles, and Cameron, I. L., Interactions of the DNA intercalator acridine orange, with itself, with caffeine, and with double stranded DNA, Biophys. Chem. 96 (2002) 53-76.

[34] E. Chargaff, R. Lipshitz, C. Green and M.E. Hodes, The composition of desoxyribonucleic acid of salmon sperm, J. Biol. Chem. 192 (1951) 223-230.

[35] J.C. Thomes, G. Weill and M. Daune, Fluorescence of proflavine-DNA complexes: Heterogeneity of binding sites, Biopolymers 8 (1969) 647-659.

[36] D.M. Rayner, A.G. Szabo, R.O. Loutfy and R.W. Yip, Singlet energy transfer between nucleic acid bases and dyes in intercalation complexes, J. Phys. Chem. 84 (1980) 289-293.

Chapter 7

Encapsulation of a Genomic DNA in a Nanocage of AOT Reverse Micelle

7.1. Introduction:

In this work we have used homo-molecular (self-quenching) Förster resonance energy transfer (FRET) technique to assess distances between probe molecules (acridine orange; AO) attached with a genomic DNA (from salmon testes) before and after encapsulation of the DNA in anionic (bis(2-ethylhexyl)sulfosuccinate; AOT) RM. We have also carried out the circular dichroism (CD) study of the DNA in buffer solution and DNA in the RM. Particular emphasis has been given to the DNA packaged in reverse micelles as a model for condensed form of DNA. By observing the picosecond to nanosecond dynamics of nonradiative energy transfer of the AO–DNA complex in buffer and in the RM, we elucidate change in distance between two AO molecules upon encapsulation of the DNA in the RM. For comparison, we have also studied AO inside the RM without the DNA. In order to unravel the change in local geometrical restriction on the physical motions of the probe we have studied picosecond time-resolved fluorescence anisotropy of AO in the RM without and with the DNA.

7.2. Direct Observation of DNA Condensation in a Nanocage by Using a Molecular Ruler [1]:

As shown in figure 7-1(a), upon complexation with the DNA, AO shows a red shift (10 nm) in absorption and blue shift (7 nm) in the emission spectra. The emission peaks for AO in buffer and AO in AO–DNA complex were obtained at 529 and 522 nm, respectively. In the emission spectrum of AO-DNA complex the full width at half maximum (FWHM) is reduced and fluorescence yield is increased significantly. From figure 7-1(a) it is evident that the spectral overlap of absorption and emission spectra of AO bound to the DNA is larger than that of AO in free buffer, which indicates efficient energy transfer in the former case. Figure 7-1(b) shows absorption and emission spectra of

AO in the RM (w_0= 5) without the DNA. A significantly large spectral overlap is also

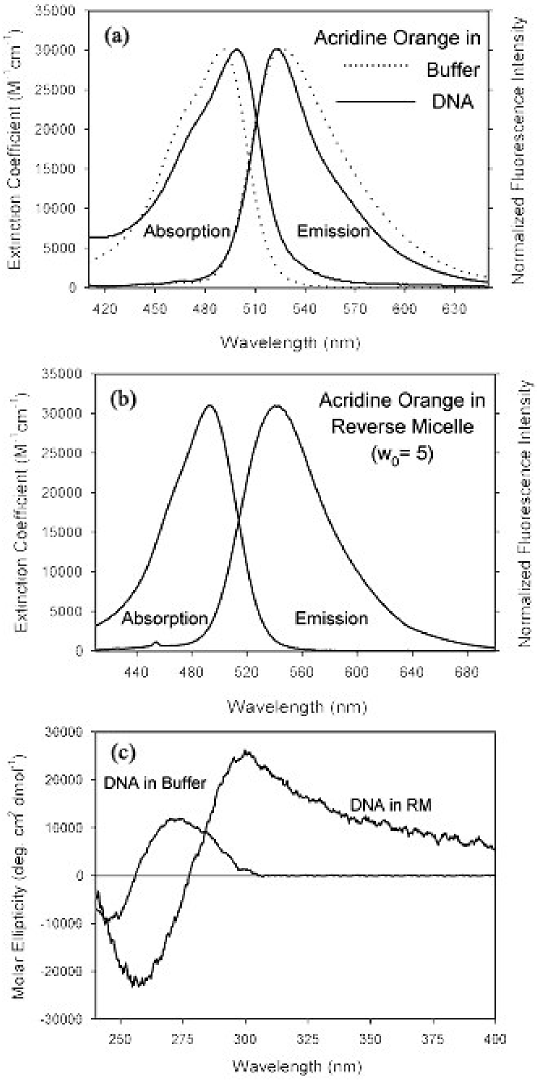

Fig. 7-1. (a) Absorption and emission spectra of AO–DNA complex and free AO in buffer. (b) Absorption and emission spectra of AO in the RM at w_0= 5. (c) CD spectra of DNA in buffer and in the 50 mM AOT/isooctane RM (w_0= 10) at 27 °C.

evident from the spectra. Figure 7-1(c) shows the CD spectra of DNA in buffer and in the RM (w_0= 10), indicative of condensed form of DNA in the latter medium (see below).

As shown in figures 7-2(a) and 7-3(a), fluorescence transients of AO were fitted (solid lines) to sum of exponentials convoluted with the instrument response function

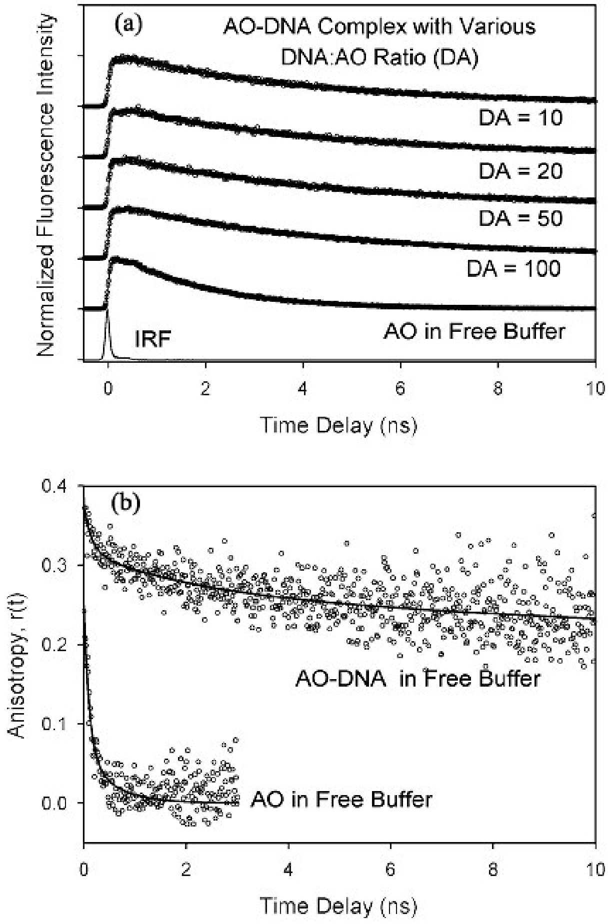

Fig. 7-2. (a) Fluorescence decay transients of AO–DNA complex with various DNA:AO ratio (DA). The instrument response function (IRF) is also shown for comparison. (b) Fluorescence anisotropy decays of AO and AO–DNA complex in buffer.

(IRF). The lifetime of AO increases from 1.8 ns in buffer to 6.1 ns upon complexation of AO with DNA. The evidence of formation of AO–DNA complex also comes from time-resolved anisotropy measurement. The anisotropy of AO–DNA complex is much slower than that of AO in free buffer (figure 7-2(b)). Relatively faster lifetime of free AO in buffer compared to that in the DNA could be due to self-aggregation of AO in the former medium [2]. The lifetime of AO in the DNA depends on the DNA:AO ratio (DA). Here, we consider concentration of base pair (bp) of the DNA as overall concentration of the DNA. As shown in figure 7-2(a) the transients of AO-DNA complex show two decay components with time constants 3.2–4.2 and 6 ns with a rise component of ~200 ps.

Relatively faster time constants (3.2–4.2 ns) reveal lifetimes of AO molecules, which undergo FRET. The longer time constant (6 ns) is consistent with the lifetime of monomeric AO intercalated between the base pairs of DNA [2]. In these studies we regard 6 ns as τ_D, i.e. lifetime of donor AO in absence of acceptor AO. The rise components in the transients might be indicative of formation of charge transfer (CT) species. The possibility of such dynamical processes (CT) is reported in the literature [2-4]. Absence of a rise component in the blue end of the emission spectrum (488 nm) of AO in buffer supports the inference.

By using FRET techniques, we measured distances 45.2, 43.9, 40.6 and 40.9 Å between two DNA-attached AO molecules in the buffer solutions for DA values 100, 50, 20 and 10, respectively. The similarity in the distances for DA values from 10 to 100 indicates unavailability of AO binding sites in the DNA. In other words, addition of extra AO molecules in the DNA solution below DA= 100 is not appreciably helping two AO molecules (donor-acceptor pair) to bind to two neighboring sites in DNA, which are more closer than 12 to 13 base pairs separation. The AO-DNA complex with DA= 10 was used here to study the structural change of the DNA upon encapsulation in the RM. The distance (40.9 Å) between two AO molecules in the complex in buffer at DA= 10 is associated with 12 bp of DNA, on taking separation between two DNA base pairs to be 3.4 Å [5].

The transients of AO in the RM without and with the DNA show two decay components, as shown in figure 7-3(a). No rise components were found in these systems, indicating absence of the CT dynamics in the microenvironments. In the w_0= 5 RM (without DNA) two decay components of 0.50 and 2.20 ns are observed, which are associated with two average separations of 27.2 and 36.8 Å, respectively between AO molecules. Note that AO is completely insoluble in isooctane phase and expected to reside in the RM. The separation 27.2 Å might be reflective of distance between two AO molecules in the same RM (intra-micellar). The separation (27.2 Å) is larger than typical diameter (20 Å) of the aqueous pool of the RM at w_0= 5 [6]. This anomaly could be due to the structural feature of AO, it has a positively charged (protonated imine) group and a hydrophobic moiety. If two AO molecules are located at diametrically opposite points at the interface of a RM (w_0= 5) in such a way that the hydrophobic moiety are buried into the interface projecting their positively charged groups toward the negatively charged

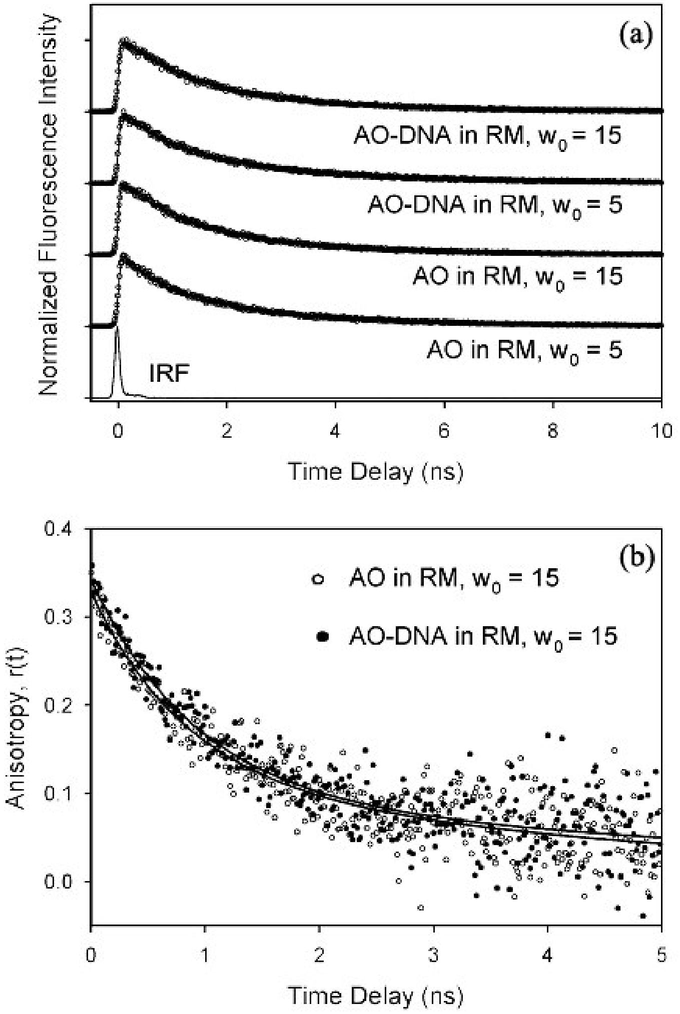

Fig. 7-3. (a) Fluorescence decay transients of AO in the RM with various degrees of hydration (w_0) in absence and presence of the DNA. The instrument response function (IRF) is also shown for comparison. (b) Fluorescence anisotropy of AO in the RM at w_0= 15, in absence and presence of the DNA.

head groups of AOT (estimated diameter ~4 Å), the inter-AO distance would be larger than the diameter of the aqueous pool. The spatial distribution of similar organic dye molecules in RM and lipid bilayer is reported in the literature [7, 8]. Other separation of 36.8 Å might indicate the distance between two AO molecules in different RM (inter-micellar). In the case of w_0= 15 RM (without DNA) two decay time constants of 1.36 and 3.10 ns are observed, which gives separations of 33.0 Å (intra-micellar) and 41.0 Å (inter-micellar) between two AO molecules. The intramicellar distance (33.0 Å) is larger than that in the RM at w_0= 5 and shorter than estimated diameter (60 Å) of the aqueous pool of the RM at w_0= 15.

The fluorescence transients (figure 7-3(a)) of AO-DNA complex in the RM show biexponential decay components, indicating two kinds separations between AO molecules bound to DNA as mentioned above. In the DNA included RM at w_0= 5 (decay time constants 1.18 and 3.20 ns), we recovered the separations to be 31.3 Å (intra-micellar) and 40.5 Å (inter-micellar), respectively. The distance, 31.3 Å between two AO molecules attached to the DNA included in the RM is definitely shorter than that in free buffer (40.9 Å). This observation clearly indicates that in the RM, DNA strand is bent and/or different DNA strands are coupled together in the nanospace revealing DNA condensation in the microenvironment. For w_0= 15 (decay time constants 1.40 and 3.20 ns), the shorter separation (intra-micellar, 32.5 Å) is similar to that in w_0= 5, which indicates that the structural compaction of the DNA is apparently unaffected by w_0 of the RM.

A recent structural study [9] on various types of DNA including a genomic DNA from herring testes, which is similar to the DNA used in our study packaged in AOT/isooctane RM (w_0= 18.5) using circular dichroism (CD) spectroscopy and dynamic light scattering (DLS) techniques has confirmed that the RM induce the configuration of a condensed form of the DNA. The particular DNA structure showed an interesting and characteristic CD feature, the so-called psi spectrum, which was indicative of super-condensed form of the DNA. The study [9] also observed three population of aggregates with an average radius centered at 5, 100 and 1000 nm, respectively, all three containing DNA. In the case of ‘empty’ RM with w_0= 18.5 (RM containing water, no DNA) an average dimension centered ~5 nm radius was found. It has been suggested that the very large components with relatively smaller percentage, which is not so stable over long time period, can be ascribed to a cluster of smaller micelles.

Our study is in agreement with the previous structural studies [9]. The CD spectrum of DNA encapsulated in RM (w_0= 10) [intermediate between w_0= 5 and w_0= 15] shows a strong negative CD signal at 260 nm and positive molar ellipticities at longer wavelengths, which is a characteristic feature of psi-form of DNA. This feature is not evident in the CD spectrum of DNA in buffer. Shortening of inter-probe distance in the

DNA upon encapsulation in the RM (~31 Å) compared to that in the buffer (~41 Å) is a clear indication of the DNA compaction in the RM. We also observed that the longer distances in the RM with DNA at w_0= 5 and w_0= 15 (40.5 Å for both the cases) are similar to those in the RM without the DNA. This separation could be indicative of the inter-micellar distance and/or inter-probe distance in a DNA strand entrapped in larger RM that may exist [8]. However, any conclusive comment requires further study. The time-resolved anisotropy studies of AO in the RM (w_0= 15) without and with the DNA show similar temporal behavior as shown in figure 7-3(b) (time constants are 0.91 ns (70%) and 7.2 ns (30%)). This observation is in agreement with the compartmentalization of DNA (oligomolecular form) in the reverse micellar system. In this case, each oligomolecule (condensed DNA) is almost dynamically independent and expectedly resembles time scales of motions of the RM. Possibility of adverse effect on the intercalation interaction due to the structural perturbation of DNA in RM has recently been reported from our group using another DNA-intercalator ethidium [10].

7.3. Conclusion:

In this study using picosecond time-resolved homo-molecular Förster resonance energy transfer of a DNA-intercalator (AO), we have shown that genomic DNA when encapsulated inside nano-space of RM is condensed. The degree of compaction has been shown to be independent of the degree of hydration of RM. CD study indicates that DNA assumes psi-form structure inside the RM. These studies attempt to explore structural features of the DNA compaction in an aqueous nanospace of the RM, which is particularly important for the biological function of DNA in nucleosome formation and chromatin condensation.

References

[1] A.K. Shaw, R. Sarkar and S.K. Pal, Direct Observation of DNA condenasation in a nanocage using a molecular ruler, Chem. Phys. Lett. 408 (2005) 366-370.

[2] A.I. Kononov, Photophysical Processes in the Complexes of DNA with Ethidium Bromide and Acridine Orange: A Femtosecond Study, J. Phys. Chem. B 105 (2001) 535-541.

[3] S. Fuzukimi, M. Nishimine, K. Ohkubo, N.V. Tkachenko and H. Lemmetiyenen, Driving Force Dependence of Photoinduced Electron Transfer Dynamics of Intercalated Molecules in DNA, J. Phys. Chem. B 107 (2003) 12511-12518.

[4] C.-C. Chiang, J.-Y. Cheng, Y.-R. Cheng, H.-S. Chen, C.-Y. Mou and T.-C. Chang, Hole-burning structure and mechanism of acridine and amino acridine doped in polyvinyl alcohol films, Mol. Cryst. Liq. Cryst. 291 (1996) 175-181.

[5] L. Stryer: Biochemistry, W. H. Freeman & Co., New York, (1995).

[6] R. Biswas and S.K. Pal, Caging enzyme function: α-chymotrypsin in reverse micelle, Chem. Phys. Lett. 387 (2004) 221-226.

[7] S.M. Andrade and S.M.B. Costa, The aqueous environment in AOT and Triton X-100 (w/o) microemulsions probed by fluorescence, Photochem. Photobiol. Sci. 1 (2002) 500-506.

[8] E. Mileykovskaya, W. Dowhan, R.L. Birke, D. Zheng, L. Lutterodt and T.H. Haines, Cardiolipin binds nonyl acridine orange by aggregating the dye at exposed hydrophobic domains on bilayer surfaces, FEBS Lett. 507 (2001) 187-190.

[9] A.V. Pietrini and P.L. Luisi, Circular dichroism properties and average dimensions of DNA containing reverse micellar aggregates, Biochim. Biophys. Acta 1562 (2002) 57-62.

[10] R. Sarkar and S.K. Pal, Ligand-DNA Interaction in a Nanocage of Reverse Micelle, Biopolymers 83 (2006) 675–686.

Chapter 8

Molecular Recognition of Human Serum Albumin in various pH-induced Folded States: Use of a Molecular Ruler to Observe Protein-Folding Intermediates

8.1. Introduction:

In this chapter we have reported the binding interaction of protoporphyrin IX (PPIX) with HSA at different pHs and temperatures using picosecond time-resolved polarization-gated spectroscopy. Utilizing the binding interaction of PPIX in domain-IB of Human Serum Albumin (HSA) and significant spectral overlap of the emission of tryptophan residue (trp214) in domain-IIA of HSA with absorption band of PPIX, we have measured the inter-domain separation in various pH-induced conformers of HSA applying Förster resonance energy transfer (FRET) theory. We have also explored another inter-domain distance between PPIX (domain-IB) and an extrinsic fluorophore 2-p-toluidinylnaphthalene-6-sulfonate (TNS) (domain-III) at different pHs. Also, to check the stability of different pH-induced conformers of HSA at different temperatures, we have also applied FRET to determine the inter-domain (IB-IIA) separation. Dynamic light scattering (DLS) and Circular dichroism (CD) have been used to further characterize the pH-induced folded states.

8.2. Resonance Energy Transfer and Ligand Binding Studies on pH-induced Folded States of Human Serum Albumin:

Figure 8-1(a) shows the size distribution graph of various conformations of HSA in buffer solutions of different pHs obtained through dynamic light scattering studies. The hydrodynamic diameters of different conformations are as follows: 16.4 nm (E-form, pH= 2), 10.2 nm (F-form, pH= 4), 10.4 nm (N-form, pH= 7), 10.7 nm (B-form, pH= 9) and 10.4 nm (A-form, pH= 11). The above hydrodynamic data indicate that in the acidic pH buffer solutions the globular structure adopted by HSA in normal pH solution undergo swelling with a significant change in tertiary structure. However, in the basic pH buffer solution such structural swelling is not observed. From the CD studies (Figure 8-1(b)) and table 8-1) it is observed that in addition to the disruption of tertiary structure (DLS studies)

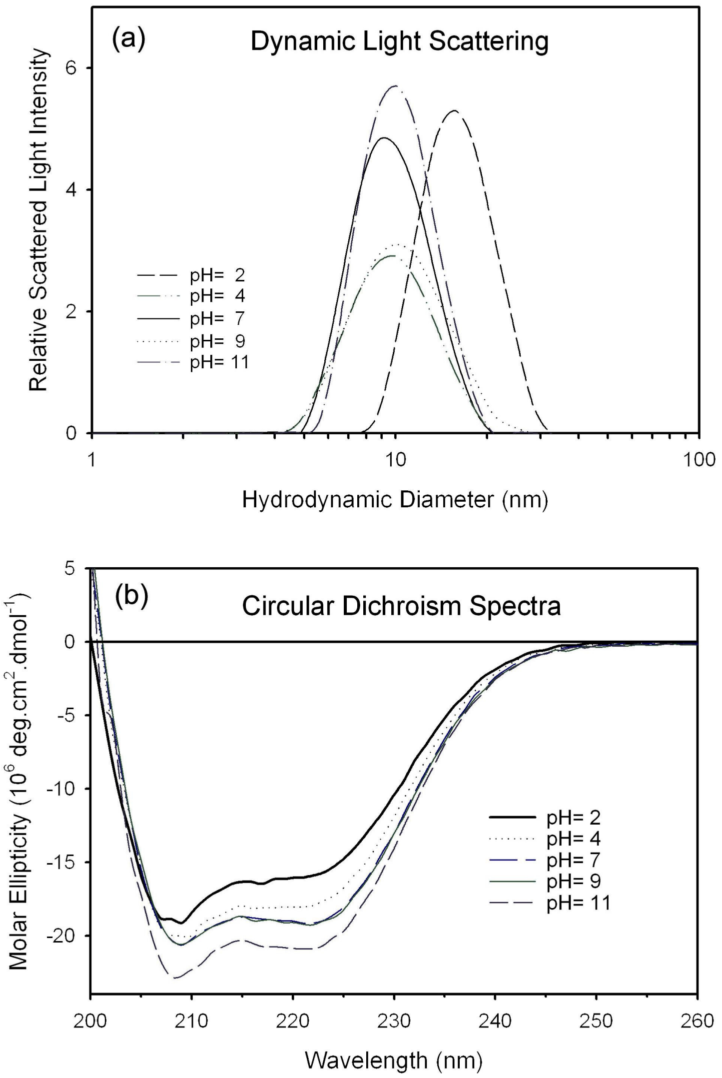

Fig. 8-1. (a) Dynamic light scattering spectra (DLS) and (b) Circular Dichroism (CD) spectra of HSA in buffer solutions of various pH.

there is a significant loss in helicity when HSA changes its conformation from N-form to E-form. The observation is consistent with another study [1] which confirms a significant loss in helical content with a structural loosening at the C-terminal end followed by separation of domains and subdomains in the N-F transition during acid-induced unfolding

Table 8-1. Percentages of secondary structures in different conformations of Human serum albumin (HSA) at different pH(s).

Secondary structures	**HSA in buffer solutions of different pH(s)**				
	2	**4**	**7**	**9**	**11**
Helix	59.0%	64.7%	67.1%	67.1%	60.4%
Antiparallel	4.0%	3.4%	3.2%	3.2%	3.9%
parallel	4.1%	3.5%	3.2%	3.2%	4.0%
Turns	13.2%	12.5%	12.2%	12.2%	13.0%
Random	19.7%	15.9%	14.3%	14.3%	18.7%

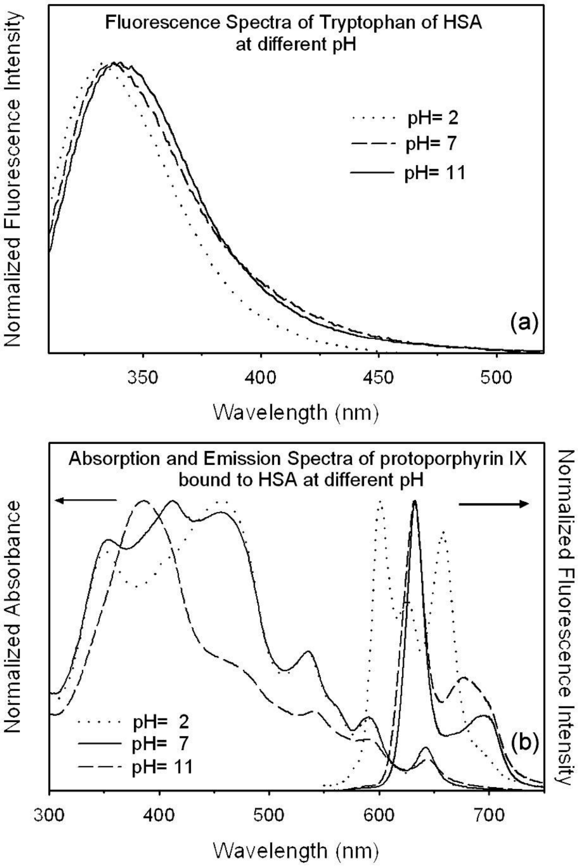

Fig. 8-2. (a) Fluorescence spectra of Tryptophan (Trp214) residue of HSA (excitation λ= 297 nm) and (b) absorption and fluorescence spectra of protoporphyrin IX (PPIX) bound to HSA (excitation λ= 409 nm) at three pH(s).

of HSA. Further reduction of pH below 3.5 when HSA assumes E-form at pH= 2, the domain-I undergoes expansion leading to the disruption of intra-domain structure in this pH region. Domain-II is, however, known to assume molten globule state in N-F transition [1]. In the alkaline pH range, during N-B transition, contrary to the previous study [1], there is no change in helicity content. However, at pH= 11, the A-conformer shows a decrease in the helicity content compared to the native form of HSA (N-form) at normal pH.

Figure 8-2(a) shows the fluorescence spectra (excitation wavelength= 297 nm) of various conformations of HSA at three different pHs. The fluorescence is solely due the excitation of Trp214 residue of HSA located in the binding domain-IIA at the bottom of a 12Å deep crevice [2]. The N-form has a fluorescence maximum at 337 nm consistent with previous studies [1, 2]. The E-form has a fluorescence maximum at 332 nm while for the A-form it is at 335 nm, both of which are blue shifted compared to the N-form. These changes are consistent with previous studies [1, 2] indicating that although at pH= 2 the inter-domain separation increases with the disruption of deep crevice, the rearrangement of the local environment around Trp214 causes it to be in more hydrophobic environment of the protein matrix [3]. At alkaline pH= 11, that is in A-form, Trp214 is present in slight hydrophobic environment due to minor changes in secondary structure. Figure 8-2(b) shows the absorption and emission spectra (excitation wavelength= 409 nm) of PPIX-labeled HSA at different pHs. Porphyrins form a class of molecules whose physicochemical properties depend on the state of ionization of the molecules [4] and the ionization is associated with the acid-base properties of both the imino and pyrrole nitrogens of the ring structures and the peripheral groups attached to the molecule [5]. The conjugated ring structure of porphyrin is responsible for the spectral feature of this drug molecule. As a result, the protonation of imino nitrogen should influence the electron distribution of the chromophore and thus its spectral properties. The N-form HSA has an absorption maximum at 412 nm corresponding to the Soret band while the other peaks between 500 nm and 700 nm are the Q-bands [6-8]. At acidic pH for E-form HSA, the intensity of soret band decreases and the absorption maximum exhibits a blue shift to 386 nm. At alkaline pH= 11, the absorption spectrum is similar to that at pH= 7 with a lower intensity of the soret band. The emission spectra of PPIX-labeled HSA at pH= 7 and 11 have an intense emission peak at 633 nm. However, at pH= 2, this band at 633 nm decreases in intensity with the appearance of two new peaks at 600 and 658 nm. These new peaks may arise due to the protonation of imino nitrogens in the porphyrin ring [5]. The

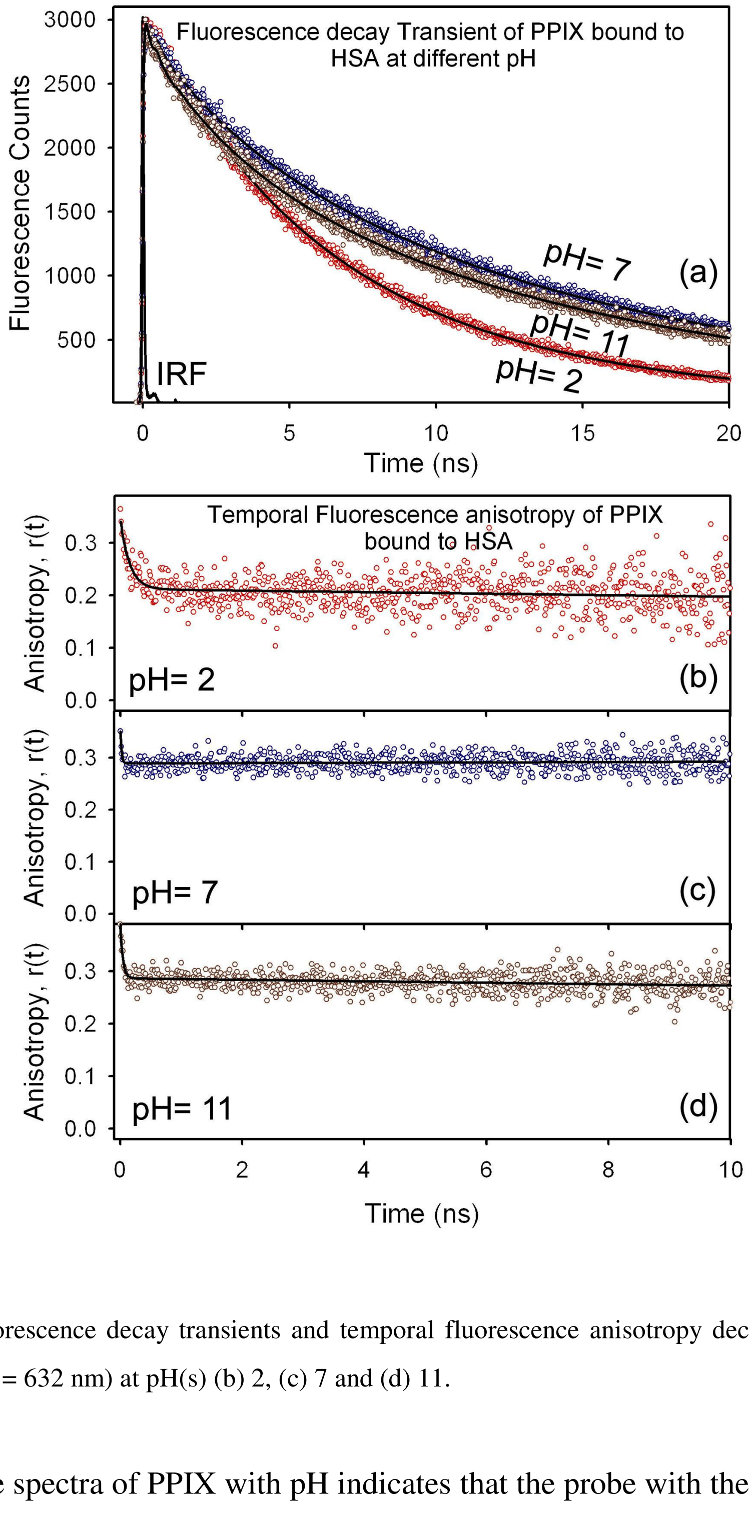

Fig. 8-3. (a) Fluorescence decay transients and temporal fluorescence anisotropy decay of PPIX bound to HSA (emission $\lambda = 632$ nm) at pH(s) (b) 2, (c) 7 and (d) 11.

variation in the spectra of PPIX with pH indicates that the probe with the protein at various conformations is efficient in sensing the immediate environment of HSA.

Figure 8-3(a) shows the fluorescence transients of PPIX bound to HSA at pH= 2, 7 and 11 at 632 nm (excitation wavelength= 409 nm). Table 8-2 depicts the fluorescence lifetime of PPIX bound to HSA at five different pH(s), which are essentially non-exponential in nature [9]. In all the cases, three time components in the range of 0.2-0.4 ns, 2-4 ns and 9-14 ns are observed. The time constants are in fair agreement with a previous study [9] except the shortest one whose contribution towards fluorescence is very small (<1%) and might have been neglected in the earlier study. Figure 8-3(b-d) depicts the temporal fluorescence anisotropy decay curve of PPIX-bound HSA at pH= 2, 7 and 11. At all pH(s) a long rotational time constant of ~100 ns (20 to 45 %) is observed which corresponds to the rotational time constant for the global motion of the HSA molecule. The longer time constant is also indicative of the rigid binding of PPIX to HSA. Except at pH= 2, a short rotational time constant of 0.03 ns-0.04 ns is also observed which may be due to librational motion of PPIX at its binding site in HSA. Similar faster reorientational motion of 15 ps or less time scale was observed, when a fluorescence probe ethidium bromide having rotational time constant of ~100 ps in water was intercalated in a rigid environment between the base pairs of genomic DNA [10]. At pH= 2, the shorter rotational time constant of 0.2 ns (78%) indicates that at this pH where domain-I expands and intra-domain structure disrupts [1], the porphyrin molecule becomes free to rotate at its binding site without actually leaving the site as evident from the longer rotational time constant. In order to quantify the inter-domain separation between domains – IB and IIA in various conformations of HSA, Förster resonance energy transfer (FRET) technique is applied. Here, the non-radiative transfer of excited state energy from the intrinsic donor fluorophore

Table 8-2. Fluorescence lifetimes (τ) of protoporphyrin IX bound to HSA at different pH(s). Values in parentheses indicate percentages.

Samples	τ_1 (ns)	τ_2 (ns)	τ_3 (ns)
PPIX (pH= 2)	0.19 (14.3)	4.77 (40.7)	8.97 (45.0)
PPIX (pH= 4)	0.34 (15.6)	3.40 (17.8)	14.55 (66.7)
PPIX (pH= 7)	0.40 (10.0)	3.75 (19.2)	14.52 (70.8)
PPIX (pH= 9)	0.43 (15.8)	3.61 (26.3)	13.39 (57.9)
PPIX (pH= 11)	0.25 (21.7)	3.11 (21.7)	14.30 (56.6)

(Trp214) in subdomain-IIA to the acceptor molecule (PPIX) in subdomain-IB is considered (Scheme 8-1). Figure 8-4(a) shows a significant spectral overlap of the Trp emission spectrum and PPIX absorption spectrum at pH= 7. Also, huge quenching of Trp fluorescence in the presence of PPIX is observed (Figure 8-4(b)). Figure 8-4(c) shows the fluorescent decay transients of N-form HSA both in the absence and presence of PPIX. The fluorescence lifetimes of Trp214 emission for various conformations of HSA are tabulated in table 8-3. As evidenced from figure 8-4(c) and table 8-3, much faster decay of tryptophan fluorescence is observed in presence of PPIX indicative of significant energy transfer. The calculated values of overlap integral (J(λ)), energy transfer efficiency (E), Förster radius (R_0) and donor-acceptor (DA) separation (R) between Trp214 and PPIX bound to different pH-induced conformers of HSA (see equations (2-43), (2-45), (2-47) and (2-48b)) are tabulated in table 8-4. The DA separation between Trp214 and PPIX for N-form HSA is 25.4 Å. This distance is in very good agreement with the distance (26.6 Å) between centers of Trp214 and Haem605 obtained from crystal structure of HSA-PPIX complex [11] (scheme 1). In the alkaline pH range the DA separation decreases for B-form while that for A-form is comparatively higher than that for N-form. In acidic pH range for F-form HSA, the DA separation is similar as that for N-form but for E-form HSA there is a large increase in DA distance from 25.4 Å to 33.9 Å. This is consistent with the increase in inter-domain separation and disruption of domain-I, thus showing a significant loss in

Table 8-3. Fluorescence lifetimes (τ) of Trp214 residue of HSA both in absence (denoted as HSA) and presence of protoporphyrin IX (denoted as HSA-PPIX). Values in parentheses indicate percentages.

Samples	τ_1 (ns)	τ_2 (ns)	τ_3 (ns)
HSA (pH=2)	0.23 (31.4)	1.97 (37.2)	5.65 (31.4)
HSA-PPIX (pH= 2)	0.09 (72.5)	1.88 (15.0)	5.60 (12.5)
HSA (pH= 4)	0.25 (34.3)	2.18 (31.4)	5.79 (34.3)
HSA-PPIX (pH= 4)	0.04 (95.0)	1.67 (2.5)	5.63 (2.5)
HSA (pH= 7)	0.28 (28.1)	2.73 (28.1)	7.01 (43.8)
HSA-PPIX (pH= 7)	0.06 (90.8)	1.22 (6.6)	5.83 (2.6)
HSA (pH= 9)	0.20 (36.1)	2.32 (25.0)	6.65 (38.9)
HSA-PPIX (pH= 9)	0.08 (88.9)	1.04 (7.4)	4.01 (3.7)
HSA (pH= 11)	0.14 (61.8)	1.90 (18.2)	5.71 (20.0)
HSA-PPIX (pH= 11)	0.09 (89.7)	1.32 (6.9)	5.33 (3.4)

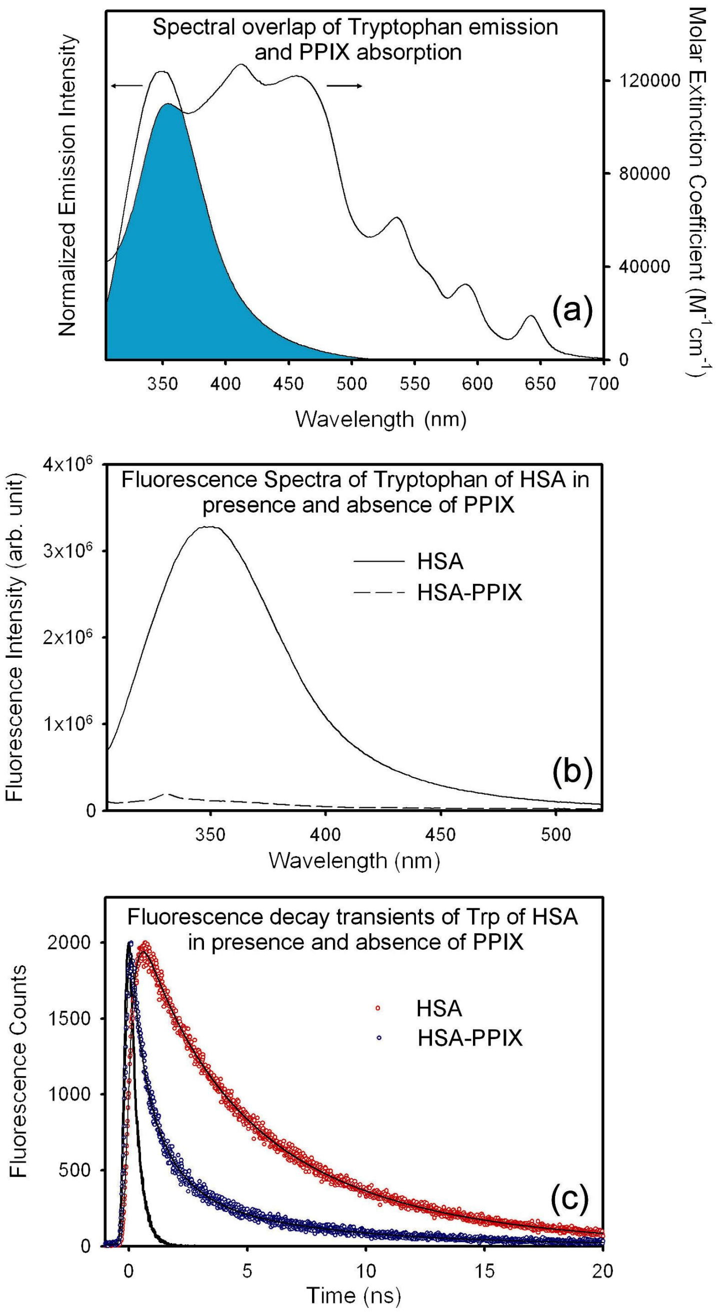

Fig. 8-4. (a) Spectral overlap of Fluorescence spectrum of Trp214 and absorption spectrum of PPIX bound to HSA at pH= 7, (b) Fluorescence spectra (excitation λ= 297 nm) and (c) Fluorescence decay transients of Trp214 (excitation λ= 299 nm, emission λ= 360 nm) in presence and absence of PPIX bound to HSA.

native structure in N-E transition. Such a high structural loss is not observed in case of N-A transition in alkaline pH range. Earlier an attempt has been made to explore the inter-domain (II-I) distance of HSA by covalent labeling of Cys34 and using steady-state fluorescence quenching of Trp214 at various pH of the host solution [12]. While the trend of the inter-domain separation qualitatively matches with our observation, the exact

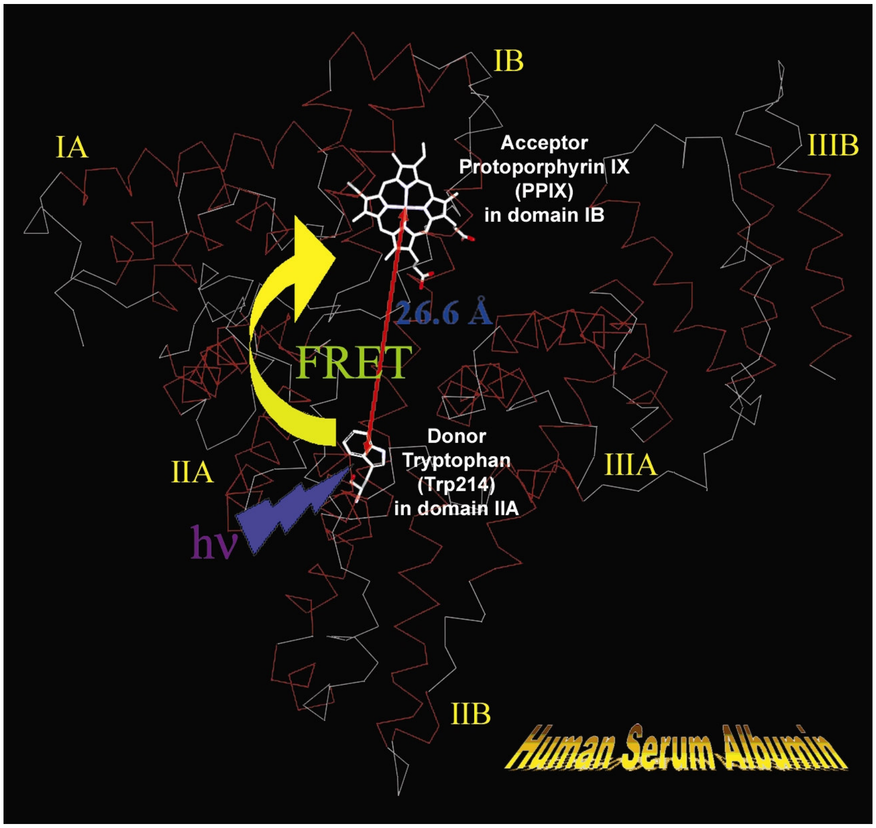

Scheme 8-1. X-ray crystal structure of Human Serum Albumin depicting the FRET between the donor tryptophan (Trp214) and the acceptor Protoporphyrin IX (PPIX). Different subdomains are marked in yellow.

inter-domain separation of 35 Å at pH 7.0 is *not* consistent with our value of 25.4 Å. The reason behind the difference between our data and the previous experimental result [12] is due to the fact that in the earlier study the donor and acceptor reside simultaneously in domains – IA and IIA, respectively and not IB and IIA, which is the case in the present study. The x-ray crystal structure of methemalbumin indicates that there is definite geometric arrangement of Haem605 and Trp214, thus κ^2 cannot be taken to be 0.67. In this case we have calculated the κ^2 value using equation (2-44) from the crystal structure of methemalbumin [11] and used the same for calculation of DA separation. The different angles were determined as follows. In the crystal structure [11] a straight line was drawn from the centre of Haem605 to the centre of indole moiety of Trp214 using WEBLAB VIEWERLITE software. Then the angles between this line and the molecular planes of Haem605 and Trp214 were measured to be 58.6° (θ_A) and 104.7° (θ_D). The dihedral angle (ϕ) between the molecular planes of Haem605 and Trp214 was measured to be 28.14°. The above measured angles gave a value of κ^2= 0.9853 and used the same for calculation of DA separation. The assumption of κ^2 value of 0.67 leads to DA separation of 23.8 Å at pH 7.0, which is 2.8 Å less than the value obtained from the crystal structure.

Table 8-4. Amplitude-weighted lifetime of HSA (τ_D) and HSA-PPIX complex (τ_{DA}), and calculated values of energy transfer efficiency (E), overlap integral (J(λ)), Förster radius (R_0) and donor acceptor distance (R) obtained from FRET between Trp214 (domain-IIA) and PPIX (domain-IB) in HSA at different pH(s).

Samples	**<τ_D> (ns)**	**<τ_{DA}> (ns)**	**E**	**J(λ)** ($M^{-1}cm^{-1}nm^4$)	**R_0 (Å)**	**R (Å)**
pH= 2	2.58	1.05	0.59	1.92×10^{15}	36.1	33.9
pH= 4	2.75	0.22	0.92	2.47×10^{15}	37.5	25.0
pH= 7	3.91	0.29	0.93	1.96×10^{15}	38.7	25.4
pH= 9	3.24	0.30	0.91	1.82×10^{15}	34.8	23.8
pH= 11	1.57	0.35	0.78	1.86×10^{15}	33.0	26.8

In order to quantify the inter-domain separation between domains (IB and IIIA) by using FRET technique, the PPIX labeled HSA molecule is further labeled with an extrinsic dye TNS, which like other hydrophobic dye (triiodobenzoic acid, TIB) expectedly occupies the hydrophobic cavity in the subdomain-IIIA of HSA [13]. Upon complexation with HSA, TNS shows a 61 nm blue shift in the steady-state emission spectrum compared to that in bulk water (485 nm). Figure 8-5(a) shows the fluorescence transients of TNS bound to three different conformers of HSA. At all pH(s), three time constants of the order ~0.3 ns, ~4 ns and ~11 ns are observed (see table 8-5). The multiple fluorescence lifetimes of TNS in HSA could be reflective of the probe in two different binding sites [14] of the protein. In such a case the distance between TNS and PPIX as revealed from FRET experiment would be an average donor-acceptor distance in the protein. The shortest time constant corresponds to the lifetime of those TNS molecules which are loosely (electrostatically) bound at the surface of HSA [14], while ~4 ns and ~11 ns components are the state lifetime of locally excited (LE) state of TNS [15] bound to HSA in the hydrophobic cavity. Figure 8-5(b-d) shows the temporal fluorescence anisotropy decay curve of TNS bound to various conformers of HSA. Three rotational time constants (ϕ) for TNS bound to HSA at all pHs are observed (table 8-6). The shortest rotational time constant may represent the local reorientational time constant for the electrostatically

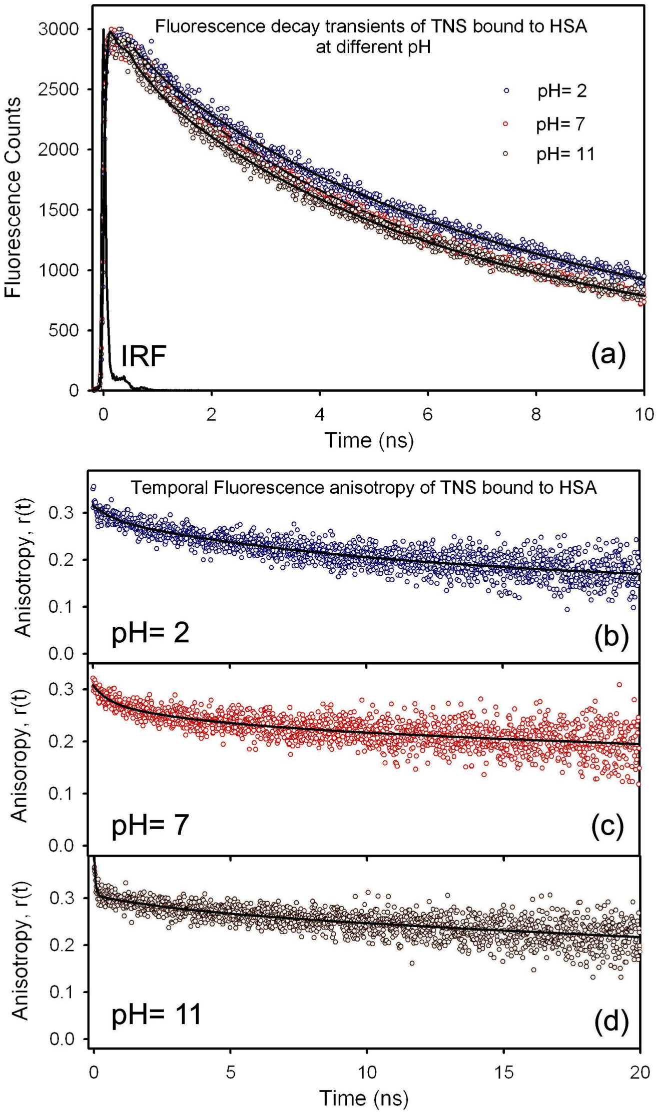

Fig. 8-5. (a) Fluorescence decay transients and temporal fluorescence anisotropy decay (excitation λ= 375 nm, emission λ= 440 nm) of TNS bound to HSA at pH(s): (b) 2, (c) 7 and (d) 11.

bound TNS at the surface of HSA, while the 4-12 ns component correspond to the reorientational motion of TNS bound inside the hydrophobic cavity of HSA. The longest rotational time constant of ~100 ns which does not decay in our experimental time window represents the time scale of global motion of HSA. The longer rotational time constants of ~100 ns differ from the values ~22 ns reported in an earlier femtosecond time-resolved study [2]. It should be noted that the longer time constant of ~100 ns cannot be reported through a femtosecond experiment using a time window of 3 ns. Moreover, the longer rotational time constants of ~100 ns match very well with the rotational correlation time (τ_{rot}) of various pH-induced conformers of HSA calculated from the Debye-Einstein-Stokes relation (equation (2-37)) [16]. Hence, the rotational time constant reported in the present study is more correct. Thus, the fluorescence anisotropy data indicates that at all

Table 8-5. Fluorescence lifetimes of TNS bound to HSA both in absence (denoted as TNS) and presence of protoporphyrin IX (denoted as TNS-PPIX). Values in parentheses indicate percentages.

Samples	τ_1 (ns)	τ_2 (ns)	τ_3 (ns)	τ_4 (ns)
pH= 2, TNS	0.29 (19.6)	3.70 (23.8)	11.14 (56.6)	-
pH= 2, TNS-PPIX	0.21 (24.3)	3.55 (23.7)	11.14 (52.0)	-
pH= 4, TNS	0.28 (23.6)	4.01 (30.6)	11.52 (45.8)	-
pH= 4, TNS-PPIX	0.26 (35.1)	3.50 (27.3)	11.43 (37.6)	-
pH= 7, TNS	0.23 (22.8)	4.39 (37.6)	11.09 (39.6)	-
pH= 7, TNS-PPIX	0.20 (56.9)	2.69 (21.6)	10.42 (21.5)	-
pH= 9, TNS	0.21 (25.7)	4.10 (34.2)	11.10 (40.1)	-
pH= 9, TNS-PPIX	0.05 (77.5)	0.58 (13.1)	3.32 (6.0)	11.73 (3.4)
pH= 11, TNS	0.27 (26.4)	3.56 (29.1)	11.30 (44.6)	-
pH= 11, TNS-PPIX	0.05 (74.0)	0.66 (13.6)	4.19 (8.3)	15.31 (4.1)

Table 8-6. Rotational time constants (ϕ) and initial anisotropy (r_0) of TNS bound to HSA at different pH(s). Values in parentheses indicate percentages.

Samples	ϕ_1 (ns)	ϕ_2 (ns)	ϕ_3 (ns)	r_0
pH= 2	0.96 (9.8)	12.4 (42.9)	500 (47.3)	0.32
pH= 4	0.40 (8.7)	10.9 (16.1)	122 (75.2)	0.31
pH= 7	0.59 (11.0)	4.5 (14.6)	130 (74.4)	0.31
pH= 9	0.55 (12.2)	5.87 (13.2)	141 (74.6)	0.33
pH= 11	0.09 (22.6)	7.32 (12.8)	130 (64.6)	0.39

pHs, TNS remains bound to HSA. It should be noted that the emission peak and nature of temporal fluorescence anisotropy of TNS in HSA in presence and absence of PPIX are same. This observation is consistent with the fact that TNS is not displaced by the incorporation of PPIX in HSA. Figure 8-6(a) shows a significant spectral overlap of the donor TNS bound to HSA (domain-IIIA) and acceptor PPIX (domain-IB) which is indicative of significant nonradiative transfer of excited state energy from TNS to PPIX. Energy transfer is also evident from the significant quenching of TNS bound to HSA fluorescence (figure 8-6(b)) and faster fluorescence decay of TNS fluorescence in presence of PPIX bound to HSA (figure 8-6(c)). The calculated values of overlap integral, energy transfer efficiency, Förster radius and donor-acceptor (DA) separation between TNS and PPIX, bound to various pH-induced conformers of HSA are tabulated in table 8-7. In this case due to the unavailability of the crystal structure of HSA with bound TNS the exact orientation of TNS and PPIX is not known. Under this circumstance κ^2 value is taken to be 0.67 [17]. From table 8-7, it is found that DA separation between PPIX and TNS is 43.3 Å in N-form HSA. This distance further confirms the possible location of TNS to be in the domain-IIIA of HSA as revealed from inter-domain separation in x-ray crystallographic studies [11]. In acidic pH range, during N-F transition the DA separation changes to 54.7 Å and then to 74.2 Å when pH is reduced to pH= 2. This is consistent with two-step expansion during N-E transition, where first a structural loosening at the C-terminal end is

Table 8-7. Amplitude-weighted lifetime of HSA-TNS (τ_D) and HSA-TNS-PPIX complexes (τ_{DA}), and calculated values of energy transfer efficiency (E), overlap integral (J(λ)), Förster radius (R_0) and donor acceptor distance (R) obtained from FRET between TNS bound to HSA (domain-IIIA) and PPIX (domain-IB) in HSA at different pH(s).

Samples	**$<\tau_D>$ (ns)**	**$<\tau_{DA}>$ (ns)**	**E**	**J(λ)** $M^{-1}cm^{-1}nm^4$	**R_0 (Å)**	**R (Å)**
pH= 2	7.24	6.68	0.08	5.36×10^{15}	49.0	74.2
pH= 4	6.57	5.35	0.19	5.38×10^{15}	42.8	54.7
pH= 7	6.1	2.94	0.52	4.46×10^{15}	43.9	43.3
pH= 9	5.91	0.71	0.88	3.41×10^{15}	36.3	26.0
pH= 11	6.14	1.1	0.82	2.86×10^{15}	34.7	26.9

observed during N-F transformation while for F-E transition further loss in tertiary

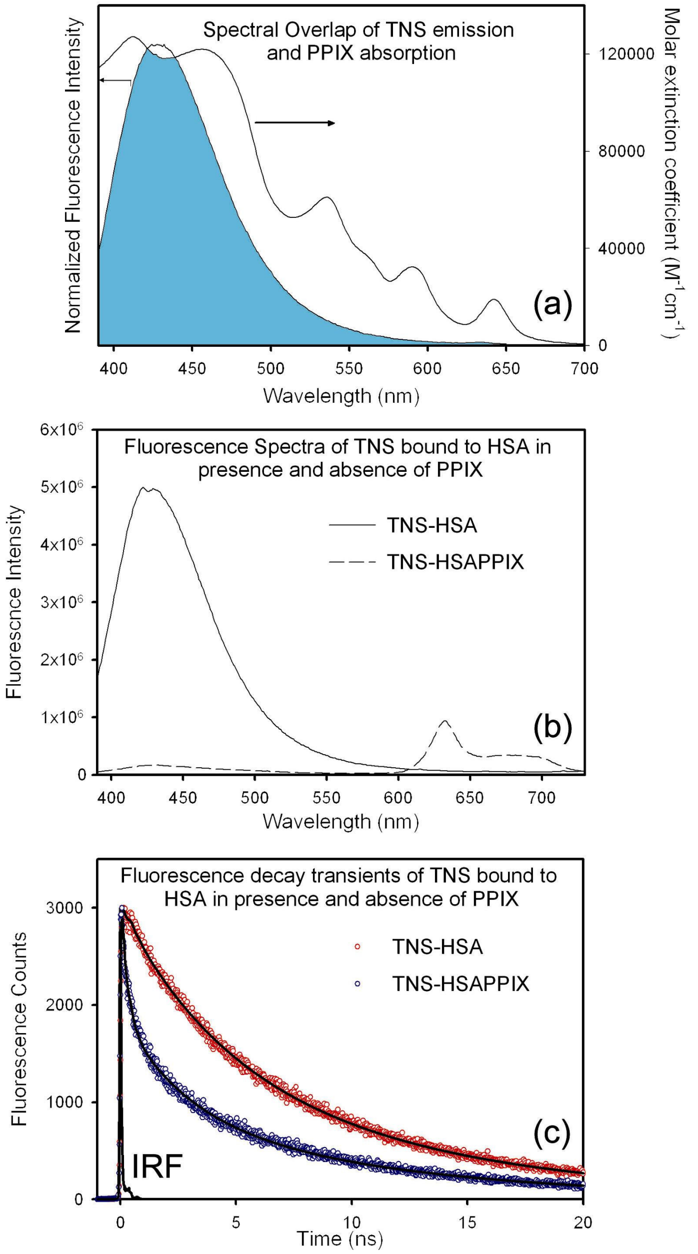

Fig. 8-6. (a) Spectral overlap of Fluorescence spectrum of TNS bound to HSA (excitation λ= 375 nm) and absorption spectrum of PPIX bound to HSA at pH= 7, (b) Fluorescence spectra (excitation λ= 375 nm) and (c) Fluorescence decay transients (excitation λ= 375 nm, emission λ= 440 nm) of TNS bound to HSA in presence and absence of PPIX.

structure along with secondary structural loss in domain-I of HSA are observed [1]. This fact is also supported by our DLS study. In alkaline pH range, decrease in DA separation is observed (table 8-7) which indicates that in alkaline pH range i.e. in N-B transition the structural rearrangement brings domain-IB and IIIA closer to each other. This is, however, not reflected through the contraction of hydrodynamic diameter in DLS study. It is worthy to mention that in the earlier study [18] the FRET using steady state spectroscopy reveals the distance between covalently labeled Cys34 (domain-I) and Tyr411 (domain-III) to be 25.2 Å which differs from our observation of the inter-domain (I-III) distance of 43.3 Å and that from the x-ray crystallographic data [11] of 42.1 Å. This discrepancy in the previous literature [18] may arise due to the incorrect assumption of κ^2 value and/or erroneous determination of fluorescence quantum yield of the donor and the overlap integral of donor emission and acceptor absorption.

8.3. Spectroscopic Studies on the Effect of Temperature on pH-induced Folded States of Human Serum Albumin [19]:

The hydrodynamic diameters (d_H) of HSA at pH(s) 2, 7 and 11 are 14.3, 10.0 and 11.5 nm, respectively. It may indicate that the N-form HSA at pH= 7 undergoes conformational transformation when pH is changed from 7 to 2, with subsequent acid-induced swelling/expansion of the HSA due to the disruption of domain structures (III and I) during N-E transition [1]. However, such structural change is not observed during N-A transition when pH is changed from 7 to 11. Another point to note from figure 8-7(a) is that N-form HSA (pH= 7) does not show an increase in d_H value until 69 ^oC, thereafter d_H starts increasing sharply indicating cooperative temperature-induced unfolding of HSA. The DLS spectra of N-form HSA at three different temperatures are shown in the insert of figure 8-7(a). The d_H value at 75 ^oC is 19.9 nm. From the DLS spectra it can be observed that the native structure of N-form HSA remains same at 25 and 60 ^oC. However, at 75 ^oC the DLS spectrum is broad with peak at higher d_H value. In contrast to N-form HSA, the E-form (pH= 2) and A-form (pH= 11) HSA does not show any change in d_H values (figure 8-7(a)) with increase in temperature. The most plausible reason behind non-occurrence of thermal unfolding of E-form HSA is that this form has already assumed acid-induced expanded form [1] and also at pH≤4 gelification of HSA [20] takes place which further interferes with the thermal denaturation of the protein. In the alkaline pH range, the reason for no change in d_H value with temperature could be the increased stability of HSA due to high ionic strength of the alkaline solution [21].

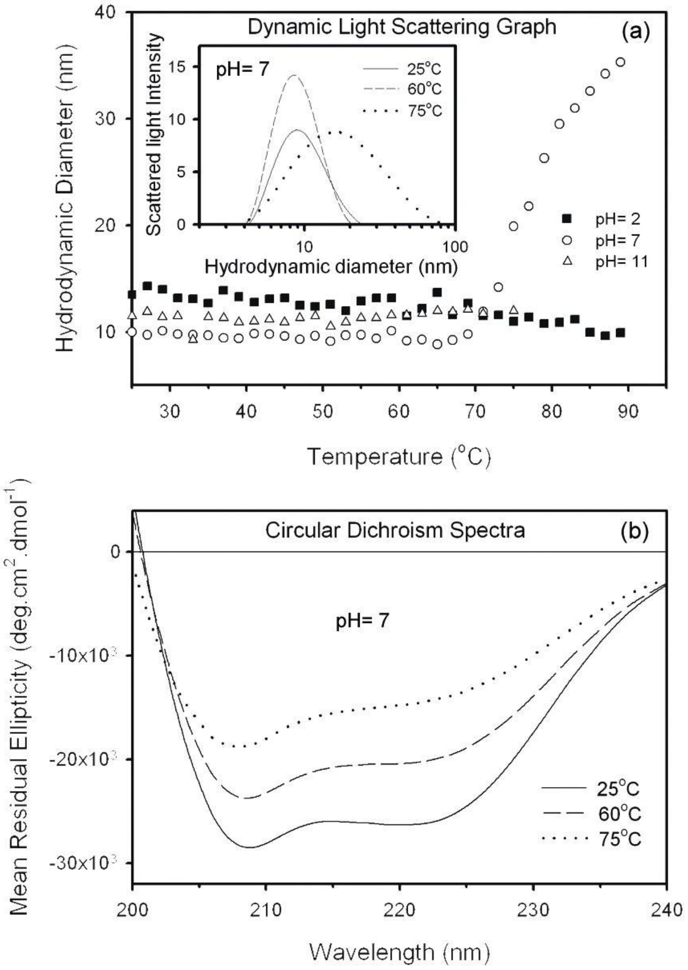

Fig. 8-7. (a) Graph of variation of hydrodynamic diameter of HSA versus temperature at pH= 2, 7 and 11. Insert: Dynamic light scattering spectra of N-form HSA at 25, 60 and 75 °C. (b) Circular dichroism spectra of N-form HSA at 25, 60 and 75 °C.

Figure 8-7(b) shows the CD spectra of N-form HSA at the above three temperatures. Comparison of the mean residual ellipticity of the three forms of HSA at 25 °C shows that there is a significant loss of helix content for E-form HSA (see table 8-8) due to disruption of inter-domain and intra-domain structure (domains – I and II) at pH= 2 [1]. At pH= 11 also, there is a decrease in helicity in comparison to native form (table 8-8).

It can be observed from figure 8-7(b) that with increase in temperature there is a gradual increase in molar ellipticity which indicates a loss of higher order secondary structure (α-helix) and increase in β-sheet and random structural content. This finding is consistent with the characteristics of HSA at higher temperature where the free –SH group at Cys34 exchanges with other disulfide bridges [20-22].

Table 8-8. Percentages of secondary structures in different conformers of Human serum albumin (HSA) at different temperatures.

pH	**Temperature (^{o}C)**	**Secondary Structures**				
		Helix %	**Antiparallel %**	**Parallel %**	**Turns %**	**Random %**
2	25	59.5	4.3	4.5	13.2	18.5
	60	39.5	8.2	7.5	15.9	28.9
	75	31.9	8.2	9.3	16.9	33.7
7	25	66.2	3.3	3.3	12.2	15.0
	60	52.0	5.4	5.8	14.1	22.7
	75	38.0	8.0	8.1	16.0	29.9
11	25	60.4	3.9	4.0	13.0	18.7
	60	32.5	8.4	8.9	17.0	33.2
	75	15.5	12.5	12.3	19.4	40.3

Figure 8-8(a) shows the fluorescence spectra of N-form HSA at three different temperatures. It is found that with increase in temperature fluorescence peak (337 nm) exhibits 5 nm hypsochromic shift with reduction in fluorescence intensity. With increase in temperature, domain-II of HSA unfolds in such a way that Trp214 residue of HSA located at the bottom of 12 Å deep crevice [2] finds itself in a more hydrophobic environment [22]. Fluorescence peak data in table 8-9 show that emission maximum at 337 nm for N-form shifts to 332 nm for E-form at pH= 2 and that to 335 nm for A-form at pH= 11. This is due the fact that at pH= 2, although there occurs an increase inter-domain separation with disruption of the crevice containing Trp214, the local environment around Trp214 rearranges in such a way that the Trp finds itself in a more hydrophobic environment of the protein matrix [3]. Similarly, at pH= 11, the minor changes in secondary structures cause it to be in hydrophobic environment. It is known that domain-II assumes a molten globule form at pH= 2 [1]. Upon increasing the temperature to 75 °C the fluorescence maximum of E-form HSA red shifts from 332 nm to 343 nm which may be due to the unfolding of domain-II below 60 °C followed by unfolding of domain-I above 60 °C causing Trp214 to come in contact with more polar environment (see table 8-9). In contrast to pH= 2, at pH= 11 there occurs a slight blue shift of emission maximum with increase in temperature indicative of slightly hydrophobic environment around Trp214 at higher temperature. At all pH(s), there occurs a decrease in average fluorescence lifetime (τ_D) of Trp214 with increase in temperature, which may be due to the increased proximity with the quenching groups such as protonated carboxyl, protonated imidazole, deprotonated ε-amino groups,

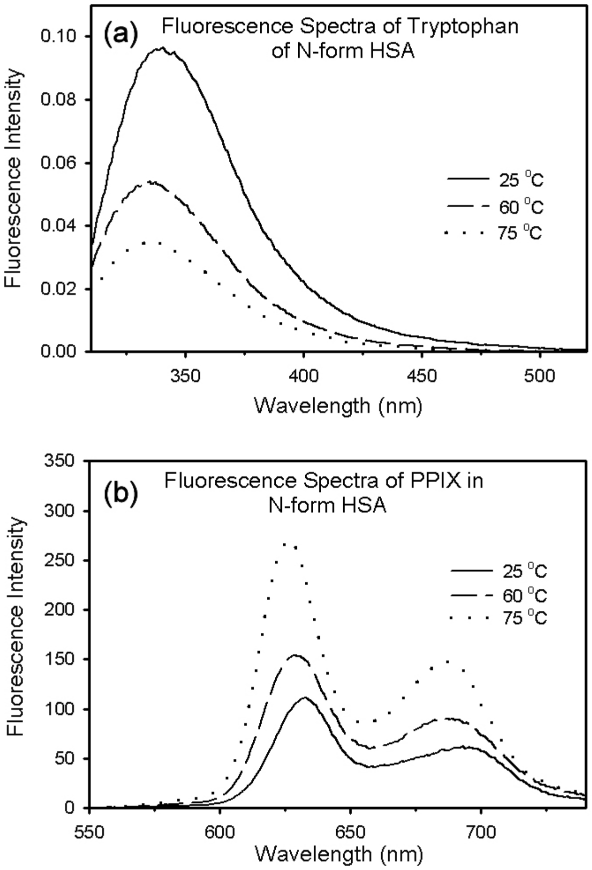

Fig. 8-8. (a) Fluorescence spectra of Tryptophan (Trp214) residue of N-form HSA (excitation λ= 297 nm) at 25, 60 and 75 °C, (b) fluorescence spectra of PPIX (excitation λ= 409 nm) bound to N-form HSA at 25, 60 and 75 °C.

and tyrosinate anion [23, 24] (see table 8-9). At higher temperatures due to increased kinetic energy of the system, high rate of collisions also contribute to the lowering of average fluorescence lifetime. The emission spectra of PPIX labeled HSA at pH= 7 and 11 are similar with intense emission peak at 633 nm. However, at pH= 2, this band at 633 nm decreases in intensity with the appearance of two new peaks at 600 nm and 658 nm due to protonation [5] of intracyclic nitrogen atoms of PPIX. Figure 8-8(b) shows the representative fluorescence spectra of PPIX bound to N-form HSA at different temperatures. Two peaks at ~630 nm and ~660 nm are observed which shows a gradual increase in fluorescence intensity with increasing temperature. However, for E-form HSA there is a gradual decrease while that for A-form HSA there is a decrease (at 60 °C) and then an increase (at 75 °C) of fluorescence intensity of PPIX. The longer fluorescence lifetime data of PPIX bound to HSA (table 8-10) rules out the possibility of PPIX aggregation in presence of HAS [25]. The shorter lifetime of PPIX in HSA at acidic pH as evidenced from table 8-10 could be due to the protonation of PPIX. Since both tryptophan [26] and PPIX [9] have multiexponential fluorescence decays, their amplitude-weighted lifetime has been compared in our present work.

Table 8-9. Calculated values of parameters obtained from FRET between Trp214 (domain-IIA) and PPIX (domain-IB) to different conformers of HSA at different temperatures.

pH	Temperature (°C)	Peak (nm)	$<\tau_D>$ (ns)	$<\tau_{DA}>$ (ns)	J(λ) $M^{-1}cm^{-1}nm^4$	E	R_0 (Å)	R (Å)
2	25	332	2.58	1.05	1.92×10^{15}	0.593	36.1	33.9
	60	334	0.99	0.50	1.87×10^{15}	0.495	30.7	30.8
	75	343	0.64	0.08	1.86×10^{15}	0.876	28.0	20.2
7	25	337	3.91	0.29	1.96×10^{15}	0.926	38.7	25.4
	60	332	1.96	0.03	1.69×10^{15}	0.984	33.9	17.0
	75	332	1.20	0.05	1.64×10^{15}	0.958	31.4	18.6
11	25	335	1.57	0.35	1.86×10^{15}	0.777	33.0	26.8
	60	331	0.38	0.11	1.75×10^{15}	0.697	33.1	28.8
	75	333	0.26	0.11	1.55×10^{15}	0.585	30.2	28.5

Figure 8-9(a-c) shows the fluorescence anisotropy decay curve of PPIX bound to E, N and A conformers of HSA at 25 and 75 °C. The data at 60 °C are not shown in figure 8-9 for the clarity of presentation. For all the conformations a longer rotational time constant of hundreds of nanoseconds consistent with the rotational correlation time (ϕ) obtained from

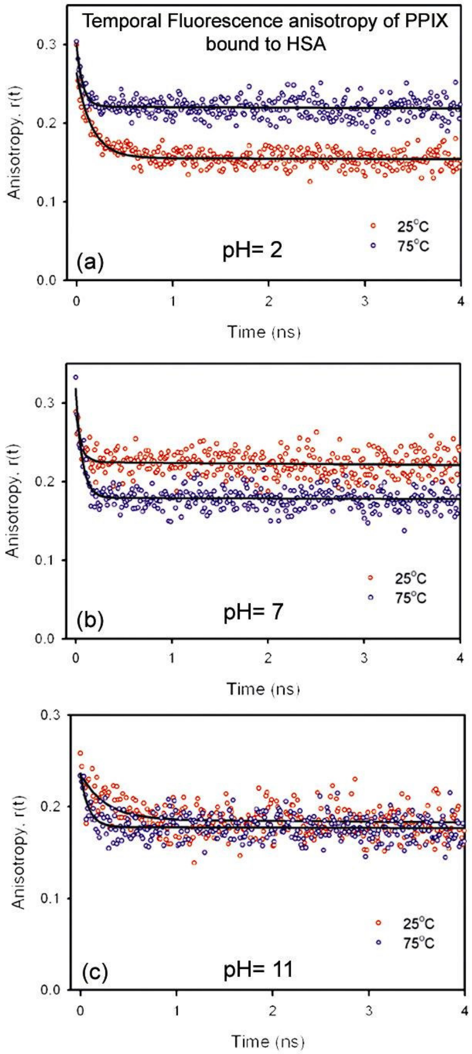

Fig. 8-9. (a) Temporal fluorescence anisotropy decay of PPIX bound to HSA (excitation λ= 409 nm) at pH(s): (a) 2 (emission λ= 605 nm), (b) 7 (emission λ= 630 nm) and (c) 11 (emission λ= 625 nm) at temperatures 25 and 75 °C.

the Debye-Einstein-Stokes relation (equation 2-37), which does not decay in the experimental time window of 50 ns is observed, indicative of restricted environment about PPIX. This time corresponds to the global tumbling time of HSA conformers, which further indicates that at all conformations PPIX remains bound to the protein. A shorter rotational time constant of 0.2 ns is observed at pH= 2 and 11 indicative of local reorientational motion of PPIX at its binding site. However, at pH= 7 a faster time constant of 60 ps is observed indicating rapid librational motion of PPIX due to tighter binding of PPIX to native HSA. Following the significant overlap of Trp214 emission with absorption of PPIX and faster fluorescence decay of Trp214 emission in presence of PPIX, FRET technique was applied in order to estimate the separation between PPIX and Trp214 and thus to determine the inter-domain separation. The average fluorescence lifetimes of Trp214 of HSA in presence and absence of PPIX are tabulated in table 8-9. The calculated values of overlap integral (J(λ)), energy transfer efficiency (E), Förster radius (R_0) and the donor-acceptor separation (R) are tabulated in table 8-9 for different conformations of HSA.

Table 8-10. Fluorescence maximum and average fluorescence lifetime (<τ >) of PPIX bound to different conformers of HSA at different temperatures.

pH	**Temperature (^oC)**	**Wavelength (nm)**	**<τ> (ns)**
2	25	604	6.62
	60	606	5.01
	75	608	4.14
7	25	633	9.74
	60	628	11.26
	75	626	12.64
11	25	625	13.98
	60	625	13.73
	75	626	13.39

The orientation factor κ^2 was calculated to be 0.9853 from the crystal structure of methemalbumin [11]. The DA separation of 25.4 Å obtained for N-form HSA at 25 ^oC is in close agreement with the distance (26.6 Å) between Trp214 and Haem605 obtained from x-ray crystallographic study of PPIX bound to HSA [11]. At pH= 2 for E-form HSA, the DA separation of 33.9 Å is larger than that of N-form HSA, which is consistent with the increase in inter-domain separation and subsequent disruption of domain-I at 25 ^oC. Thus, significant loss of tertiary structure is observed at pH= 2. Upon increasing the temperature, the separation decreases to 17.0 Å in N-form HSA indicating closer approach of Trp214 and PPIX. This may be due to disruption of domain-II of HSA due to which Trp214 becomes a bit flexible and moves closer to PPIX in domain-I. Again at 75 ^{o}C, a slight increase in DA separation to 18.6 Å may indicate the parting away of donor and acceptor due to disruption of domain-I above 60 ^{o}C. For E-form HSA at pH= 2, however, there is a decrease in DA separation from 25 ^{o}C till 75 ^{o}C. This may be due to the fact that in this acid-induced unfolded HSA where domain-II was in molten globule state, starts unfolding with increase in temperature due to which DA separation decreases leading to proximity of donor and acceptor. Further increase in the temperature to 75 ^{o}C causes the conformation to change in such a way that there occurs a further reduction in DA separation. However, the A-form HSA at pH= 11 shows almost no change in DA separation. This may be due to the fact that HSA attains greater stability in alkaline solution compared to that in neutral and acidic pH solutions.

8.4. Conclusions:

In these studies we have explored the ligand binding interaction of a very important transporter protein, human serum albumin (HSA) in its different pH-induced folded states and at different temperatures using picosecond time-resolved polarization gated spectroscopy and Förster resonance energy transfer technique. HSA is a multi-domain protein and adopts various conformations at different pHs, a property that is very important for delivery of different kinds of drugs/ligands to their target cells. Two instances of energy transfer are considered – (a) between intrinsic fluorophore Trp214 (donor) and PPIX (acceptor) and (b) between an extrinsic probe TNS (donor) and PPIX (acceptor). A good correlation of DA distances between the crystal structure of PPIX bound HSA [11] and our study is observed. The DA distances between PPIX and TNS bound to HSA at normal pH direct towards the probable location of TNS to be in domain-IIIA. Also, the study indicated significant structural perturbation of HSA at acidic pH, which is consistent with our CD and DLS data. At alkaline pH, not much change in tertiary structure is observed. The time-resolved fluorescence anisotropic studies reveal that at all pHs, TNS and PPIX remain bound to HSA. DLS studies show that although there occurs a significant temperature-induced unfolding for N-form HSA, no such unfolding is observed for the other acid and alkali induced conformers. From the FRET study, it is observed that with increase in temperature the distance between donor and acceptor decreases for E and N conformers of HSA while that for A conformer the distance remains unchanged which is consistent with the salt-stabilized HSA at higher ionic strength in alkaline solution. Finally, this study on pH-induced conformers of HSA at different temperatures reflects the efficiency of a non-covalently bound probe, PPIX to act as an acceptor for applying FRET technique.

References

[1] M. Dockal, D.C. Carter and F. Ruker, Conformational Transitions of the Three Recombinant Domains of Human Serum Albumin Depending on pH, J. Biol. Chem. 275 (2000) 3042-3050.

[2] W. Qiu, L. Zhang, O. Okobiah, Y. Yang, L. Wang, D. Zhong and A.H. Zewail, Ultrafast Solvation Dynamics of Human Serum Albumin: Correlations with Conformational Transitions and Site-Selected Recognition, J. Phys. Chem. B 110 (2006) 10540-10549.

[3] M.R. Eftink and C.A. Ghiron, Exposure of tryptophyl residues in proteins. Quantitative determination by fluorescence quenching studies, Biochemistry 15 (1976) 672-679.

[4] J.N. Phillips, Physico-chemical properties of porphyrins in: M. Florkin and E. Stotz (Eds.), Comprehensive Biochemistry. Elsevier, Amsterdam, (1963), p. 34.

[5] R.C. Srivastava, V.D. Anand and W.R. Carper, A fluorescence study of hematoporphyrin, Appl. Spectrosc. 27 (1973) 444-449.

[6] U. Hofstra, R.B.M. Koehorst and T.J. Schaafsma, Excited-state properties of water-soluble porphyrin dimers, Chem. Phys. Lett. 130 (1986) 555-559.

[7] N.C. Maiti, S. Mazumdar and P. N., J- and H-Aggregates of Porphyrin-Surfactant Complexes: Time-resolved Fluorescence and Other Spectroscopic Studies, J. Phys. Chem. B 102 (1998) 1528-1538.

[8] A.S.R. Koti and N. Periasamy, Self-Assembly of Template-Directed J-Aggregates of Porphyrin, Chem. Mater. 15 (2003) 369-371.

[9] L. Brancaleon, S.W. Magennis, I.D.W. Samuel, E. Namdas, A. Lesar and H. Moseley, Characterization of the photoproducts of protoporphyrin IX bound to human serum albumin and immunoglobulin G, Biophys. Chem. 109 (2004) 351-360.

[10] D.P. Millar, R.J. Robbins and A.H. Zewail, Direct Observation of the Torsional Dynamics of DNA and RNA by Picosecond Spectroscopy, Proc. Natl. Acad. Sci. USA 77 (1980) 5593-5597.

[11] M. Wardell, Z. Wang, J.X. Ho, J. Robert, F. Ruker, J. Ruble and D.C. Carter, The Atomic Structure of Human Methemalbumin at 1.9 Å, Biochem. Biophys. Res. Comm. 291 (2002) 813-819.

[12] M. Suzukida, H.P. Le, F. Shahid, R.A. Mcpherson, E.R. Birnbaum and D.W. Darnall, Resonance Energy Transfer between Cysteine-34 and Tryptophan-214 in Human Serum Albumin. Distance Measurements as a Function of pH, Biochemistry 22 (1983) 2415-2420.

[13] X.M. He and D.C. Carter, Atomic structure and chemistry of human serum albumin, Nature 358 (1992) 209-215.

[14] R. Wang and F.V. Bright, Detailed Investigation of 2-(p-Toluidinyl) naphthalene-6-sulfonate (TNS) Binding to Bovine Serum Albumin (BSA) by Steady-tate and Time-resolved Fluorescence Spectroscopy, Appl. Spectrosc. 47 (1993) 792-799.

[15] D. Zhong, S.K. Pal and A.H. Zewail, Femtosecond studies of protein-DNA binding and dynamics: Histone I, Chem. Phys. Chem. 2 (2001) 219-227.

[16] P. Debye: Polar Molecules, Dover, New York, (1929).

[17] J.R. Lakowicz: Principles of Fluorescence Spectroscopy, Kluwer Academic/Plenum, New York, (1999).

[18] N. Hagag, E.R. Birnbaum and D.W. Darnall, Resonance Energy Transfer between Cysteine-34, Tryptophan-214, and Tyrosine-411 of Human Serum Albumin, Biochemistry 22 (1983) 2420-2427.

[19] A.K. Shaw and S.K. Pal, Spectroscopic studies on the effect of temperature on pH-induced folded states of Human Serum Albumin, J. Photochem. Photobiol. B: Biol. (2007) (in Press).

[20] G. Barone, C. Giancola and A. Verdilova, DSC studies on the denaturation and aggregation of serum albumins, Thermochim. Acta 199 (1992) 197-205.

[21] M. Yamasaki, H. Yano and K. Aoki, Differential scanning calorimetric studies on bovine serum albumin: I. Effects of pH and ionic strength, Int. J. Biol. Macromol. 12 (1990) 263-268.

[22] K. Flora, J.D. Brennan, G.A. Baker, M.A. Doody and F.V. Bright, Unfolding of Acrylodan-labeled Human Serum Albumin Probed by Steady-State and Time-Resolved Fluorescence Methods, Biophys. J. 75 (1998) 1084-1096.

[23] C.J. Halfman and T. Nishida, Influence of pH and electrolyte on the fluorescence of bovine serum albumin, Biochim. Biophys. Acta 243 (1971) 284-293.

[24] C.J. Halfman and T. Nishida, Nature of the alteration of the fluorescence spectrum of bovine serum albumin produced by the binding of dodecyl sulfate, Biochim. Biophys. Acta 243 (1971) 294-303.

[25] N.C. Maiti, S. Mazumdar and N. Periasamy, Dynamics of Porphyrin Molecules in Micelles. Picosecond Time-Resolved Fluorescence Anisotropy Studies, J. Phys. Chem. 99 (1995) 10708-10715.

[26] X.H. Shen and J. Knutson, Subpicosecond Fluorescence Spectra of Tryptophan in water, J. Phys. Chem. B 105 (2001) 6260-6265.

List of Publications

1. A. K. Shaw and S. K. Pal
"Spectroscopic studies on the effect of temperature on pH-induced folded states of Human Serum Albumin", J. *Photochem. Photobiol. B: Biol.* (2007) (in Press).

2. A. K. Shaw and S. K. Pal
"Fluorescence Relaxation Dynamics of Acridine Orange in Nano-sized Micellar Systems and DNA", *J. Phys. Chem. B* 111 (2007) 4189-4199.

3.* R. Sarkar, A. K. Shaw, S. S. Narayanan, C. Rothe, S. Hintschich, A. Monkman and S. K. Pal
"Size and Shape-dependent Electron-Hole Relaxation Dynamics in CdS Nanocrystals", *Optical Materials* 29 (2007) 1310-1320.

4. A. K. Shaw and S. K. Pal
"Activity of Subtilisin Carlsberg in Macromolecular Crowding", *J. Photochem. Photobiol.* B*: Biol.* 86 (2007) 199-206.

5. A. K. Shaw, R. Sarkar, D. Banerjee, S. Hintschich, A. Monkman and S. K. Pal
"Direct Observation of Protein Residue Solvation Dynamics", *J. Photochem. Photobiol. A: Chem.* 185 (2007) 76-85.

6.* R. Sarkar, A. K. Shaw, S. S. Narayanan, F. Dias, A. Monkman and S. K. Pal "Direct Observation of Protein Folding in Nanoenvironments using a Molecular Ruler", *Biophysical Chemistry* 123 (2006) 40-48.

7.* R. Sarkar, A. K. Shaw, M. Ghosh and S. K. Pal
“Ultrafast Photoinduced Deligation and Ligation Dynamics: DCM in the Micelle and Micelle-Enzyme Complex”, *J. Photochem. Photobiol. B: Biol.* 83 (2006) 213-222.

8.* P. Majumder, R. Sarkar, A. K. Shaw, A. Chakraborty and S. K. Pal
“Ultrafast Dynamics in a Nano-Cage of Enzymes: Solvation and Fluorescence Resonance Energy Transfer in Reverse Micelle”, *Journal of Colloid and Interface Science* 290 (2005) 462-474.

9. A. K. Shaw, R. Sarkar, and S. K. Pal
“Direct Observation of DNA Condensation in a Nano-Cage by Using a Molecular Ruler”, *Chemical Physics Letters* 408 (2005) 366-370.

10.* R. Sarkar, M. Ghosh, A. K. Shaw and S. K. Pal
“Ultrafast Surface Solvation Dynamics and Functionality of an Enzyme alpha-Chymotrypsin Upon Interfacial Binding to a Cationic Micelle”, *J. Photochem. Photobiol. B: Biol.* 79 (2005) 67-78.

* Not included in the thesis.